Design, Modeling, Fabrication and Control of PMN-PT Piezoelectric Systems.

Adrian Dragos Ciubotariu

SPIM

Thèse de Doctorat

école doctorale **sciences pour l'ingénieur et microtechniques**

UFC UNIVERSITÉ DE FRANCHE-COMTÉ

Design, Modeling, Fabrication and Control of PMN-PT Piezoelectric Systems

DRAGOS ADRIAN CIUBOTARIU

SPIM

Thèse de Doctorat

école doctorale **sciences pour l'ingénieur et microtechniques**

UFC UNIVERSITÉ DE FRANCHE-COMTÉ

N° | X | X | X |

THÈSE présentée par

DRAGOS ADRIAN CIUBOTARIU

pour obtenir le

Grade de Docteur de
l'Université de Franche-Comté

Spécialité : **Microfabrication and Electric Engineering**

Design, Modeling, Fabrication and Control of PMN-PT Piezoelectric Systems

Unité de Recherche :
FEMTO-ST, UMR CNRS 6174

Soutenue publiquement le 4 mars 2016 devant le Jury composé de :

FRÉDÉRIC LAMARQUE	Rapporteur	Professeur à l'UTC, Compiègne
CONSTANTIN NITU	Rapporteur	Professeur à l'UPB, Bucarest
JACQUES LOTTIN	Examinateur	Professeur à l'US, SYMME, Savoie
SIMONA NOVEANU	Examinateur	Maître de Conférences à l'UTCN, Cluj-Napoca
PHILIPPE LUTZ	Directeur de thèse	Professeur à l'UFC FEMTO-ST / AS2M
DINU COLTUC	Directeur de thèse	Professeur à l'UVT, Targoviste
CÉDRIC CLÉVY	Encadrant de thèse	Maître de Conférences, UFC, Besançon
IOAN ALEXANDRU IVAN	Encadrant de thèse	Maître de Conférences, ENISE, Saint-Etienne

"I have a friend who's an artist and has sometimes taken a view which I don't agree with very well. He'll hold up a flower and say "look how beautiful it is," and I'll agree. Then he says "I as an artist can see how beautiful this is but you as a scientist take this all apart and it becomes a dull thing," and I think that he's kind of nutty. First of all, the beauty that he sees is available to other people and to me too, I believe. Although I may not be quite as refined aesthetically as he is ... I can appreciate the beauty of a flower. At the same time, I see much more about the flower than he sees. I could imagine the cells in there, the complicated actions inside, which also have a beauty. I mean it's not just beauty at this dimension, at one centimetre; there's also beauty at smaller dimensions, the inner structure, also the processes. The fact that the colours in the flower evolved in order to attract insects to pollinate it is interesting; it means that insects can see the colour. It adds a question: does this aesthetic sense also exist in the lower forms? Why is it aesthetic? All kinds of interesting questions which the science knowledge only adds to the excitement, the mystery and the awe of a flower. It only adds. I don't understand how it subtracts."

Richard Feynman, *BBC Interview, 1981*

This thesis is dedicated to my wife, Marina, who has not only been a constant support, but has put my well being above hers, has put her life on hold and has helped me improve. Without her, pushing through would have been an impossible feat.

Thank you with all my being

CONTENTS

List of Acronyms

ADMAN - Advanced Devices for micro- and nano-scale MANipulation and characterization

AFM - Atomic Force Microscopy

AS2M - Automatic Control and Micro-Mechatronic Systems

CODE - COntrol and DEsign

DE - Dielectric Elastomer

DEA - Dielectric Elastomer Actuator

DMD - Digital Micro-mirror Device

DoF - Degree of Freedom

DRIE - Deep Reactive Ion Etching

EDS - Energy-Dispersive Spectroscopy

FEM - Finite Elements Method

FEMTO-ST - Franche-Comté Electronique, Mécanique, Thermique et Optique - Sciences et Technologies

GLV - Grating Light Valve

LN - Lithium(Li) Niobate(Ni)

LT - Lithium(Li) Titanate(Ti)

MEMS - Micro-Electro-Mechanical-Systems

MIOP - Micro-systems for Instrumented OPtical chips

MOB - Micro-Optical-Benches

MOEMS - Micro-Opto-Electro-Mechanical-Systems

MOT - Micro-Optical Table

MPB - Morphotropic Phase Boundary

OCT - Optical Coherence Tomography

OXC - Optical Cross Connectors

PCB - Printed Circuit Board

PMN-PT - Lead(Pb) Magnesium(Mg) Niobate(Ni) - Lead(Pb) Titanate(Ti)

PZN - Lead(Pb) Zinc(Zn) Titanate(Ti)

PZT - Lead(Pb) Zirconium(Zr) Titanate(Ti)

RFS-MOB - Reconfigurable Free Space - Micro Optical Bench

RFS-MOB - Reconfigurable Free-Space Micro-Optical Bench

SEM - Scanning Electron Microscope

SMA - Shape Memory Alloy

SOI - Silicon-On-Insulator

SSH - Synchronized Switch Harvesting

STM - Scanning Tunnelling Microscopes

GENERAL INTRODUCTION

There is an ever increasing need for miniaturised systems in today's technological world and this presents new challenges for scientists and industry. There are a number of advantages that miniaturization brings, such as increase in performances, reduction of energy requirements, low costs due to their batch fabrication, storage, transport and the ability to integrate several functions in small volumes.

This has lead to the development of specific technologies aimed to the design, fabrication and integration of special systems that incorporate mechanical, electrical and even optical features. Initially Micro-Electro-Mechanical Systems (MEMS) started being developed, focusing on the integration of, what are now called, smart materials, due to their capability to react to environment changes and giving a measurable reaction (temperature variations, electrical current intensity or potential etc.). After decades of research and development, optical capabilities have been added, thus creating Micro-Opto-Electro-Mechanical Systems (MOEMS). They have aided in the implementation of optical data communication, increasing speeds by using optical routers and optical storage mediums. They have also helped the development of new imaging technologies like Optical Coherence Tomography (OCT) and measurement tools like microspectrometers, laser vibrometers or interferometers. With newer materials being developed, these systems too have been reduced in size, a trend that is still followed today. This trend has also been helped by the development of micro-fabrication tools and the reduction in size of complex systems. The use of smart materials also allowed for the micro-assembly tools used to gain in dexterity while reducing their overall complexity. This is the case of microgrippers.

The fabrication of MOEMS using an approach combining advanced micro-fabrication and robotic micro-assembly techniques has been presented in several works [Bargiel et al., 2010, Dechev et al., 2004, Das et al., 2012] and has shown its effectiveness in the fabrication of complex, out-of-plane MOEMS structures. The contribution of the micro-assembly notably relies on the cost reduction, design flexibility and optimisation in order to guarantee the best final component, which presents all the required features. The issues that still present themselves while developing both micro-robotic techniques and the MOEMS on which they are used, count actuator and sensor integration ease, degrees of freedom of these systems, dynamics and displacement ranges.

Some of these issues are tackled in this work, which has been conducted in the FEMTO-ST (Franche-Comté Electronique, Mécanique, Thermique et Optique - Sciences et Technologies) Institute in Besançon. The work is part of a co-supervised thesis with the "Valahia" University of Targoviste. This has been set up as advancements in micro-manipulation technologies have been noted at "Valahia" University of Targoviste since the early 2000s. This PhD work has been funded by the Bourgogne-Franche-Comté region, in the framework of MIOP (Micro-systems for Instrumented OPtical chips) project and the

”Valahia” University of Targoviste, in the framework of the ADMAN (Advanced Devices for micro- and nano-scale MANipulation and characterization) project. The Automatic Control and Micro-Mechatronic Systems (AS2M) department of the FEMTO-ST Institute has been interested in the micro-manipulation and the fabrication of MEMS and MOEMS using robotic micro-assembly for several years [Agnus et al., 2013]. AS2M department is divided in four research teams with the main topics being control, micro-mechatronics, micro-robotics, nano-robotics, biomedical robotics, micro-assembly, micro-manipulation, sensors, actuators, prognostics and health management. This PhD has been done as part of the research team CODE (COntrol and DEsign) of the AS2M department since October 2012. The CODE team investigates innovative control solutions well adapted for micro-systems while considering the design, modeling and control of micro-mechatronic and micro-robotic structure.

The objectives of these projects are, under MIOP, to design and develop three-dimensional (3D) reconfigurable micro-optical benches using micro-fabrication technology for the fabrication of silicon-based MOEMS and, under ADMAN, to design and develop a robotic, multi-DoF micro-assembly capable structure (MEMS). In both cases a very potent, highly integrated solution is sought. Robotic micro-assembly tools directly impact the assembly of several MOEMS, called hybrid MOEMS, as they issue from different micro-fabrication processes. It is thus needed to optimize each of them and consequently to increase the performances of the resulting structure. The main challenge is to find a material that's suitable for integration into these studied structures (MEMS and MOEMS) while also bringing performance improvements in terms of displacement, both range and accuracy, and control. As piezoelectric materials offer the best option for size reduction while maintaining their properties, a novel one is chosen called lead magnesium niobate - lead titanate (PMN-PT).

During this PhD work, two specific cuts of this piezoelectric material (PMN-PT) were investigated, in order to quantify their performances as integrated actuators in both micro-robotic structures and MOEMS. The monocrystalline structure is also taken into account when the performances of PMN-PT as the integrated solution for an actuator is first analysed. In the case of a microgripper the study is done with the aid of a cantilever structure. The focus is then set on the performances PMN-PT presents when integrated in a MOEMS structure. Experimental demonstrators have been fabricated in both cases.

In chapter 1, the need for improvements in the micro-robotics and MOEMS fields of study is presented through examples of current applications and their limitations both in terms of usefulness and cost. The current challenges are briefly enumerated, highlighting the most researched topics. They account for the micro-fabrication constraints, the dynamics of micro-systems and their dependency to environment parameter variation as well as the employed materials. As these works have been financed by two distinct projects, they are also described, focusing on the technological aspects each of them tackles and what constraints they bring to the work, such as large displacement and high dynamic needs, while not compromising accuracy. The use of several, commonly used, smart materials is highlighted, presenting some of their features as well as their downsides and limitations. Emphasis is made on the piezoelectric materials, as they present a very wide variety of features and properties, very useful in both MEMS and MOEMS.

In chapter 2, a description of the chosen material is presented, PMN-PT, presenting the influencing factors that stem from its fabrication and how it influences its characterising coefficients. Experimental work has been carried out to identify the numerical values

of the influencing coefficients, for which special devices have been developed. Values that concur with literature have been found for the piezoelectric coefficients and the coercive field values. The electric an mechanical properties are then presented, focusing on the crystalline orientation influence. Two cuts, which present particular interest, are presented, highlighting their most important attributes.

In chapter 3, the study of the PMN-PT[011] anisotropic cut is furthered studied. This is done based on an actuator which brings together large displacement with small volume. This case study is done by implementing PMN-PT in a well knows structure, cantilever beams. A static model that takes into the account the addition of a 3rd DoF and the influence of the forces generated at the tip of the cantilever is proposed. The displacement capabilities and force generation are then studied in order to asses the usability of PMN-PT[011] as the integrated actuator in a microgripper. Values that surpass those of PZT by twofold have been found in displacement and generated forces, while nonlinearities close to three times lower have also been observed. The contribution PMN-PT brings to the capabilities of micro-assembly technologies are exemplified both by generating complex trajectory with the cantilever tip and a 6 DoF capable microgripper.

In chapter 4, the study of the PMN-PT[001] longitudinal cut based actuator is presented, bringing together large displacement and very high dynamics with small volume. According to the encompassing project limiting conditions, the model for a rectangle structure is presented. The displacement study is done with the aid of an actuator of varying width and a $0.2\ mm$ thickness. High displacements, without the need of amplification structures, usable in interferometry, were observed. This has been achieved by implementing a special design. As the actuator is meant for MOEMS integration, surface quality is very important, alongside the displacement dynamics ranges. Nonlinearities, like hysteresis, the working frequencies (in the MHz region) and the formation of surface aberrations were also studied. The better results, when compared to classic materials like PZT, and the ease of integration have helped to use a bulk PMN-PT micro actuator into a Reconfigurable Free Space - Micro Optical Bench (RFS-MOB) compatible structure and presented.

After the presentation of these works, the results are discussed and future works are proposed.

1

INTEGRATED MICRO-ACTUATORS FOR MICRO-MECHANICAL SYSTEMS

This chapter sets the contour of the PhD works presented by introducing the current technological developments, limitations and needs for continuing the miniaturization of complex systems used in different areas of interest (such as consumer electronics, medical applications and the improvement of research tools). The collaborative framework of the two encompassing projects, MIOP and ADMAN, that are responsible for funding are also presented. The end-needs account for actuators capable of delivering high displacement while maintaining system simplicity and reliability. A short overview on the materials and technologies used nowadays follows. The focus is on the versatility of piezoelectric materials, a group from which the chosen PMN-PT material stands out, due to its electromechanical properties.

1.1/ INTRODUCTION

The technological requirements of today are at very high levels in areas such as consumer electronics (computers, GPS devices and especially mobile phones), medical and surgical equipment and other systems that integrate several complex functions. Each of the mentioned categories impose strict conditions in terms of size, dynamics, costs and fabrication.

Advancements in miniaturizing have been achieved at a seemingly accelerated pace as new technologies are developed to fulfil more and more complex tasks, similar to *Moore's law* for computational devices. The development of special materials and their understanding is a driving force in the development of micro-systems that meet functions previously accomplished by large and cumbersome ones. The size reduction brings a number of constraints to the fabrication procedure, but is the catalyst to developing materials which integrate two or more functions is novel design micro-systems like integrated actuation, self-sensing and structural properties.

The following sections focus on the current developments in domains of interest such as micro-robotics (generally used in micro-assembly tasks) and complex micro-

systems as developed through the frameworks of different projects. The challenges met while working at these scales are then exemplified as well as the development of very capable so-called *smart-materials*. The focus is set on a category that's ever increasing and offers solutions to a lot of applications, piezoelectric materials. This also serves as an introduction to the description of the chosen material, PMN-PT, a man-made crystal that presents very high piezoelectric properties.

1.2/ CONTEXT OF THE WORK

Nowadays, the micro-systems functional requirements keep ever increasing. Many products notably require the integration of smart materials for actuation and/or sensing purposes. Micro-assembly allows the construction of complex micro-systems which can not be fabricated using micro-manufacturing processes alone [Gauthier et al., 2011]. Micro-robotics advancements in the area of micro-assembly are most notably of interest as they enable the fabrication of out-of-plane micro-structures that require micro-components obtained from two or more different micro-fabrication processes. These processes apply not only to the more common micro-components of energy harvesters or sensors, but are also used in when developing micro-systems that incorporate optical functions. This new category of micro-optical devices allows for the development of ever improving and more reliable materials. The works presented in this thesis set to tackle some of the problems encountered in these fields of study.

An overview of the current technologies and techniques is presented, for a better situation of the work. Each area of interest is presented to highlight the advancements so far attained. The following sections address micro-robotics and micro-opto-electro-mechanical systems, respectively. After their presentation, the challenges still to be addressed are presented.

1.2.1/ MICRO-ROBOTICS USED FOR ASSEMBLY

For micro-assembly to be performed, several steps have to be realized in sequence: take, remove, displace, insert, release, etc. These steps can be done manually or with the aid of robotic systems. Several micro-assembly approaches have been studied and can be classified into several categories depending on the considered approach.

Several methods exist for the manipulation of the micro-components and are divided in non-contact and contact manipulation technologies. The non-contact manipulation can be done by the use of an external driving force and the contact manipulation can be done by the use of a microgripper which is convenient to the application. A particular type of micro-assembly technology is self assembly. It consists of assembling micro-components together spontaneously by subjecting them to the influence of an external driving force. However, the self-assembly technique is most frequently used in combination with contact manipulation (*serial* - one by one or *parallel* - batch of components at a time). This results in hybrid techniques. In medical applications non-contact solutions are preferred, such as magnetic [Zou et al., 2001] or dielectrophoresis [Kharboutly, 2011]. The use of self-assembly limits the effect of contact forces in the micro-assembly which is an important issue at the micro-scale and take benefit form surface forces which are predominant at the micro-scale (electrostatic forces or capillary forces). Their advantages is

the capability of producing large quantity of micro-components in a small operating time and with high precision. High volume micro-assembly is often done with the aid of capillary forces [Srinivasan et al., 2001] present in liquids, a good example of such handling techniques being shown in Figure 1.1.

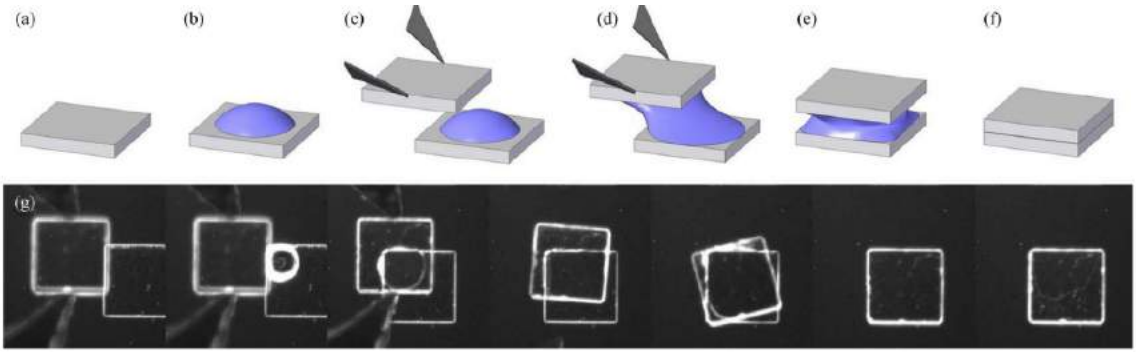

Figure 1.1: Hybrid handling technique [Sariola et al., 2010] of a $50x50x40\ \mu m^3$. (a) Assembly site is on top of a micro-components. (b) Droplet of water is dispensed on the bottom part. (c) Microgripper approaches the release site with a part. (d) Droplet contacts with the top part and wets between the parts, which forms a meniscus. (e) Microgripper releases the part and the capillary force aligns the parts. (f) Water between the two parts evaporates, which leaves the two parts aligned. (g) Image sequence of the actual experiment, as viewed from the top.

Depending on the application some solutions are preferred over others. While low frequency procedures make use of capilary forces in liquids, in the case of high frequency applications electrostatic forces [Böhringer et al., 1998] are combined with contact manipulation, either for fixing the micro-object or releasing it. Heat [Ebefors et al., 1999] can also be used to similar effect when the frequency is not an important factor.

Classifications can be based on the throughput of fabrication (serial or parallel), type of end-effectors (contact or non-contact) or level of human intervention (manual, teleoperated or automated).

Contact Manipulation is a sequential process in which assembly tasks are performed one after the other. To complete one micro-assembly, series of subtasks are required, such as grasping micro-components, manipulating them, joining them to others, etc. Often the use of a microgripper is required, depending on what is convenient for the application. Many researches have been done on the microgrippers [Lang, 2008]. The choice of microgripper is done relatively to the application and to the microassembly constraints. The microgrippers can be divided into two parts: passive, that don't have actuators, and active, that include/integrate actuators.

Microgrippers can be divided into two categories: passive and active. The passive ones do not have actuators and, in general, the compliance in the passive fingers is introduced either in the microgripper [Dechev et al., 2004, Tsai et al., 2005, Wang et al., 2008a] or the micro-object [Das et al., 2007, Das et al., 2012]. In terms of active microgrippers, multiple types of actuators are employed such as electrostatic actuators [Beyeler et al., 2007, Piriyanont et al., 2013], electrothermal actuators [Kim et al., 2008, Sun et al., 2014] and piezoelectric actuators [Pérez et al., 2005,

Wang et al., 2013].

Passive microgrippers
Several works using passive microgrippers are presented in [Bahadur et al., 2005, Tsai et al., 2005, Das et al., 2008, Das et al., 2012]and while these papers deal a conventional microgripping configurations, an orthogonal two passive fingers microgripper has been proposed in [Thompson et al., 2001]. While this system can do pick and place task with micro-objects, it's best used for reorienting them (as seen in Figure 1.2) When

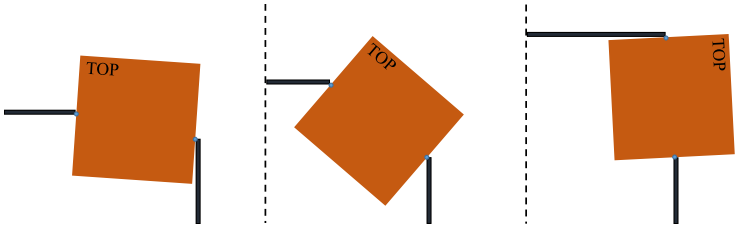

Figure 1.2: Orthogonal passive fingers gripper rotating a micro-object by 90°, as proposed by [Thompson et al., 2001].

using passive microgrippers, the design of the micro-components is changed to accommodate some interfaces. This is done in order to manipulate the micro-component and can be eliminated after installation. The microgripper is pushed so that is enters in contact with the component and when that happens, the compliant fingers of the gripper deform and the micro-component is and fixed between the two fingers of the microgripper.

The setback of using these passive microgripper is that, due to usage specificity, if the micro-component is altered ever so slightly, the microgripper design needs to be altered as well.

Active-finger Microgrippers also have passive components (like the end effectors) but bring the precision movements closer to the manipulated object, thus making them more versatile. There is a wide range of Microgrippers used for micro-manipulation and micro-assembly [Carrozza et al., 2000, Kohl et al., 2002, Kim et al., 2004, Millet et al., 2004, Chronis et al., 2005]. They can be used in a variety of scenarios as they can manipulate different materials, from passive micro-components to biological matter. This is also due to them being able to integrate different sensors or even having self-sensing abilities [Dosch et al., 1992]. A multi purpose active microgripper is presented in [Beyeler et al., 2007] through the design of an electrostatic actuated, capacitive force sensing Microgripper (Figure 1.3). It was fabricated by expanding the design of a multi-DoF capacitive force sensor [Sun et al., 2002b, Sun et al., 2005].

Micro-assembly can also be classified in terms of level of human intervention into two categories: when there is involvement, either direct (*manual*) or indirect (*teleoperated*) and where the process is completely *automated*. For teleoperated and automated micro-assembly there is a need for robotic stations to help perform complex 3D assembly tasks with high precision. These stages bring additional degrees-of-freedom to the micro-assembly station.

One objective of the work detailed here is the usage of a novel material that adds degrees of freedom to the Microgrippers as well as reduce the number of steps needed to assemble micro-systems. This is considered because micro-positioning stages are multiple times larger than the manipulated micro-object, they can not be brought in the proximity of the work space and always require external sensors for their precise con-

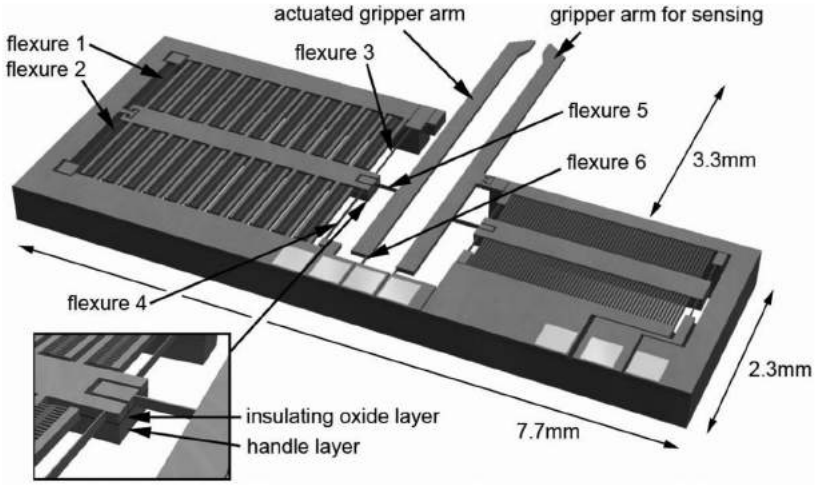

Figure 1.3: Solid model of the microgripper with integrated force sensor [Beyeler et al., 2007].

trol. By using a smart material to act both as actuator and as structure of an assembly Microgripper these work space limitations are overcome.

Technologies are being developed to aid manipulation at the micro scale. They range from more conventional ones like contact manipulation using Microgrippers to more exotic solutions like contactless micro-manipulations. While the first are straightforward and use structures similar to tweezers, only of very small dimensions, the latter can be done by the use of an external driving force (magnetic, electrostatic, sound waves etc.)

1.2.2/ MICRO-OPTO-ELECTRO-MECHANICAL SYSTEMS

Demands in a variety of industries, such as telecommunications, automotive, IT or medical instrumentation biomedical, have yielded in a growth of Micro Systems manufacturing and their development. The reduction in size has a direct impact on their costs and manufacturing time as batch fabrication techniques are developed and optimized to incorporate high capabilities in more integrated solutions.

Micro-Opto-Electro-Mechanical Systems (MOEMS) are micro-systems which combine electrical and mechanical functions to optics thus opening the doors to a variety of applications such as sensors, optical switches [Yeow et al., 2001] or accelerometers [Zuwei et al., 2012]. This is due to the advantages of using optical signals within the micro-system, such as being not susceptible to magnetic or electromagnetic perturbations, making them ideal for difficult environments. They carry a very low amount of noise, in comparison with electrical signals, making MOEMS a reliable technology for high volume data transfer. This makes them preferable not only in information processing, but also in high precision measurements like interferometry or spectrometry. Although they present advantages, MOEMS also have some downsides, as presented in [Syms et al., 2002] and reminded here:

As the MOEMS advantages outweigh the inconveniences, which are related to particular usages, researches have been motivated to develop more applications

Advantages	Disadvantages
Little signal loss	*Complex manufacturing*
Low signal interference	Vibration sensitive *
Polarization insensitive	Temperature sensitive
Wavelength sensitive	Poor power handling
Compact and scalable	Low speed *
Low holding power	High Voltage

* applies only to complex structures and they are very dependent on the materials used

that cover a more and more wide scope such as Optical Coherence Tomography [Aljasem et al., 2011], optical interconnects [Deeds et al., 2005],micro-spectrometers [Gorecki et al., 2011], implantable optical sensors [Fiala et al., 2013], photon counters [Niclass et al., 2012], endomicroscopy [Weber et al., 2012] etc. The development of these applications have lead to them being commercialized as a result to the need and pertinence, small size, reduced costs and high efficiency.

The key point is the issue of manufacturing. Its complexity makes it a disadvantage. This is due to the number of individual components that make a functioning MOEMS, as well as the intermediary steps required for a component to be fabricated. An extra degree of difficulty is added by optical components having out-of-plane functionality. This is to say that, although fabricated on wafers as in plane components, in order to fulfil the intended optical function they have to be repositioned, as exemplified in Figure 1.4.

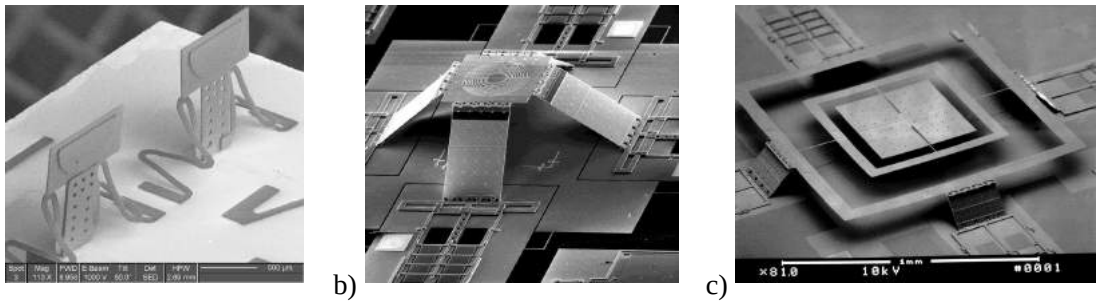

Figure 1.4: MOEMS components with a) static function micro-mirror [Sameoto et al., 2007], b) actuated as the XYZ displacement capable micro-lens, c) the tip-tilt scanning micro-mirror [Wu et al., 1999].

MOEMS can be divided, according to use, in three categories, each to be detailed here. While some systems are developed to be commercialized, others remain in research stages as new materials and concepts bring great variation.

Sensors

There are a wide variety of uses for MOEMS, from sensors that require high precision like accelerometers, frequency detectors or medical instruments needed in surgery, to distance controllers and barcode readers. Most recently, with the proliferation of mobile phone technologies, MOEMS have started to become standard components because of image correction needs, laser based focusing or display casting in the form of pico projectors.

In terms of precision, two very common applications are those of interferometry

and, the very closely related, micro-spectrometry (Figure 1.5). The first is used for highly accurate, but simple, distance measurements, where the use of a fixed mirror is augmented by a moving one and the resulting interference pattern on the sensor are then registered and analysed. The latter relies on more data being carried by the laser beam used. While interferometry is dynamic and modifies the path difference δ (between the optical path of the two beams), micro-spectrometry is stationary and relies on interference pattern recognition. With light coming from the light source S, passing through the beam splitter hitting the reference mirror M_2 and the actuated mirror M_1 (a), or the stationary mirror M_3 (b), creating the image of the mirror M_2', the two different patterns emerge: optical path difference S_1'-S_2' or the interference pattern, respectively. This is achieved by having an actuated mirror capable of out of plane motions - translation for M_1 and rotation for M_3.

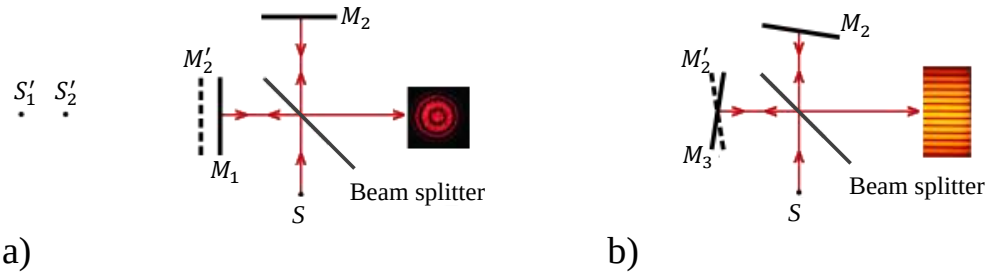

Figure 1.5: a) Interferometer working principle and b) spectrometer working principle. [Epzcaw, 2012]

An optical micro-spectrometer enables the decomposition of light in its spectrum, with detectors for each wavelength. The measurement of the sensor is the comparison between the initial spectrum (emitted) and the returned signal that has been altered by the sample, either through absorption or shifts, as seen in Figure 1.6. This is applicable to

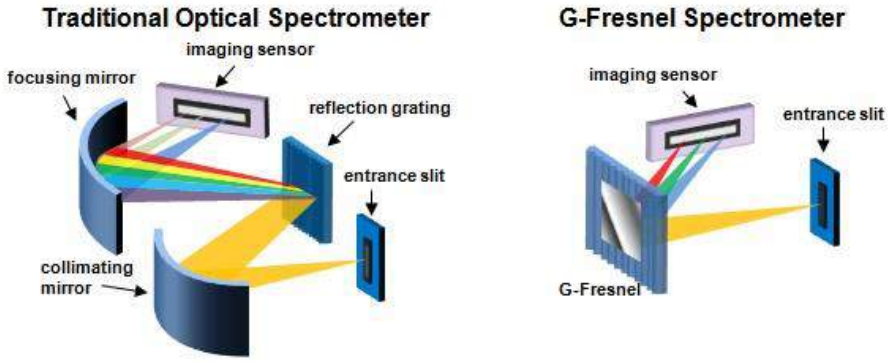

Figure 1.6: Common spectrometer setups used [Yang et al., 2010].

medical diagnosis tools, detection of chemical elements or composition, colour detection

etc. Two configurations for the fabrication of micro-spectrometers exist: either using time dependent scanning or using the diffraction phenomena.

In the case of Michelson interferometer, it is often observed that one of the mirrors is driven to scan. In this case, of great importance is the integration of the actuator to the mirror. The travel range of the mirror defines the spectral resolution achieved by the spectrometer at a given wavelength. Works such as [Manzardo, 2002, Noell et al., 2002] describe potential actuation solutions for these mirrors. The specific configuration of the actuator reduces the nonlinearities of moving the mirror through its push-pull actuation. Though at large scales, these issues have a number of solutions, at the micro-scale, they persist as high displacements in small volumes require complex structures, which are difficult to assemble and often fail to last.

MOEMS have also helped enrich the capacities of computational imaging. One such way is the development of Optical Coherence Tomography (OCT) tools, an established medical imaging technique that benefits form MOEMS technology for more than 20 years [Huang et al., 1991]. This technology has been introduced in medical fields like dermatology and ophthalmology as early as the 90s [Puliafito et al., 1995, Welzel, 2001, Fujimoto, 2003, Thomas et al., 2004]. It has also been successfully used in imaging internal organs such as the Gastrointestinal apparatus [Jackle et al., 2000, Sivak et al., 2000] and, due to its micro-scale resolution capabilities of 1 to 15 μm (depending on the light source employed), it enables the early stages detection of cancer.

The first MEMS-based OCT endoscope employing a one-dimensional (1D) electrothermally actuated MEMS mirror [Pan et al., 2001] was introduced, with the development of MOEMS technology and demonstrated a (2D) cross section image. Various other forms of MEMS mirrors have been developed as the scanning engine in endoscopic probes for OCT systems including electrostatic [Jung et al., 2006], magnetic [Kim et al., 2007], piezoelectric [Gilchrist et al., 2009], electrothermal [Xie et al., 2003] and pneumatic actuated mirrors [Aljasem et al., 2008]. Figure 1.7 shows an endoscopic OCT system [Boppart, 2012] equipped with an actuated micro-mirror developed by [Xie et al., 2003]. This is a perfect example of how advancements done in micro-mirror

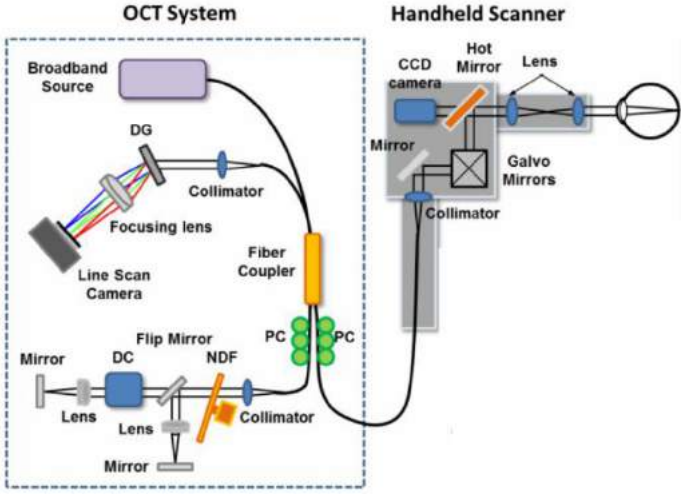

Figure 1.7: OCT System diagram with functional components [Boppart, 2012].

research help improve current technologies. The challenge now is to further reduce the complexity of actuated micro-mirrors, something this work sets to do. Another major ben-

efit of using MOEMS in the medical field is that, like the OCT, these devices are optical fibre based system, and thus they are compact, portable, free of radiation, and affordable.

All the presented applications have as the common denominator micro-structures, such as the actuated micro-mirrors, and although they use different working principles, they rely on the integrating system being compact. Thus improvements in their fabrication are sought, as well as materials that work reliably at high frequencies while also reducing the overall dimensions of the system. These requirements also apply to the infrastructure around transmitting and storing information.

Data communication and storage

In the case of communication, MOEMS have gained ground with the development of optical fibre based networking and in the case of storage it's the development of optical disc technology, such as CD/DVD/BLU-RAY, that increased the demand for more reliable and easy to produce MOEMS.

Due to its physical properties, light began being used more and more in the transmission of data on large scale and this has brought about an issue that has been around ever since the development of telephone networks: connection and data flow switches. An Optical Cross Connect (OXC) has been developed with the use of MOEMS at Bell Laboratories. The factors that were taken into consideration fall under financial reasoning: best value for the size and overall cost and fabrication: form factor and durability. The latter is also something that aids with incorporating MOEMS in large scale integrated circuits, an example of which are optical mesh networks used in telecommunications, be it due to volume of data or due to required speeds. While in the beging the vast majority of optical switches were simple re-routers of different wavelength light signals (so that they do not interfere, today, optical switches actually have one or more input ports and two or more output ports, thus bearing the names 1 x N or N x N optical switch. This is because light signals can be manipulated in a multitude of ways so that they carry useful information. Figure 1.8 references such optical switches.

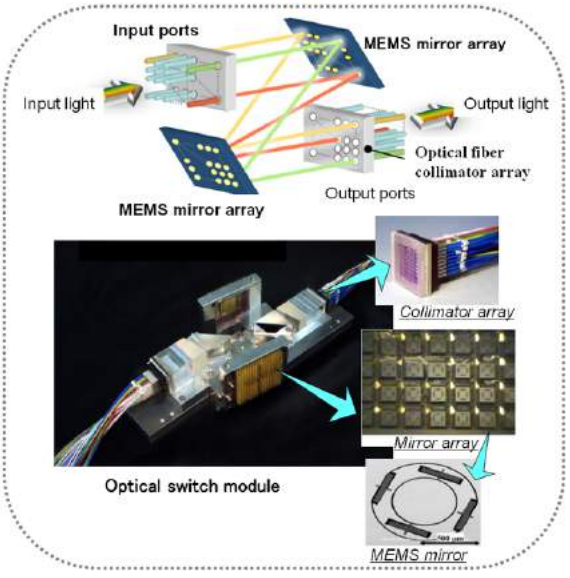

Figure 1.8: The composition of an NxN type optical switch alongside a commercialized product [Boppart, 2013].

In this example, a stream of photons in a wavelength, coming in through an input port, bounces off a series of micro-mirrors and then is sent out through one of many output ports, as required and decided by sophisticated controllers that mange the motion of the mirrors. The controller decides how the mirror needs to tilt in order to bounce the stream of light onto the appropriate output [Silberberg et al., 1987]. An example based on the above principle is the Lambda Router. The accuracy of displacement control is critical, as well as the high frequency work loads. The incoming white light wave gets filtered into separate wavelengths, each of which hits one of the input mirrors positioned in a $16\ x\ 16$ units matrix. The wavelengths bounce off the input mirrors and get reflected off another mirror onto output ones that then direct the wavelength into another fibre. The time the entire process takes to complete is in the order of a few milliseconds which is fast enough for most demanding switching applications [Bishop et al., 2002].

The way MOEMS technology is applied to storage, as mentioned, involves a physical environment that underwent a modification - CD, DVD, BLU-RAY - and has the data accessed with laser of different wavelengths. As the data access is done at high speeds and due to the density of it, precision is key for these task specific MOEMS. The different optical storage environments function very much like old vinyl discs, where the information is placed on a continuous spiral from the centre to the edge. The difference is that the information is stored as sections of ones and zeroes - the light is reflected or not. Different wavelengths are used because of compacting the data and it translates into the precision of MOEMS, as mentioned previously.

The micro-assembled components used by these storage and communication systems all have in common highly accurate motion capable micro-mirrors. The challenge is to further reduce the complexity of the actuated micro-mirrors by integrating high performance actuators capable of more complex tasks. This sets to continue the trend micro-mirror actuators have, from bistable actuation solutions to discrete positioning, as seen in Figure 1.8, to which the works presented in this thesis now bring a continuous displacement approach, opening up new, integrated, high frequency, highly precise actuation solutions.

Display and imaging

MOEMS technology combining MEMS and micro-optics is well suited for manipulating light. Electromechanical structures can be used to scan, steer or modulate light beams. MOEMS display and imaging products have been used in defence, aerospace, medical, industrial in the form of small, portable displays, projection solutions, barcode readers and infrared imaging cameras.

Although there is a wide variety of imaging products, they function by employing a few proven to be reliable technologies. The most common are Grating Light Valve (GLV) used in bar code scanners and are simple 1D pixel array technology and, more recently, Digital Micro-mirror Device (DMD), which are 2D pixel array technology used in High Definition projectors (from large conference room to compact pocket projectors). They each have a different system architecture and uses a different optical principle for light modulation.

The first DMD product was launched by the Texas Instruments in 1996. It has probably the largest number of moving mechanical components of any product [Noell et al., 2002, Dudley et al., 2003]. They present a matrix of actuated micro-mirrors that redirect light away from the light source through an RGB colour wheel to the screen, where an image is formed. Figure 1.9 shows the integration of a DMD chip inside one

DLPTM projection system from Texas Instruments. An elementary unit of the DMD is composed of two mirror-pixels where one mirror-pixel is turned on and reflects incoming light through a projection lens to the screen and the other mirror-pixel is turned off reflecting the light away from the lens.

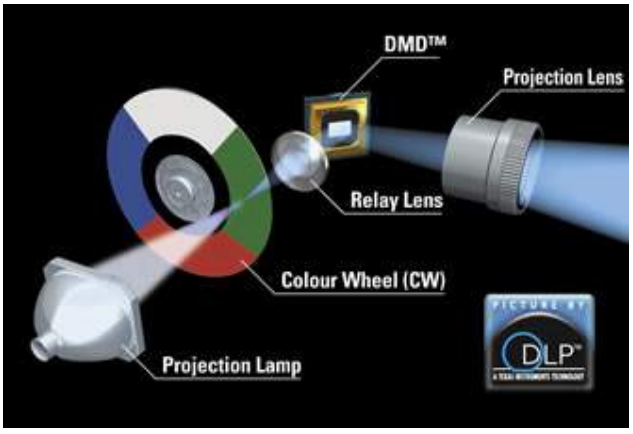

Figure 1.9: System for the display device that controls the DMD chip, which contains thousands of micro-mirrors on a silicon chip, reflecting light to display images [Hornbeck, 2012].

The optical functions of the considered devices are fulfilled by *Micro-Optical-Benches*(MOB). In the MOB, the optical signals are transmitted in plane of silicon substrate through vertically positioned micro-optical elements that can be directly fabricated on the substrate (monolithic integration) or inserted as a discrete elements into dedicated mounting slots (hybrid integration). In both cases, the assembly process is significantly simplified. The position accuracy is also improved since the optical system can be *pre-aligned* by an appropriate design of photo-lithographic masks. The MOB structures can be fabricated with excellent precision and uniformity taking advantage of the novel achievements in micro-machining and MEMS technology. surface micro-machining has opened up an exciting opportunity to integrate monolithically the diffractive micro-optics with micro-positioners, micro-actuators and optoelectronic elements (photodetectors) on a single silicon chip using basically the same technology [Syms, 2005]. In it, the micro-components (micro-mirrors, Fresnel micro-lenses etc.) are first fabricated on a silicon multi-layer that presents hinges, atop supporting plates by a planar machining process and then raised into vertical position. The raising can be done manually or by use of integrated scratch-drive actuators.

Self-assembled micro-three-dimensional stages with position accuracy in the nanometre range have already been demonstrated [Lin et al., 1997]. Other complex MOEMS devices (optical disk pickup head [Lin et al., 1996]), require little assembly for fabrication. The optimisation of surface-machined micro-optical elements is often challenging ([Rastani et al., 1991]). Although the optical structures of arbitrary shape can be fabricated during planar process, the intrinsic stress in thin multi-layer silicon often deteriorates their optical performance. By micro-machining single-crystal silicon the contrary is observed: low intrinsic stress, high aspect ratio and excellent surface smoothness for various three-dimensional structures. Different fabrication procedures can be used, as seen in the works of [Aoki et al., 1999, Malek et al., 2004, Yu et al., 2006, Hsieh et al., 2007]. The concept of Micro-Optical Table (MOT) has been introduced by [Descour et al., 2002]

and relies on refractive and diffractive optical components to be assembled into micro-machined slots in the MOT substrate. This is so that different optical systems, that use complex, previously fabricated, components can be assembled on a fixed substrate.

Despite the impressive progress in MOB fabrication, when the micro-assembly requires a human operator for the pick and place task, using high power microscopes and Microgrippers, the assembly is tiresome, time consuming and causes lots of losses. Using micro-manipulation stations, appropriate for the positioning of micro-optical components, can seriously impact the development of MOB applications. The challenge is always the streamlining of integration, fabrication, assembly and improvement of micro-structures that can fulfil more functions while reducing the micro-components number. These challenges are addressed in the following section.

1.3/ CURRENT CHALLENGES

There are several challenges due to the micro-scale. While some specificities are convenient for a multitude of applications, others present themselves as obstacles. They are detailed in [Régnier et al., 2010] and can be summarized here:

- Micro-fabrication constraints
- Very high dynamics of the micro-systems
- Micro-systems dependency to environment parameter variation
- Widespread active materials

Micro-fabrication constraints

Due to their size and material used, the micro-components that make up MEMS and MOEMS are often very fragile and can be broken by applying even the smallest forces. This is, in part, what increase the complexity of manual tasks in the system because the forces that human can apply are big enough to break the micro-components. Such examples are the force sensors and the microgripper developed by the company *FemtoTools* (Figure 1.10). The sensor can be deformed up to $2\ \mu m$ for the maximal force measurement range. The Microgrippers come with an initial opening of $30\ \mu m$, $60\ \mu m$ or $100\ \mu m$.

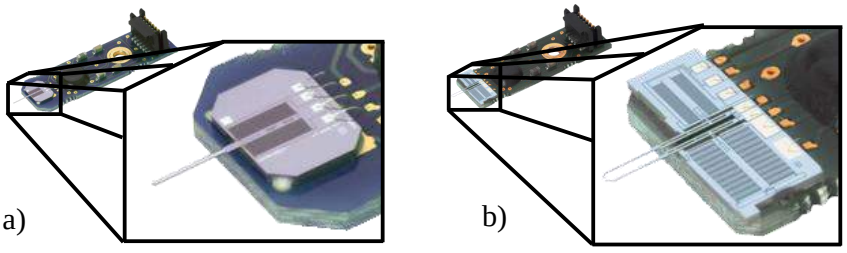

Figure 1.10: FemtoTool developed a) micro-force sensors and b) Microgrippers [Beyeler et al., 2014].

Apart from the size constraint, the safety of such sensors cannot be guaranteed even with the use of micro-positioning stages. This is because the displacement errors can surpass the $2\ \mu m$ maximum due to the added effect of backlash, nonlinearities, perturbations, etc. This, of course, can easily break the force sensor and/or the sample. This stays true even with very accurate well mastered position control. Consequently, more precise and less complex positioning devices are sought, both with the employment of novel materials as well as new designs. These devices need to have better actuator integration and position control.

The size of the components being fabricated and assembled also increase the influence of specific forces such as the capillary and electrostatic ones. *Capillary forces* appear in liquids at the bridging between two solids, called meniscus and are usually used in hybrid fabrication procedures. They depend on a number of factors such as: the type of liquid involved, the support material, the volume of the liquid in the actual bridge, the distance between the two solids and their geometry. there are also environmental factors like temperature and overall humidity. This makes for the fabrication of certain components very susceptible to environmental changes. *Electrostatic forces* are either caused by the appearance of charges generated through triboelectrification or occur through the Coulomb interactions in presence of charged particles. The electrostatic forces are inversely proportional to the separation distance which increases their effects when small distances exist. If the two charges have the same sign, the force is repulsive and may have an uncontrolled impact on the system and some displacements may occur. Due to the complexity of the phenomena, research is still focusing on the quantification and identification of the effects [Derjaguin et al., 1975, Johnson et al., 1987]. These forces also depends on several simultaneous parameters like: load forces, contact angles, environmental conditions - temperature and humidity, materials involved, the roughness of the surfaces, etc. These greatly impact the speeds involved in microassembly and also affect the precision of the micro-fabrication devices.

In order to reduce the number of inconveniences, different materials are investigated due to their stability and high performances, some of which will be described in a different section. The work presented also aims towards an integrated actuation solution to further reduce the number of unknown or difficult to control micro-fabrication parameters.

Very high dynamics of the micro-systems

The dynamics of a system depends on the geometry and the scale of the system. A simple example, illustrated in Figure 1.11 will be given in order to emphasize the dynamics of the system related to the size of the system. Considering two silicon cantilever beams, whose one end is fixed and the other end is free, with the same geometry but with different sizes. The first beam, B_1, has L in length, W in width and h in thickness where the other, B_2, has $L/10$ in length, $w/10$ in width and $h/10$ in thickness. The natural frequency of a cantilever beam is given by:

$$f_n = \frac{\omega_n}{2\pi} = \frac{\beta_n^2}{2\pi L^2}\sqrt{\frac{EI}{\rho A}} \tag{1.1}$$

where f_n is the natural frequency in Hz of the n^{th} vibration mode, ω_n is the natural frequency in rad/s of the n^{th} vibration mode, β_n is a constant corresponding to the n^{th} vibration mode, E is the Young Modulus of the material, I is the moment of inertia of the beam cross-section, ρ is the density of the material and A is the area of the cross sec-

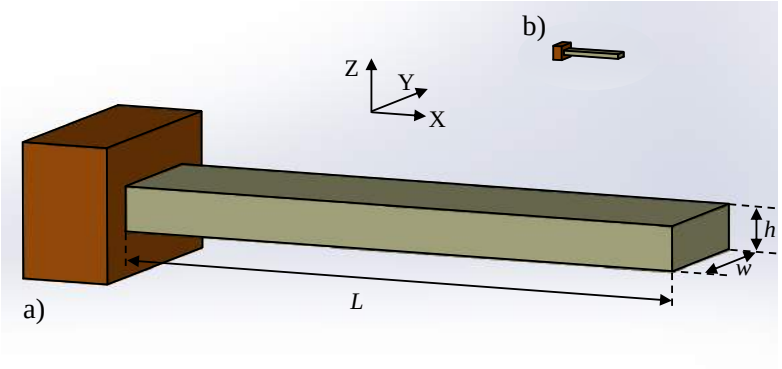

Figure 1.11: Scale induced dynamic changes for a a) generic cantilever B_1 and an identically designed b) downscaled (to 10%) cantilever beam B_2

tion. Considering a rectangular cross-section, the area and the moment of inertia of the cross-section, I_x along the X axis Figure 1.11, can be given as follows:

$$\begin{cases} A = Wh \\ I = \frac{Wh^3}{12} \end{cases} \tag{1.2}$$

Written for the large beam, and replacing 1.2 in equation 1.1 we now get:

$$f_n^{B_1} = \frac{\beta_n^2 h}{2\pi L^2} \sqrt{\frac{E}{12\rho}} \tag{1.3}$$

Writing the equation for the small beam (B_2) we get:

$$f_n^{B_2} = \frac{\beta_n^2 \frac{h}{10}}{2\pi(\frac{L}{10})^2} \sqrt{\frac{E}{12\rho}} = 10 f_n^{B_1} \tag{1.4}$$

So, by reducing all the beam dimensions by a factor of 10, the natural frequencies of the system is multiplied by 10. This means that the dynamics of micro-systems are naturally higher than those of macro-systems. In the case of robotic micro-assembly, the dynamic control of the robotic station and the microgripper is the key for high speed and high dynamics micro-assembly. The dynamic control requires the presence of high dynamics sensors and to choose a well adapted control scheme. Thus, high dynamics position and force sensors are required in addition to an efficient control law. This overall system complexity makes for its dynamics to be lower than that of the individual components. At the same time the complexity of the micro-structures has an inverse effect on the dynamics.

As micro-components have more and more integrated features, and the fabrication procedures tend to unify certain aspects, the overall dynamics tends to drop. Coupled with the very different properties of the materials used for such micro-structures and micro-systems, the dynamics become more difficult to model, predict and control. For this reason, novel materials are always sought so that an integrated actuator provides high performance while maintaining simplicity. The work presented in this thesis addresses both the dynamics of integrated actuators and the performance expectations for more straightforward designs.

Micro-systems dependency to environment parameter variation

Most of the materials used in the fabrication of micro-components are influenced by the environmental conditions, be they passive or active components. As a result of the accentuated effects at the micro-scale micro-systems can suffer unwanted thermal elongation in the μm range with an environmental temperature change of only 1 ° C [Tan, 2013], something which is typical even for controlled environments such as clean rooms. These changes get amplified and have important consequences at the microscale where structures are complex and heavily rely on compliance for controlled displacement. Furthermore, materials such as the piezoelectric or piezoresistive ones (making up sensors for example), are widely influenced by temperature change. In the case of long experiments, it can vary from one day to other due to arbitrary environment changes. This dependency weighs in the choice of the micro-assembly automation where closed-loop control is better suited to overcome these effects, compared to open-loop based automation. Thus more sensors need to be integrated so that these changes are evaluated and taken into consideration. This only ads to the complexity of the micro-systems and reduces their functionality. They also add extra levels of difficulty in terms of mathematical modeling.

This is addressed by choosing a material that has stable properties under stress conditions, electric and mechanical, while bringing improvements in actuation ranges, expected displacements and dynamic behaviour.

Widespread active materials

A wide variety of smart materials are used nowadays [Kuhnen et al., 2001, Smith, 2005], with some standing out not only through their quantifiable qualities, like displacement through controllable deformation or large bandwidth and high dynamics, but also in commercial use. This means that not only are they inexpensive solutions, but are also easily produced and fabricated. While the newer ones are more exotic in nature, like photo-deformable polymers [Yu et al., 2005], self-oscillating gels [Yoshida, 2010] or even cellulose [Kim et al., 2006], the ever increasing research done with well established materials has improved their usability and exploitation.

Active materials, although widespread in use, present three major challenges. The most important one is their non-linear behaviour, manifested either through hysteresis or creep. This makes for the control to be very difficult as, due to them being primarily needed for very small applications, sensors cannot be introduced in the encompassing system. Another challenge is to amplify their small deformations to the point of being useful. This is usually done with compliant structures, but, as already mentioned, this also reduces the dynamics of the system, crippling one of their most important features (high dynamics). The third challenge active materials present is their complex manufacturing procedures. As it will be described in a following section, very precise conditions have to be met in order to obtain certain high performance materials. This raises their cost, but also, more importantly, translates into not having the same behaviour come from the same type of material.

A more detailed description of these materials, their advantages and disadvantages will be presented in a following section, as they are developed or adapted to suite very specific applications.

1.4/ COLLABORATIVE CONTEXT OF THE PHD

The PhD is co-supervised and supported by the ADMAN (**A**dvanced **D**evices for micro- and nano-scale **MAN**ipulation and characterization) Romanian project and in the French MIOP (**M**icro-systems for **I**nstrumented **OP**tical chips) program. The proposed work falls within the general context of micro-assembly (assembly of components with dimensions generally comprised between $1\ \mu m$ and $1\ mm$) and control of microscale devices, fields where many important scientific issues and applications still remain unsolved. The AS2M department and Valahia University have world-class expertise in these areas. They have proposed many solutions for the design, implementation and control of various micro-mechatronic devices. Several micro-assembly stations have notably been developed enabling teleoperated and automated tasks. The objective of the proposed PhD consists in creating innovative and widely useful optical functionalities taking advantages of micro-scale specificities by using novel actuation principles. The PhD topic also aims at tackling generic principles and devices such as developing a 3D tool for independent component bonding of micro-scale devices (Figure 1.12), improving the knowledge on innovative materials, working on a new class of micro-systems.

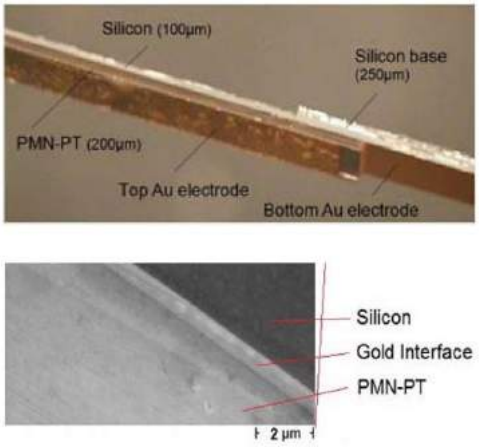

Figure 1.12: Example of a Piezo-on-Silicon micro-actuator using a customized thermo-compression bonding process.

1.4.1/ M.I.O.P.

The micro-optical technologies have made a significant progress in the past two decades and have found widespread applications in many areas, including telecommunications, sensors and biomedical fields [Tolfree et al., 2007].While these applications require high precision for optical alignment they also involve the precise movement of small optical components for proper functionality [Sun et al., 2002a, Wolffenbuttel, 2005, Syms et al., 2006, Chau et al., 2008]. The desire is to integrate various functional elements of micro-optical system on a single chip with sub-micron position accuracy to build cost- and space-effective optical modules. They involve free-space micro-optical components (lenses, gratings, mirrors, prisms), guided wave components (fibres, wave guides),

micro-actuators or optoelectronic devices (laser diodes, photodetectors), each resulting from very different micro-fabrication processes.

Micro-Optical Benches (MOB) assembly based on active gripping strategies have also been designed and fabricated (Figure 1.13 - a and b). Such micro-assembled MOB are very promising solutions for the production of new classes of micro-systems. Nevertheless, further functionalities remain to be developed to enable a wider variety of MOBs. The purpose of the thesis is to add to the existing functionality of these MOB elements by adding a smart material in order to develop actuator-enabled elements.

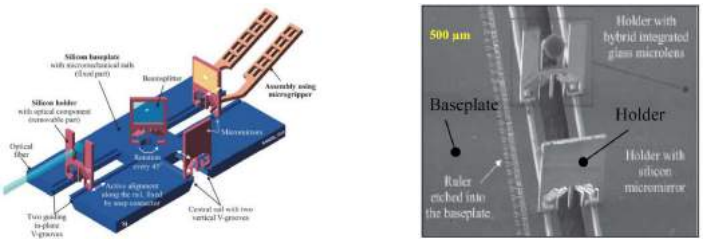

a) b)

Figure 1.13: (a) et (b) Examples of Assembled Micro-Optical Benches.

The MIOP project is in progress at the FEMTO-ST Institute in Besançon. This program brings together very dynamic and promising activities of the AS2M and MN2S departments dealing with Optical micro-systems manufactured by micro-assembly. The fabrication of micro-systems by micro-assembly is an alternative to monolithic approach, where micro-components are fabricated by layering different materials and etching them. Several micro-assembly techniques are available where we can notice that dedicated tools are required for each assembly process depending on the desired application. A technique allowing the assembly of various sizes, shapes and types of micro-objects is not fully developed in literature, though work has been done towards this goal [Carrozza et al., 2000, Komati, 2014].

Current progress

In the case of various micro-optical elements fabricated through processes which require very different conditions will be the starting point for a new generation of MOEMS called hybrid MOEMS. These have been developed during a different project, also as a collaboration between two departments of the Femto-ST institute: AS2M and MN2S. During this project, a technology platform for the hybrid integration of MOEMS components on a silicon Reconfigurable Free-Space Micro-Optical Bench (RFS-MOB) has been developed (Figure 1.14. In this approach, a desired optical component (e.g. micro-mirror, micro-aperture) is integrated with a removable and adjustable silicon holder. It presents spring-based snap connectors, and can be manipulated, aligned and fixed in the precisely etched rail of the universal bulk-micro-machined silicon baseplate by use of a robotic micro-assembly station.

The components of the two-level architecture of the RFS-MOB are shown in Figure 1.15 as they would be assembled. This would be achieved by the usage of active Microgrippers. The modular design enables the holder alignment with the silicon baseplate along the x or y-axis, in the micro-machined rails. This also allows quick and coarse positioning of the holder perpendicularly to the optical axis. The silicon baseplate constitutes the mechanical reference for various free-space micro-optical chips carried by the holder

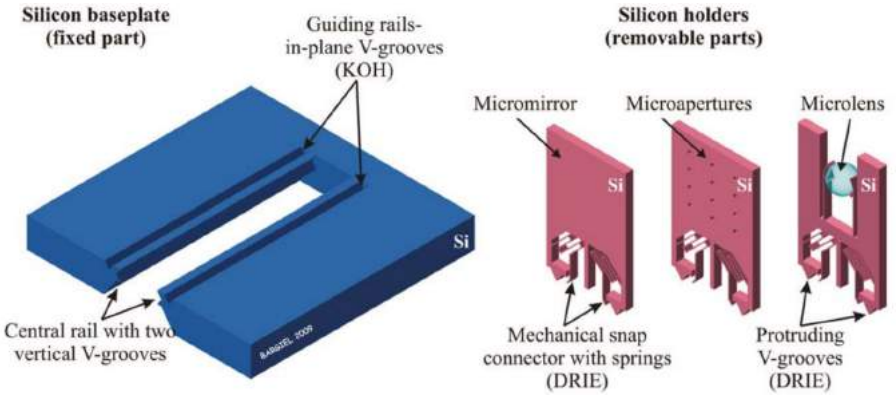

Figure 1.14: Individual components of the RFS-MOB as presented in [Bargiel et al., 2010]: details of the silicon bulk-micro-machined baseplate and silicon holder (with the ball microlens as a micro-optical component).

for precise alignment.

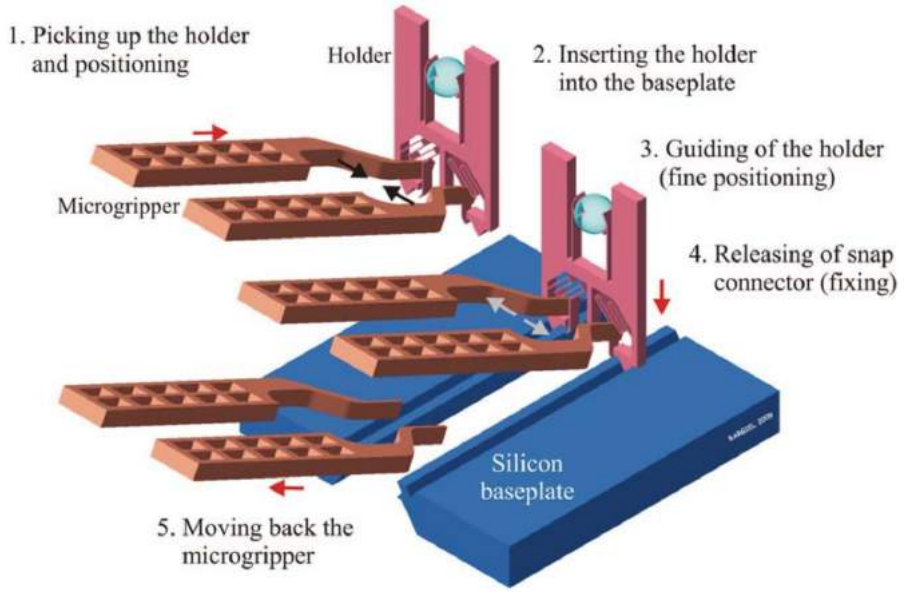

Figure 1.15: The assembly concept as presented in [Bargiel et al., 2010]: holder assembled into the central rail of the silicon baseplate and V-groove enabled alignment.

A strategy for the assembling of the silicon holders has been presented in [Bargiel et al., 2010] is is summarized here:

- picking up of the holder by active opening and closing motions of the Microgripper's fingers and pre-positioning of the holder in front of the rail,
- insertion of the holder into the baseplate,
- guiding of the holder within the guiding rails to get the fine positioning of the holder,
- releasing of the snap connector springs through opening motion of the microgripper, which enables the fixing of the holder onto the baseplate,

- retraction of the Microgripper with the holder self-support on the rail.

Considering the results that have already been attained, the objective now becomes that of integrating smart materials into the silicon holder design as to create active components, such as actuated micro-mirrors (Figure 1.16), while also integrating compatible power solutions. This design includes electrode disposition, actuator design and integration as well as the micro-mirror preparation and positioning.

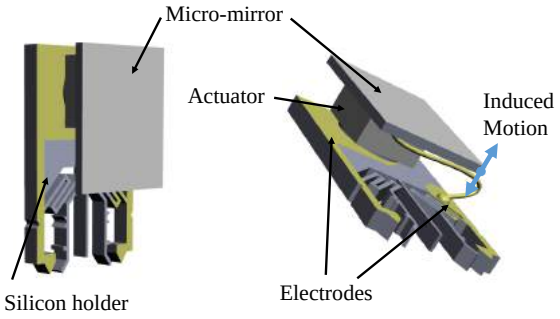

Figure 1.16: Smart component compatible with the RFS-MOB as presented in [Bargiel et al., 2010] that also includes the power solution.

1.4.2/ A.D.M.A.N.

ADMAN is the acronym of the Romanian young research teams project PN-II-RU-TE-2011-2, a government sponsored project. It aims at developing new miniaturized micromechatronic devices for in-contact micro and nano manipulation and characterization tasks, in line with the actual trend for advanced miniaturization combined with high precision and dexterity.

The project tackles with multidisciplinary technological and scientific issues related to smart materials modeling and control, sensors and actuators design and development, micro-robotics design and control, electronics, embedded electronics and systems integration. Among the targets of the project we can count the advanced designs will be: a bio-compatible micro-robotic manipulation cell, a micro-assembly station featuring an innovative 3D gripper of original design, a nano-positioning stage and a resonant nanoforce sensor for Atomic Force Microscopy (AFM).

Approached manipulation technologies

In the framework of the ADMAN project, contact micro-manipulation is considered, as it's been thoroughly investigated [Lang, 2008]. The choice of microgripper is done with the application and the micro-assembly constraints in mind.

A hybrid microgripper has been developed by [Ivan et al., 2012] that uses electromagnetic handling for the moving in the XY-plane and piezoelectric for the XZ-plane. It has been improved by [Despa et al., 2013], making it viable for organic matter manipulation. Figure 1.17 shows the outline constructive design of the magneto-piezoelectric device for micro-manipulation. The effector elements are the two beams rigidly attached to the frame, which is displaced by bending due to the magnetic interaction between solenoid and the permanent magnet rigidly fixed on the active arm.

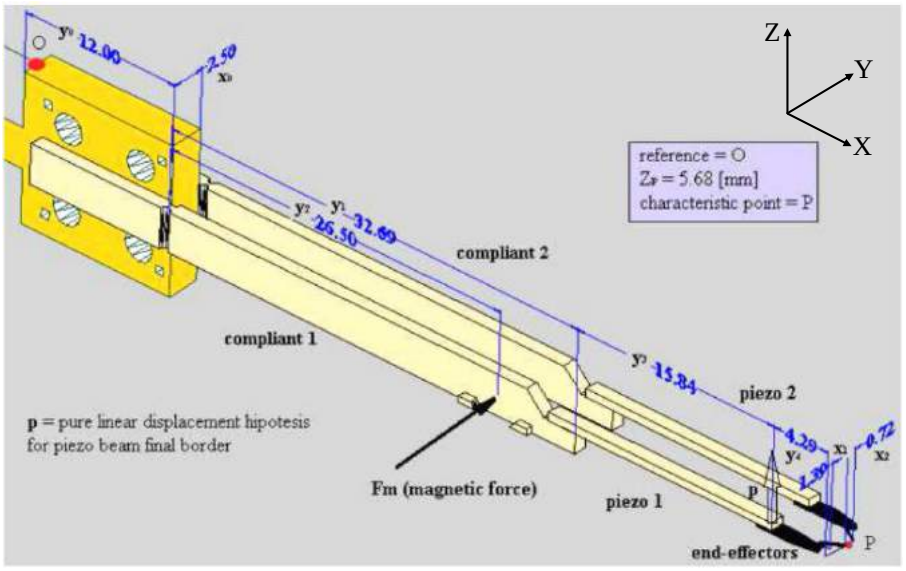

Figure 1.17: Schematic representation of the magneto-piezoelectric device for micro-manipulation as presented in [Despa et al., 2014].

The ADMAN project is also focused on developing the control for active-finger Microgrippers [Despa et al., 2014] that can be used in rapid assembly systems. It offers a reduction in complexity of the overall manipulation stage, by adding degrees of freedom to the Microgripper itself as well as reducing the complexity of the assembly units - larger displacement range for the Microgripper arms as well as increasing the precision of the manipulation task. The work presented here aims to do that by employing a novel smart material that has been shown to have very promising characteristics. A detailed description of the chosen material will be provided in the next chapter.

1.5/ SMART MATERIALS COMMONLY USED

In micro-scale applications there has been an ever increasing demand for highly accurate and highly integrated actuation solutions. This has resulted in the study and usage of materials which present very little to no backlash, high dynamics and on which existing micro fabrication techniques can be applied. While solutions do offer increasingly higher precision the scale of the multi-DoF robot often exceeds the micro-scale. Platforms as those mentioned in [Kim et al., 2012b, Toz et al., 2013, Li et al., 2014, Coppola et al., 2014] while having high manoeuvrability are cumbersome. Localized and precise actuation has led to different approaches to be employed. Applications such as MEMS [Alogla et al., 2012], biomedical [Zhong et al., 2006], [Wester et al., 2011], micro-robotics or micro-manipulation [Kim et al., 2012a] require the use of easy to integrate, precise smart materials, capable of a high dynamic response range. As previously mentioned, great interest is also found in the area of MOEMS, where highly accurate actuation is needed. Such adaptive optics applications are found in measurement devices for interferometry [Blomberg et al., 2009] and spectrometry [Zhihai et al., 2011], consumer products like scanners [Lin et al., 2012] and image aberration correction [Tortschanoff et al., 2010] devices, both in consumer imaging and high precision telescopes.

Among smart materials, there are some more versatile ones, not limited to usage in only very specific systems. Examples are *Shape Memory Alloys* (SMAs) *Dielectric Elastomers* (DEs), *Thermoelectric Materials*, *Ferrofluids* and *Piezoelectric Materials*. Their characteristics, advantages and disadvantages are succinctly presented here.

Shape Memory Alloy

They are lightweight, solid-state alternatives to conventional actuators. They are a smart material also known as memory metals, muscle wires or smart alloys. The dominant characteristic is that after being mechanically deformed, they return to their original shape in the presence of heat. They are used in the automotive and aerospace industry, biomedical applications and robotics (micro-robotics in particular). As being dependent on temperature variations and thus on transient times, the research focuses on improving the dynamics of the incorporating systems [Huang et al., 2012, Lara-Quintanilla et al., 2013].

In medicine, SMAs are mostly used as fixation devices during surgery, like coronary stents (Figure 1.18) inserted in blood vessels to allow for surgical tools to pass, for applying constant forces in dental braces [Otsuka et al., 1999] and in consumer products, such as glasses frames.

Figure 1.18: A coronary stent before and after activation. They come in different sizes and are either reshaped mechanically or are activated by the body's own heat after being inserted [Serruys et al., 1994].

Although biologically compatible and usable in micro-robotics [Zhong et al., 2006], the downside of SMAs is their response time and temperature dependencies. These characteristics make them an unsuitable choice for high speed assembly technologies and other types of MEMS adn MOEMS.

Dielectric Elastomers

They are a type of material called elastomers that produces large strains when under an external exciter such as an electrical field. This is due to the weak inter-molecular forces, being both elastic and viscose properties. They are relatively novel materials, being researched since the early '90s. They are used as actuators (DEA) with a very high strain coefficient and thus achieving a surface gain of up to 300% by sandwiching a passive elastomer between two electrodes [Pelrine et al., 2000, Pelrine et al., 2001] (Figure 1.19) and applying an application restricted voltage.

They are bio-compatible [Zhang et al., 2002a, Keplinger et al., 2013] and thus

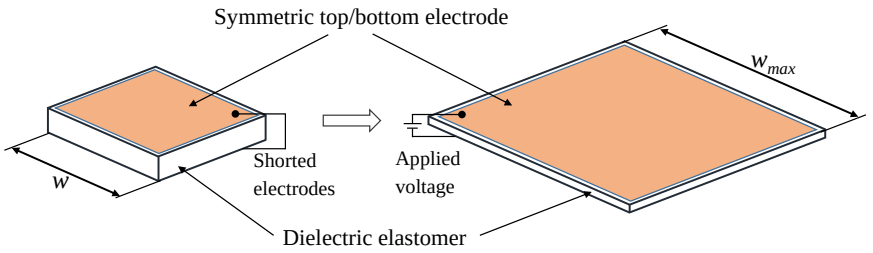

Figure 1.19: Working principle of dielectric elastomer actuators. For a w wide DEA, after applying voltage the width becomes $w_{max} \approx \sqrt{3}w$

present interest in surgical interventions targeting tissue reactive to electricity, like the heart muscles [Brochu et al., 2010]. Being a versatile smart material it can be fabricated in different configurations, depending on the usage. *Framed* or in-plane actuators, as the one presented in Figure 1.19, although they are also disc shaped; *cylindrical*, used for their axial elongation as artificial muscles [Pelrine et al., 2002]; *diaphragm* actuators capable of out-of-plane motion [Goulbourne et al., 2005] and *stack* actuators, which are usually used to increase deformation (especially contraction) [Carpi et al., 2006]. They are most common in macro-applications, although their usage in micro-applications is gaining interest in biomedical research as cell stretchers [Akbari et al., 2012] and even micro-pupms [Asaka et al., 2014].

DEAs offer great shape versatility and are also bio-compatible, but they need a support structure in order to generate motion and this complicates not only the solution for micro-scale actuation and pre-assembly but also increases costs. This reduces their usability greatly.

Thermoelectric Materials

While there are a multitude of materials that present thermoelectric effect, and in most, it is too small to be useful. They either generate electric potential with temperature variations or heat is generated when voltage is applied. They are very widely used in a variety of applications that are not dependent on the environmental temperature. However, low-cost materials that have a sufficiently strong thermoelectric effect (and other required properties) could be used in applications including power generation and refrigeration.

Several factors determine the usefulness of a material in thermoelectric systems: their power factor and incorporating device efficiency. These are determined by the material's electrical and thermal conductivity, *Seebeck* coefficient (measure of the magnitude of an induced thermoelectric voltage in response to a temperature difference) and behaviour under changing temperatures. The power factor determines if the material can be used as a generator or a coolant and is directly proportionate with its electrical conductivity. Recent studies have resulted in organic materials that have better conductivity properties than inorganic ones [Sun et al., 2012, Zhang et al., 2014].

The insufficiencies these materials do present are in applications where high temperature variations are not desirable. This applies to exterior influences as well. Although micro-scale applications have short transient times for the incorporated thermoelectric actuator, their control is difficult and is the subject of ongoing research [Tiwari et al., 2013, Tuzcu et al., 2013, Meisner et al., 2014]. They are mostly used as bistable actuators, being too dependent on environmental temperature for discreet

control.

Piezoelectric materials

They are materials that either generate electric potential when an external force is applied or change their shape when voltage is applied. They were discovered in the late XIX-th century by the French physicists Jacques and Pierre Curie. There are naturally occurring materials that have this property, crystals that don't have an internal structural symmetry [Gautschi, 2002]. Other naturally piezoelectric occurring materials include quartz and the structurally identical Berlinite , cane sugar, Rochelle salt, topaz, tourmaline, and bone.

Piezoelectric materials have had a rich history regarding the investigations and utilization of novel, increasingly promising piezoelectric composites. They focus mostly on the property of these materials having spontaneous electric polarization that can be reversed, called *ferroelectricity*. Materials such as Barium Titanate ($BaTiO_3$) have an internal structure made up of randomly oriented crystalline parts and is called *polycrystalline*. This is why it presented a reduction in the amount of displacement generated for a specific electric field when it is applied in reverse, known as *depoling*. Although it still started to gain ground in the late $'40$s [Mason, 1948], other materials that had a more stable piezoelectric effect were being developed. What later became Lead Zirconium Titanate or PZT ($PbZrO_3$–$PbTiO_3$) started to gain ground in the early $'50$s. Decades of development have made its family the most versatile compositional base for piezoelectric elements.

Other materials, with more specific uses have been developed, like Lead Niobate (PN) due to its high-sensitivity to frequency variations; Barium Niobate for its lower *Curie temperature* (where a material's ferroelectricity changes to the induced electric polarization) which makes it perfect for non-destructive evaluation or testing applications; crystals like Lithium Niobate (LN) or Lithium Titanate (LT), which were studied in depth by [Smith et al., 1971] and, a decade later, by [Weis et al., 1985].This is also because they present very good acoustic properties and high Curie temperatures.

In the early $'70$s, a different type of piezoelectric material was being developed called Lead Magnesium Niobate (PMN). This is a material that present high *electrostriction*, the property of electrical non-conductors (*dielectrics*) to change their shape under an electric field, called *relaxor ferroelectric*. PMN presents a partially distorted structure which, in part, lead to extremely large dielectric constants. This benefits the induced electric field and results in low hysteretic behavior [Alberta et al., 2001, Hao et al., 2008, Hao et al., 2009, Wang et al., 2012, Tang et al., 2013]. Just like PZT ceramics, the relaxor components are able to form solid solutions with Lead Titanate (PT). Of these resulting materials, of very high importance is that they can be grown as single crystals like $Pb(Mg_{1/3}\ Nb_{2/3})O_3$ - $PbTiO_3$ (PMN-PT) and $Pb(Zn_{1/3}\ Nb_{2/3})O_3$ - $PbTiO_3$ (PZN-PT). These materials have been in focus since the early $'80$s [Kuwata et al., 1982], though advancements in their understanding has come since the late $'90$s.

The piezoelectric effect is very useful within many applications that involve the production and detection of sound, generation of high voltages or electronic frequency, micro-balances, and the ultra fine focusing of optical assemblies. Due to being studied for such a long time, they have also become the basis of a number of scientific instruments and instrumental techniques with atomic resolution, such as Atomic Force Microscopes (AFM) and Scanning Tunnelling Microscopes (STM). They are so well spread that they are used even in very common applications, such as igniters. In the scientific domain the

most common usages are that of **sensors** and **actuators**.

Sensors operate by the principle that a physical dimension, transformed into a force, acts on two opposing faces of the sensing element. The most common sensor application is the detection of pressure variations in the form of sound, which is seen in piezoelectric microphones and piezoelectric pickups for electrically amplified guitars. Other applications count micro-balances [Battaglia et al., 2004], miniaturized strain gauges [Gullapalli et al., 2010] and ultrasonic transducers [Wang et al., 2006], as those used in medicine [Ritter et al., 2002, Shung et al., 2007], where the piezoelectric element acts both as an actuator and as a sensor. The high and very high frequencies at which piezoelectric materials can operate make them ideal for industrial non-destructive testing [Shin et al., 2008].

Actuators make use of the small size differences observed when applying an electric field. This means the actuator dimensions can be manipulated with higher-than-micrometer precision, making piezoelectric materials an important tool for positioning objects with high accuracy. Amplifying the necessary motion is as simple as the stacking of active layers or increasing any of the actuator's dimensions.

Rotary motors result when a force is applied to an axle [Glenn et al., 1997, Qi et al., 2012], thus replacing stepper motors when the application precision requirements are not met, while *linear motors* use the direct deformation and are found in mirror repositioning systems for different devices, from microscopes to telescopes. Linear actuators are also found in AFMs and STMs [Chen, 2008], micro-positioning stages [Tan et al., 2001] and active vibration dampeners [Hawwa et al., 2001].

In Figure 1.20 the evolution in piezoelectric material fabrication and study can be observed that can be broken up in 4 regions: the *pre-PZT* age (until the mid 1950s), when piezoelectric materials were still exotic and studied for the understanding of their working principles; the *PZT* age (until the late 1980s), when PZT based ceramics have been used not only in research but also in a large variety of commercial product and other, better performing materials started to be developed; the *post PZT* age (until the late 1990s), when relaxor based piezoelectric materials have gained ground, slowly replacing PZT and the age of *PMN-PT like crystals*, in which we currently are.

Overall, smart materials offer a variety of properties that can be used in very specific applications but none show as much versatility as piezoelectric materials. Although they are not ideal as they do present non-linearities, which can complicate the control, they are fairly predictable, aiding to the development of mathematical models describing them. They present large bandwidth and forces and are capable of multi DoF motions while having motion resolutions of less than a micrometer. This ads as another reason for the selection of a piezoelectric material as the integrated actuation solution for the micro-applications required by the two encompassing projects (ADMAN and MIOP) and their framework.

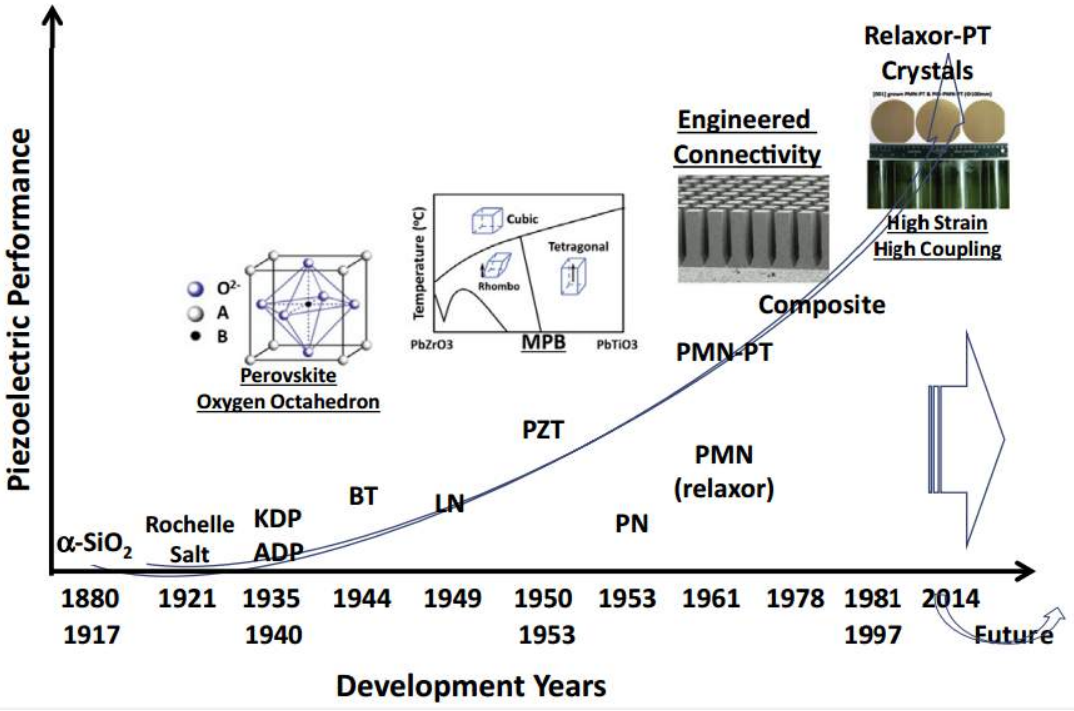

Figure 1.20: Piezoelectric material development evolution [Zhang et al., 2015b].

1.6/ CONCLUSION

There are multiple options that relate to both the solutions and the current stage in micro-robotics and complex micro-systems (MEMS and MOEMS). Coupled with the ever increasing variety of materials available, they point to better accuracy and performances. The domains in which micro-systems are used vary from simple, like the SMA coronary stent, to very complex, like the optical, multiple stage assembly elements used in OCTs. Although there are limitations caused by the size reduction in terms of the fabrication of systems that incorporate multiple functions, the development and understanding of smart materials direct to micro-robotic systems that can be fabricated easier and can themselves be more precise and fast. This applies not only to smart materials, in general, but also to piezoelectric ones, in particular, as more materials are being developed presenting fewer compatibility issues. They also allow for system to reduce the assembly complexity of multi-dimensional (3D) micro-structures.

The work presented here aims to address some of these issues by utilizing a novel piezoelectric material that has shown very promising properties and performances. First, an introduction to PMN-PT is presented, highlighting what aspects need to be considered when choosing this piezoelectric mono-crystal, such as the production procedure chosen and how this influences the properties of the material. A point is made to its importance over the piezoelectric coefficients. Some of the advantages of using PMN-PT are also mentioned, followed by the electric and mechanical properties that allow PMN-PT to be more and more popular.

Second, the integration of PMN-PT into micro-robotic systems is addressed,

through the design of a flexural actuator. An adapted mathematical model is proposed, that takes into account its specificities, thus allowing for displacement and force predictions. The high performances are furthermore contoured through the generation of complex trajectories, without the need of dedicated control loops. A microgripper is then fabricated to further demonstrate the material's capabilities, one capable of large displacement, pick-and-place tasks.

Thirdly, the usability of PMN-PT as an integrated MOEMS actuator is addressed. With a straightforward model, a deeper study into the design of such an actuator is presented, highlighting some of the influencing factors and how their effects can be reduced. The static and dynamic capabilities of the PMN-PT based actuator are then compared with a proposed solution for a reconfigurable MOEMS compatible element.

Lastly, all the findings are then grouped and presented in a conclusion, alongside proposed courses of action for furthering the study and usage of PMN-PT both in microrobotics and micro-optics.

2

SPECIFICATIONS OF PMN-PT

This chapter presents the properties and characteristics that place PMN-PT in front of other piezoelectric materials. After a brief introduction into PMN-PT and its main characteristics, a more detailed view over the piezoelectric properties PMN-PT has, then follows. This includes production issues and their direct impact on the electro-mechanical properties. What makes PMN-PT a good candidate for integration is then presented with focus on two, though different, very potent cuts: anisotropic [011] and longitudinal [001].

2.1/ INTRODUCTION

Piezoelectric materials have the property of generating an electric charge when acted upon with an external force. They are particularly interesting because the inverse effect is also true, as they can change their shape when an electric field is applied. Higher interest is found when working with fabricated piezoelectric materials, like lead zirconate titanate (PZT), but more recent ones, presenting a higher piezoelectric effect are gaining ground. They are bi-composites like lead zirconium niobate - lead titanate (PZN-PT) and lead magnesium niobate - lead titanate (PMN-PT) [Lim et al., 2007].

PMN-PT has a particular internal structure that induce different but specific characteristics. They influence the fabrication and implementation and help reduce control complexity. These characteristics and their importance are studied in the chapter that follows. A brief description of the internal structure of PMN-PT and how it affects the relation between the two components ratio (PMN and PT) and the more relevant coefficients is presented. Considering the importance of the monocrystal fabrication process, the most common are briefly described, noting what advantages and disadvantages each presents, in relation the PhD needs. The piezoelectric coefficients of importance are then described, focusing on the PMN-PT monocrystals with a $31 - 25$ % component ratio, cut along the [001] and the [011] crystalline direction. The versatility of PMN-PT is then presented showcasing its integrability and implementation. A short mathematical description of the inverse piezoelectric effects, depending on the crystalline orientation the follows. An introductory description of the electrical and mechanical properties of PMN-PT ([001] and [011]) follows. Large values of the piezoelectric coefficients, like the d_{33}, (up to 6 times larger than for piezoceramics, like PZT $d_{33} = 2500\ pm/V$) and responses of $> 2\ nm/V$ have been measured for PMN-PT. These values are much larger than for other piezoelectric

materials and have stimulated extended research on such compositions.

2.2/ MAIN CHARACTERISTICS OF THE PMN-PT MATERIAL

PMN-PT is a relatively novel material that exhibits piezoelectric properties and is composed of two different groups of atoms that behave as a unit, each an oxide, called radicals: **Pb(Mg**$_{1/3}$ **Nb**$_{2/3}$**)O**$_3$ and **PbTiO**$_3$. It is, as mentioned, part of the relaxor-ferroelectric material class. It has a monocrystalline structure, unlike commonly used piezoelectric materials that have a granular piezoceramic structure (Figure 2.1). This means that defects and grain boundaries are absent and thus PMN-PT can be machined to a more precise degree, with optical grade finish. Other properties that differentiate PMN-PT from granular piezoelectric materials, such as PZT, are also directly linked to the monocrystalline structure. Such properties are optical, mechanical or electrical and can be anisotropic (directly dependent). Another advantage of PMN-PT having a monocrystalline structure is its uniformity, ensuring consistent values for the piezoelectric coefficients.

Its two radicals influence the behaviour of the material thus, by changing the ratio of PMN and PT, it is possible to tune the properties of the composition. The different PMN

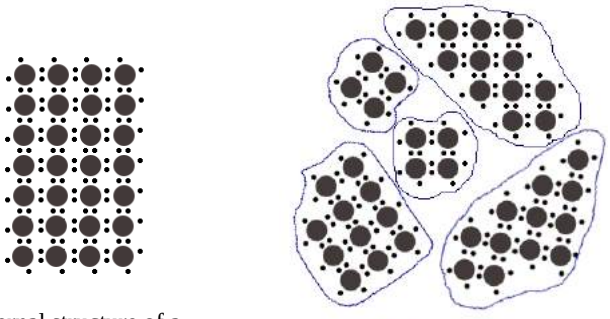

Figure 2.1: a) Monocrystalline internal structure for materials, like PMN-PT and b) a multigranular one common for ceramics, like PZT.

to PT ratio induced piezoelectric properties have to do with the strength of the bonds between radicals. These two components have intersecting structures, at the atomic level, as presented schematically in Figure 2.2. The arrows indicate the direction of displacement once an electric field is applied. This is what causes the material to chage shape and generate displacements.

Depending on the ratio of the two components, along with electrical and mechanical properties (electric field orientation, capacitor effect or stiffness, respectively), the temperature at which the mono-crystal losses its piezoelectric properties changes as well. This temperature, called *Curie Temperature* (T_C)is determined by the PT contents. A phase diagram of PMN-PT is depicted in Figure 2.3. The lines in the graph represent *morphotropic phase boundaries*, where the material changes composition. Above the angled line the cubic phase is present while the dotted vertical line is between a rhombohedral and a tetragonal phase of crystal symmetry.

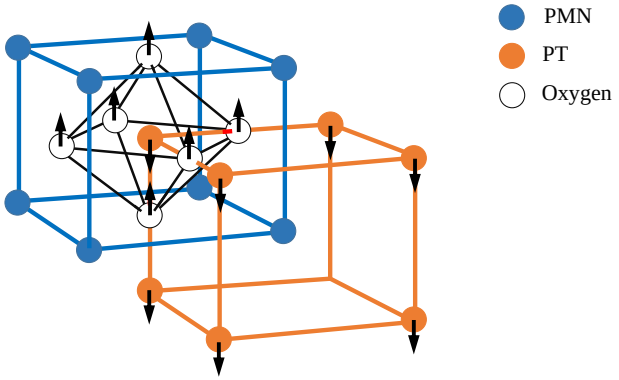

Figure 2.2: PMN-PT detailed crystal structure.

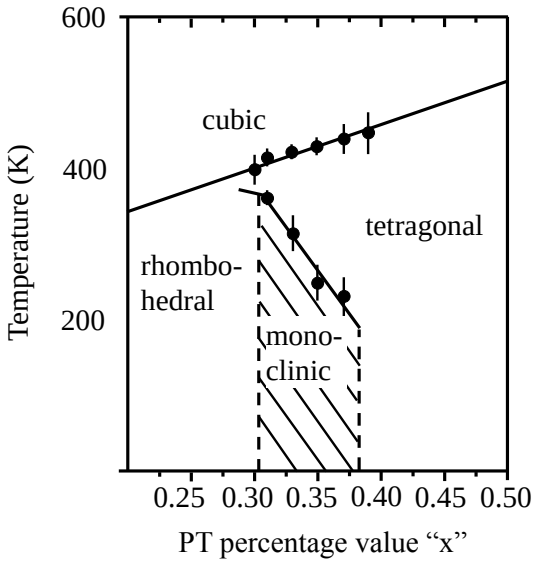

Figure 2.3: Phase diagram for (1-x)PMN-xPT.

The coexistence of regions with monoclinic symmetry has been reported for PT ratios of $31\% \leq x \leq 37\%$. The close proximity and coexistence of several crystal symmetries is probably the origin of the very large piezoelectric coefficients of PMN-PT. This means that, for applications where large displacements (high piezoelectric coefficients) are required, the best suited PMN-PT crystals are those with a monoclinic internal structure. This is due to its phase boundary proximity with the tetragonal phase at room temperature.

These materials can potentially offer significantly improved performance of ultrasonic transducers through enhanced bandwidth and sensitivity, both in transmission and transmit-receive configurations [Coutte et al., 2002] [Marin-Franch et al., 2004] [Hosono et al., 2006]. Like mentioned previously, PMN-PT is a relaxor ferroelectric and a bicomposit. Ferroelectricity is the material's property to have a spontaneous electric polarization which can be reversed, in special conditions, by applying an external electric field [Smolenskiy, 1972] [Lines et al., 1977]. The particularity of PMN-PT is that it also ex-

hibits very high electrostriction. This means that under the application of an electric field the electrically non-conductors (dielectrics) change their shape. Electrostriction is caused by the slight displacement of ions in the crystal structure. Positive ions get displaced in the direction of the field, while the negative ones get displaced in the opposite direction. The connection between an applied electric field and displacement generated is quantified by piezoelectric coefficients. Their specific notation will be detailed in a following section.

The PMN-PT monocristal shows another connection between the operation frequency and the dielectric constant. Chaipanich et al. present in [Chaipanich et al., 2012] that the dielectric constant (ϵr) measured at $1\ kHz$ was found to be ≈ 1500. Increasing the frequency 20 fold reduces this value to ≈ 1300. This study also brings to attention something called "instantaneous" remnant polarization (P_{ir}), which is directly correlated to hysteretic behavior of the material. It reaches a value of $\approx 10\ \mu C/cm^2$.

All the above mentioned properties result directly from and are controlled by the crystal manufacturing process. The following section deals with the benefits and insufficiencies of the most common fabrication processes, all of which are used both by researchers, as well as suppliers.

2.2.1/ PMN-PT PRODUCTION - OBTAINING THE MONOCRYSTAL

Recently, a new class of single-crystal piezoelectric materials such as Lead Magnesium Titanate doped with Lead Titanate (PMN-PT) has been synthesized and was found to further enhance the electro-mechanical coupling factor and piezoelectric constant compared to PZT. The preferred methods of fabricating the mono-crystal are presented here, each of them having advantages that can be exploited in either research or for commercial purposes.

Although these are reliable methods of fabrication, they all influence the final properties and qualities of the mono-crystal. Most importantly, they affect the piezoelectric capabilities through coefficient variation, crystal orientation and final ingot size. This is particularly important when wanting to integrate the material as an actuator. The following sections present fabrication methods of interest, leading to the one preferred and sought when the PMN-PT plates were purchased.

The Flux Method

As it has a mono-crystalline structure, PMN-PT crystals can be grown using a flux method. This is a method where the components of the desired product are dissolved in a solvent, also called flux. For PMN-PT, a stable environment is provided by using the PbO–Pb_3O_4–B_2O_3 system as a solvent. This solvent allows for the capability of controlling the ratios between the two elements of the bicomposit. This method is predominantly used as it is very much suitable for crystals that need to be free of thermal strain - this is especially important to PMN-PT as its piezoelectric coefficients can be changed with electrical fields even at room temperature.

It takes place in a crucible (Figure 2.4) made of a non-reactive material. In the case of metallic crystals, as is the case of PMN-PT, crucibles made from ceramics are employed (boron nitride, alumina and or zirconia). The crystal growth is done in an air-isolated environment either by placing the crucible in a quartz ampoule or an atmosphere-controlled furnace. The saturated solution is prepared by keeping the constituents (crystal

and flux) at temperatures slightly above the saturation temperature for a long enough period to form a complete solution. The crucible is then cooled down and the PMN-PT solution is allowed to precipitate. Another particularity of PMN-PT is that it does not require a seed (a small piece of crystal that provides the structure for the new one).

Figure 2.4: A ceramic crucible used in crystal growth.

One advantage of this method is that the crystals grown often display natural facets (Figure 2.5), which often makes preparing crystals for measurement significantly easier. A major advantage of using the procedure is that, unlike most flux method syntheses that produce relatively small crystals, PMN-PT can be grown in bars with diameters larger than $25\ mm$.

Due to factors such as the very high evaporation rate of PbO at high temperature and complex composition, it is difficult to grow large high-quality crystals - a reason why there are only very few PMN-PT manufacturers. The chemical composition of single crystals is usually determined by energy dispersion spectrometry EDS technique, as demonstrated by Kania et al. [Kania et al., 2006]. Figure 2.5 presents PMN-PT single crystals grown using the Flux Method, wothout a seed, thus the relative small crystal size.

Figure 2.5: 0.68PMN-0.32PT single crystal (placed on millimetre paper) [Luo et al., 2009].

The crystals shown consist of the perovskite phase only (having the same crystal structure as Calcium Titanium Oxide - $CaTiO_3$). By using X-ray diffraction it can be observed how changing the bicomposit ratio affects the symmetry. This passes from pseudo-cubic (100% PMN), to rhombohedral, to monoclinic and lastly to tetragonal (100% PT). Table 2.1 presents the phase transition for the most commonly used $(1-x)$PMN–xPT single crystals ratios, which can also be confirmed by dielectric measurements. It points to the gradual evolution of the crystal from a full relaxor ($PbMg_{1/3}Nb_{2/3}O$) to a full ferroelectric one ($PbTiO_3$).

Table 2.1: The symmetry of the $(1-x)$PMN-xPT single crystals.

Compound	***Symmetry***
PMN	Cubic
0.91PMN-0.09PT	Cubic
0.79PMN-0.21PT	Rhombohedral
0.72PMN-0.28PT	Rhombohedral
0.68PMN-0.32PT	Monoclinic
0.65PMN-0.35PT	Monoclinic
0.62PMN-0.38PT	Monoclinic
0.50PMN-0.50PT	Tetragonal
0.36PMN-0.64PT	Tetragonal
PT	Tetragonal

Although this method provides very good quality crystals, for which the ratio between the bi-composites can be precisely controlled, only small crystals can be grown. This makes the method more suitable for research crystal composition determined properties, mechanical and electrical. For applications, such as microgripper integration or flexural transducers, larger crystals are needed, something that can be done with the following method.

The Czochralski Method

The Czochralski Method for crystal growth is gaining ground in regards to usage due not only to its cost efficiency, but also the size of the resulting crystals. Although usually used in growing semiconductors (like silicon [De Mattei et al., 1981], gallium arsenide [McCluskey et al., 2012] or germanium) or metals (silver, gold, palladium [Yokoyama et al., 1992] or platinum [Vasiliev et al., 1996]), this process proves to be very useful for growing PMN-PT. Although this method is used very successfully to grow large crystals, it does bring the disadvantage of allowing for impurities from the crucible, as it can dissolve. Discoverd in 1916 by the Polish scientist it is named after, Jan Czochralski, it is vastly used in the electronics industry as it is able to produce large, cylindrical ignots of semiconductors - the integrated circuits industry.

The procedure involves five major steps (represented schematically in Figure 2.6). Inside a crucible, the crystal components are mixed under a powder form, melted and doped (a). When the appropriate parameters are reached the PMN-PT crystal seed is introduced (b) and the growth can begin (c). This is done by rotating the seed holder and lifting/pulling it (d). Finally, the process is halted and the formed crystal bar is removed (e). A major difference in comparison to the Flux Method is the mandatory use of a seed (step b). Another is the need of mechanized motions as pointed in Figure 2.7 by the red arrows for both the seed holder and the crucible support.

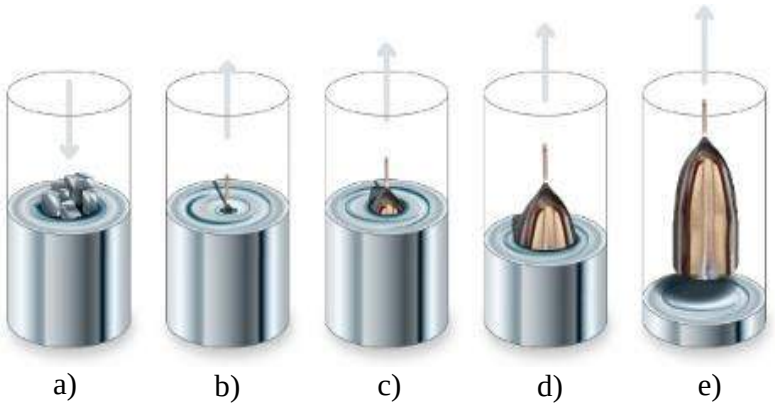

Figure 2.6: The five main stages of single crystal growth for the Czochralski Method [Kenjiro, 2012].

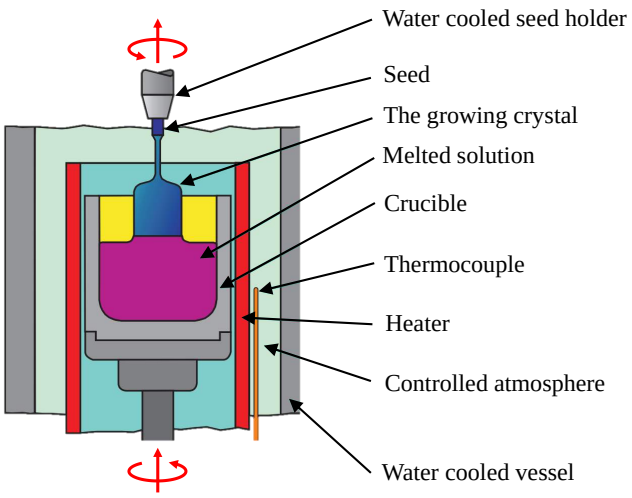

Figure 2.7: The components of the Czochralski crystal growing method system.

Figure 2.8 depicts a PMN-PT crystals grown using the Czochralski Method. Not only is the size apparent, but also the impurities as seen in the layering in (a) and the colour of the separeted plates in (b). Wafers are cut depending along the crystalline growth direction in relatively thin layers. Manufacturers cut the crystal depending to the buyer's need, but it is usually in the range of $200\ \mu m$-$350\ \mu m$. This technique is also suitable for growing a large array of non-PZT crystals, some of which are presented in Annex A.1.

Unlike the previous method, this one can produce large crystals. This, however, comes with a compromise between crystal purity and bicomposite ratio control. This method is preferred for crystals used in energy harvesters or different transducers.

The modified Bridgeman technique

The modified Bridgeman technique is a single-crystal ingot growing method that involves the heating of a polycrystalline material above the melting point followed by the

(a) (b)

Figure 2.8: A $100\ mm$ diameter PMN-PT crystal grown along [001] - (a) and $100\ mm$ diameter [001] wafers (in comparison with $75\ mm$ diameter ones) - (b) [Luo et al., 2014].

cooling of the container from one end to the other, where the crystal seed is located. This method works both for a vertical geometry, as well for a horizontal one. This method is preferred over the Czochralski process in the case of semiconductor crystals. While this method also uses a moving crucible and a temperature gradient, like the flux method, it utilizes the relatively uncontrolled gradient produced at the exit of the furnace.

The shape and position of a solid–liquid interface are readily controlled during growth because the temperature at the solid–liquid interface is kept almost unchanged, being equal to their melting points [Xu et al., 2001]. Modifications are necessary though in the starting materials and growth method in order to obtain PMN-PT crystals with large size, high perfection and uniformity in composition and properties as presented in [Miyagawa et al., 2013]. Figure 2.9 presents the vertical Bridgeman method alongside the temperature vs. position curve. The raw materials are put into a Molybdenum (Mo) or Tungsten (W) crucible from above and a c-axis seed crystal is inserted in the seed well at the bottom of the crucible (a). An advantage of using these materials for the crucible is the minimum dissolving and contamination of the growing PMN-PT crystal. The growth processes consists of first seeding, after melting of all raw material and a part of seed crystal (b) and then, as the crucible is pulled down, formation of thin neck (c), and growth of the crystal body (d). After cooling to room temperature, the seed and the body grown can be easily separated and released from the crucible.

Although the modified Bridgeman method is a very promising technique, the composition segregation issue has to be addressed. Since PMN-PT is a complete solid-solution system, as shown by its high temperature phase diagram, it inevitably exhibits an inhomogeneous composition distribution along crystal boules grown by the Bridgeman method [Luo et al., 1999] [Zawilski et al., 2005] resulting in the variation of dielectric and piezoelectric properties along the growth direction. The different crystal colour (comparing with Figure 2.8) is due to a combination of temperature variations, the doping element used (Mn in the case presented in Figure 2.10) and the fewer impurities.

This method brings together the positives of both previously presented techniques as it is able to not only produce large crystals, but, because of the precise temperature control and crucible construction, not only are the impurities eliminated, but can be added on demand (doping), depending on the specific use of the grown crystal.

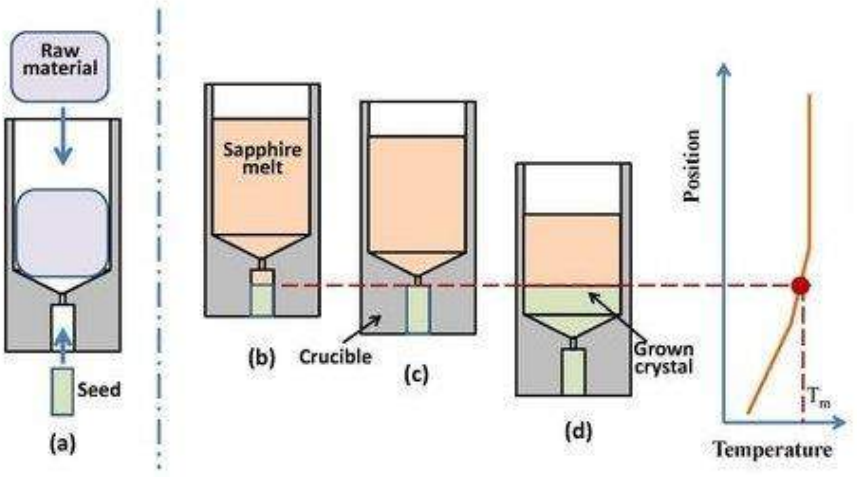

Figure 2.9: Vertical Bridgeman growth with thin neck formation process [Miyagawa et al., 2013].

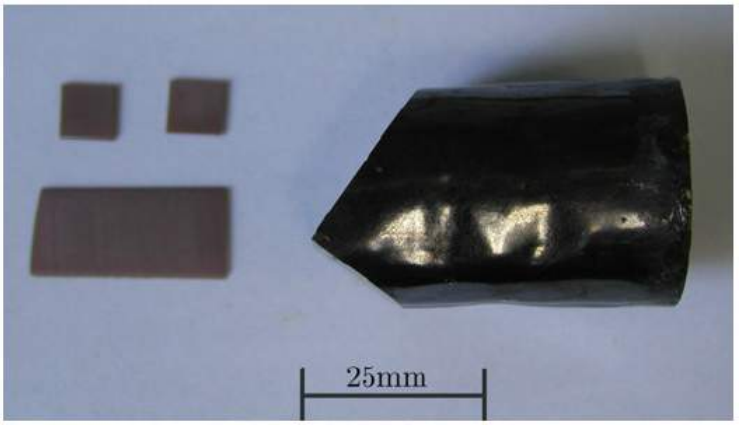

Figure 2.10: 0.71PMN-0.29PT crystal grown [Luo et al., 2009].

An advantage of this techniques is the control of spontaneous nucleation (the formation of a new thermodynamic phase) and parasitic growth. This allow for the crystal size and perfection to be better predicted, in comparison to other methods. For PMN-PT it is particularly effective as it can allow for the production of large and stable crystals, with uniformly distributed piezoelectric properties. It also allows for repeatability of production.

The requirements and limitations imposed by the two aforementioned projects, ADMAN and MIOP, point to the need of PMN-PT crystals that have very high piezoelectric coefficients, components ratio, crystal structure uniformity and lack of impurities as well as ingots large enough to allow for the fabrication of large structures. Taking this into account, the modified Bridgeman technique is preferred over others when purchasing the PMN-PT piezoelectric material.

The properties mentioned are needed in both microrobotic applications (beam actuators) and MOEMS (very compact actuators with large displacement). The most important ones are further detailed in the following section.

2.2.2/ PIEZOELECTRIC COEFFICIENTS AND THE COMPONENTS RATIO IMPORTANCE

The most important characteristic of a piezoelectric material is defined by the displacement to applied voltage ratio (piezoelectric coefficient). This section focuses on the importance of the PT to PMN-PT ratio and how the material choice for the projects of was made.

Chemical analysis shows that, except for Pb, all other elements in PMN-PT crystals exhibit composition segregation during crystal growth, with effective segregation coefficients of Nb and Mg larger than one, while that of Ti is smaller than one. Figure 2.11 compares the piezoelectric coefficient (d_{33}) variation with the composition distributions measured by EPMA [Hackenberger et al., 2008], which shows the region between two peaks roughly corresponding to a PT ($PbTiO_3$) concentration of 31% to 37%, which is basically consistent with the broad MPB region between rhombohedral and tetragonal phases proposed by Guo et al. [Guo et al., 2002], [Zhao et al., 2003]. The simulated effective segregation coefficient of Ti in this run was around 0.83. Studies show that the mixed phases, including metastable ferroelectric monoclinic (FE_m) and ferroelectric orthorhombic (FE_o) phases, are possibly present in this region [Guo et al., 2002], [Zhao et al., 2003], [Davis et al., 2006].

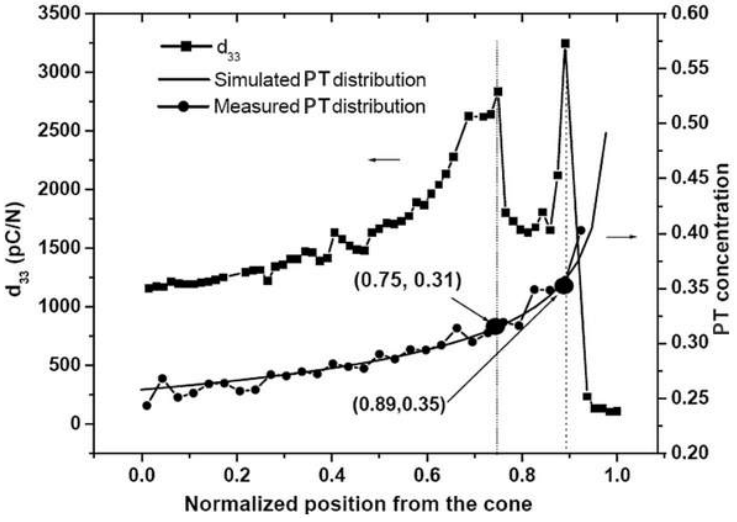

Figure 2.11: A comparison of piezoelectric property (d_{33}) variation with the composition distribution [Hackenberger et al., 2008] along the length of a PMN-PT crystal. The slope of the two curves are similar pointing to a correlation between the PT concentration and the d_{33} coefficient.

As mentioned, the piezoelectric coefficients can reach very high values, but vary in direct correlation to the mole fraction. Some examples that highlight this are seen in [Kim et al., 2010] where $d_{33} = 1780\ pm/V$ for a PMN-PT ratio of $2/3$ to $1/3$ or 0.66PMN-0.33PT sample or in [Shen et al., 2014], where, for 0.68PMN-0.32PT, the value drops to approx. half, $d_{33} = 900\ pm/V$. Another example is found in [Cao et al., 2004] for 0.58PMN-0.42PT, where the measured piezoelectric constant d_{33} is $260\ pm/V$. PMN-PT presents high resonance frequencies, as shown in [Kim et al., 2010] or [Tang et al., 2014], of above $5MHz$ for $0.36mm$ think films for transducers and above $400\ Hz$ for energy harvesters. The

wide variety of piezoelectric coefficients is controlled through the crystal growth procedure, as mentioned in the Chapter 1 and through a close communication with the producer/seller.

The PMN-PT high value piezoelectric coefficients can be altered after the crystal is grown. PMN-PT can be polled at room temperature, though it has been observed that special polling conditions [Shen et al., 2014] do have an effect on the piezoelectric coefficients. After repoling in special conditions of either specific temperatures or frequencies the piezoelectric coefficient can reach values of up to and, in rare occasion, surpass $4500\ pm/V$ [Yamamoto et al., 2013].

The first observation is that the majority of studied mono-crystals present a PT percentage in the $31 - 35\ \%$ range, and that there are two preferred crystal orientations: [001] and anisotropic [011]. This is due to the fact of manufacturing being more reliable and stable for these percentages and that in this range, the piezoelectric coefficients present the highest values, translating into larger displacements.

Another observation is that out of all the mono-crystals, PMN-PT presents the highest piezoelectric properties for both the [001] and [011] cuts. In Figure 2.12 some PMN-PT and PMN-PT-like crystals are arranged, according to their bicomposite ratio and the piezoelectric coefficient of importance. This allows for an overview on the optimal PT based crystals and percentage for large displacement to voltage coefficients. There are two outlined areas: a square one, marking the interest in the [011] anisotropic cut, with PMN-PT presenting the highest piezoelectric coefficient and a circular one, marking the interest in the [001] cut, where PMN-PT also stands out.

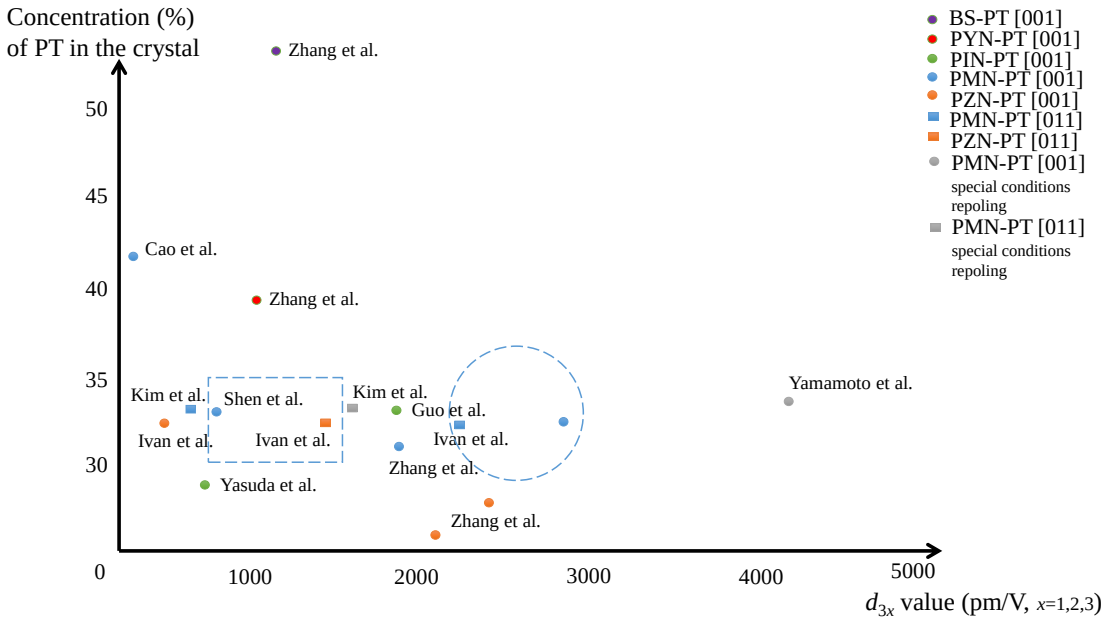

Figure 2.12: The piezoelectric coefficient of interest d_{3i} (where $i = 1, 2, 3$) variation with the bicomposit ratio (PT percentage) [Yamashita et al., 1997, Yasuda et al., 2001, Yasuda et al., 2002, Zhang et al., 2002b, Guo et al., 2003, Zhang et al., 2003, Zhang et al., 2004a, Zhang et al., 2004b]

Other independent electromechanical constants for the [001] crystalline direction cut, such as the elastic or the dielectric ones, are presented in the tables from Annexes B.1, B.2 and B.3 as studied in [Cheng et al., 2000, Zhang et al., 2008, Luo et al., 2010] by using the resonance method for determination. In the case of [011]-polled crystals, either a resonance or a hybrid method was employed to collect the full sets of properties. There are a total of 17 independent electromechanical coefficients, nine elastic, five piezoelectric and three dielectric. Detailed procedures are presented in [Wang et al., 2007, Huo et al., 2012, Huo et al., 2013].

The [001]-poled PMN-PT crystals possess extremely high k_{33} and d_{33}, so the longitudinal extension mode is very attractive for high power transducer design or compact actuators. Extensive static tests have been done on PMN-PT and PMN-PT-like single crystals under stress as well as high electric field [Janolin et al., 2007, Shanthi et al., 2009, Finkel et al., 2010, Ivan et al., 2013, Ciubotariu et al., 2014b]. The dynamic tests have been conducted only under small electric field [Sherlock et al., 2010], [Sherlock et al., 2012]. These features are important as they point to PMN-PT[001] as a viable candidate for actuators in high frequency applications that require well integrated solutions. In the case of PMN-PT[011], in focus shifts towards other coefficients such as the k_{15}, d_{32} or d_{31} as the material is better suited for flexural actuators. These aspects will be expanded in a following section.

PMN-PT plates have been purchased from TRS TEchnologies®, measuring $200\ \mu m$ in thickness. Depending on the cut, the other dimensions were $20\ x\ 20\ mm^2$ for the [001] cut and $20\ x\ 25\ mm^2$ for the [011] cut. The latter was dimensioned differently to better differentiate between the d_{31} and d_{32} piezoelectric coefficients. They all present gold electrodes, $350\ nm$ thick. All plates have undergone experimental measurements for coefficient value determination. For this, a special rig was designed and fabricated using rapid prototyping. The rig offers support on one side of the plate, while ensuring clamping with the aid of two compliant arms. These arms also provide the electrodes for voltage signal delivery. The positioning of the plate was done with agreement between the polarisation direction, marked by a black dot, and the applied voltage. The rig can be fixed to an experiment table via the two $6\ mm$ holes, as seen in Figure 2.13.

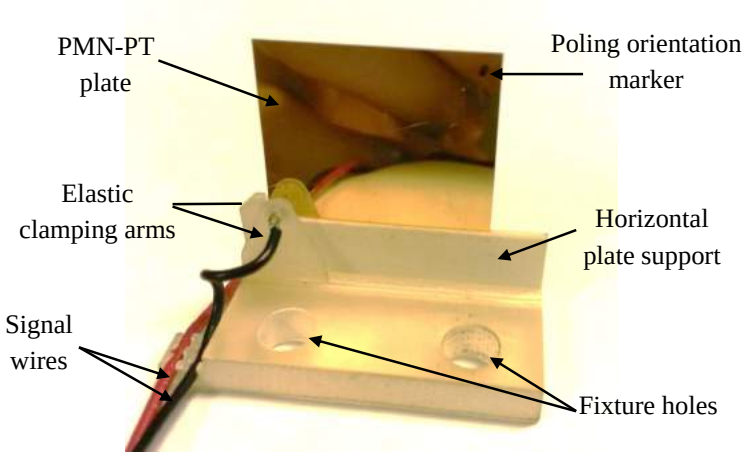

Figure 2.13: The clamping rig used for the experimental measurements of the d_{31}, d_{32} and d_{33} piezoelectric coefficients for both the [001] and the [011] cut.

The measurements have been done following the same procedure for all plates,

indifferent to the cut. For accurate measurements, an interferometer was used with two optican heads registering the variations on opposite ends of the clamped plate. This way, a relative measure could be performed. Figure 2.14 presents the experimental setup. While the d_{31} and d_{32} coefficients can be measured alternatively, for each plate, by repositioning the plate from its length on its width, respectively, for the d_{33} piezoelectric coefficient, the clamping rig was rotated $90°$ in respect to the interferometer optical heads, although in the schematic representation, the plate is fixed. The new relative position is represented by the dotted interferometer heads. In order to identify the piezoelectric coefficients, a low frequency ($0.33\ Hz$) sine signal was applied, the same for all the measurements. With a peak-to-peak amplitude of $400\ V$, the signal was shifted by $200\ V$ in the positive front, to protect the plates from repoling. The interferometer heads allow for tip/tilt manual orientation and were positioned on manually actuated X-Y positioning stages.

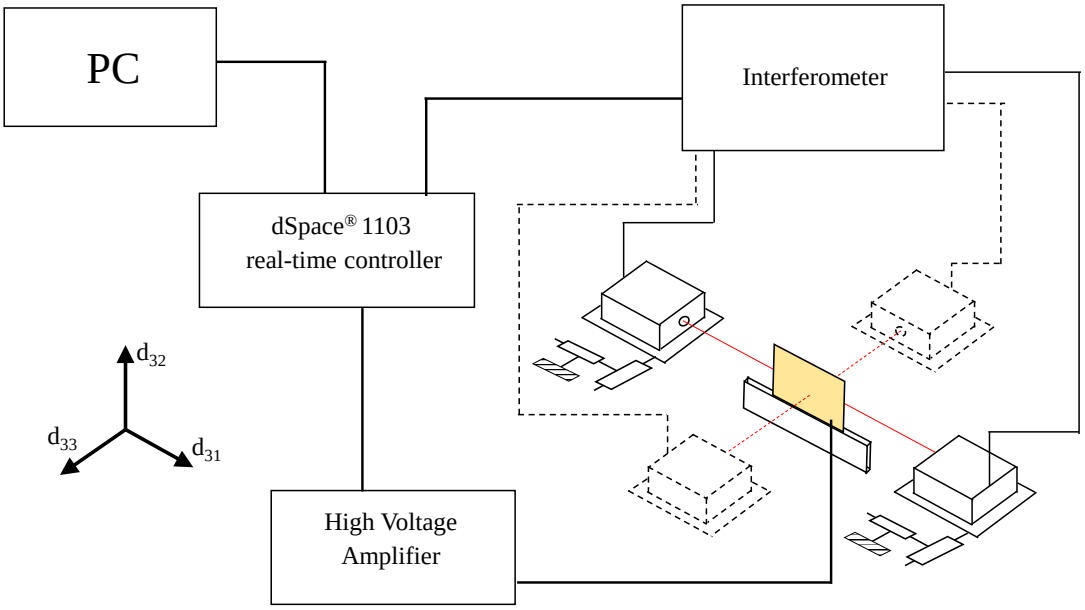

Figure 2.14: The experimental setup used to find the d_{31}, d_{32} and d_{33} piezoelectric coefficients numeric values, for both the [001] and the [011] cut.

The values found are consistent between plates and with those found in literature for this ratio PMN-PT crystal. For the anisotropic [011] cut the values are $476\ pm/V$ for d_{31}, $-1480\ pm/V$ for d_{32} and $2480\ pm/V$ for d_{33}. Not only does the d_{31} coefficient have a positive value, but it is double that of PZT ceramics and offers a new approach for actuators used in microrobotics. For the longitudinal [001] cut the values are $-1066\ pm/V$ for d_{31}, $-1047\ pm/V$ for d_{32} and 2520 for d_{33}. The very close d_{31} and d_{32} values, coupled with the very large d_{33} make PMN-PT [001] a promising candidate for integrated micromirror actuation. These high piezoelectric coefficients, along with how PMN-PT can be machined, without losing its properties make the crystal a very interesting integrated actuation solution. The advantages of using PMN-PT in MEMS and MOEMS are discussed in the following section. While the setup is delicate, the values found present an error of under 9% for the larger d_{33} coefficient and under 6% for d_{31} and d_{32}.

2.3/ ADVANTAGES FOR INTEGRABILITY

As exemplified in the previous section, PMN-PT stands out among other single crystal piezoelectric materials as presenting very high voltage to displacement coefficients as well as having very high dynamics. This has prompted more and more for the use of this ferroelectric-relaxor to be used in transducers and energy harvesting applications and, more recently, as the solution for integrated actuation. The following examples attest to the versatility of PMN-PT, from transducers and energy harvesters, to sensors and actuators, where the focus of this work is.

Transducers

Being devices that transform one form of energy intro another, a material that has a high performance regarding conversion is needed. PMN-PT addresses this need with its very short transient time and high bandwidth. Out of the different transducers in use, PMN-PT is ideal for real time applications. This is the case for high frequency intravascular ultrasound imaging, as presented in [Zhang et al., 2015a]. Figure 2.15 presents a lateral view for a PZT and a PMN-PT sample with Ni mask that was etched using a Deep Reactive Ion Etching (DRIE) machine for $3h$. The surface quality of the micro-actuator matrix is another reason why PMN-PT gains ground in imaging applications.

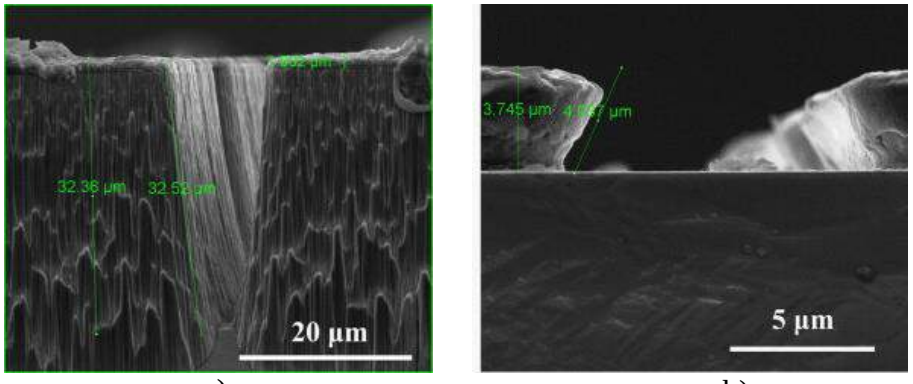

a) b)

Figure 2.15: SEM surface morphologies of (a) PMN-PT after DRIE etching for 3 h and PZT, under the same conditions [Zhang et al., 2015a].

Another benefit brought by PMN-PT is its versatility in being machined. An example is the specially dimpled transducer presented in [Chen et al., 2015] presenting similar or higher performances than a PZT probe. The fabrication of an angled-focused transducer [Yoon et al., 2015] ads to PMN-PT's usages as a trasducer.

As Pb is a metal with high restrictions in the medical field, PMN-PT is in the focus of NDE applications which have been recently developed. One such case is presented in [Edwards et al., 2006] or [Zhang et al., 2011b].

Energy Harvesting

The process in which energy is derived from external sources to be stored is another area of interest where PMN-PT is gaining ground. This is also due to the monocrystal's ability to provide close to double the energy density of previously used PZT ceramics [Ren et al., 2006] or [Rakbamrung et al., 2010] when used in standard forms.

Rakbamrung et al. continues and demonstrates that PMN-PT still outperforms standard piezoelectric materials even in the case of applying Synchronized Switch Harvesting on Inductor (SSHI) technique. (Figure 2.16)

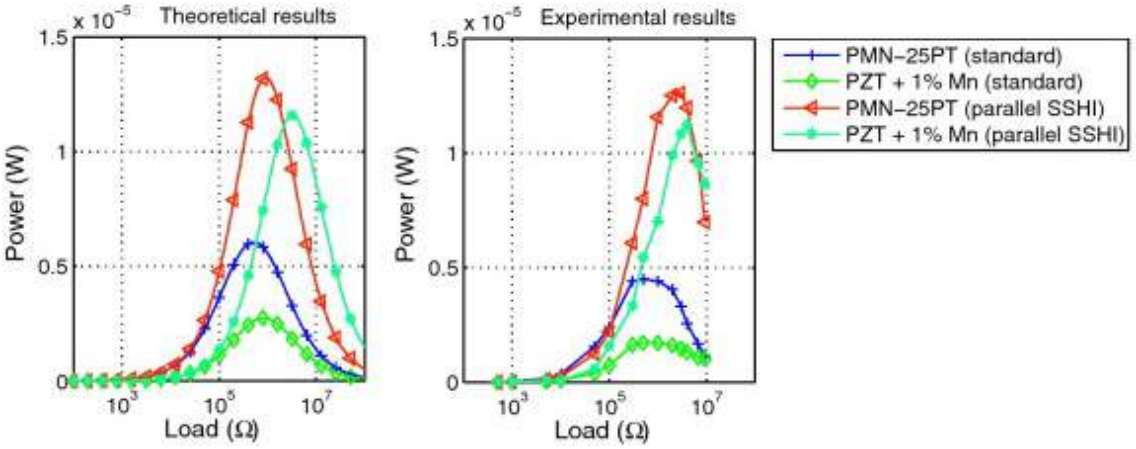

Figure 2.16: Experimental harvested power using standard and SSHI approaches [Rakbamrung et al., 2010].

It was shown in [Rakbamrung et al., 2010] that there is a dependence between the thickness of the piezoelectric material and the energy density harvested. This lead to the development of PMN-PT single crystal film d_{33} mode MEMS vibration energy harvesters. Such an example is presented by Tang et al. in [Tang et al., 2014]. Their device is schematically presented in Figure 2.17. The very high d_{33} piezoelectric coefficient is what allows for a large potential difference between the alternating electrodes deposited on top of the PMN-PT film. Table 2.2 brings together the performances of other energy harvesters in literature, based on PZT ceramics to point out the two to threefold increase when using PMN-PT.

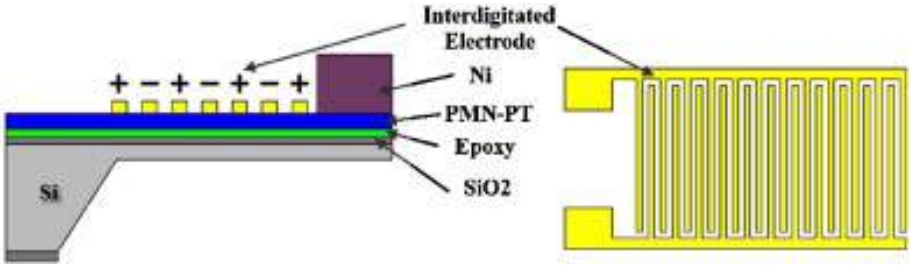

Figure 2.17: Schematic of the d_{33} mode piezoelectric MEMS generator proposed in [Rakbamrung et al., 2010].

PMN-PT can also have its shearing effect capitalized and, by making use of its high d_{15} piezoelectric coefficient, planar energy harvesters can be fabricated, capturing other, previously disregarded, vibration modes. Such an approach is presented in the work of Zhou et al. in [Zhou et al., 2012] where the single degree of freedom model of the cantilever is combined with the piezoelectric constitutive equations in order to describe the energy harvesting performance.

Table 2.2: MEMS piezoelectric harvesters performance comparison.

Device	***Effective volume*** (mm^3)	***Frequency*** (Hz)	***Power*** (μW)	***Power density*** $(\mu W/cm^3)$
d_{31} PZT [Fang et al., 2006]	0.196	608	2.16	11020
d_{31} PZT [Shen et al., 2008]	0.652	461	2.15	3272
d_{33} PZT [Lee et al., 2009]	0.612	214	1.28	2104.5
d_{31} PZT [Lei et al., 2011]	12.88	235	14	1086
d_{33} PMN-PT [Ren et al., 2010]	0.185	60	4.16	10670
d_{33} PMN-PT [Tang et al., 2014]	0.418	406	7.18	17181

Sensors and Actuators

In recent years the usage of PMN-PT has seen a transition from transducers and energy harvesters, that use the direct piezoelectric effect, towards sensors and actuators. This is thanks to the very high dynamic response [Sun et al., 2010, Lau et al., 2010, Li et al., 2011] and large piezoelectric coefficient values [Yamashita et al., 1997, Yasuda et al., 2001, Zhang et al., 2002b, Guo et al., 2003, Zhang et al., 2004b].

Work towards the wide use of PMN-PT as multi-domain frequency sensors has been the focus of recent years such as the work of J.Kim and Y.Roh. In [Kim et al., 2014], where a 72PMN-28PT crystal was analysed through a resonant frequency approach, results place the matrix structure presented in Figure 2.18 in line with the results of [Kim et al., 2010, Tang et al., 2014] not only due to the ease and precision of fabrication, but also in outperforming PZT as an energy harvester, respectively.

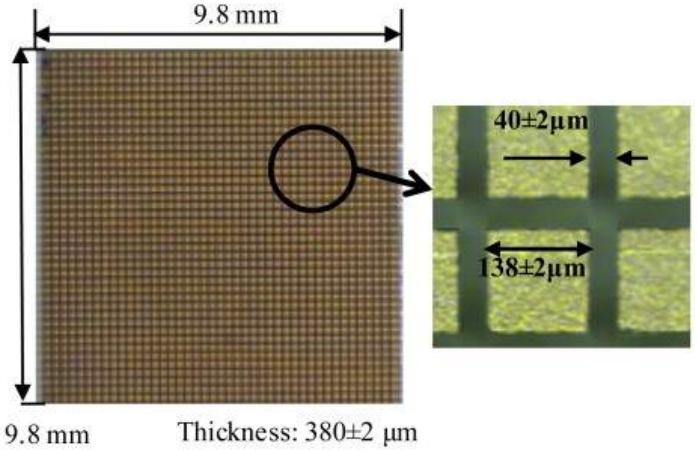

Figure 2.18: PMN-PT/epoxy 1–3 composite plate showing the fabrication tolerances.

Other uses are oriented towards the bio-medical domain and, as such, applications using PMN-PT crystal resonators for microfluidic are being developed. Zhang et al. have used standard soft photolithography techniques to integrate PMN-PT into a microfluidic system [Zhang et al., 2011a]. Relative to conventional thickness shear mode piezoelectric sensors (quartz crystal microbalance), the PMN-PT mono-crystal resonator behaves less resonance-damping with the increase of frequency. The PMN-PT resonator shows responses to the changes of fluids in the microchannel, suggesting that it is potentially

useful for microfluidic systems. The device consists of two major parts: (1) Polydimethylsiloxane (PDMS) microchannel on the top and (2) a shear mode PMN-PT piezoelectric sensor mounted on a glass slide (cross-sectional and top view Figure 2.19(a) and (b)). The full bottom electrode of the PMN-PT piezoelectric resonator acts as the ground plane. The active area of the resonator is a $1\ mm$ diameter "spot" connected to a ground-signal-ground (GSG) pad to facilitate subsequent impedance measurement using a microprobe. The upper PDMS microchannel with a width of $400\ \mu m$ covered the top active electrodes of the resonator

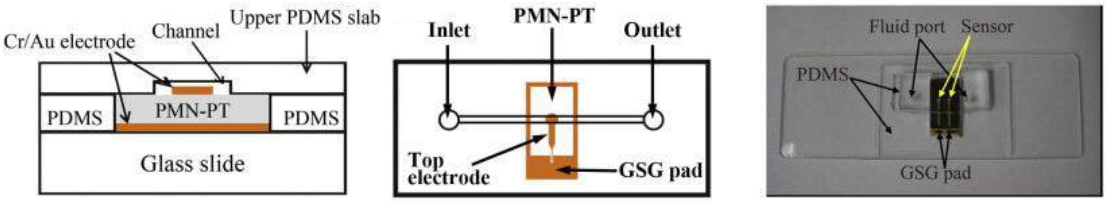

a) b) c)

Figure 2.19: Cross sectional schematic (a), top view configuration (b), and photograph (c) of the microfluidic acoustic device integrated with a shear mode PMN-PT piezoelectric single crystal resonator [Zhang et al., 2011a].

The inverse effect of piezoelectricity can be effectively used with PMN-PT, thus bringing a series of integrated actuation solutions to light. From micro-mirror displacement [Ivan et al., 2010], lens position [Wilkie et al., 2006, Park et al., 2011] or image correction [Woody et al., 2005, Park et al., 2008], fluid ejectors [Lam et al., 2005] or cantilever actuators [Hall et al., 2005, Uršič et al., 2008] to surgical tools [Kuang et al., 2015], PMN-PT proves to be extremely versatile and compatible with traditional fabrication techniques.

2.4/ ELECTRIC AND MECHANICAL PROPERTIES

The importance of the crystal composition over its piezoelectric properties, as well as how to best exploit these characteristics through integrated solutions, have been brought forth in the previous sections.

Of great importance is that the already studied and understood effects of piezoelectricity are observable with PMN-PT. That is to say that the four possible forms for the constitutive equations of piezoelectric materials apply to it. All presented variables are explained in Table 2.3. These forms have been named by the variables on the left side of the equations.

The subscripts in piezoelectric constitutive equations have very important meanings. They describe the conditions under which the material property data was measured. The subscript E, like on the compliance matrix s_E means that the compliance data was measured under at least a constant, and preferably a zero, electric field. Likewise, the subscript T, like on the permittivity matrix ε_T means that the permittivity data was measured under at least a constant, and preferably a zero, stress field and the D, like on

Table 2.3: Variables used in the piezoelectric constitutive equations.

Notation	***Type***	***Dimension***	***Unit***	***Definition***
σ_1	vector	$6X1$	N/m^2	Stress components
ε_1	vector	$6X1$	m/m	Strain components
E	vector	$3X1$	N/C	Electric field components
D	vector	$3X1$	C/m^2	Electric potential density displacement components
s	matrix	$6X6$	m^2/N or TPa^{-1}	Compliance coefficients
c	matrix	$6X6$	N/m^2	Stiffness coefficients
ε	matrix	$3X3$	F/m	Electric permittivity
d	matrix	$3X6$	C/N or pm/V	Piezoelectric coupling coefficients for the Stress-Potential form
e	matrix	$3X6$	C/m^2	Piezoelectric coupling coefficients for the Strain-Potential form
g	matrix	$3X6$	m^2/C	Piezoelectric coupling coefficients for the Stress-Voltage form
q	matrix	$3X6$	N/C	Piezoelectric coupling coefficients for the Strain-Voltage form

the stiffness matrix c_D means that the stifness was measured under at least a constant, and preferably a zero, electric potential displacement field. The superscript t annotates in which matrix the couplings terms are found.

1. Strain-Charge

$$\begin{aligned} \varepsilon_1 &= s_E\sigma_1 + d^tE \\ D &= d\sigma_1 + \varepsilon_T E \end{aligned} \tag{2.1}$$

2. Stress-Charge

$$\begin{aligned} \sigma_1 &= c_E\varepsilon_1 - e^tE \\ D &= e\varepsilon_1 + \varepsilon_s E \end{aligned} \tag{2.2}$$

3. Strain-Voltage

$$\begin{aligned} \varepsilon_1 &= s_D\sigma_1 + g^tD \\ E &= -g\sigma_1 + \varepsilon_T^{-1}D \end{aligned} \tag{2.3}$$

4. Stress-Voltage

$$\begin{aligned} \sigma_1 &= c_D\varepsilon_1 - g^tD \\ E &= -q\varepsilon_1 + \varepsilon_s^{-1}D \end{aligned} \tag{2.4}$$

In order to pass from one form to another, the following tensor transformations are used:

1. Strain-Charge to Stress-Charge

$$\begin{aligned} c_E &= s_E^{-1} \\ e &= ds_E^{-1} \\ \varepsilon_S &= \varepsilon_T - ds_E^{-1}d^t \end{aligned} \tag{2.5}$$

2. Strain-Charge to Strain-Voltage

$$\begin{aligned} s_D &= s_E - d^t \varepsilon_T^{1-} d \\ g &= \varepsilon_T^{-1} d \end{aligned} \tag{2.6}$$

3. Stress-Charge to Stress-Voltage

$$\begin{aligned} c_D &= c_E - e^t \varepsilon_S^{1-} e \\ q &= \varepsilon_S^{-1} e \end{aligned} \tag{2.7}$$

4. Strain-Voltage to Stress-Voltage

$$\begin{aligned} c_D &= s_D^{-1} \\ q &= g s_D^{-1} \\ \varepsilon_S^{-1} &= \varepsilon_T^{-1} - g s_D^{-1} g^t \end{aligned} \tag{2.8}$$

Although work on the analysis of the micro-structure of PMN-PT has been done, with examples as [Detalle et al., 2007, Zhao et al., 2009, Jiang et al., 2011, Wei et al., 2012], these focus mostly on the indirect piezoelectric effect. It has been noted that the PMN-PT mono-crystal shows an important connection between the operation frequency and the dielectric constant. [Chaipanich et al., 2012] found that the dielectric constant (ε_r) measured at $1\ kHz$ of $\backsim\ 1500\ F/m$ changes with the frequency. A 20 fold increase reduces this value to $\backsim\ 1300\ F/m$. This study also brings to attention something called “instantaneous” remnant polarization (P_{ir}), which is directly correlated to hysteretic behaviour of the material.

Measuring the Young Modulus on a beam actuator made of PMN-PT brought forth that the capacitor effect of the single crystal is indeed very elevated. A reason why, coupling this with the consistent values for the dielectric constant showed in [Chaipanich et al., 2012], it makes PMN-PT suitable for dynamic transducers. Figure 2.20 illustrates this capacitor effect and how it varies with frequency. This points to PMN-PT being better suited for high-frequency applications.

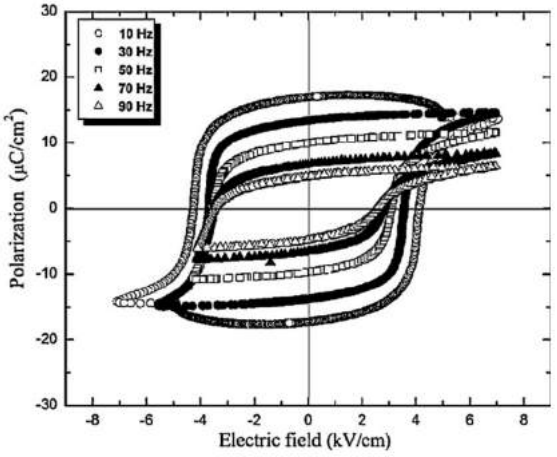

Figure 2.20: Ferroelectric polarization–electric field (P–E) hysteresis loops of PMN–PT/PC composites at 10–90 Hz [Chaipanich et al., 2012].

By using the descriptive piezoelectric equations, understanding the tight connection between the operation frequency and the dielectric constants and utilizing the capacitor effect better behaviour predictions can be made (self sensing becomes possible), aiding in the development of a more accurate control, when using the indirect effect of piezoelectric materials. This, of course applies to PMN-PT as well.

When choosing PMN-PT for any application another factor must be carefully taken into account, namely the crystalline orientation and polarization. Figure 2.21 summarizes the notation for each possible orientation. Depending on how a crystal is grown and cut, and PMN-PT is no exception, different displacements can be observed thus making the development for application oriented actuators possible. There are three effects of most common use, each being mathematically described in the following paragraphs.

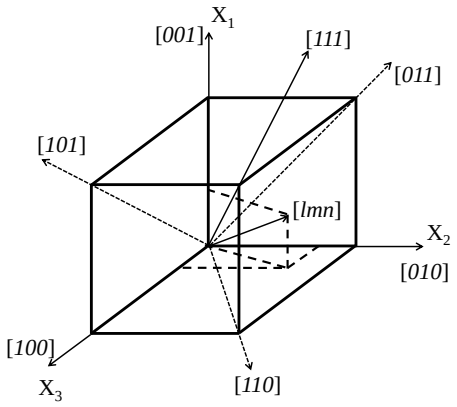

Figure 2.21: The notation of crystalline direction in regards to the Cartesian system $X_1X_2X_3$.

The longitudinal effect

This is the first and most commonly used effect. The deformation is generated in the same direction as the applied electric field. This effect is also how the maximum force output can be generated, as well as the highest precision displacements, by piezoelectric materials. Figure 2.22 is a generic representation of this effect.

For each varying dimension, following the mathematical model presented in [Bourjault et al., 2002], these equations emerge, presenting the achievable displacements when there are no constraints (bounding conditions are null):

$$S_3 = \frac{\Delta L}{L} = d_{33}E_3 = d_{33}\frac{V}{L} \tag{2.9}$$

$$S_i = \frac{\Delta w_i}{w_i} = d_{3i}E_3 = d_{3i}\frac{V}{L}; \quad i = 1,2 \tag{2.10}$$

The direct results of which can be written as:

$$\Delta L = d_{33}V \tag{2.11}$$

$$\Delta w_i = d_{3i}\frac{w_i}{L}V; \quad i = 1,2 \tag{2.12}$$

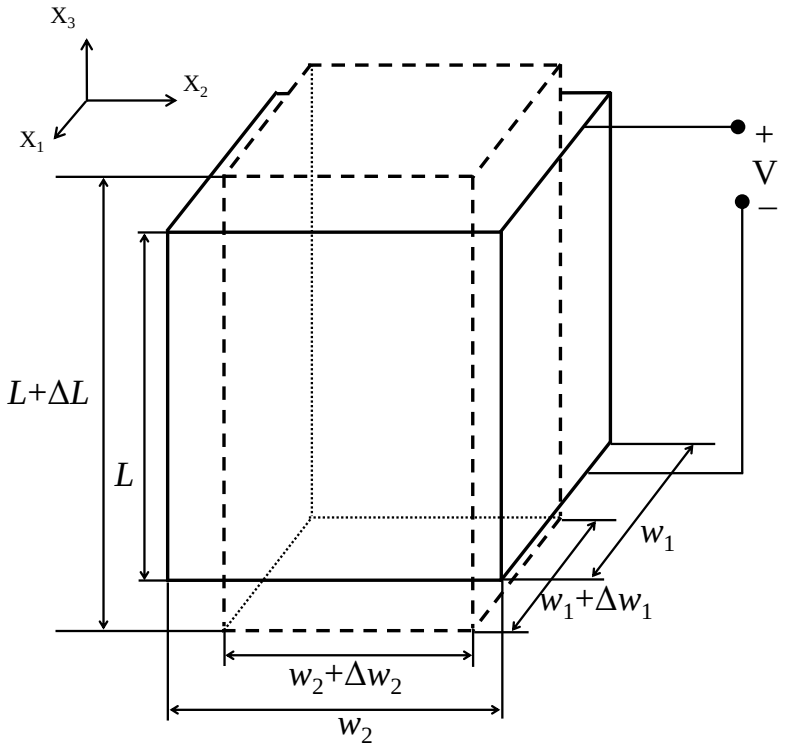

Figure 2.22: The longitudinal piezoelectric effect (usage of the d_{33} coefficient) for a generic piezoelectric actuator of hight L, width w_1 and thickness w_2. The dotted line represents the deformed shape.

The electrical capacitance (C) presented by the piezoelectric material can be written as:

$$C = \varepsilon_{33} \frac{w_1 w_2}{L} \tag{2.13}$$

The driving capability of an actuator is defined as the force that needs to be overcome, i.e. the one that cancels the displacement produced. It is also found in literature as being the Blocking Force (F_b) and it's measured along the displacement direction.

$$F_b = -\frac{d_{33}}{s_{33}} \frac{w_1 w_2}{L} V \tag{2.14}$$

The transverse effect

This effect is mostly used when fabricating bending sensors or actuators (flexural deformation either through the direct or indirect piezoelectric effect). The main deformation (along the X_1-axis) is measure perpendicular to the electric field (along the X_3-axis).

The same as in the previous case, the dimension variations are given by the following equations:

$$S_1 = \frac{\Delta L}{L} = d_{31} \frac{V}{w} \tag{2.15}$$

$$\Delta L = d_{31} \frac{L}{w} V \tag{2.16}$$

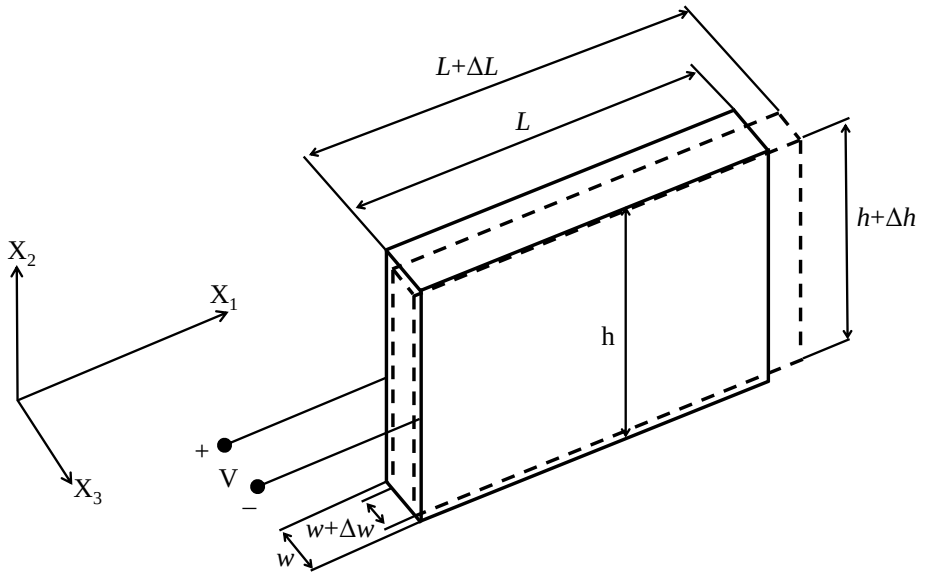

Figure 2.23: The transverse piezoelectric effect (usage of the d_{31} or d_{32} coefficients) for a generic piezoelectric actuator of length L, width w and height h .

The other two dimensional variables are given by the equations:

$$\Delta w = d_{33} V \tag{2.17}$$

$$\Delta h = d_{32} \frac{h}{w} V \tag{2.18}$$

The capacitance of the actuator is given by the following equation:

$$C = \varepsilon_{33} \frac{hL}{w} \tag{2.19}$$

The shearing effect

This is more rarely used effect, but it's the one utilized when there is a need for workspace restricted accelerometers and when there is a need for planar displacements with high and very high working frequencies. The particularity of this effect is that is has three subcategories: (a) parallel shearing (Figure 2.24), (b) transverse shearing (Figure 2.25) and (c)flexural shearing (Figure 2.26).

In the case of **parallel shearing** (with displacement on the X_1 axis) there is only one deformation (S_5) to be described. δx_1 represents the deformation measured along the X_1 axis, while δu_3 is the deformation measured along the X_3 axis.

$$S_5 = \frac{\delta u_3}{\delta x_1} = d_{15} \frac{V}{h} \tag{2.20}$$

If the displacement along the X_1 axis is zero, then the displacement is observed only on one side and is measured in relation to the stationary one at the height h having the notation $u_{3(+h)}$. It has the following mathematica expression:

$$u_{3(+h)} = d_{15} V \tag{2.21}$$

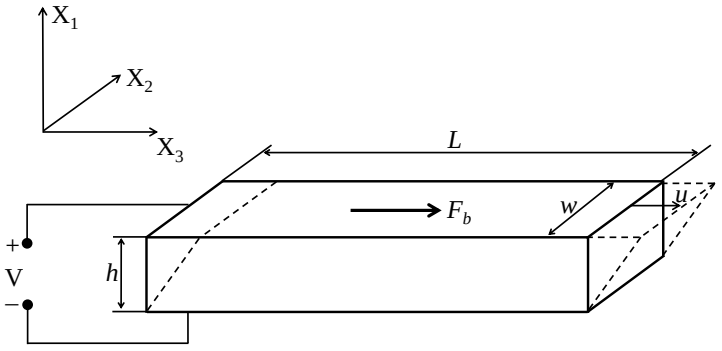

Figure 2.24: The parallel shearing effect (usage of the d_{15} coefficient) for a generic piezoelectric actuator of length L, width w and height h .

The blocking force, in this shearing case, is tangent to the X_3 axis and takes the following form:

$$F_b = \frac{d_{15}}{s_{55}} \frac{Lw}{h} V \tag{2.22}$$

Transverse shearing (Figure 2.25) has to do with the clamping position and where the power supply is placed. Two relations are representative of this kind of shearing, one involving the electric charge - equation (2.23) and another, the applied voltage - equation (2.24).

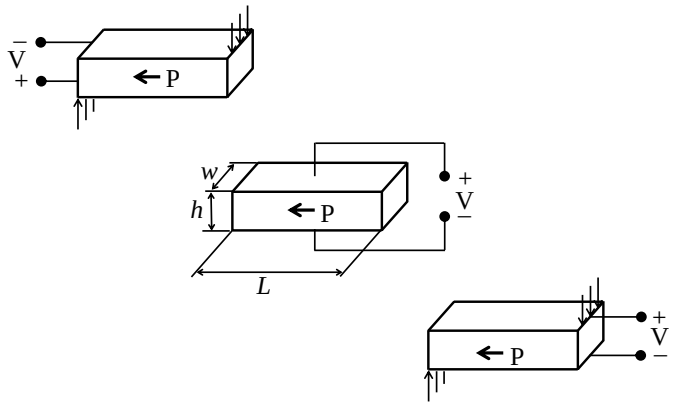

Figure 2.25: The transverse shearing effect (usage of the d_{15} coefficient) for a generic piezoelectric actuator of length L, width w and height h The points where the voltage is applied and the polarization field orientation are important in order to generate displacement.

$$Q = \frac{LFd_{15}}{h} \tag{2.23}$$

$$V = \frac{Fg_{15}}{h} \tag{2.24}$$

In the case of **flexural shearing** (Figure 2.26) the displacement to voltage equations differ depending on the type of connection. Another thing to consider is the po-

larization field orientation, especially when working with PMN-PT. The equations are as follows:

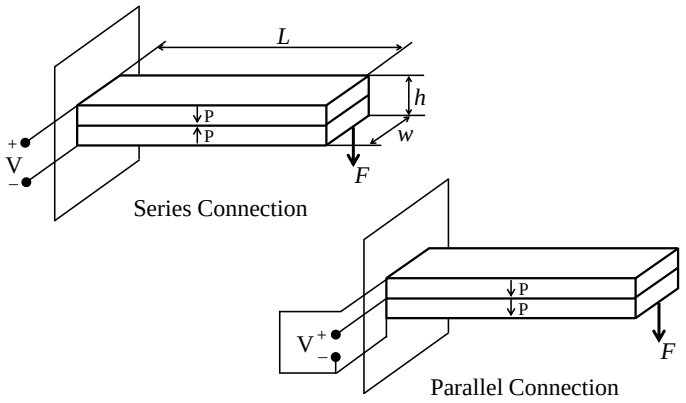

Figure 2.26: The flexural shearing effect (usage of the d_{31} coefficient) for a generic piezoelectric actuator of length L, width w and height h.

1. Series connection (both Electric charge and Voltage):

$$Q = \frac{3FL^2 d_{31}}{2w^2} \tag{2.25}$$

$$V = \frac{3FLg_{31}}{2hw} \tag{2.26}$$

2. Parallel connection (both Electric charge and Voltage):

$$Q = \frac{3FL^2 d_{31}}{w^2} \tag{2.27}$$

$$V = \frac{3FLg_{31}}{4hw} \tag{2.28}$$

Knowing the type of crystal orientation is important, but there is another electromechanical feature that needs considering when using PMN-PT as an actuator (making use of the inverse piezoelectric effect): **the value of the coercive field**. At this electric field value is where the ferroelectric material starts to repolarize.

The value (in modulus) of PMN-PT's coercive field (V_c) is between 15 and $45\ V$ [Ivan et al., 2011], depending on the cut. This results in the material being used in bipolar manner only partially. These values are true for poling procedures that start from room temperature and stop at the Curie temperature (where a material's spontaneous electric polarisation changes to induced electric polarisation, or vice versa [Sadoc et al., 2010]).

A generic (Figure 2.27) bimorph PMN-PT beam actuator was fabricated in order to demonstrate this actuation principle. Two plates, $200\ \mu m$ thick, were soldered together using EpoTek® H22 silver based solder with a shift, in order to access the common electrode. The individual beams were separated using a saw dicing machine at $1\ mm$ intervals. On a PCB, three electrodes are etched, one on which the 1 DoF beam is soldered (E_1) and two more, for GND and the second electrode (E_2).

The measurements were done using a Keyence® LK-G series laser displacement sensor connected to a dSpace® 1103, following the setup in Figure 2.27. Using Matlab®,

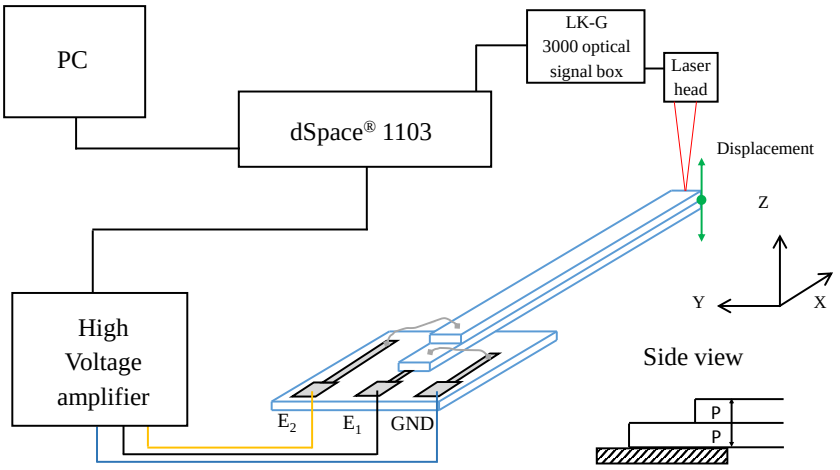

Figure 2.27: Experimental setup for a generic $1\ DoF$ bimorph cantilever actuator with opposing polarization fields.

a specially defined sine signal was applied to the bimorph PMN-PT beam. Two cases were studied, one taking V_c into account, resulting in a partially bipolar actuation and another, where signals are applied to generate pure unipolar actuation. Both cases are described in the following paragraphs.

The following Figures depict the two mentioned actuations applied to the PMN-PT bimorph beam. Figure 2.28 presents the actuation signals for a $1\ DoF$ PMN-PT cantilever actuator for which V_c is known. In this case the applied voltages have a region of overlapping (between the dashed vertical lines, in the centre region) and thus the displacement is amplified. In the following figures V_{E1} and V_{E2} represent the voltages applied to the top and bottom electrodes in order to achieve deflection, δ_Z is the measured displacement for the applied V_Z. The slight asymmetry of the measured displacement in reference to the equilibrium ("zero") position is due to the imperfect clamping for both following cases.

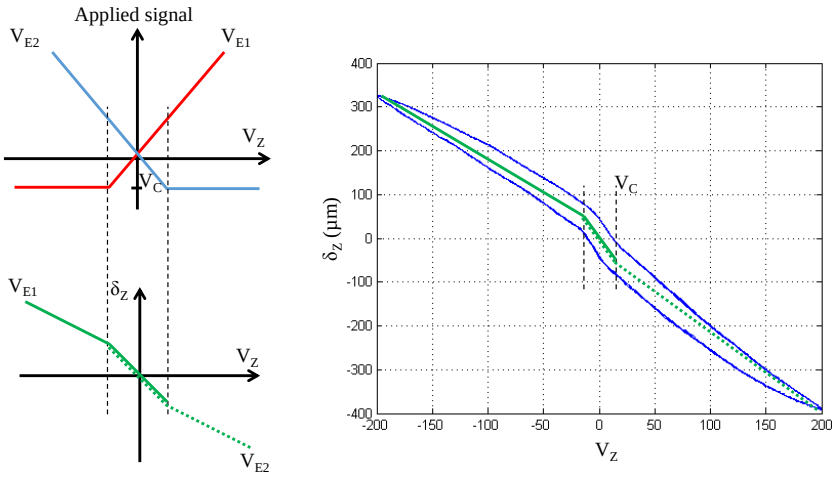

Figure 2.28: Partial bipolar actuation principle and the generated displacement.

If the value of V_c is not to known, then a similarly built bimorph actuator is better actuated in pure unipolar manner, as presented in Figure 2.29. This way, the displacement becomes more ”linear”, each layer being activated at the ”zero” position (the point of equilibrium). Although this causes losses in the displacement magnitude it protects the material from being repolarized.

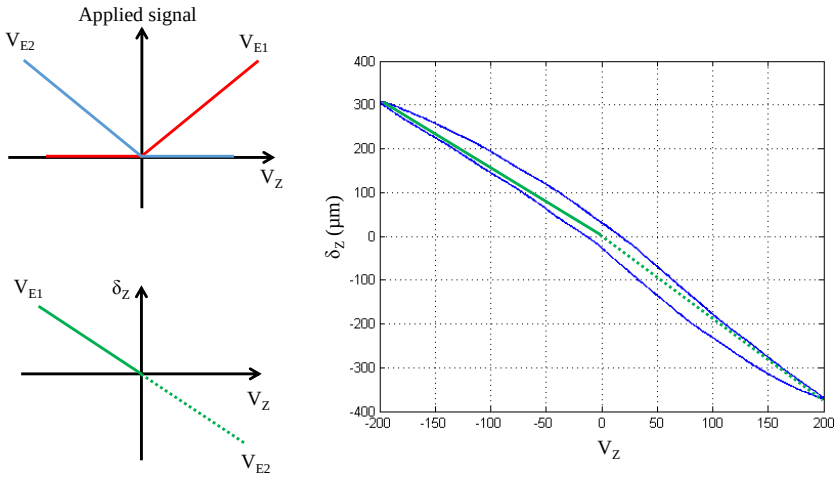

Figure 2.29: Pure unipolar actuation principle and the generated displacement.

Even with this limitation PMN-PT still outperforms PZT ceramics in terms of displacement. Considering the low V_c value and that PMN-PT can be repoled at room temperature, it is clear that the conditions in which PMN-PT is used can lead to performances variations. Figure 2.30 presents a comparison between PMN-PT (A) and a Mg doped PIN-PMN-PT sample (B) in terms of variations with temperature of both the dielectric permittivity and its loss. This illustrates the temperature limits to which PMN-PT can be subjected not only during operation but also during preparation and prefabrication procedures .

Apart from large tip displacement, for a cantilever actuator to be functional it needs to have good mechanical properties and, comparing to hard PZT ceramics, PMN-PT has a high mechanical quality factor. This will be further investigated in the following chapter.

2.4.1/ PMN-PT [011]

This specific cut of PMN-PT (anisotropic) is studied for its suitability of usage as a beam actuator. In this section the piezoelectric and mechanical properties will be discussed. PMN-PT [011] makes use of the d_{31} coefficient, responsible for the indirect transverse displacement effect of piezoelectricity. As mentioned in the previous subsection, this coefficient is what connects the physical deformation of the crystal along it's length (or along the X1 axis per Figure 2.26) when an electric field is applied. This is the effect that is most exploited when the piezoelectric material is used in the fabrication of microgrippers (as cantilevered beam actuators).

Samples of PMN-PT cut and polarized along the [011] crystalline direction were compared by [Ivan et al., 2010] with other piezo-materials, such as PZT-5H. Figure 2.31

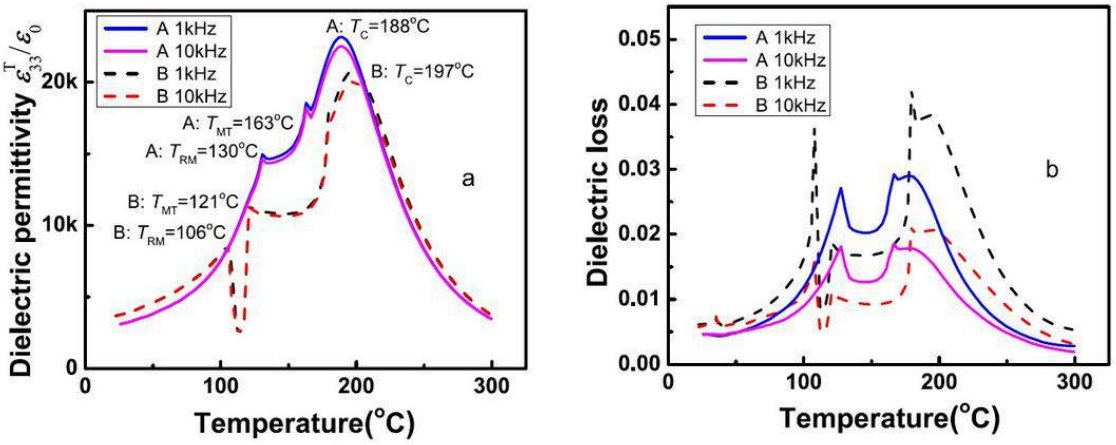

Figure 2.30: The transverse piezoelectric effect variation for PMN-PT sample (A) compared to a Mg doped PIN-PMN-PT one (B)(usage of the d_{32} coefficient) [Huo et al., 2013].

brings together the experimental results. An important observation is that for similar dimensions, PMN-PT can generate displacements close to an order of magnitude larger. This study also shows that the differences between the Finite Elements Modeling (FEM) and the experiments can reach up to 37% in the case of PMN-29PT (the number represents the PT percentage). According to [Smits et al., 1991] and [Weinberg, 1999] this is due to the planar capacitor effect coupled with the fact that the stress and strain are not taken into account. At the same time the mechanical coupling also impacts the electric displacement, a reason why this anisotropic cut is preferred in the development of energy harvesters.

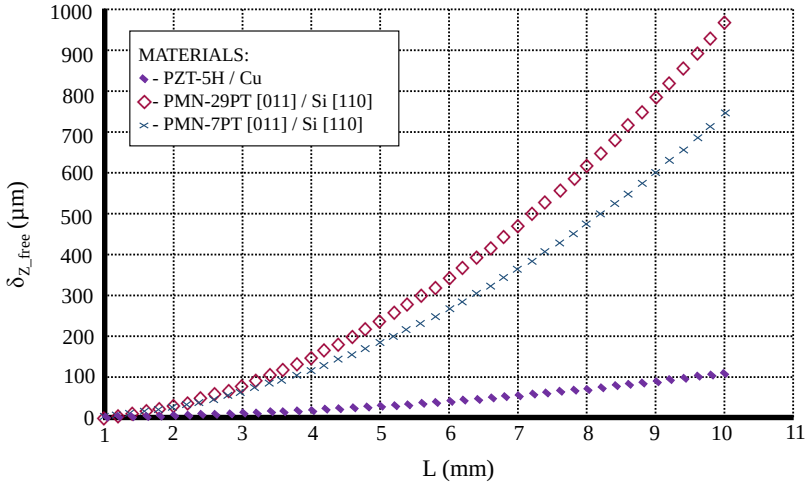

Figure 2.31: The transverse piezoelectric effect (usage of the d_{31} coefficient) [Ivan et al., 2010].

Looking at the properties of PMN-PT close to the morphotropic phase boundary (the zone at which the crystal changes its internal structure), it was noticed that it not only

outperforms other bicomposites, but it offers a wider range of use. Table 2.4 brings together values for the parameters of importance when fabricating actuators out of PMN-PT in comparison to PZN-PT. The elastic compliance coefficients s_{11} and s_{22} are measured in TPa^{-1}, while the d_{31}, d_{32}, d_{33} and d_{15} piezoelectric coefficients are measured in pm/V.

Table 2.4: Overview of main parameters close to the morphotropic phase boundary (PMN-PT vs. PZN-PT)

	s_{11}	s_{33}	d_{31}	d_{32}	d_{33}	d_{15}
PMN-PT [011]	$\backsim 18$	$50 \rightarrow 90$	$-1/3\ d_{32}$	$-1900 \rightarrow -1200$	$400 - 1000$	$1100 - 2500$
PZN-PT [011]	$\backsim 68$	$\backsim 60$	$-1/3\ d_{32}$	$\backsim 1460$	$\backsim 1500$	$\backsim 1800$
Hard PZTs	$8 - 13$	$8 - 14$	$-42 \rightarrow -140$		$130 - 475$	

Another important advantage PMN-PT brings is its positive transverse piezoelectric coefficient d_{31}. As noted in Table 2.4, not only does it offer a wider range of flexibility, in terms of the d_{32} value, allowing for very specific applications, but it reaches values north of $600\ pm/V$, making possible the design of beam actuators capable of 3 DoF or more [Ivan et al., 2013].

There are other, also important, parameters which need to be taken into account when manufacturing sensors or actuators from PMN-PT. These coefficients, 17 in total [Nye, 1985], can be found using ultrasonic pulse-echo measurements, specifically with the aid of longitudinal and shear wave transducers, as described in [Zhang et al., 2006]. These give the resonance and antiresonance frequencies from which the d_{31} and d_{32} piezoelectric coefficients, the elastic compliance s_{11}, s_{22} and s_{33} and the elastic stiffness c_{33} can be calculated. The d_{33} strain coefficient can be measured directly with a piezo-d_{33} meter. Capacitance measurements allow for the identification of the dielectric permittivity coefficients ε_{11}, ε_{22} and ε_{33}.

Knowing all these parameters allows for the fabrication of high performing actuators. Other benefits coming from working with this single crystal is its ability to be processed in non clean room environments and that it can also be used in bulk. This translates to faster fabrication times, as opposed to traditional piezoelectric materials, and higher integrability. Work has been done towards the study of PMN-PT based beam actuators as efficient replacements for similarly structured PZT ones [Ko et al., 2006, Herdier et al., 2008, Wang et al., 2008b, Yi et al., 2009]. One major advantage of using PMN-PT is that it has higher work frequencies than an equivalent, traditional PZT-5H structure (for example), meaning that the dynamics of integrating system is mostly influenced by the structure and not the actuator. As it can be seen in Figure 2.32, the frequencies at which the structure becomes unstable are close to the $1\ KHz$ mark. This is due to the integrating structure (Figure 2.33) and not to a limitation of PMN-PT.

2.4.2/ PMN-PT [001]

As in the case of PMN-PT [011], the properties close to the crystal's morphotropic phase boundary are analysed and, similarly, it was noticed that PMN-PT [001] also outperforms other bicomposites. Table 2.5 brings together values for the parameters of importance when fabricating actuators out of PMN-PT in comparison to PZN-PT. The same elastic compliance coefficients s_{11}, s_{22}, the d_{31}, d_{32}, d_{33} and d_{15} piezoelectric coefficients are presented (measured in TPa^{-1} and pm/V, respectively).

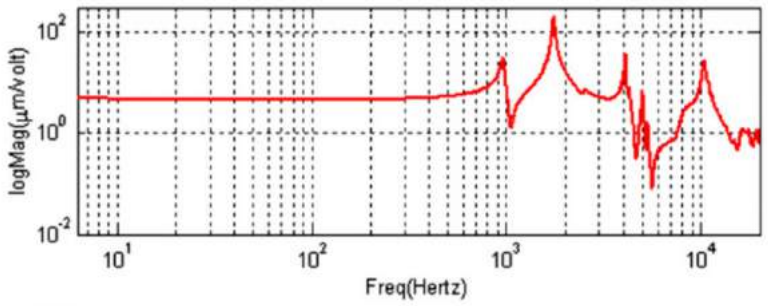

Figure 2.32: Frequency response plot of the pick-up actuator using PMN-PT flexing cantilevers [Ko et al., 2006].

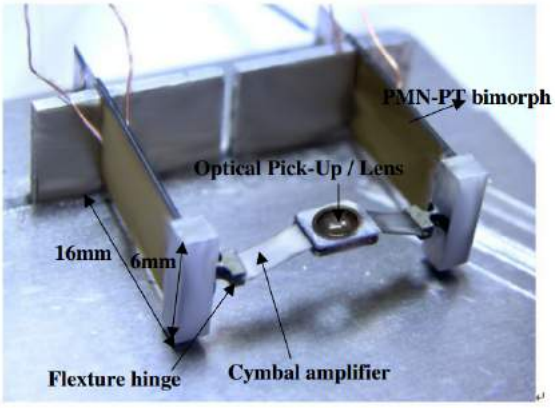

Figure 2.33: Prototype of the PMN-PT symmetric bimorph pick-up actuator using cymbal displacement amplifiers [Ko et al., 2006].

Table 2.5: Overview of main parameters close to the morphotropic phase boundary (PMN-PT vs. PZN-PT)

	s_{11}	s_{33}	d_{31}	d_{32}	d_{33}	d_{15}
PMN-PT [001]	$50-70$	$40-120$	$-1500 \rightarrow -800$	$= d_{31}$	$1500-3200$	< 160
PZN-PT [001]	$80-90$	$110-145$	$-1600 \rightarrow -950$	$= d_{31}$	$2000-2900$	$140-180$
Soft PZTs	$15-17$	$19-22$	$-140 \rightarrow -280$		$300 \rightarrow 600$	

A thorough analysis of PMN-PT[001] has been done in [Ivan et al., 2011]. As it can be seen in Figure 2.34, FEM simulations done for a $20x20x0.2\ mm^3$ [001] crystalline direction polarized PMN-PT (30%) plate show a very significant surface change. This is due to the very high d_{33} piezoelectric coefficient.

Comparing the values from Table 2.5 with those from Table 2.4 two things appear: first, although the values for the d_{31} piezoelectric coefficient for PMN-PT[001] overlap with those for PMN-PT[011], in the case of the d_{32} piezoelectric coefficient the relations change from $d_{32} = \backsim 1/3\ d_{31}$ to $d_{32} = d_{31}$. This means that the in plane motions are symmetrical on the X_1 and X_2 axes (Figure 2.22) in reference to the centre of the actuator fixture. Second, the value for the d_{33} piezoelectric coefficient is at least three

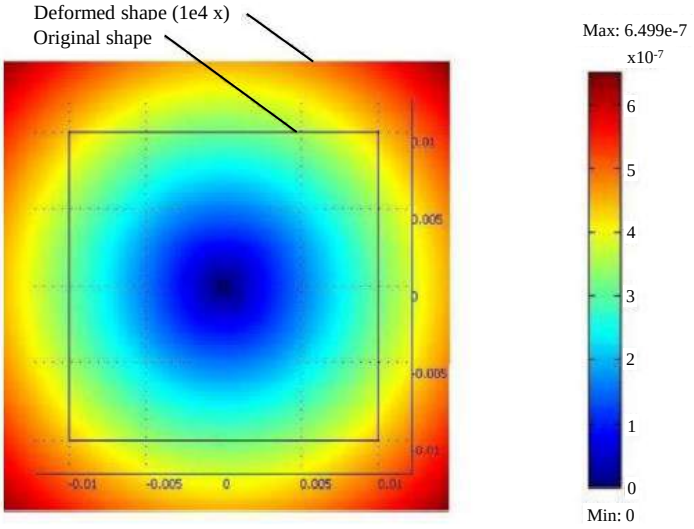

Figure 2.34: Surface variation FEM simulation for a PMN-PT[001] (30% PT) plate, measured in mm [Ivan et al., 2010] . Deformed shape is magnified 10,000 times for optimal visualization.

times larger than PZT and offers the capability of out of plane actuation - suitable for compliant, displacement-amplifying-mechanism free, micro-mirrors displacements.

Similar to the [011] cut PMN-PT, here too the coercive field values are of importance. Since the property of being able to be repolarized PMN-PT applies to all cuts and variants (like Mn doped crystals or PIN-PMN-PT), here too the value, in module, for V_c is important. It was experimentally found to be $\backsim 45\ V$. Although three times larger than that of PMN-PT[011], this value also inhibits full bipolar actuation.

But the differences do not stop here between the [001] and the [011] cut. Figure 2.35 presents the first mode for a generic square bulk PMN-PT[001] actuator soldered on one side of an applied peak voltage of $10\ V$. It can be seen that the first mode is found in the MHz region (with very low amplitudes). In terms of nonlinearities, PMN-PT[001] presents similar low hysteresis values of $4-5\ \%$, as the [011] cut, and very low creep.

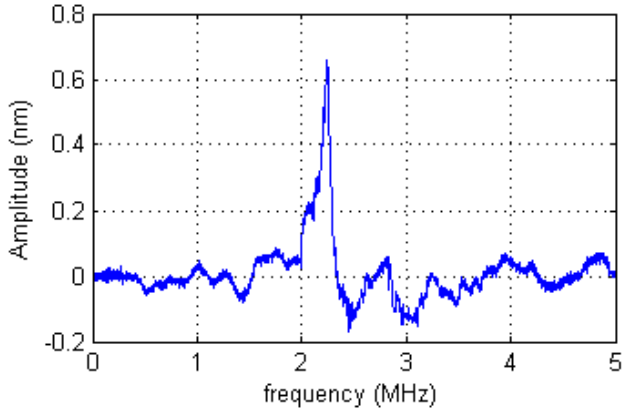

Figure 2.35: First mode of a one sided soldered bulk PMN-PT[001] actuator with a $0.5x0.5\ mm^2$ footprint, for a $10\ V$ peak voltage.

While the [011] cut presents high dynamics for a cantilever style actuator, because PMN-PT[001] can be expressively used for out of plane actuation, the work frequencies are limited only by the integrating system.

2.5/ CONCLUSION

PMN-PT offers a wide diversity, through crystalline orientation, of piezoelectric capabilities and electro-mechanical properties. Not only can it be manufactured with techniques very specific to its end use, but it can also be grown in large crystals with good control over the bicomposite ratio. This is highly important as depending on that ratio and the orientation of the cut in relation to the crystalline growth, PMN-PT can exhibit very different behaviours and is capable of generating variant types of displacement like flexure, longitudinal or shearing, each beneficial for very specific applications. This benefit is only augmented by the fact that PMN-PT exhibits very high piezoelectric and mechanical coefficients, thus reducing the complexity of some systems or simplifying the manufacturing procedures of different integrated actuators and their encompassing systems. The most recent materials with a similar structure as PMN-PT (like PZN-PT) although have been found to present coefficients that rival and perhaps surpass those of PMN-PT, are a lot more difficult to produce. The piezoelectric coefficients which they present are usually found through experimental growth procedures, thus making them unsuitable for mass production. PMN-PT thus presents itself as the candidate with the higher potential regarding the requirements set by the two encompassing projects: PMN-PT[011] for a cantilevered actuator suitable for the ADMAN project and PMN-PT[001] for an integrated, patch micro-mirror actuator suitable for the MIOP project. This applies to its integrability, displacement, high bandwidth and frequency response.

3

BEAM ACTUATOR BASED ON PMN-PT [011] CUT FOR MULTI DOF DISPLACEMENTS

This chapter consists in studying the PMN-PT [011] anisotropic cut based actuator that brings together large displacement with small volume. This case study is done by implementing PMN-PT in a well knows structure, cantilever beams. For an actuator of $23\ mm$ *length,* $0.6\ mm$ *width and* $0.41\ mm$ *thickness, displacements of over* $650\ \mu m$ *with under* 6% *hysteresis was achieved while also generating over* $0.104\ mN/V$ *. The contribution PMN-PT brings to the capabilities of micro-assembly technologies are exemplified with a 6 DoF capable microgripper.*

3.1/ INTRODUCTION

There are multiple solutions regarding the fabrication of micro-components. As the trend of micro-assembly veers towards more complex, out-of-plane micro-structures, more capable actuation solutions are sought out. In the case of micro-scale manipulation, recent developments and applications focus on microgrippers for task completion and micro-assembly. Piezoelectric material based actuators have been developed and exist in commerce. The need for actuators which are not only better integrated, but also have higher performances than traditional piezoelectric ceramics is ever increasing. A solution to this is the development of smart, piezoelectric materials that have a much more linear behaviour.

After a brief presentation of the chosen structure and how the specificities of PMN-PT [011] affect the generation of displacement, a static mathematical model that takes into account the forces that can be generated is presented, adjusting for the experimental conditions. This is followed by a short description of the fabrication procedure of duo-bimorph beams on which the experimental validation of both the static displacement and force models. The findings are enforced by the fabrication, control and experimental use of a microgripper.

3.2/ STUDY OF PMN-PT [011] THROUGH A DUO-BIMORPH STRUCTURE

3.2.1/ DESIGN OF A FLEXURAL ACTUATOR

There are different types of flexural beam actuators, depending on their structure, but all are cantilevered beams which bend away from an equilibrium point, using different actuation principles. When the active material is soldered to an inactive one, a **unimorph** results. Such actuators can be found in raster scanning machines, energy harvesters or tension sensors. Soldering together two or more layers of active material results in either a **bimorph** or a **multimorph** actuator, respectively. While the latter type beams are commonly made of piezoceramics, such as PZT, in order to have notable displacement, the choice was made to use a specific type of bimorph actuators called **Duo-Bimorps**. This is a structure that already allows for 2DoF (for PZT based actuators), is well understood and it does not present technical manufacturing difficulties.

The duo-bimorph cantilever presented in Figure 3.1 shows the electrode disposition, as to achieve XYZ displacements. It makes use of the transverse piezoelectric coefficient (d_{31}) of the active material, which, in the case of the chosen PMN-PT [011] material, is positive and of over $+450pm/V$. Classical piezoceramics, like PZT, have a negative d_{31}, usually in the range of $-250pm/V$. This translates in PMN-PT [011] being capable of almost doubling the displacement of a cantilever of the same dimensions and enables the structure to have a 3rd Degree of Freedom, contrary to PZT.

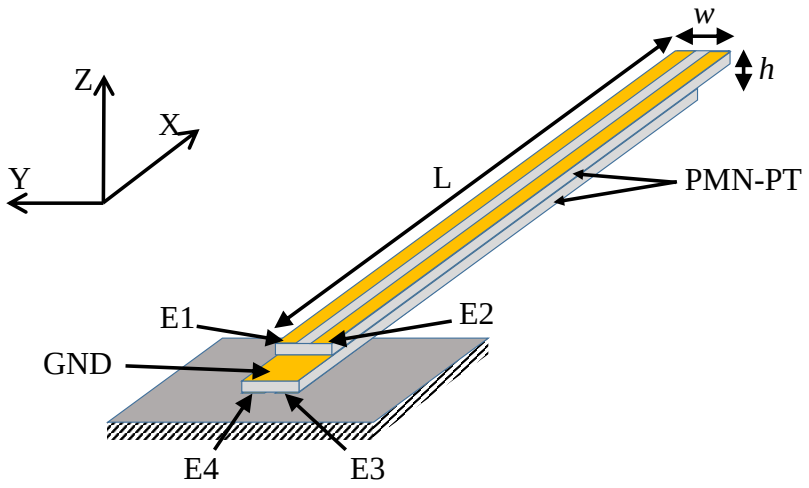

Figure 3.1: Duo-bimorph shape (length L, width w and height h) and electrode disposition ($E1$ to $E4$) for the selected structure.

Depending on the two layers poling direction and on the piezoelectric transverse coefficients signs, a strict convention must be established for the applied voltages as shown in Figure 3.2.

Each hp thick layer of PMN-PT [011] has a pair of electrodes on the visible face and a common *GND* electrode on the soldered face (also common to both layers). The voltages applied to each electrode (with the value V_{apl} ranging between 0 and a maximum V_{max})will be named V_{E1}, V_{E2}, V_{E3} and V_{E4} respectively and by pairing them in the way

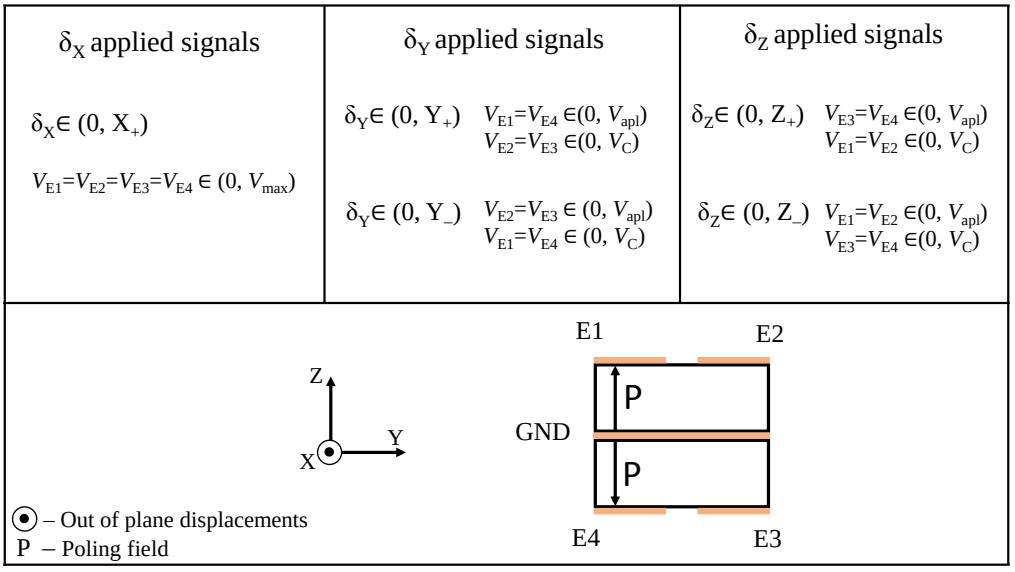

Figure 3.2: Opposite-direction poling for a duo-bimorph (section view). The applied voltages signs to obtain the desired displacement.

exemplified in Table 3.1 will allow for the duo-bimorph beam to generate displacements along the X, Y and/or Z axes, in situations where the Coercive field value (V_C) is unknown. As PMN-PT [011] has a low coercive field value [Ivan et al., 2010], the command must take it into account, as well as the polarization orientation convention established during the fabrication procedure. The full range of transverse motion is achieved by alternating the applied voltage as shown while also protecting the material from depolarizing.

3.2.2/ Theoretical performances - Static Displacement and Force Model

The duo-bimorph presented can be modelled, from the working equations point of view, as other classic piezoelectric materials, by linking the displacements and/or generated forces to the applied voltages. The analytical modelling is essential for the design of a suitable structure, not only for control purposes (as detailed in the previous sub-chapter) but also for micromanipulation specifications. This is especially important because of the great difficulty of integrating sensors. A model has been proposed in [De Lit et al., 2003] linking the applied voltage to the displacement and forces generated, but only along the Y and Z axes and for bipolar PZT piezoelectric materials. The model has thus been extended to encompass the third axis to be used (X). Figure 3.3 brings together all the dimensional information regarding the duo-bimorph structure used in the mathematical model, while Table 3.2 gives the numerical values of these parameters.

The first modeling of a duo-bimorph piezo-beam has been performed in [De Lit et al., 2003]. Provided the PMN-PT particularities, the constitutive equations should be updated for PMN-PT because of the lower, limiting coercive field [Ivan et al., 2010]. Still provided the large actuation, adding the modeling of the duo-bimorph in the third longitudinal X-direction is also preferable. The end-effector is also added to the model. Multiple factors have led to this choice, such as: being very easily integrable into MEMS, being present in the majority of devices related to micro-manipulation

Table 3.1: Applied voltage convention for beam tip displacement.

Axis	***Direction***	***Voltage on electrodes***
X	+	$V_{E1} = V_{E2} = V_{E3} = V_{E4} = V_{E_X} > 0$
Y	+	$V_{E1} = V_{E4} = 0, V_{E2} = V_{E3} = V_{E_Y} > 0$
	-	$V_{E1} = V_{E4} = V_{E_Y} > 0, V_{E2} = V_{E3} = 0$
Z	+	$V_{E1} = V_{E2} = 0, V_{E3} = V_{E4} = V_{E_Z} > 0$
	-	$V_{E1} = V_{E2} = V_{E_X} > 0, V_{E3} = V_{E4} = 0$

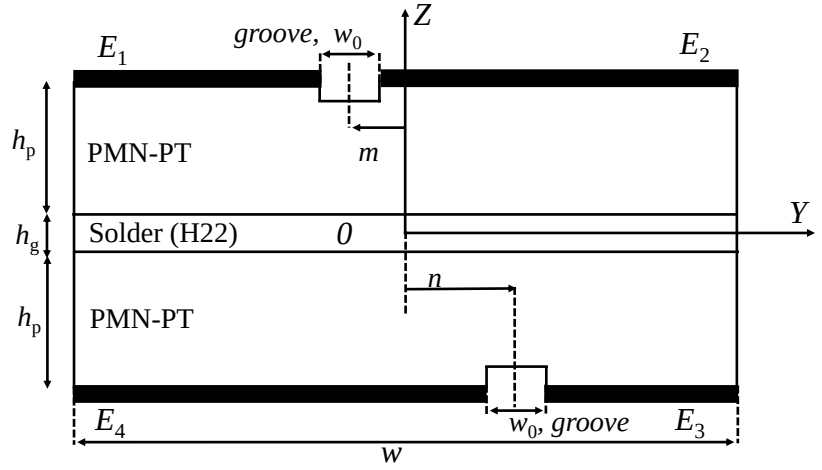

Figure 3.3: Cross section of a generic duo-bimorph structure with parameters.

Table 3.2: The experimental parameters and coefficients.

Parameter	*Description*	*Value*
L	Cantilever length	$21\ mm$
L_{ee}	End-effector length	$3\ mm$
w	Cantilever width	$600\ \mu m$
w_0	Groove width (electrodes gap)	$100\ \mu m$
m	Groove shift for the top layer	$18\ \mu m$
n	Groove shift for the bottom layer	$22\ \mu m$
h_p	Piezo-layer thickness	$200\ \mu m$
h_g	Solder-layer thickness	$10\ \mu m$
d_{31}	Transverse piezoelectric coefficient	$456,55\ \frac{pm}{V}$
s_{11}	PMN-PT elasticity coefficient	69 x $10^{-12}\ \frac{m^2}{N}$
E_g	Young's modulus of solder	1 x $10^{12}\ \frac{N}{m^2}$

and allowing for the amplification of the movement. As already noticed in Figure 3.1, the duo-bimorph displacement is controlled by applying high voltage signals to the 4 electrodes (V_{E1}, V_{E2}, V_{E3}, and V_{E4}).

Voltage-Displacement static model

The complete 3D voltage-to-displacement static model may be expressed in matrix form as follows:

$$\begin{pmatrix}\delta_X\\ \delta_Y\\ \delta_Z\end{pmatrix} = (C+F)S\,V_E \tag{3.1}$$

Where δ_X, δ_Y and δ_Z are the deflections on the X, Y and Z axes, C is the piezo-bimorph constitutive matrix, F is the end-effector (if present) displacement matrix which is effective only transversally, S is the sign matrix depending on the electrodes notation, piezoelectric material poling direction (Figure 3.2) and the transverse piezoelectric coefficient (d_{31} or d_{32}) sign and V_E is the array of voltages across the electrodes:

$$V_E = \begin{pmatrix}V_{E1}\\ V_{E2}\\ V_{E3}\\ V_{E4}\end{pmatrix} \tag{3.2}$$

$$C = \begin{pmatrix}C_{11} & C_{12} & C_{13}\\ C_{21} & C_{22} & C_{23}\\ C_{31} & C_{32} & C_{33}\end{pmatrix} \tag{3.3}$$

$$F = \begin{pmatrix}0 & 0 & 0\\ 0 & F_{22} & 0\\ 0 & 0 & F_{33}\end{pmatrix} \tag{3.4}$$

$$S = \begin{pmatrix}1 & 1 & 1 & 1\\ 1 & -1 & -1 & 1\\ 1 & 1 & -1 & -1\end{pmatrix} \tag{3.5}$$

The coefficients C_{11} to F_{33} are calculated starting from the strain-charge constitutive matrix of the piezoelectric effect [De Lit et al., 2003].

$$C_{11} = \frac{d_{31}L}{4h_p} \tag{3.6}$$

By using the modeling from [De Lit et al., 2003] derived:

$$C_{22} = \frac{3d_{31}L^2(w^2 - w_0^2)}{4As_{11}w^3} \tag{3.7}$$

$$C_{33} = \frac{3d_{31}L^2(w - w_0)(h_p + h_g)}{4Bs_{11}w} \tag{3.8}$$

Coefficients C_{11}, C_{22} and C_{33} could be taken from expressions (3.6), (3.7) and (3.8) but, provided the measurement uncertainty of piezoelectric and stiffness tensors, these coefficients could be also identified experimentally. The remaining unknown ones (all C_{ii} with $i \neq j$, $C_{ij} \neq 0$), called coupling coefficients can be identified empirically.

And by re-modeling the equation described in [Pérez et al., 2005], to fit the duo-bimorph, we derived:

$$F_{22} = \frac{3d_{31}L_{ee}^2(w^2 - w_0^2)}{2As_{11}w^3} \tag{3.9}$$

$$F_{33} = \frac{3d_{31}L_{ee}^2(w - w_0)(h_p + h_g)}{Bs_{11}w} \tag{3.10}$$

With:

$$A = \frac{2h_p}{s_{11}} + E_g h_g \tag{3.11}$$

$$B = \frac{2h_p(2h_g^2 + 6h_g h_p + 4h_p^2)}{s_{11}} + E_g h_g^3 \tag{3.12}$$

We shall make the following notation of three voltage signals, for a more direct correlation between displacement and the axis -specific voltage:

$$V_\delta = \begin{pmatrix} V_X \\ V_Y \\ V_Z \end{pmatrix} = \frac{1}{4} S \begin{pmatrix} V_{E1} \\ V_{E2} \\ V_{E3} \\ V_{E4} \end{pmatrix} \tag{3.13}$$

By combining expressions (3.1) with (3.13), we get the following linear, theoretically decoupled system:

$$\begin{pmatrix} \delta_X \\ \delta_Y \\ \delta_Z \end{pmatrix} = 4(C+F) \begin{pmatrix} V_X \\ V_Y \\ V_Z \end{pmatrix} = 4(C+F) V_\delta \tag{3.14}$$

Voltage-Displacement static model with coercive field specificities

In the case of piezoelectric materials, the operating voltage must be greater than the one related to the *coercive field value* V_C and being equal with $-E_C h_p$. For a $200\ \mu m$ plate, we experimentally determined the and, while for PZT $V_C = -150\ V$, for PMN-PT V_C was found to be $V_C = -45\ V$ and $V_C = -15\ V$ for PMN-PT [001] and PMN-PT [011], respectively.

For the unipolar operation mode, the restricted voltages are formulated as follows:

$$\begin{pmatrix} V_{E1}^* \\ V_{E2}^* \\ V_{E3}^* \\ V_{E4}^* \end{pmatrix} = H^* \begin{pmatrix} V_{E1} \\ V_{E2} \\ V_{E3} \\ V_{E4} \end{pmatrix} \tag{3.15}$$

Where:

$$H^* = \begin{pmatrix} H(V_{E1}+V_C) & 0 & 0 & 0 \\ 0 & H(V_{E1}+V_C) & 0 & 0 \\ 0 & 0 & H(V_{E1}+V_C) & 0 \\ 0 & 0 & 0 & H(V_{E1}+V_C) \end{pmatrix} \tag{3.16}$$

and $H(x)$ is the Heaviside step function defined as:

$$H(x) = \begin{cases} 1, x \geq 0 \\ 0, x < 0 \end{cases} \tag{3.17}$$

Equation (3.13) thus becomes:

$$\begin{pmatrix} V_X^* \\ V_Y^* \\ V_Z^* \end{pmatrix} = H^* \frac{1}{4} S \begin{pmatrix} V_{E1} \\ V_{E2} \\ V_{E3} \\ V_{E4} \end{pmatrix} \tag{3.18}$$

The resulting displacement for the unipolar case may be expressed in the following manner, where δ_X^*, δ_Y^* and δ_Z^* are the generated displacements when applying the heaviside (H^*)matrix:

$$\begin{pmatrix}\delta_X^*\\ \delta_Y^*\\ \delta_Z^*\end{pmatrix} = 4(C+F)\begin{pmatrix}V_X^*\\ V_Y^*\\ V_Z^*\end{pmatrix} = (C+F)H^*S\begin{pmatrix}V_{E1}\\ V_{E2}\\ V_{E3}\\ V_{E4}\end{pmatrix} \tag{3.19}$$

In the above model, C is an ideal, diagonal matrix. In experimental conditions, besides the typical piezoelectric nonlinearities like hysteresis and creep, coupling effects could be present, in this case, some or all off the C-matrix coefficients will be non-zero (for all $i \neq j$, $C_{ij} \neq 0$). This is due to there not being any physical separation between the PMN-PT crystal directly under the electrodes.

As noticed, in the case of PMN-PT the $|V_C|$ is much lower than in the case of PZT. Therefore we have to restrict the reverse operating field to a safety zone. We call this type of driving: unipolar operation (Figure 3.4). This is needed as to not repolarize the PMN-PT cantilever since, as mentioned in Chapter 2, PMN-PT can have its polarization filed at room temperature.

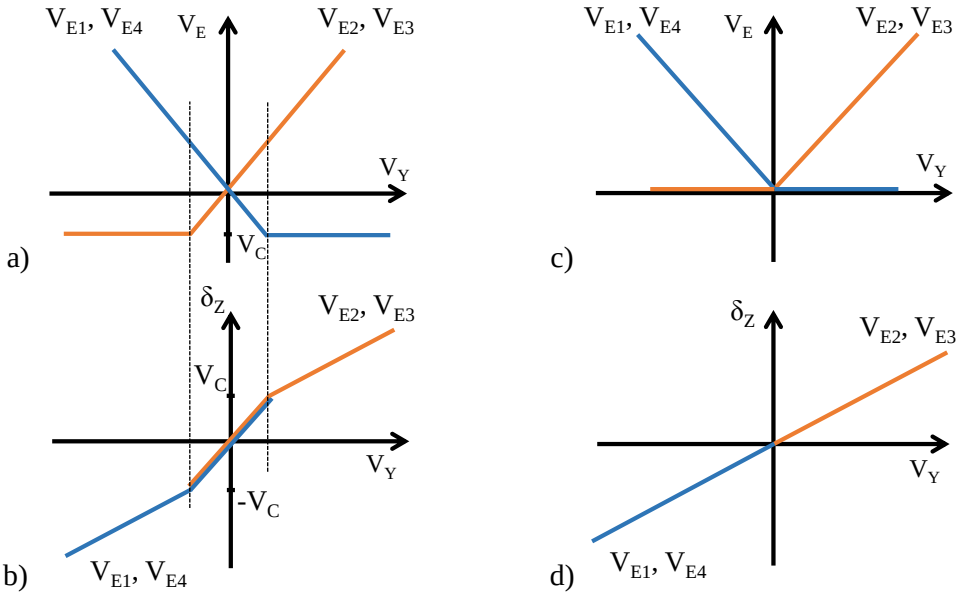

Figure 3.4: Unipolar operation mode in the case of coercive field limitation. Example for displacement along the Y-axis: a) operating voltage V_E derived upon applying H^* Heaviside operator b) theoretical resulting displacement as a function of the input voltage variable c), d) same characteristics, but in pure unipolar operation (when $V_C = 0V$)

Force and voltage to displacement static model

In the case of micro-manipulation, apart from the displacement capabilities of a beam actuator, the force that can be generated at the tip, also called a blocking force, is of high importance. Depending on the configuration used, this force can be present along each axis of movement, resulting in F_{b_X}, F_{b_Y} and F_{b_Z}. Simplifying the calculations by using the equations (3.6) to (3.12) in equation (3.14) and the blocking force expressions

derived from [De Lit et al., 2003] we get the simplified version of the *Force and voltage to displacement static model*(Equation 3.20).

In the following model, δ_X, δ_Y and δ_Z, are the displacement values along each axis, A, B are size-related parameters, d_{31} is the transverse piezoelectric coefficient; s_{11} is the PMN-PT elasticity coefficient, L is the length of the cantilever active region, w is the width of the cantilever, w_0 is the width of the electrode separating groove, h_p and h_g represent the thickness of the PMN-PT layers and of the soldering layer, respectively and E_g is Young's Modulus of the soldering layer. The resulting equations are as follows:

$$\begin{cases} \delta_X = \frac{s_{11}L}{w^2} F_{b_X} + \frac{d_{31}L}{4h_p} V_X \\ \delta_Y = \frac{4L^3}{Aw^3} F_{b_Y} + \frac{3d_{31}L^2}{4As_{11}w^3} V_Y \\ \delta_Z = \frac{4L^3}{Bw^3} F_{b_Z} + \frac{3d_{31}L^2(h_p+h_g)}{2Bs_{11}w} V_Z \end{cases} \tag{3.20}$$

Where, by notation:

$$\begin{cases} V_X = \frac{V_{E1}+V_{E2}+V_{E3}+V_{E4}}{4} \\ V_Y = -w_1^2 V_{E1} + w_2^2 V_{E2} + w_3^2 V_{E3} + w_4^2 V_{E4} \\ V_Z = -w_5 V_{E1} + w_6 V_{E2} + w_7 V_{E3} + w_8 V_{E4} \end{cases} \tag{3.21}$$

$$\begin{cases} w_1^2 = w^2 - (2m - w_0)^2 \\ w_2^2 = w^2 - (2m + w_0)^2 \\ w_3^2 = w^2 - (2n - w_0)^2 \\ w_4^2 = w^2 - (2n + w_0)^2 \\ w_5 = w - (2m - w_0) \\ w_6 = w - (2m + w_0) \\ w_7 = w - (2n - w_0) \\ w_8 = w - (2n + w_0) \end{cases} \tag{3.22}$$

The model validation, that takes into account the actual parameter values specified in Table 3.2, will be presented in a following section, after the brief description of the fabrication procedure.

3.2.3/ FABRICATION PROCEDURE

As previously mentioned, PMN-PT presents the advantage of being able to be processed with non-cleanroom procedures. In this case we used a high speed saw-dicing machine. The micro actuator is fabricated starting from two plates of PMN-PT manufactured by TRS Technologies, each $200\ \mu m$ thick, bonded using a silver-based EPO-TEK® H22 adhesive, $10 - 20\ \mu m$ thick. Following the procedure detailed in Annexe C.1 the two PMN-PT layers were soldered together with a $2\ mm$ shift, thus leaving room to access the common GND electrode. Another $200\ \mu m$ piece of PMN-PT was glued in the resulting shift gap, creating support for when soldered plates are turned over to cut the electrode separating groove on the opposite side. The cuts were done at $30.000\ rpm$ with an advancing speed of $0.3mm/s$. This is so the edges of the cuts would retain their integrity. Prior to the final and separating cut, superficial grooves were patterned on the opposite faces. These grooves, separating the electrodes $E1$ from $E2$ and $E3$ from $E4$, are $100\ \mu m$ wide and $40\ \mu m$ deep.

The depth was chosen at the lower limit of preventing possible short circuitry from taking place.

Individual beams of $600\ \mu m$ wide, $27\ mm$ long and $410\ \mu m$ thick were then precisely cut, as shown in Figure 3.5. The common electrode, situated at the solder interface is the one connected to ground (GND). The width of the actuator was chosen as to allow for

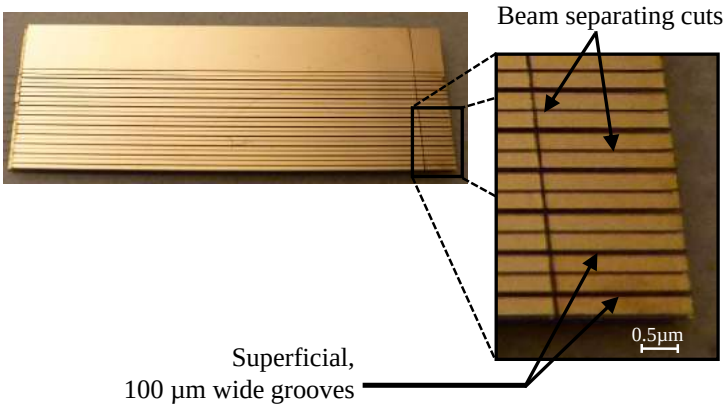

Figure 3.5: PMN-PT duo-bimorph beams after saw dicing

displacement along the Y-axis while not sacrificing the structural integrity (the thickness of the beam is driven by the PMN-PT layer thickness).

The duo-bimorph beam, measuring $27\ mm$ in total, was aligned in place on a PCB (printed circuit board) and glued to the bottom face $(E3 - E4)$ using a non-conductive hard bi-composite resin. The remaining active actuator length is $23\ mm$. The connection between the PCB and electrodes has been done by wire-bonding. Figure 3.6 visualizes close-up details of the mentioned stages. The end-effectors, or MEMS fingertips, are micro-fabricated in pairs in a silicon-on-insulator (SOI) wafer shaped by Deep-RIE etching. The details for the SOI end-effectors fabrication are presented in [Agnus et al., 2009]. They were positioned in such a way that the micro-gripping fingers are aligned with the centre of the beam, ensuring the symmetry of the microgripper. Figure 3.7 gives a close-up view of the end-effectors.

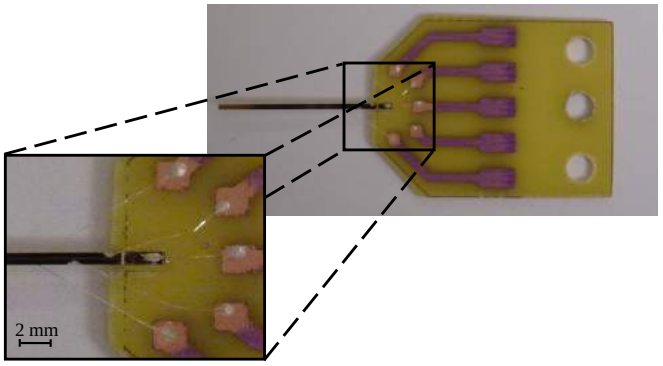

Figure 3.6: Cantilevered duo-bimorph beam with close-up of the soldering point and the electrode connections to the PCB through wire-bonding.

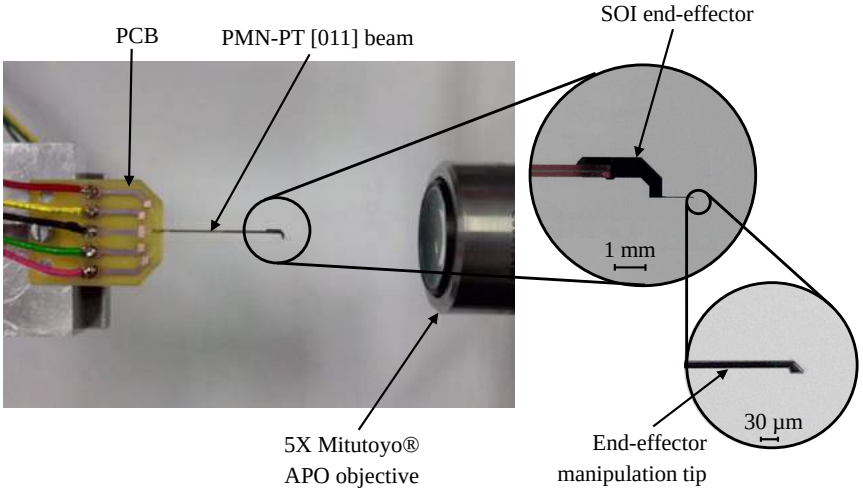

Figure 3.7: Close-up of the beam in the experimental setup for PMN-PT cantilever voltage vs. displacement model verification setup with detailed structure.

3.2.4/ Performances analysis: Displacement and Force model validation

Piezoelectric parameters identification

In order to ascertain whether the model is accurate, certain coefficients needed to be experimentally identified, such as d_{31} and d_{32}. These transverse coefficients were calculated separately on the initial plain rectangular plates of $20x25\ mm^2$ using the same image processing method. As known [Pérez et al., 2005], PMN-PT [011] has a positive value for d_{31} and a value for d_{32} which is approximately $-1/3$ x d_{31}. A batch of six plates were individually tested, d_{31} values ranged from $420\ pm/V$ to $485\ pm/V$ and d_{32} ranged from $-1000\ pm/V$ to $-1360\ pm/V$. Table 3.3 shows the values used in the model. For comparison, we also measured the d_{31} and d_{32} coefficients of some PMN-PT [011] and PZT-5H plates. The s_{11} = 69 x $10^{-12} m^2/N$ coefficient has been taken from [Kim et al., 2003].

Table 3.3: Experimental values found for PMN-PT and PZT piezoelectric materials.

Material type	***Transverse piezoelectric coefficients***	
	d_{31}	d_{32}
PZT-5H	$-274\ pm/V$	$-274\ pm/V$
PMN-PT [011]	$+476\ pm/V$	$-1480\ pm/V$

Voltage/Displacement measurements

The displacement was measured using image analysis from a frontal position for the Z and Y axes. The images for the displacement along the X-axis were acquired by repositioning the camera at a 90^o angle relative to the PMN-PT cantilever. The images were captured using a Guppy® camera F 046B with a 1-7X video tube and a 5X long-distance Mitutoyo® objective connected to a dSpace® 1103 rapid control prototyping controller which also provided the triggering signal. The images provide a resolution of

$1.66\ \mu m/px$. The images were fed to the cvlink Matlab module, developed at Femto-ST, for real-time analysis and correlation with the command signals, also generated using Matlab. A four-channel, high-voltage amplifier was connected between the controller and the cantilever actuator. Figure 3.8 depicts the system put in place for the image capture and displacement analysis.

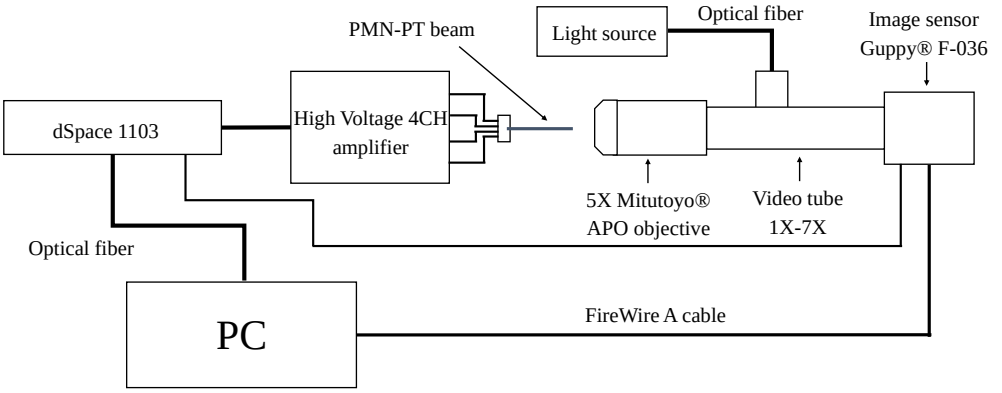

Figure 3.8: Schematic of the experimental setup for PMN-PT cantilever voltage vs. displacement model verification setup.

In order to determine the maximum free displacement, a series of experiments was initiated, in the same controlled environment. The measurements were done along the main actuation axis, independently, in three experiments. For the X-axis, voltage was applied in the nominal range of 0 to $400V$ (for increased displacement values), in a sine wave of 0.5Hz. For the Y and Z axes, voltage was applied following the conventions presented in Figure 3.1 and Table 3.1. Figures 3.9, 3.10 and 3.11 present the comparison between the static free displacement model and the measured displacements along the X, Y and Z-axis respectively. An analysis of the measurements is presented after the figures.

Table 3.4 groups together the most relevant data regarding the total displacement measured along the X, Y and Z axes for a potential difference of 400V. Alongside the displacement values, the calculated hysteresis is presented, an important value for displacement prediction in automated, open loop control applications.

Table 3.4: Experimentally measured performances.

Voltage range	***Axis***	***Measured displacement***	***Hysteresis***	***Model accuracy***
$400\ V$	X	$41.5\ \mu m$	6.05%	98%
$400\ V$	Y	$465\ \mu m$	4.86%	86%
$400\ V$	Z	$653.7\ \mu m$	2.83%	91%

The displacement observed does not only surpass that of a similarly dimensioned PZT beam, but presents non-linearities that are at least threefold lower for displacement along each axis. The largest value for displacement hysteresis barely goes over 6% while a regular expected value for PZT is in the range of $18 - 22\ \%$. The elongation of over $40\ \mu m$ along the X-axis, provided by the positive d_{31} piezoelectric coefficient, transforms a generic duo-bimorph cantilever from a 2DoF capable structure to a 3DoF capable one.

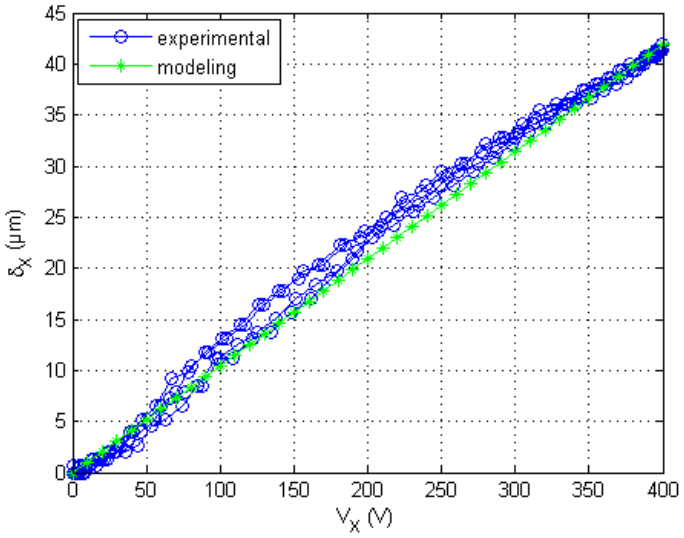

Figure 3.9: Comparison between the experimental values measured along the X-axis (-o-): 41.5 μm and the afferent modeling (-*-): 42.83 μm .

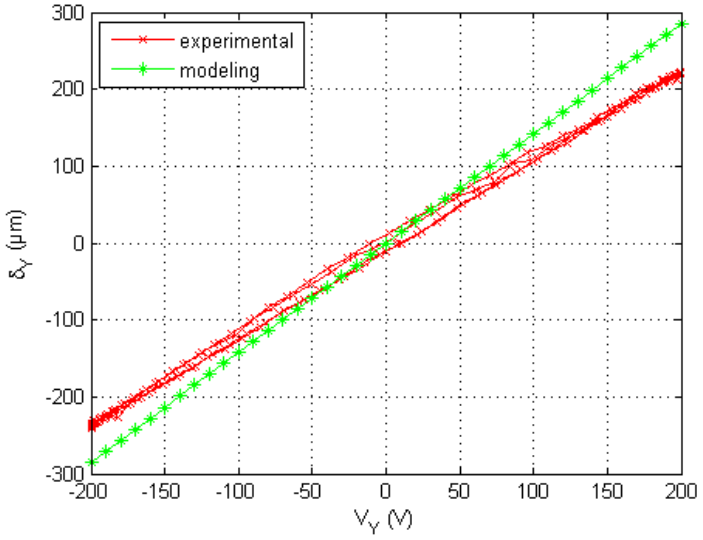

Figure 3.10: Comparison between the experimental values measured along the Y-axis (-x-): 465 μm and the afferent modeling (-*-): 569.34 μm .

The elasticity coefficient s_{11} is what influences the accuracy of the model, reason why the best prediction is for the X-axis with the accuracy decreasing for the Y and Z axes. A fair agreement between the analytical modeling and experimental data can be concluded, meaning that the user could rely on the provided 3D displacement static mathematical model in his designs.

With a duo-bimorph structure, some coupling between the axes exists. FEM simulations (COMSOL) regarding the disposition of the generated field lines in one layer of the duo-bimorph have shown that, as it can be seen in Figure 3.12, when acting upon a single electrode, the field lines (irregular) vary greatly from the ideal case (vertical arrows). This

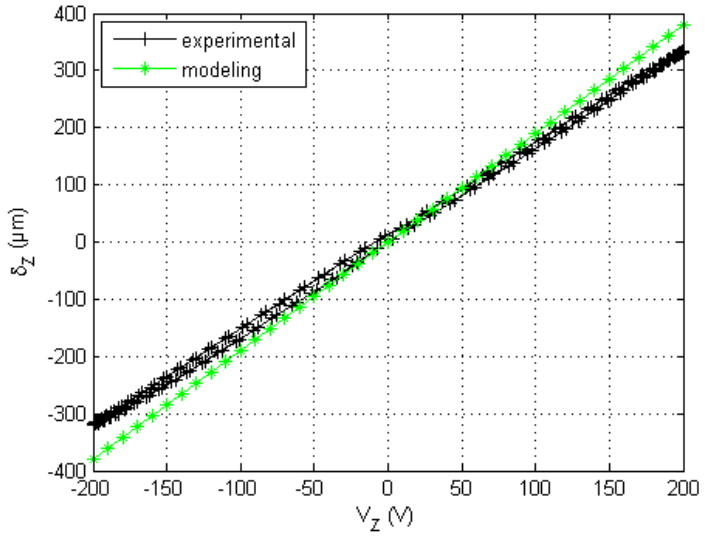

Figure 3.11: Comparison between the experimental values measured along the Z-axis (-+-): $653.7\ \mu m$ and the afferent modeling (-*-): $760.6\ \mu m$.

is valid for any situation where only one electrode is energized, in the respective PMN-PT layer. It was given the dimensions of the beam and was fixed at one end.

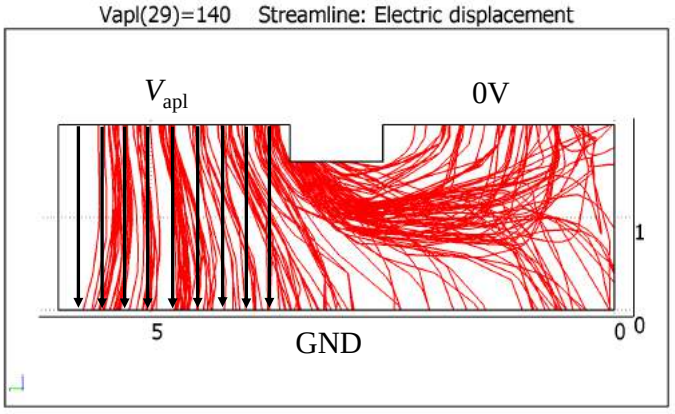

Figure 3.12: Field lines (red) in one layer of the actuator when applying voltage on only one electrode ($E1$), while the other is held at GND in comparison with the ideal case (black arrows).

Since we are working in special conditions: unipolar and symmetrical layer actuation, this coupling effect is close to fully compensated. Figure 3.13 present the coupling measurements, also done with the aid of image processing. The images were captured using the same setup as for the displacement previously presented (Figure 3.8). The largest coupling is observed when measuring the displacement along the X-axis. Apart from the electrical coupling this behaviour is also due to the one sided clamping of the beam to the PCB. Considering the very small hysteresis observed when actuating along the Z and Y axis, this coupling can easily be compensated for, without the need for dedicated control, by simply taking into account the unwanted displacement measured along

the Y and Z axes, respectively, and adjusting the maximum voltage per electrode. All this with insignificant loss to the X-axis displacement (Figure 3.13 - b)). This is to say that even after compensation, the beam retains 3 DoF. The coupling values are grouped in Table 3.5.

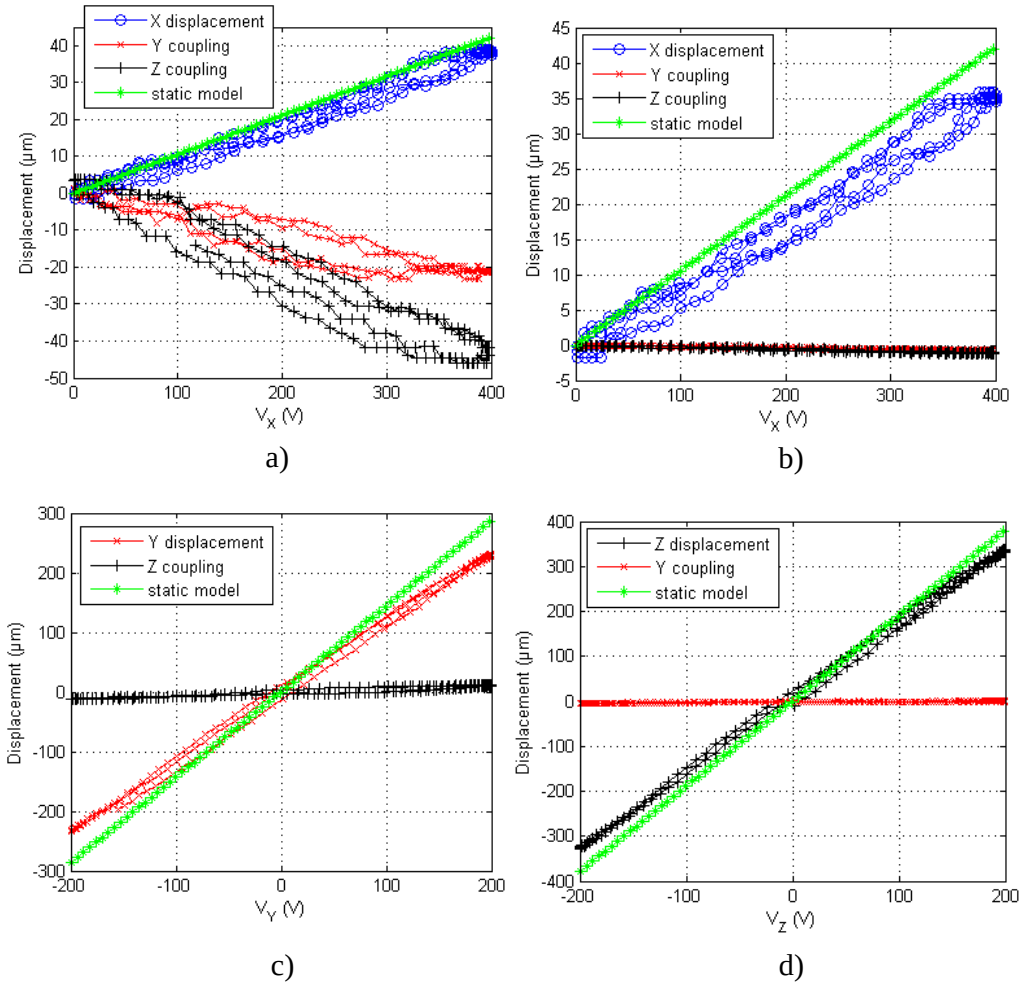

Figure 3.13: Measured coupling for the fabricated PMN-PT duo-bimorph beam. a) Coupling measured along the Y and Z axes when actuating along the X-axis; b) impact over the displacement after coupling compensation (11% loss); c) Coupling measured along the Z-axis for actuation along the Y-axis; d) Coupling measured along the Y-axis for actuation along the Z-axis

Table 3.5: Experimentally measured coupling

Voltage range (V)	***Axis***	***Measured coupling***	
		Axis (µm)	***%***
0 to 400	X	Y-axis: 21	55.26
		Z-axis: 43	113.16
-200 to 200	Y	Z-axis: 23	4.94
-200 to 200	Z	Y-axis: 5.6	0.85

What remains to be compensated is the dimensional ratio between the electrode width and the thickness of the active layer. This gives us a theoretical displacement compensation coefficient of $c^* = 1.5$. From the presented displacement curves along the Z-axis (Figure 3.11) and along the Y-axis (Figure 3.10) we get a maximum real displacement compensation coefficient of $c = 1.42$.

Voltage/Force measurements

As PMN-PT [011] demonstrates abilities regarding displacement, in order to be successfully integrated, an overview of the forces that can be generated is required. As in the previous section, the same generic cantilevered duo-bimorph structure will be tested, this time to evaluate the obtainable forces along each of the 3 axes. The measurements would be done at the tip of the beam and, given its dimension-induced frailty, the characterization of these forces (called Blocking Forces) with applied voltages becomes of high interest. The blocking force (F_b) is the parameter that states whether PMN-PT based cantilever actuator may provide sufficient force at its tip for micro-object manipulation.

For this a new experimental layout has been set up. In Figure 3.14 the command and power generation is structured in a similar fashion to the setup for displacement measurement (Figure 3.8).

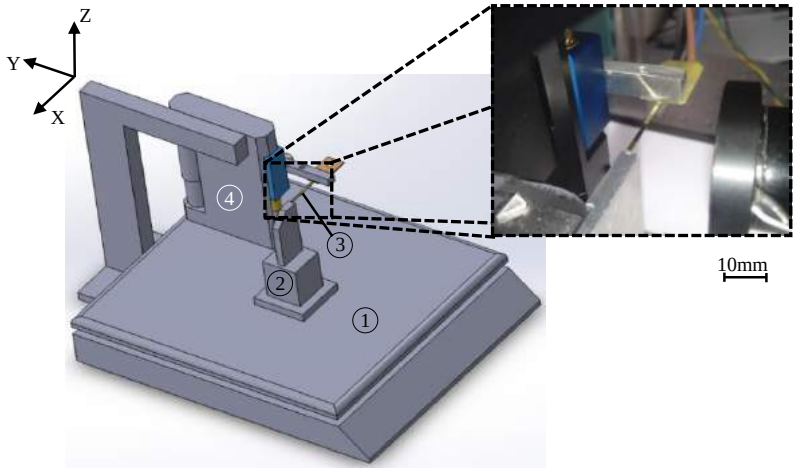

Figure 3.14: Experimental setup for PMN-PT cantilever Voltage vs. Force model validation: 1) micro-balance; 2) rigid element; 3) PMN-PT cantilever; 4) vertically actuated stage.

The force values were captured using a micro-balance connected to a PC running Matlab via a 232 serial interface. The measurements were correlated with the command signals, also generated using Matlab. A four-channel, high-voltage amplifier was connected between the controller and the cantilever actuator. Vertical displacement (along the Z-axis) was provided by a PI®MD-1112 actuated stage to which the cantilever is fixed with stiff glue. The stage lowered the PMN-PT cantilever until it achieved contact with the rigid element placed on top of a 232 serial-interfaced micro-balance.

Tests have also been done in order to take into account and compensate against the micro-balance displacement for different loads. It was determined that the exerted influence on the measurements is negligible (0.08%). The beam was therefore repositioned for measuring the blocking force generated by the beam along each main axis in independent experiments.

The voltage was applied by triangular signals of constant slope and variable amplitude $60\ V$, $120\ V$, $180\ V$ and $240\ V$ respectively. Figures 3.15, 3.16 and 3.17 present the measured values along the X, Y and Z axis respectively, each being compared with its corresponding model shown in the previous section. It is observed that the measured values are very consistent with the model predictions: along the X-axis

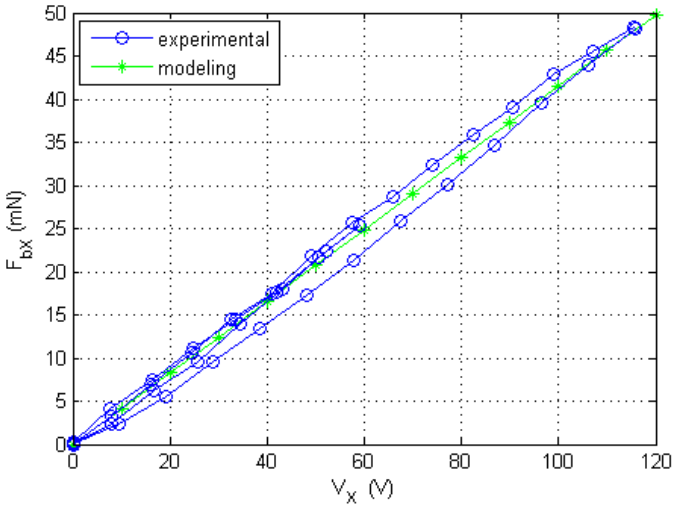

Figure 3.15: Measured blocking force F_{bx} along the X-axis (-o-)compared with the afferent model (-*-).

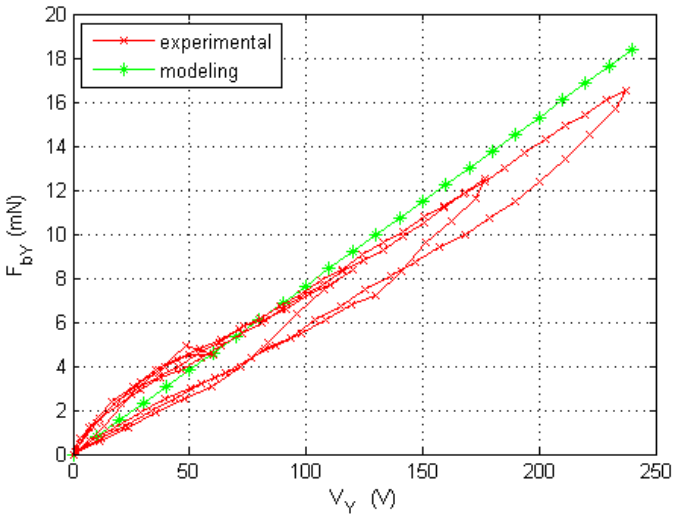

Figure 3.16: Measured blocking force F_{by} along the Y-axis (-x-)compared with the afferent model (-*-).

In the case of the longitudinal force (along the X-axis), the experiment was halted at $120\ V$ because the generated force value $(48.2\ mN)$ already surpassed considerably the force needed to manipulate micro-sized objects by an order of magnitude. This translates into the microgripper being able to generates forces capable of fixing the manipulated micro-object doruing other procedures, as is soldering. For the other two axes Y and Z

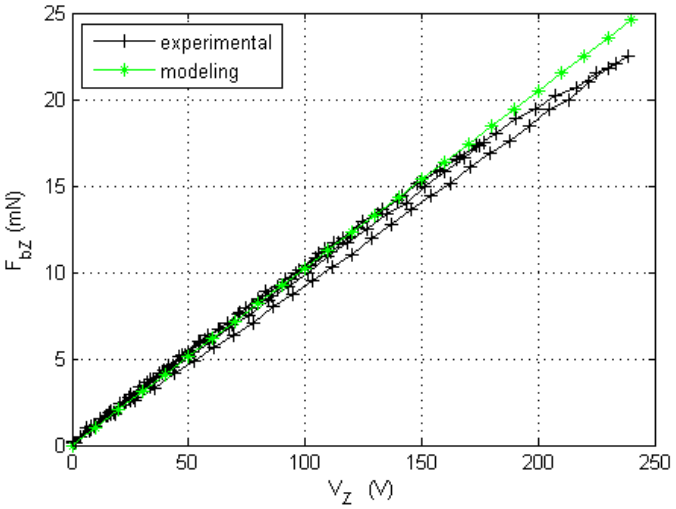

Figure 3.17: Measured blocking force F_{bz} along the Z-axis (-+-) compared with the afferent model (-*-).

the resulted values were $16.5\ mN$ and $22.5\ mN$ respectively. These values are 2-3 times larger than what is considered sufficient for micro-object manipulation and, considering the beam dimensions, more than promising.

A hysteresis behaviour may be also observed in the three cases: 9.1% for the X-axis; 12.9% for the Y-axis; 6.3% for the Z-axis. These are due to the inherent ferroelectric nonlinearities. The material capacitor effect also adds to the nonlinear behaviour. Table 3.6 brings together the measured experimental values:

Table 3.6: Experimentally found values.

Voltage range	***Axis***	***Measured blocking force***	***Hysteresis***	***Model accuracy***
$120\ V$	X	$48.2\ mN$	9.1%	99%
$240\ V$	Y	$16.5\ mN$	12.9%	90%
$240\ V$	Z	$22.5\ mN$	6.3%	92%

These measurements have been performed at lower applied voltage values than those used in the displacement measurements in order to avoid damaging the PMN-PT cantilever. Taking into account the good agreement between the force model predictions and the experimental results, for voltages reaching $400\ V$, forces of up to $150\ mN$ are expected along the X-axis.

3.2.5/ CONCLUSION

The presented model brings compensation for the coercive field value, as well as force generation predictions, which are very important, not only in the case of PMN-PT [001], but other piezoelectric materials. PMN-PT presents qualities that not only fulfils the integrability needs in terms of micro-fabrication and usage, but is also capable of very large displacements (double that of a similarly sized PZT actuator), enables the usage of the 3rd DoF and generates forces more than suitable for micro-manipulation. It was observed

that although unwanted coupling exists, it can be compensated for without complex control loops. Coupling this with the small nonlinearities exhibited, PMN-PT is a material that's well suited for micro-systems integration.

3.3/ LARGE STROKE 6 DOF MICROGRIPPER

3.3.1/ MICROGRIPPERS STATE OF THE ART

In order to prove the large-stroke capabilities of PMN-PT as an integrated actuator, as well as its very low hysteretic behaviour, a cantilever based microgripper was fabricated. Traditional contact manipulation technologies require large structures for accurate position control. The work space can also be reduced due to the sensors used (position or force). The aim is to simplify the structure while retaining or adding to the displacement capabilities and, as demonstrated, PMN-PT has the qualities to do just that.

Microgrippers are widely used for micromanipulation and microassembly [Andersen et al., 2008] [Boudaoud et al., 2010] [Hériban et al., 2008] and [Pérez et al., 2005]. Their advantage is that they can be used to manipulate several objects with different shapes and sizes. In the AS2M department of the FEMTO-ST institute, a microgripper based on two piezoelectric fingers is proposed. This is also where different micro-assembly stations were developed to achieve 3D micro-assembly. A station was used to assemble a micro-cow using five micro-fabricated pieces where each piece has $5\ \mu m$ of thickness. The micro-cow has $830\ ng$ of weight, $500\ \mu m$ of length and $500\ \mu m$ of height.

Another project is The European integrated FP6 project HYDROMEL, which focused on the development of a robotic station capable of automated, vision-based controlled micro-assembly, as seen in Figure 3.18. The aim of the project was to develop a new and versatile 3D automated production system with a positioning accuracy of 100 nm for complex micro-devices, based on ultra precision robots.

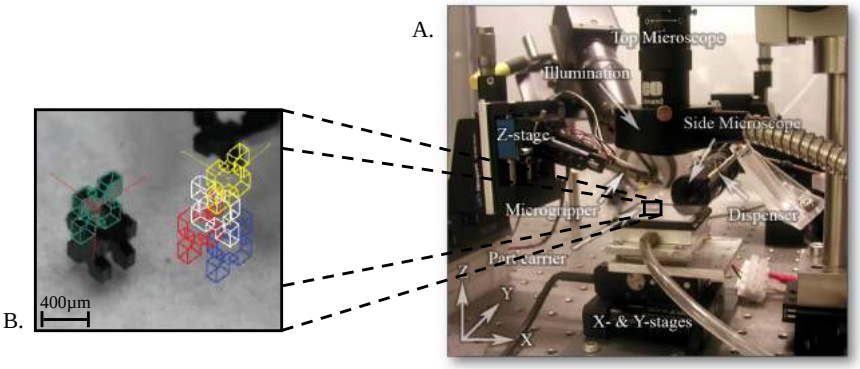

Figure 3.18: A. Hybrid ultra precision manufacturing process based on positional- and self-assembly for complex micro-products [Chang et al., 2010] and B. one of the tasks it is capable of: micro-assembly of complex and solid 3D MEMS by 3D vision-based control.

The tendency is to use microgripper (either alone or in hybrid configurations) to perform a complete task-exercise. Usually microgrippers are placed on micro-positioning

stages similar to those used in the experimental, blocking force measurements setup. In our approach, as the intend is to use only one multi-DoF capable microgripper, a vertical configuration was chosen because thus avoiding the extra, large actuation stages.

3.3.2/ DEVELOPMENT AND FABRICATION

A PMN-PT [011] actuator, due to its high piezoelectric coefficients, can generate usable displacement along all 3 axes. This means that by pairing two such beams a 6DoF microgripper will emerge. Two duobimorph beams were thus aligned on a PCB (Printed Circuit Board) and fixed in place with non-conductive glue. The remaining active part of the actuator was $21\ mm$ in length. Electrical connections between the cantilevers electrodes and PCB pads were done by wire-bonding

Each beam has been fitted with a passive SOI (Silicon-On-Insulator) end-effector [Ivan et al., 2013] that adapts to the object size and exhibits elastic deformation while microgripping. Figure 3.19 presents the microgripper with detailed view of the end effectors and the gripping tips. The end-effectors have been glued in place with the aid of non-conductive thermal glue.

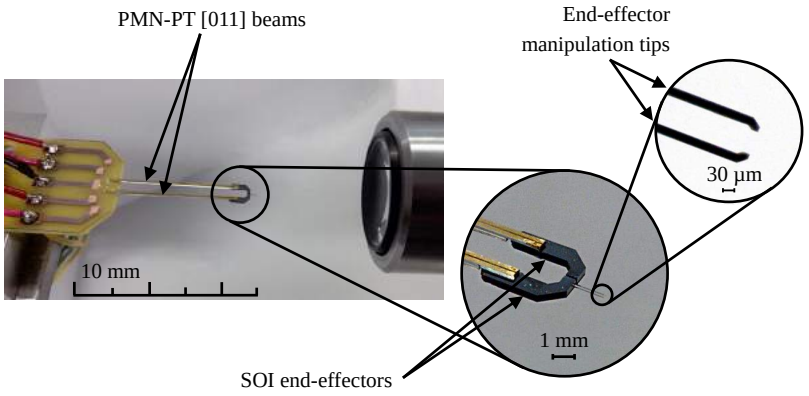

Figure 3.19: Closeup of the microgripper in the experimental setup for PMN-PT [011] cantilever voltage vs. displacement model verification setup with detailed structure.

PMN-PT [011], as mentioned, can generate usable displacement along all 3 axes while also having very low nonlinearities (6% hysteresis). This can allow for the control of a manipulated micro-object, in a large work volume, without the need of sensors. The accuracy is tested with a pick-and-place exercise done only with the microgripper, with open loop control based on the static model presented previously.

As the manipulation exercise is done using open loop control, by using the images provided by the monitoring cameras, approximations can be made regarding the forces exerted on the end-effector tips. For this, two conditions must be fulfilled simultaneously so that the SOI end-effectors can be used in the manipulation exercise. First the longitudinal force (F_{bX}) generated by the piezo-actuator (Figure 3.20) must not be larger than the shear limit of the solder between the actuator and the end-effector and second the lateral force generated (F_{bY}) must not be larger than the one that would break the end-effector.

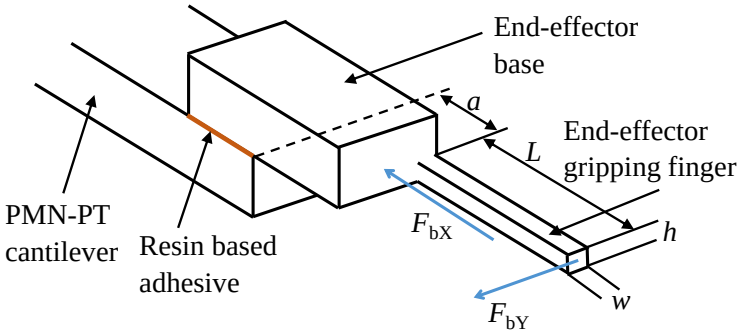

Figure 3.20: End effector components, structure, dimensional variables and applicable forces.

$$F_{bY} = \frac{4Ehw^3\delta_Y}{L^3} \tag{3.23}$$

The maximum applicable force to the end effector F_{bX} was found to be $51.8\ mN$, and it's the maximum shearing force the thermo-resin can withstand, given the applied surface. The maximum gripping force can be calculated using equation (3.23), with the parameters listed in Table 3.7. Having a value situated between $72.8\ mN$ and $105.28\ mN$, it is more than sufficient to manipulate micro-objects, being at least an order of magnitude larger than the commonly found forces.

Table 3.7: The parameters and coefficients related to the Si end-effector.

Parameter	***Description***	***Value***
a	End-effector base length	$3\ mm$
L	End-effector tip length	$1.5\ mm$
w	End-effector width	$15\ \mu m$
h	End-effector thickness	$10\ \mu m$
E	Silicon Young's Modulus	$130 - 188\ GPa$
δ_Y	Allowed maximum tip displacement	$14\ \mu m^*$

(*Experimentally determined value)

3.3.3/ CAPABILITIES

Considering the very low hysteresis values for free displacement, complex trajectories can be mapped out with the tip without the need for closed loop control.

Circular trajectory generation

When generating displacement, under ideal conditions, there are compensation coefficients for each generated signal: $c_i = 1\ (i = 1 \ldots 4)$. The tips can thus describe a circular motion upon application of sine signals of equal amplitude and frequency, but with phase shifts of $\pi/2$. In equation 3.24 V_{max} is the voltage amplitude applied per electrode.

The maximum experimental displacement compensation coefficient c was found when applying voltage in Y direction, namely ($E1$, $E4$) and ($E2$, $E3$) pairs of electrodes and it reaches $c = 1$ when the tip is in the maximum/minimum position along the Z-axis. Expression 3.25 presents the displacement compensation coefficient value dependency to the position on the circular trajectory.

$$\begin{cases} V_{E1} = V_{max}\frac{sin(2\pi t)}{c_1} \\ V_{E2} = V_{max}\frac{sin(2\pi t+\frac{\pi}{2})}{c_2} \\ V_{E3} = V_{max}\frac{sin(2\pi t+\pi)}{c_3} \\ V_{E4} = V_{max}\frac{sin(2\pi t+\frac{3\pi}{2})}{c_4} \end{cases} \tag{3.24}$$

By replacing the voltage signals applied to the electrodes V_{E1} through V_{E4} from the static model presented in this chapter with the ones resulting from equation 3.24, a theoretical circular trajectory results. This is compared in Figure 3.21 with the experimentally resulting trajectory. No feedback loop is considered.

It can be observed that the deviation from the theoretical trajectory in under $10\ \mu m$, in both directions, representing less than 7%. This is an expected value when taking into account the low hysteresis values. Another observation is related to the amplitude of the motion. The lower values are explained with the aid of Figure 3.22, presenting the command signal.

$$c_i = \frac{c-1}{2}sin[2\pi t - (-1)^{i+1}\frac{\pi}{4}] + \frac{c+1}{2} \tag{3.25}$$

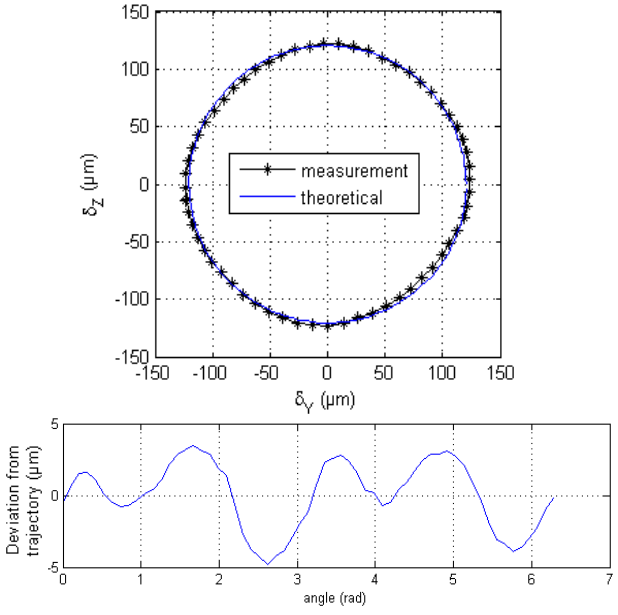

Figure 3.21: The circular experimental vs. theoretical free tip trajectory and the error variation plot.

Following the deviation from the circular trajectory, the top-bottom symmetry of the beam becomes apparent. Another observation is the influence the potion of the separating groove has over the displacement, pointing to the beam's lateral asymmetry. High-

lighting the intersections with the Z and Y axes, respectively, each curve represents the voltage variation on the four electrodes of the beam. Their shape is due to the modified sine signals which take the displacement compensation coefficient into account, $c = 1.42$. A breakdown of the signal amplitude at the intersecting points between the Y and Z axes and the trajectory is presented in the table.

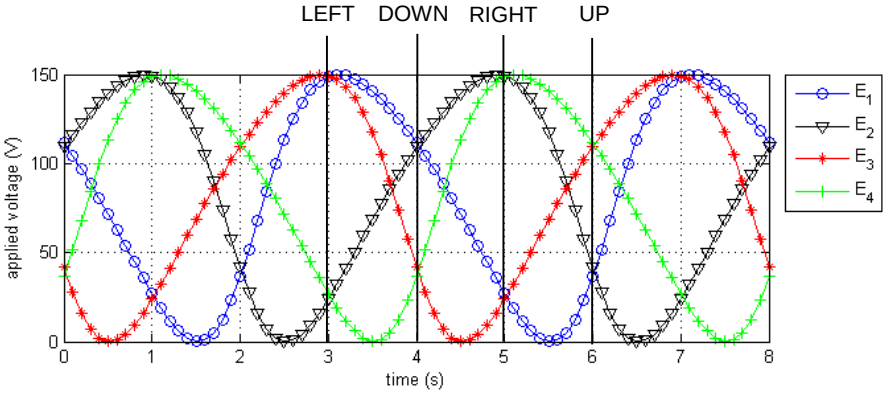

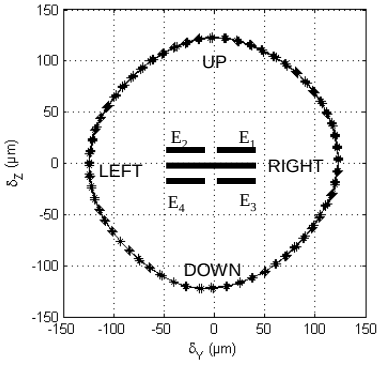

DOWN		RIGHT	
electrode	voltage	electrode	voltage
E_1	84% V_{max}/1.42	E_1	15% V_{max}
E_2	84% V_{max}/1.42	E_2	84% V_{max}
E_3	15% V_{max}	E_3	15% V_{max}
E_4	15% V_{max}	E_4	84% V_{max}
UP		LEFT	
electrode	voltage	electrode	voltage
E_1	15% V_{max}	E_1	84% V_{max}
E_2	15% V_{max}	E_2	15% V_{max}
E_3	84% V_{max}/1.42	E_3	84% V_{max}
E_4	84% V_{max}/1.42	E_4	15% V_{max}

Figure 3.22: Voltage variation curves, highlighting the trajectory intersections with the Y and Z axes, and the maximum displacement breakdown at these intersections. The displacement compensation coefficient is presented in numerical value, $c = 1.42$

Because of having voltage on all four electrodes, in the points where the circle intersect the Y and Z axes, the displacement generated by one pair of electrodes is countered by the other pair, thus reducing it overall. During circular motion, the maximum displacement measured at the intersection with the Z-axis, above the equilibrium position, for a maximum voltage, V_{max}, is generated to the equivalent of 69% of the displacement measured for the same V_{max}, in the case of Z-axis displacement.

Square diamond trajectory generation

Another way to highlight the large displacement with low hysteresis capabilities of the PMN-PT cantilever actuator is by having the tip of the beam describe a square diamond shape. The command signal varies greatly from the one used cor circular trajectory generation. It was built using Matlab Simulink®. The resulting trajectory presented in Fig-

ure 3.23. Similar to the previous described case, the cantilever top-bottom symmetry and lateral asymmetry are apparent, when observing the deviation curve.

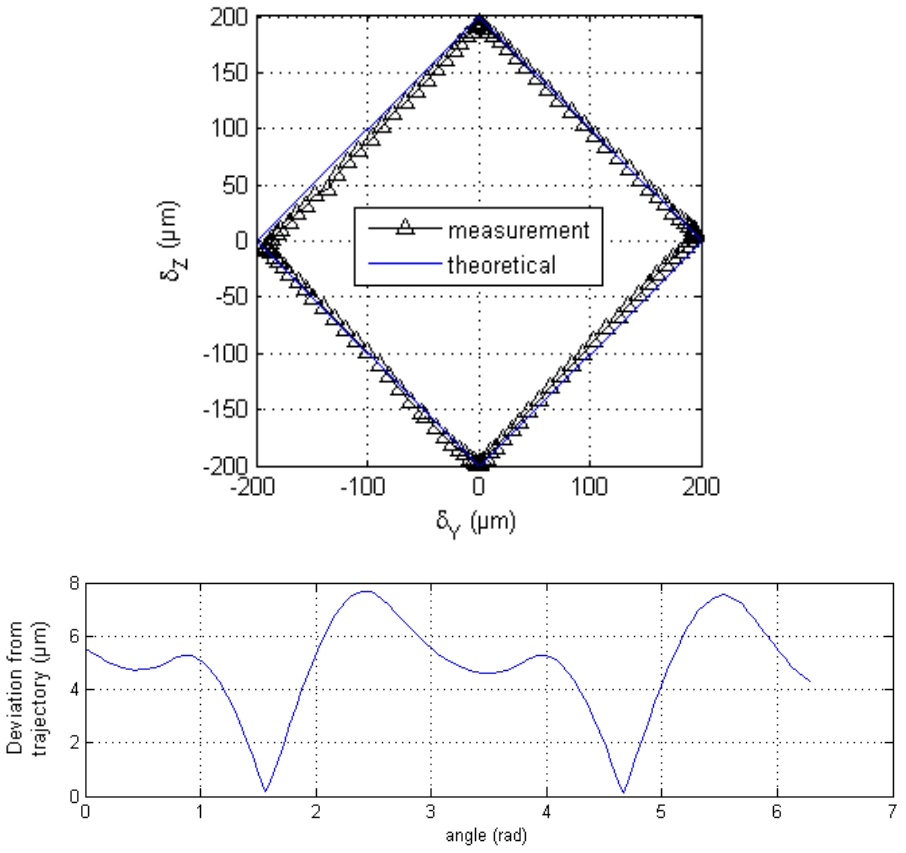

Figure 3.23: The square diamond experimental vs. theoretical free tip trajectory and the error variation plot.

The voltage variation on each of the four electrodes is presented in Figure 3.24. Although the same V_{max} is reached in the experiment, the displacement values found at the trajectory intersection with the Y-axis correspond to those found in the linear displacement experiments presented in a previous section. The values measured at the intersection with the Z-axis differ from those seen in the linear displacement experiments as for the square trajectory, the displacement compensation coefficient is considered. The deviation from the theoretical trajectory, although similar in numerical value at $8\ \mu m$, represents less than 4% of the generated motion, an twofold improvement over the circular trajectory. This translates in a higher precision for linear motions. As previously noted, a breakdown of the signal amplitude at the intersecting points between the Y and Z axes and the trajectory is presented in the table.

Both presented trajectories have been possible to generate thanks to the very low hysteresis values PMN-PT presents, as well as the high coercive field values. This is proof of not needing complex displacement control for positioning tasks, as is highlighted in the following section, by performing a manipulation task.

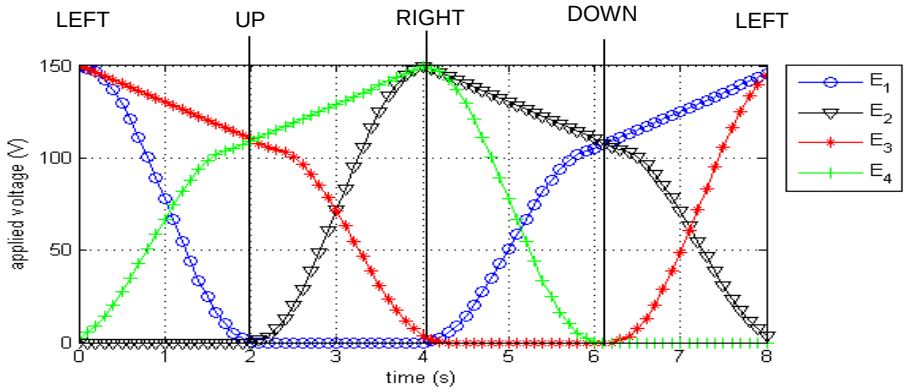

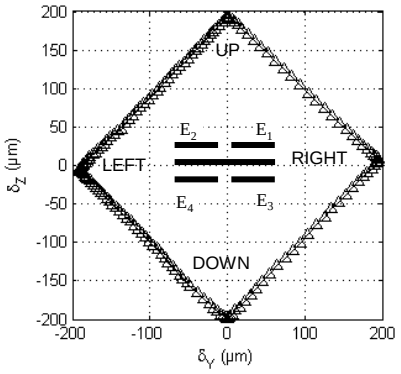

DOWN		RIGHT	
electrode	voltage	electrode	voltage
E_1	$V_{max}/1.42$	E_1	0
E_2	$V_{max}/1.42$	E_2	V_{max}
E_3	0	E_3	0
E_4	0	E_4	V_{max}
UP		LEFT	
electrode	voltage	electrode	voltage
E_1	0	E_1	V_{max}
E_2	0	E_2	0
E_3	$V_{max}/1.42$	E_3	V_{max}
E_4	$V_{max}/1.42$	E_4	0

Figure 3.24: Actuation curve shape and maximum displacement breakdown at trajectory intersection with the Z and Y axes.

Manipulation exercise

An exercise experiment was performed in order to demonstrate the Multi-DoF capabilities of the PMN-PT actuated microgripper in manipulation scenarios. Another reason is to see the exploitable working area, without the need of extra actuation stages.

The experimental setup consisted of a dSpace®1104 real-time microcontroller board connecting the PC running Matlab®and a high frequency, high voltage, 8 channels voltage amplifier, capable of delivering $150\ V$ per channel with a peak current of $300\ mA$. Two cameras were placed along the X and Y axes each capturing a pair of the three movements (along X and Y axes and along X and Z axes). Apart from giving a direct view of the manipultation task, the cameras can also be used to predict the force acting on the micro-object itself, using equation 3.23. The two cameras were equipped with 4X optical objectives, although already featuring 1-5X zoom (resulting in 4-20X magnification). The images were captured on the PC through a standard s-video connection. The micro object was placed on a spring loaded table, which was positioned atop a man-

ually controlled in plane actuation stage, for initial image centring. The setup follows the schematic presented in Figure 3.25.

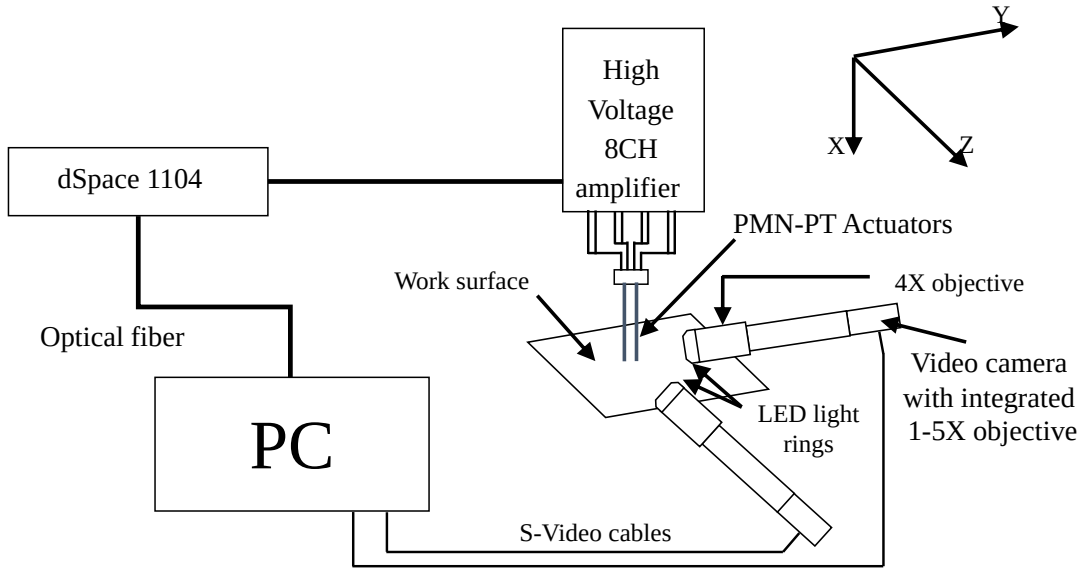

Figure 3.25: Experimental setup for the duobimorph cantilever-based microgripper in an object manipulation task.

In the case of a pick-and-place, task the following scenario is proposed, with the micro-object pre-positioned under the microgripper with the aid of a mechanical X-Y stage. The steps which need to be completed are as follows: a) opening the gripper arms; b) 3D positioning of the end-effectors alongside the object; c) gripping the object; d) lifting the object; e) moving the object; f) placing down the object; g) opening the gripper; h) returning the microgripper arms to the idle position on the X axis; i) returning the microgripper arms to the idle position on the Y axis; j) returning the microgripper arms to the idle point on the Z axis. The applied signal for the X and Z axes were symmetrical between the microgripper arms, while asymmetrical for the Y axis. These moments can be viewed in Figure 3.26.

This command signal results in the following tip trajectory (Figure 3.27), describing the work volume attainable for a voltage applicable to each electrode $V_{applied} < 150V$ (limited only by the voltage amplifier). The stages of the exercise are identified on the trajectory of one arm, the procedure being mirrored to the other one.

Using image analysis, the exact moment of coming into contact of the end effectors with the manipulated object was observed. An estimation for the gripping force, based on the presented model, was done with the aid of equation (3.23) of $\sim 225\ \mu N$, more than enough to pick and place such a large object and far from what can break the end effector fingers.

A visual walk-through the manipulation task can be viewed in Figure 3.28, following the same a) to j) steps enumerated previously.

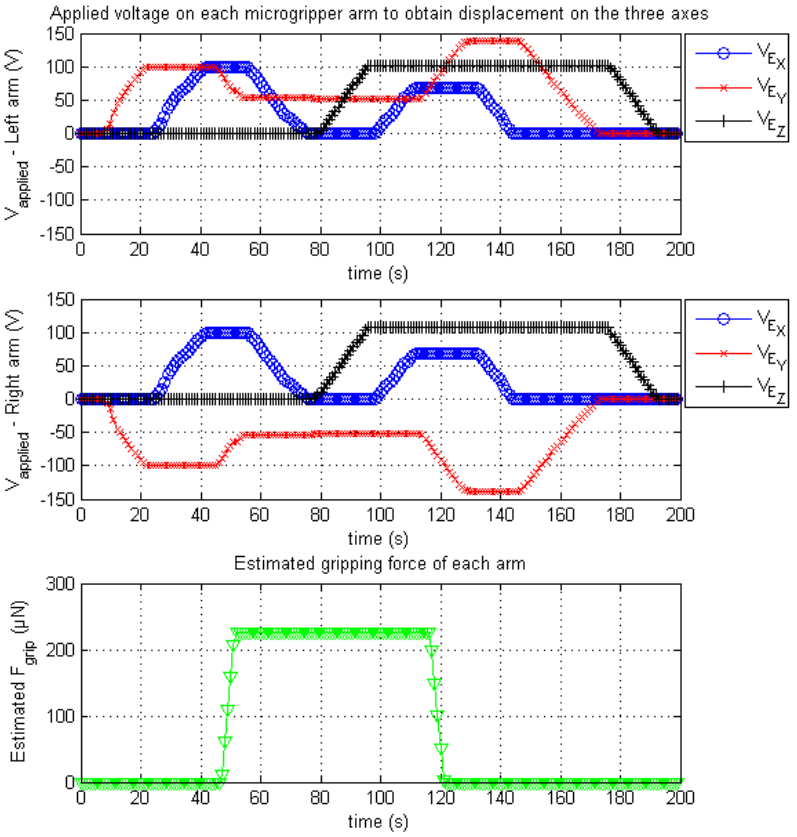

Figure 3.26: Applied command signals for the microgripper in a pick-and-place task: key moments and the calculated gripping force (F_{b_Y}) using the model (3.23).

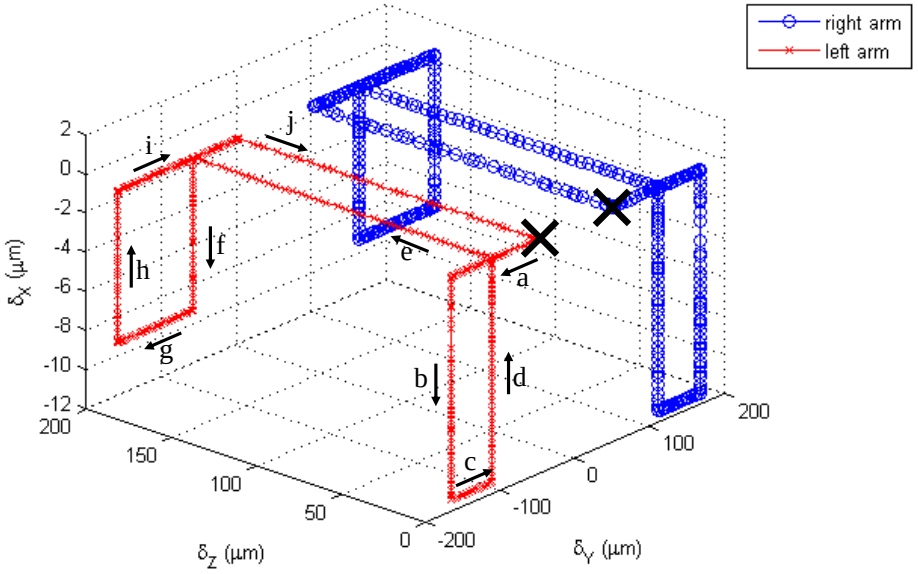

Figure 3.27: Defined work volume for $V_{applied} < 150V$. The manipulation stages are identified. The initial and final position are marked with "X".

Figure 3.28: Key moments in the pick-and-place manipulation task. Each step presents a front and side view of the gripper tips and object to be manipulated.

3.4/ CONCLUSION

In this chapter, the model used for predicting the PMN-PT based cantilever behaviour is first presented and then verified through experimental measurements. Given the much more linear behaviour of PMN-PT, in comparison to other, more traditional piezoelectric

materials, such as the popular PZT piezo-ceramic, complex trajectories can be generated, without the need of closed loop controllers.

PMN-PT [011] proves to be a well suited candidate for a large-stroke, integrated actuation solutions. It has a high enough d_{31} piezoelectric coefficient to induce 3DoF to a generic duo-bimorph cantilever actuator. As seen from the flexural beam actuator, it offers large displacements along all axes: over $650\ \mu m$ along the Z-axis, over $460\ \mu m$ along the Y-axis and over $40\ \mu m$ along the X-axis, for a 25 x 0.6 x $0.41\ mm$ beam. This is achieved while having a very low hysteresis ($\approx\ 6\%$), as it is demonstrated by the describing of complex trajectories with the tip of the PMN-PT duo-bimorph. The forces generated are also comparable to hard PZT cantilever actuators of similar dimensions: over $22\ mN$ along the Z-axis, over $16\ mN$ along the Y-axis and over $48\ mN$ along the X-axis. The presented PMN-PT specific Voltage / Force / displacement model is in agreement with the experimental results. These results were first highlighted through two proposed experimental trajectories. The variation from the theoretical trajectories are under 7% error for the intended circular one and under 4% for the square diamond one.

As it can be integrated using simple, current, non-cleanroom, micro-fabrication techniques, PMN-PT [001] was successfully integrated in a microgripper, the capabilities of which have been demonstrated through a pick-and-place manipulation task.

4

PATCH ACTUATOR USING THE PMN-PT [001] CUT FOR HIGHLY INTEGRATED PIEZO-SYSTEMS

This chapter presents the PMN-PT [001] longitudinal cut based actuator study, that brings together large displacement and very high dynamics with small volume. This case study is done by using PMN-PT as a simple, easy to integrate, bulk actuator. For a rectangle structure of varying width and a $0.2\ mm$ *thickness, displacements of over* $680\ nm$ *with under* 6% *hysteresis is achieved while also working at frequencies in the MHz region (* $> 2.2\ MHz$*). This demonstrates the improvements PMN-PT brings to micro-spectrometry and image correction with micro-mirror displacement. A bulk PMN-PT micro actuator was integrated into a Reconfigurable Free Space - Micro Optical Bench (RFS-MOB) compatible structure and presented.*

4.1/ INTRODUCTION

Among the applications where miniaturization is sought we can also count optical applications as following the trend. A field of great interest thus becomes Micro-Opto-Electro-Mechanical Systems (MOEMS), a hybrid system, where highly accurate actuation is needed. These applications involve the notion of adaptive optics commonly found in interferometry [Blomberg et al., 2009], spectrometry [Xiang-Xia et al., 2011, Zhihai et al., 2011] (Figure 4.1), scanners [Lin et al., 2012] and image aberration corrections [Tortschanoff et al., 2010].

Although piezoelectric materials, like PZT (Lead Zirconium Titanate), are widely used in multi DoF applications, where large bandwidth and forces [Gebhardt et al., 2007, Lee et al., 2010] are needed, other materials are being developed in order to gain in performance. As mentioned in Chapter 2, such a material is PMN-PT (Lead Magnesium Niobate-Lead Titanate). It's of particular interest due to its very high piezoelectric coefficients (up to 6 times than those of PZT) responsible for longitudinal displacement. Recent improvements in fabrication techniques have shown the possibility of obtaining d_{33} values of up to $4500\ pm/V$ [Yamamoto et al., 2013], making PMN-PT useful in transducers [Zhang et al., 2011b] and other types of sensors (mechanical properties aren't

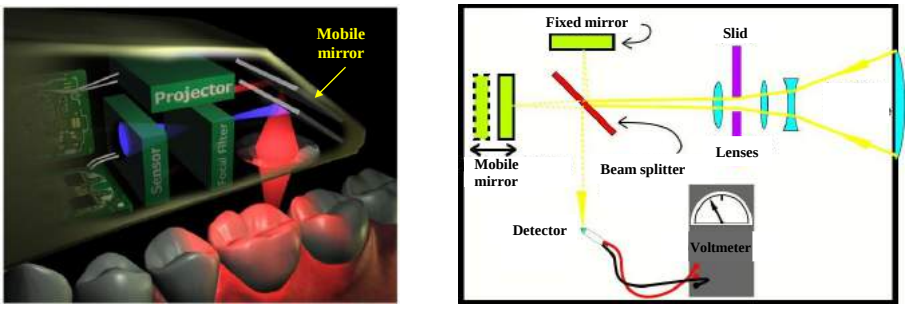

a) b)

Figure 4.1: a) The iTero©Intra-Oral Dental Scanner - Universty of Groningen [Van der Meer et al., 2012], b) Michelson Interferometer working principle, employed by the scanner.

well known due to the wide variety of sub-groups in the PMN-PT family and the fact that it is relatively new – available since early 2000). An advantage that stands out when using PMN-PT is the capability of it being used in bulk [Bargiel et al., 2010], to which existing micro-fabrication techniques compatibility [Kim et al., 2003] is added.

In this chapter, after a brief introduction in how piezoelectric materials are used in MOEMS, the usage of PMN-PT is highlighted in common applications. This is followed by the restrictions these incorporating structures bring with correlation to the project requirements like compatibility, integrability size and displacement. The following sections deal with the model of the actuator as well as the chosen design. As the clamping influences the displacement, a study of the factors influencing it is presented focusing on the size and shape of both the actuator and the soldering interface. The study continues with the static and dynamic behaviour analysis. The findings are then highlighted with the fabrication of an RFS-MOB compatible smart element that encompasses PMN-PT [001].

4.2/ INTEGRATION OF PIEZOELECTRIC ACTUATORS IN MOEMS

Common actuation solutions extend to, and not only, polymers [Wang et al., 2010, Yan et al., 2011], ferromagnetic [Ahmed et al., 2013] or thermoelectric [Boukai et al., 2008]. The best results, however, are found when piezoelectric materials [Liu et al., 2010] are being used, due to their integrability, resolution and dynamics. Such applications are for the optics used in astronomy, where adaptive lenses and mirrors improve imaging [Ma et al., 2011] (Figure 4.2).

Due to the displacement necessities in various optical applications, different actuator designs are used in order to achieve specific surface deformation. Some of the designs used with piezoelectric actuators have been adapted starting from electrostatic to thermoelectric actuated micro-mirrors.

One such design is the one presented in Figure 4.3. The height of the actuators varies with the applied voltage causing for the top membrane to deform. There are limitations to this design in terms of dynamics and manageable deformation. The latter is directly connected to the elasticity of the membrane, its proneness to shearing and the

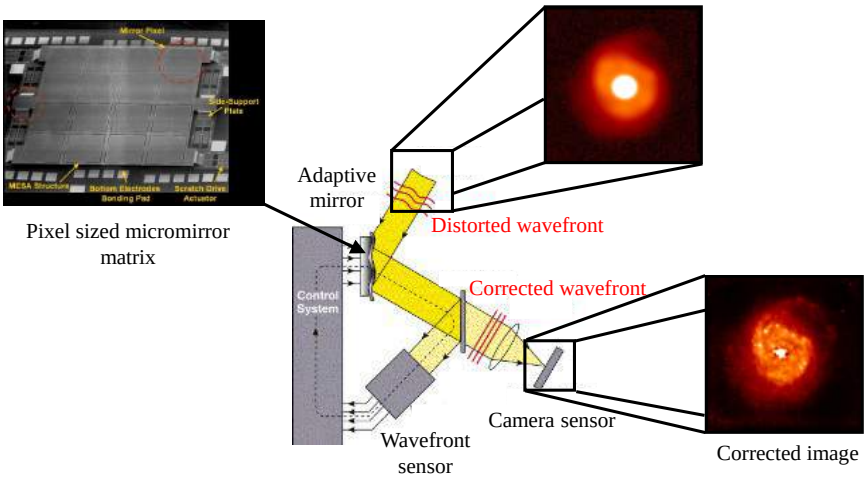

Figure 4.2: The principle used in astronomy for atmospheric aberration correction that includes an analogue micro-mirror matrix [Sameoto et al., 2007].

compliance of the connection points. This kind of design is usually used in low frequency applications.

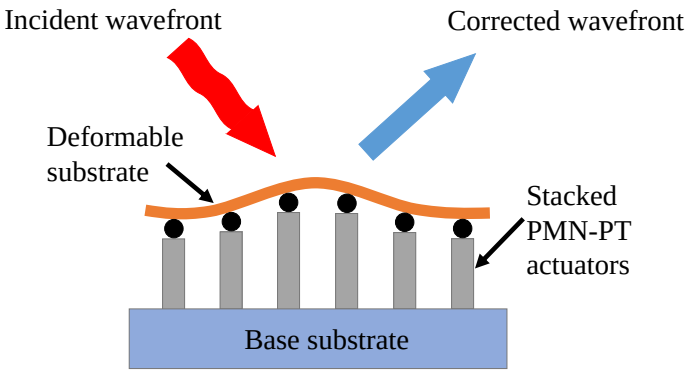

Figure 4.3: Stacked PMN-PT actuator based deformable mirror used in low frequency applications.

Borrowing from the thermoelectric design, adaptive mirrors can be constructed as presented in Figure 4.4. Positioned in a radial pattern, this design is mostly used in situations where light signals (laser beams) need to be reconstructed in order to not loose the carried information. As pointed out in the figure, the connections are done in such a way as to result in different electric field densities, which in turn bring rise to different curvature radii of the same beam (layer). This design is used in fields such as laser based topography, where two laser beams (different wavelengths) are used in tandem, one for reading the disturbances which get fed into the adaptive control system and apply to the actuated micro-mirror for the other laser beam.

Another design that's commonly found in MOEMS is the matrix based structured

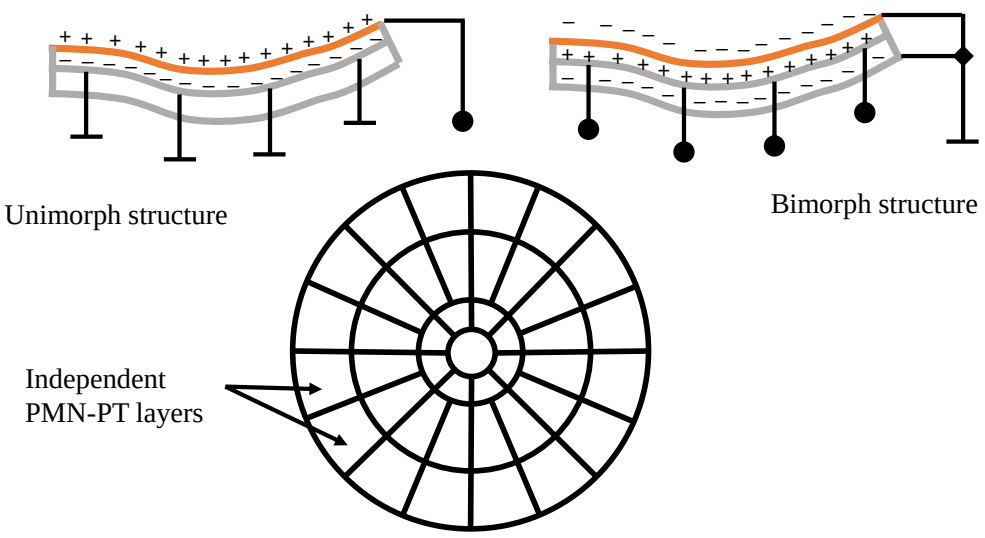

Figure 4.4: Unimorph and bimorph structured mirrors for laser beam focusing and reconstruction.

mirrors, where the surface is discretized, each element corresponding to one light receptor (pixel) of the camera sensor. Depending on the type of apparatus, the employed design can vary in terms on independent micro-mirror shape. This is exemplified in Figure 4.5 where a hexagonal pattern is etched into PMN-PT[001], atop of which an elastic electrode can be added.

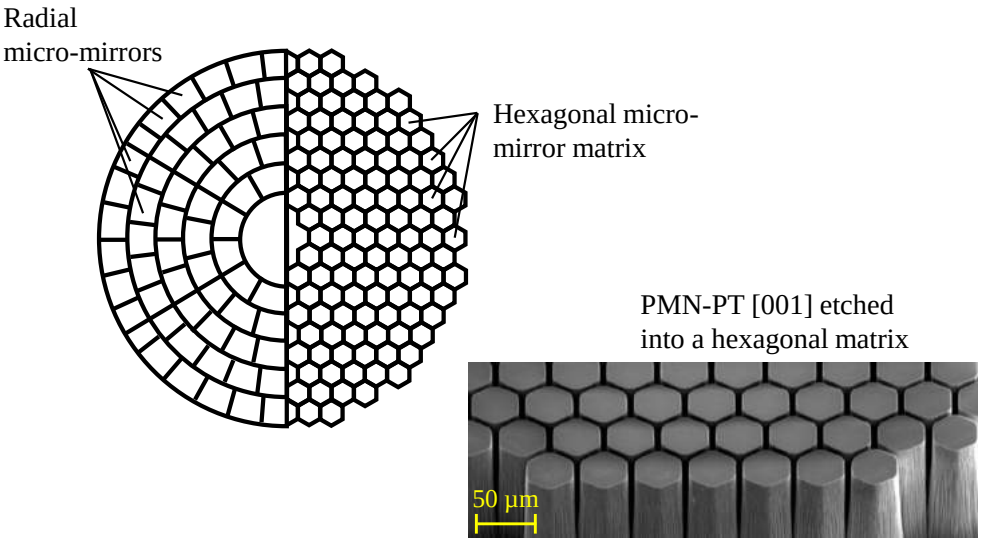

Figure 4.5: Matrix disposition of independently actuated pixel-size micro-mirrors .

These designs enforce the idea that, after a specific size, the unimorph/bimorph structure is changed in favour of micro-actuator matrices for micro-mirror actuation. A bulk actuator solution thus becomes relevant for reduced work spaces, provided the displacement needs. The following section deals with these restrictions and requirements.

4.2.1/ STUDY OF PMN-PT [001] AS A PATCH ACTUATOR

PMN-PT[001] offers the distinct feature of making use of the indirect piezoelectric effect as a directly proportionate relation between the applied voltage and the resulting displacement. The correlation is made with the aid of the d_{33} piezoelectric coefficient which, in the case of PMN-PT surpasses values of $4500\ pm/V$.

As laid out in the first chapter, there are some specific restrictions in terms of size, displacement needs and ease of integrability. Attempts have been made towards the miniaturization of optical devices, such as special purpose laser amplifiers (Figure 4.6 -a) or optical switches (Figure 4.6 -b). Though these commercially available solutions offer reduced size, their usage is still limited to low volume restrictions such as industrial communications systems or laser aided telemetry. For medical applications the size requirements are even more strict. Figure 4.7 presents and overview of our designed RFS-MOB, outlining the removable components and their features: simple and/or actuated micro-mirror, micro-lens, beam splitter, micro-aperture. This system sets to push the dimensions limit even further while also allowing for diverse functionality through the repositioning of the components.

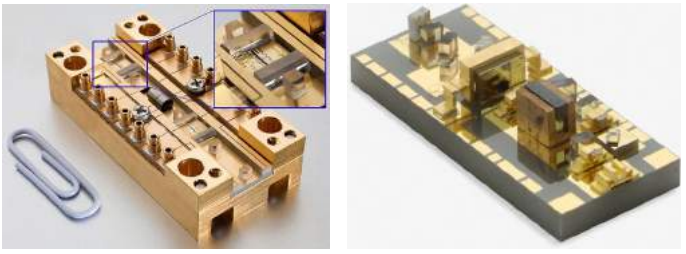

a) b)

Figure 4.6: Commercialy available MOEMS: a) laser amplifiers [Spießberger et al., 2011] and b) optical switches [Flanders et al., 2003] .

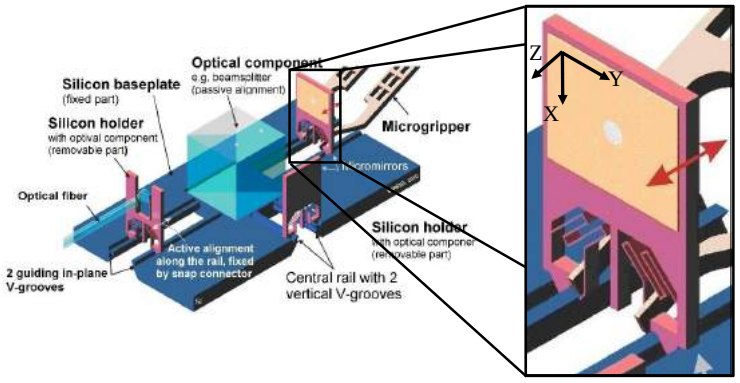

Figure 4.7: Reconfigurable micro optical system. Femto-ST design [Bargiel et al., 2010].

The goal being the integration of a PMN-PT based micro-actuator for a micro-mirror, the aforementioned restrictions are as follows:

Actuators compatible with Optical applications

Applications that use the longitudinal piezoelectric effect are most commonly found in matrix like structures for varying shape surface displacement. This makes it particularly useful in micro-mirror displacement, be it for image correction where the actual mirror also acts as the top and common electrode, or for colour aberration corrections (induced by lenses in specialized magnification camera objectives). Another case is that of spectrometry, or interferometry as is the Michelson interferometer.

Other MOEMS requirements can relate to the optical properties of the actuator itself, be it surface finish or features such as transparency or refraction index change with an applied electric field. PMN-PT also has an edge here as it can be used directly as the micro-mirror, provided that the top electrode fulfils the application requirements for reflection.

Integrability

As the RFS-MOB relies on removable silicon components, the streamline of the integration procedure of the PMN-PT based actuator is of high importance. As previously mentioned, PMN-PT can be used in bulk. In terms of integrability, this means that no special preparation or pre-fabrication procedure need to be adapted. The available usable surface on a silicon holder, due to its design, brings limitation as well, measuring $670\ x\ 800\ \mu m^2$. Coupled with the simplicity of the actuator design and lack clean room conditions requirements for micro-machining make PMN-PT a reliable candidate for a highly integrated micro-mirror actuator.

Size

The PMN-PT actuator has firstly and foremost a thickness (h) restriction, this being due to the displacement being out of plane. As viewed in previous figures (Figure 4.7) the actuator needs to be positioned on a vertical Si spring fixed support measuring $100\ \mu m$ in thickness. In Figure 4.8 the reasoning behind choosing the thickness is presented. If a too thick actuator is chosen, not only is the dynamics of the structure affected but also its stability as the centre of mass would be too far from the contact and fixture points. Considering the dimensions of the Si support, so too the PMN-PT actuator needs to be as thin as possible, without sacrificing performances. A thickness of $200\ \mu m$ was chosen,

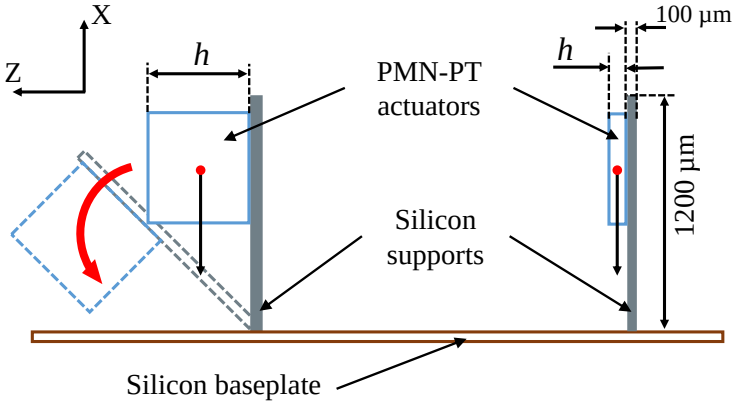

Figure 4.8: Explanatory thickness choice schematic with relevant Si support dimensions.

being the minimum guaranteed by all manufacturers to have reliable electromechanical properties.

Displacement

Being part of a laser based optical application, the displacement needs have to meet two requirements. First, depending on the wavelength (λ) of the laser used, the actuator displacement δ_Z has to surpass a minimum of half the chosen wavelength ($\lambda/2$). For our application, as mentioned in the first chapter, the limit was set at $325\ nm$, for a wavelength of $650\ nm$, i.e. visible red light (Figure 4.9). Second, the maximum accepted aberration (δ_{ab}) is a tenth of the same wavelength, which translates into a surface displacement variation for the actuator of under $\delta_{ab} < 32.5\ nm = \frac{\lambda}{2}$. This is so that enough information travels through the MOEMS and back to the detector (direct influence over the quality of the signal). Figure 4.10 schematically presents how these aberrations can be present on the moving surface and what displacement is taken into account.

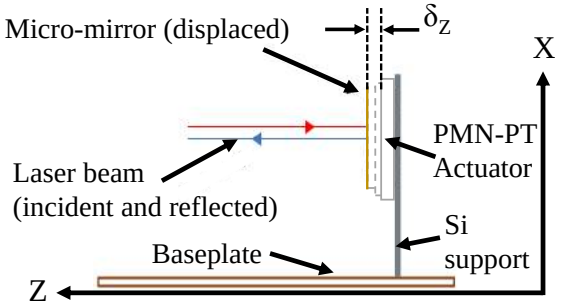

Figure 4.9: Explanatory thickness choice schematic with relevant Si support dimensions.

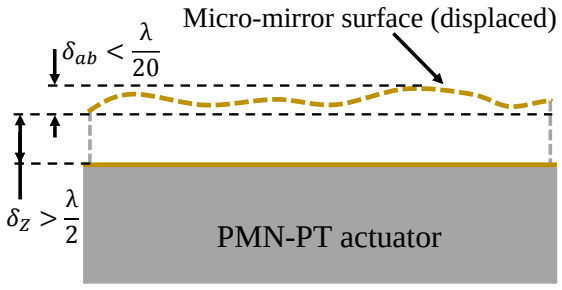

Figure 4.10: Explanatory thickness choice schematic with relevant Si support dimensions.

4.3/ MODELING THE ACTUATOR AND THE INTEGRATING STRUCTURE

For the micro-mirror actuator, a very straightforward design was chosen for preliminary studies: $200\ \mu m$ thick with a square footprint actuator used in bulk. The result is presented both schematically and with images in Figure 4.11.

The model is also straightforward and relies on the direct correlation between the piezoelectric coefficient d_{33} and the applied electric field. Rewriting the equations from

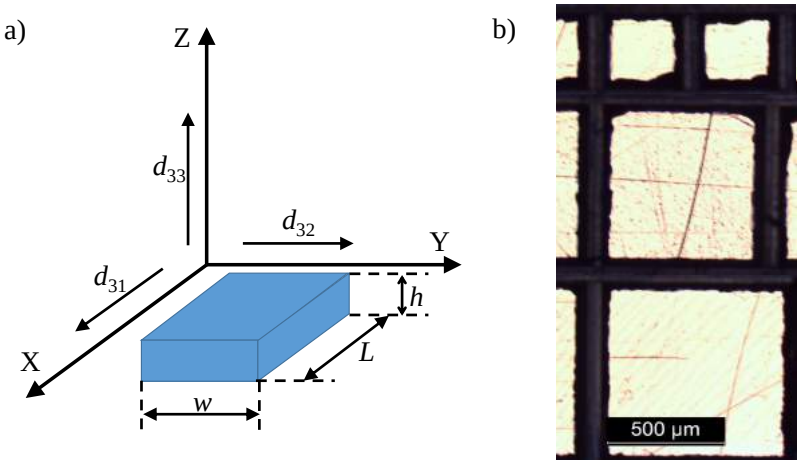

Figure 4.11: Chosen design for the PMN-PT [001] based actuator: a) schematic, b) composed image of different size cut actuators.

the second chapter with the notations from Figure 4.11 produces:

$$S_1 = \frac{\Delta h}{h} = d_{33}E_3 = d_{33}\frac{V}{h} \tag{4.1}$$

This results in the Voltage to displacement model:

$$d_{33}E_3 = d_{33}\frac{\Delta h}{V} \tag{4.2}$$

or

$$\Delta h = d_{33}V \tag{4.3}$$

Considering the presented model, the most influencing factor in regards to the displacement generated by a PMN-PT patch micro-actuator is the fixture. In particular the contact shape, its surface and the nature of the solder.

4.3.1/ THE DESIGN OF THE MICRO-ACTUATOR

In order to maximize displacement, different sizes and shapes PMN-PT actuators were taken into consideration. In terms of **size**, the width of the actuator was varied and to ensure symmetry a square shape employed (Figure 4.11, b). In terms of **shape**, grooves were etched onto a patch actuator in order to create a matrix-like solution. Figure 4.12 presents experimental samples.

The etching on the actuator is meant to simulate a peg-like structure, similar to a matrix constituted of multiple, smaller surfaced actuators. The downside of reducing the structural integrity of the actuator, other than adding pre-fabrication steps, is the reduction in displacement and overall unwanted shape changes (as shown by the simulation presented in Figure 4.13). Another problem that arises from having an etched surface is either the necessity of adding a micro-mirror and not relying on the actuator surface for reflection or reduce the usable area, by flipping it, due to the free face shape change. Design changes have been made, in terms of shape, it being improved after experimental surface measurements, resulting in an easy to fabricate, chamfered edge patch micro-actuator.

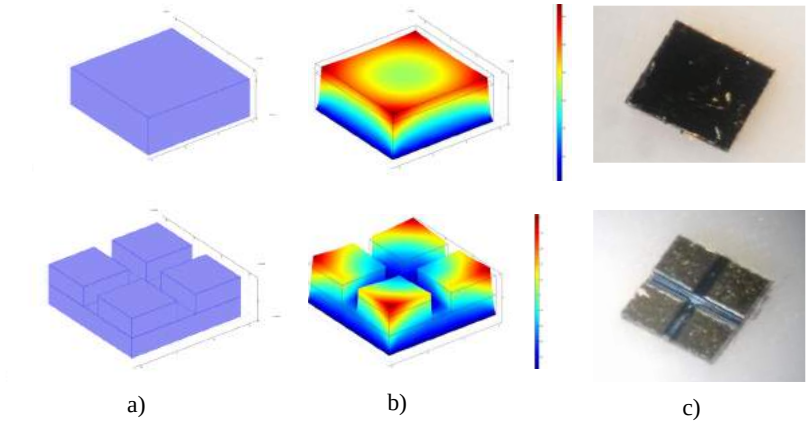

Figure 4.12: PMN-PT based micro-actuator designs: a) Concept, b) Simulated behaviour (displaced) c) Cut samples.

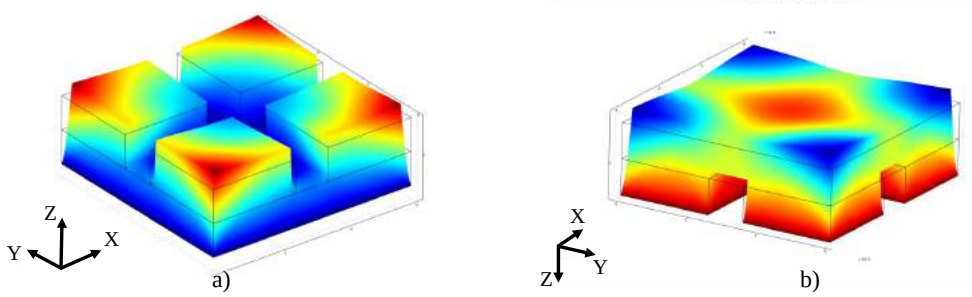

Figure 4.13: FEM results for an etched PMN-PT[001] actuator with either a) the flat face fixed or b) the etched one considered as fixed (the bottom face in both cases).

4.3.1.1/ THE TWO DERIVED SCENARIOS: FIXED-FREE AND FREE-FREE

For the actuator to be properly integrated, a soldering solution has to be found that doesn't limit the dynamics of the structure, nor does it affect the displacement capabilities. For this two scenarios are devised, schematically presented in Figure 4.14: a) **fixed-free**, where one actuator face is completely soldered and the other is left to move freely out of plane and b) **free-free**, where both faces are unrestricted.

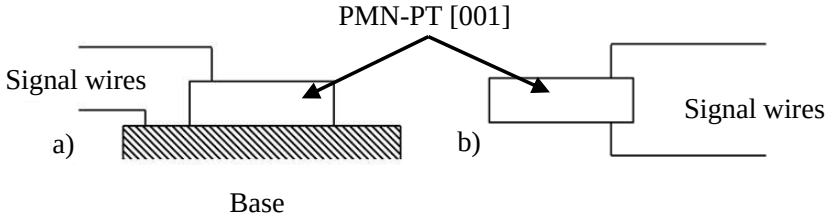

Figure 4.14: The two clamping/fixture scenarios a) Fixed-Free, b) Free-Free.

Preliminary measurements were done on a square $600x600x200\ \mu m^3$ (w_1, w_2, h) dimensioned actuator PMN-PT [001] actuator in order to validate both the displacement

expectations and the influence over the structure's dynamic response to the actuator. As seen in Figure 4.15 a one face soldered patch actuator (indicative of the fixed-free scenario) had a lower displacement than a suspended one of the same size and for the same applied electric potential (indicative of the free-free scenario). Looking at the system response when a step signal is applied $(200\ V)$ it observed that the increase in displacement is gained at a cost to the structure's stiffness. Figure 4.16 shows that, although the same material is used and the same voltage applied, the doubling in displacement comes with the structure damping time increase to a few seconds.

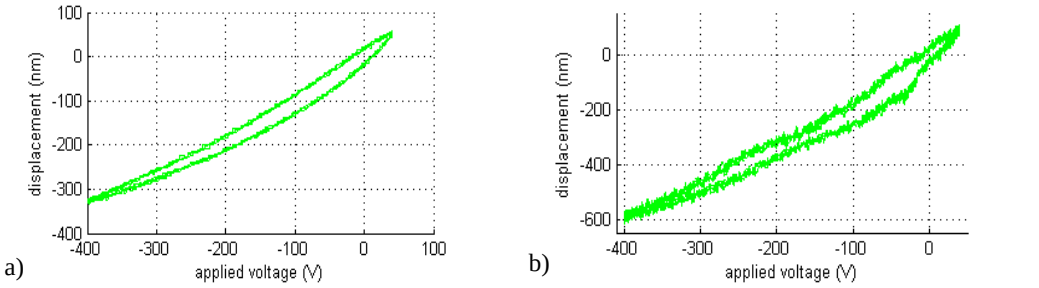

Figure 4.15: Preliminary displacement tests for the a) Fixed-Free and b) Free-Free scenarios.

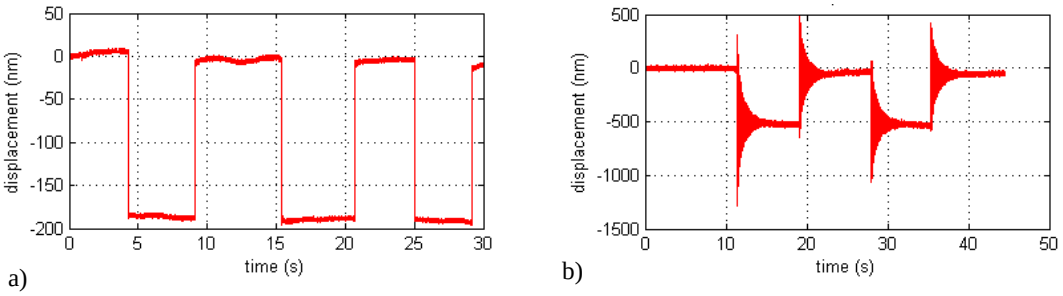

Figure 4.16: Step response for the a) Fixed-Free and b) Free-Free scenarios.

4.3.1.2/ INFLUENCE OF ACTUATOR PARAMETERS OVER DISPLACEMENT AND THE GENERATED SHAPE

Fully soldered face, varying width

Considering the dynamics requirements of the RFS-MOB, a structure that allows for large displacements and keeps the dynamic response above $5\ KHz$ is sought. Following the fixed-free one, the behaviour of the PMN-PT [001] actuator is studied so that there is a minimum dynamics compromise. Finite Elements Method (FEM) simulations show an interesting behaviour for the free surface of the actuator with the increase of its width. This is visible in Figure 4.17 where actuators with widths of a) $w_1' = 200\ \mu m$, b) $w_1'' = 500\ \mu m$ and c) $w_1''' = 800\ \mu m$ are compared side by side to point out the free face shape change. The more the width increases, the more complex the shape becomes, from a close to flat

surface, to a curved one , to another that has both flat regions and curved ones, for each of the aforementioned dimensions respectively. Another factor to take into consideration is that these surfaces get generated with the increase of the potential difference applied. This makes the ability to generate the minimum necessary displacement ($\lambda/2$) al lower voltages a high priority.

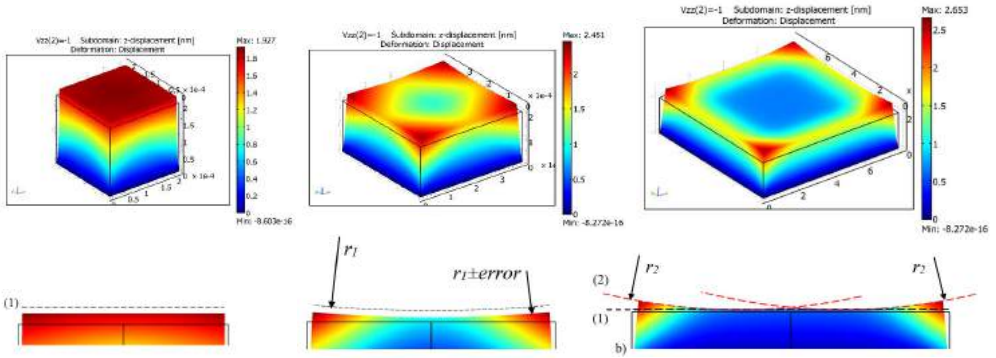

Figure 4.17: Isometric (top) and diagonal section (bottom) views for PMN-PT[001] based actuators. Free face shape change: a) close to a flat surface (1); b) rounder shape, close to an approximate sphere (radius r_1); c) complex shape: a planar surface at the centre (1) and spherical ones towards the corners (2) of similar radii r_2.

Fixed actuator size with varying soldering area influence over the displacement and shape of the free surface

A silicon support intended for use with the integrated PMN-PT actuator, as mentioned in previous section, has a maximum working surface of $675x800\ \mu m^2$ thus simulating actuators with widths $w_1 = w_2 \geq 700\mu m$ does not bring useful information. The displacement results at the centre and opposing corners of the free surface for a patch actuator measuring $600x600x200\ \mu m^3$ for which the soldering surface, positioned at the centre of the PMN-PT actuator, is varied between $100x100\ \mu m^2$ and $550x550\ \mu m^2$ can be seen in Figure 4.20. A separation in noticed between the points of interest for soldering areas between $100x100\ \mu m^2$ and $350x350\ \mu m^2$, with a reduction in centre displacement and an increase in the corner one(Figure 4.18). Continuing with the soldering surface augmentation,from $350x350\ \mu m^2$ to $550x550\ \mu m^2$, a downwards drift is then noticed, the level difference between the centre and the corners being stable although both values decreasing (Figure 4.19).

Fixture shape/design influence over the displacement and shape of the free surface

Changing the design of the fixture interface has a direct impact on the displacement generated by the PMN-PT actuator under potential difference. A preliminary example compares the results of simply changing the support structure from a flat surface to a matrix of peg supports for the same outer perimeter, arbitrarily chosen to have a width of $250\ \mu m$. Figure 4.21 brings together and compares the results in terms of displacement in the area of interest (centre) as well as the outer corners for a $600x600x200\ \mu m^3$ actuator.

As there is not only a gain in displacement noticeable at the centre, but also a more

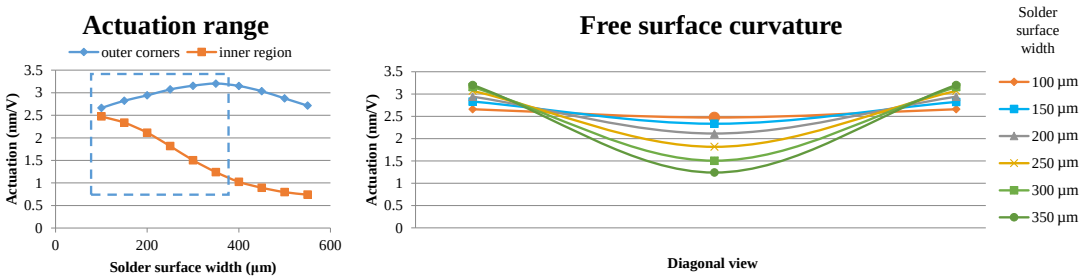

Figure 4.18: Free face shape change.

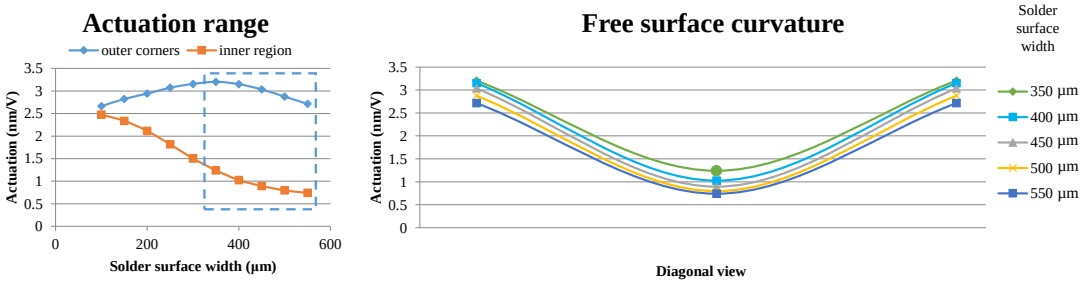

Figure 4.19: Free face displacement reduction.

Figure 4.20: FEM analysis results for displacement variation at the centre and outer corners of a PMN-PT [001] based actuator when the soldering surface is varied.

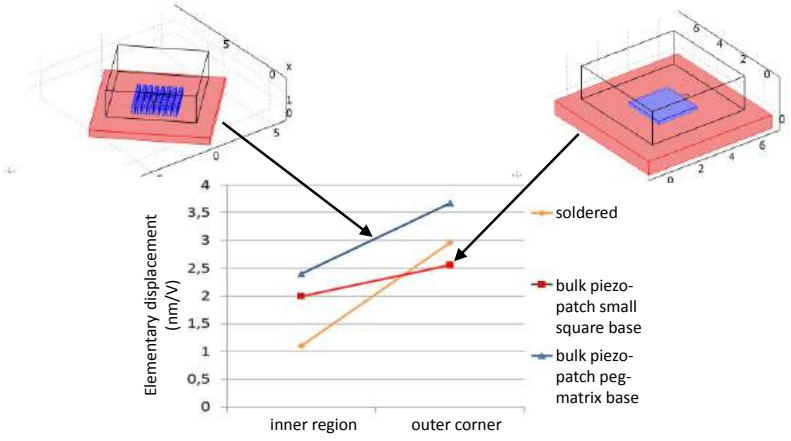

Figure 4.21: Fixture surface distribution influence over the PMN-PT[001] actuator displacement through the adoption of a matrix of support pegs.

accentuated level difference, a FEM simulation study follows in order to quantify the effect of the support pegs on the actuator surface. Figure 4.22 a) presents the schematic of one quarter of the actuator, since it has XZ and YZ plane symmetry, atop one peg for which height is varied alongside a diagonal cut through it highlighting the points of interest (Figure 4.22 b)). The results presented in Figure 4.23 point to a flexible support structure. This is due to the very high d_{31} and d_{32} piezoelectric coefficients of over $1050\ pm/V$ that

translates into large in-plane motion at the solder interface. Because the pegs act like

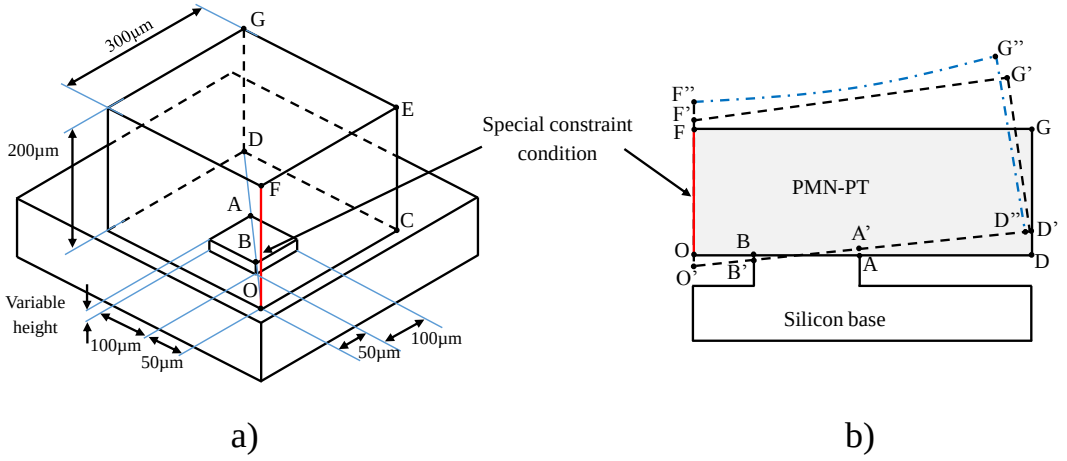

Figure 4.22: Schematic representation of the simulated PMN-PT actuator support.

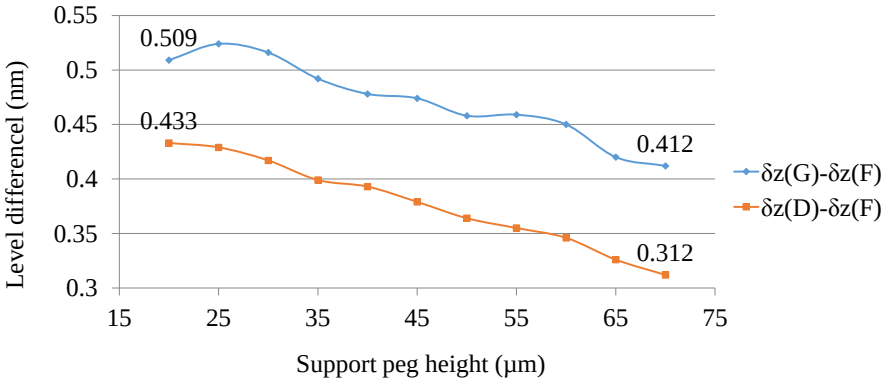

Figure 4.23: The influence of the lever effect with the peg height increases.

leavers, although the displacement at the centre increases, the one at the corners gets amplified even more. A solution is to continue increasing the peg height until the behaviour presented in Figure 4.24 is achieved. This would bring the actuator behaviour closer to the Free-Free scenario. This is, however, not feasible as it would drastically reduce the system dynamics, would make the structure unstable and would greatly increase the fabrication difficulty. The solution is the replacement of the rigid soldering - flexible structure combination to a conductive elastic solder that allows for in plane movement while is resistant to shearing. A silver-based EPO-TEK® H22 adhesive was chosen as it has been shown in [Siewert et al., 2002] that silver based solders can have a relative elongation of up to 31% while still retaining their conductivity.

Another benefit of using an elastic solder is that the curing procedure induces a compression force in the solder layer itself, one that acts parallel to the actuator surface. This is beneficial as it aids to the residual in plane displacement caused by the high negative values of both d_{31} and d_{32} piezoelectric coefficients. Direct results count not only the reduction of the free surface curvature but also of overall aberrations.

The resulting shape of the free surface under applied voltage can be further improved by changing the micro-actuator profile. By chamfering the sides of the PMN-PT

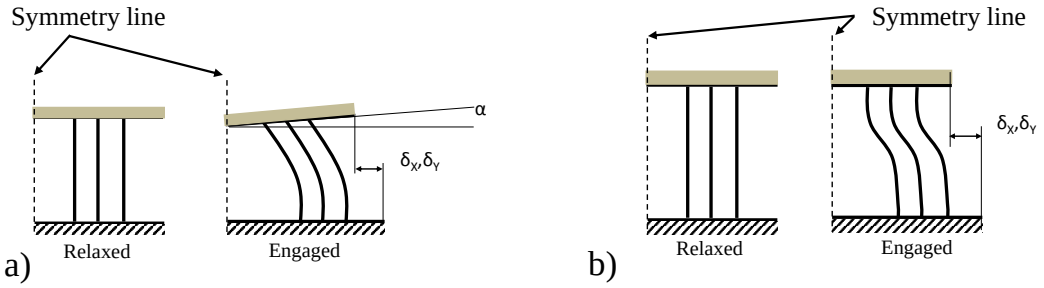

Figure 4.24: Support structure influence on the actuator displacement and the desired in-plane movement. a)If the support pegs are too short then the contraction generated in the XY-plane will act to generate a lever effect and lift the sides of the actuator; b)the peg structure hight needs to increased until the actuator contraction does not create the lever effect. This type of support would make the structure unstable and large

patch actuator the free surface area gets reduced and will deform less. This is due the in-plane contraction of the micro-actuator being dependent on the amount of material available (from the base W towards the top w). This behaviour is exemplified in Figure 4.25 with the aid of same-level displacement lines (the red and black dotted lines correspond to the same displacement levels). FEM simulations also point towards another benefit of changing the profile and that is the achievement of higher displacement at the centre.

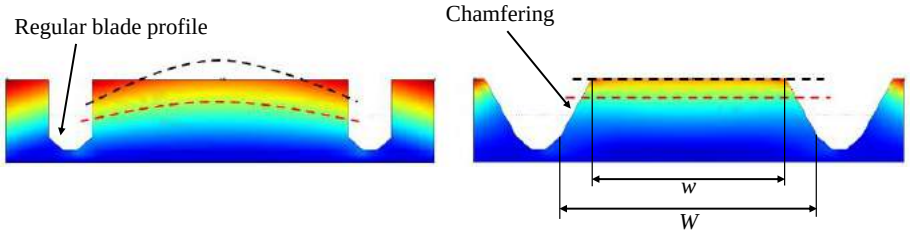

Figure 4.25: PMN-PT [001] actuator profile change and the displacement distribution.

4.3.1.3/ STATIC AND DYNAMIC BEHAVIOUR

The behaviour of the PMN-PT [001] actuator under different working conditions is analysed. In order to have reliable measurements, separation between samples is required. This is achieved by ensuring the conductive solder film allows for the samples to be cut as depicted in Figure 4.26. This allows for the solder to be used as a common electrode, while the top faces of the independent actuators are available for wire bonding and can be connected individually. First a **static** analysis is undertaken in order to better characterize the actuator free surface displacement and shape. This is of high importance as in **dynamic** work modes the quality of the signals is very dependent on the PMN-PT actuator behaviour.

Static behaviour

The PMN-PT[001] actuator has one face soldered to a glass baseplate using a silver based conductive adhesive and the opposing face free to move and covered with a

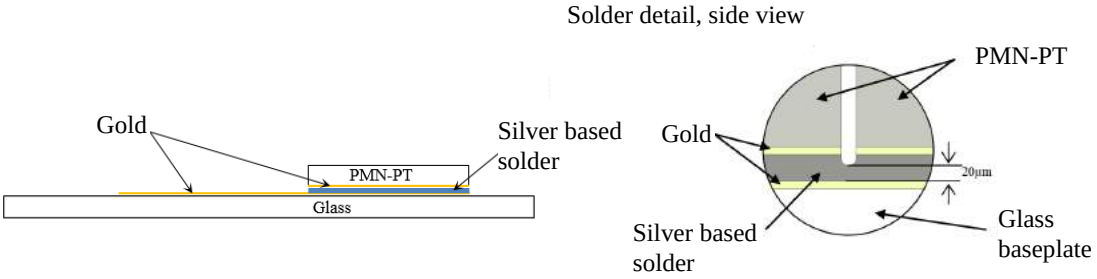

Figure 4.26: Adhesive and thickness solution, the sample separation.

gold electrode presenting mirror qualities (due to the optical finish cut PMN-PT crystals have). To do this a change was made from a regular interferometer (like the one used in the preliminary measurements) to a MEMS analyser, specifically a Polytec MSA-500 Micro Systems Analyser ©. The connection to the power source is made possible throw a gold wire soldered to the free surface with a low temperature wire-bonding procedure. Although the MEMS Analyser laser beam measures only $10\mu\ m$ in diameter, a relatively small dot matrix for measurements was chosen, specifically a $7\ x\ 7$ dots for the cut actuators with sizes between $800\ x\ 800\ \mu m^2$ and $400\ x\ 400\ \mu m^2$. In Figure 4.27 different size actuators with the dot matrices can be seen. They are laid by the MEMS Analyser software and can be manually repositioned. Measures can be independently made by selecting specific dots. All measurements were done automatically by moving through the

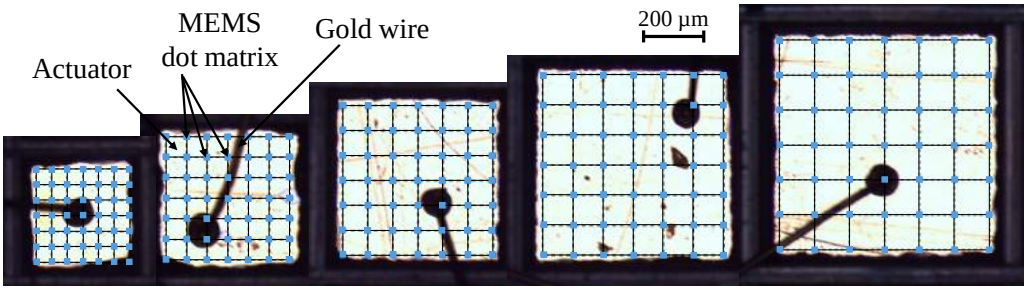

Figure 4.27: PMN-PT patch actuators as viewed through the MEMS Analyser camera, along the Z axis. Size increases by $100\ \mu m$ from $w = 400\ \mu m$ to $w = 800\ \mu m$, from left to right

specified points while also having one manual measure in the start point at the end of one complete automated measure. The applied command follows a sine wave of $f = 3\ Hz$ with a peak-to-peak amplitude $A = 400\ V$ with a shift of $200\ V$ as to keep the actuation unipolar. Figure 4.28 presents the experimental setup with detailed views of the Polytec MSA-500 MEMS analyser as well as one for the PMN-PT micro-actuator. The measurements were then used to generate a mesh surface of the actuator. Although PMN-PT [001] has very high values for the d_{31} piezoelectric coefficient directly after fabrication (crystal growth) by applying a high temperature repoling procedure a gain of close to 60%, as presented in Figure 4.29. $400\ V$ were applied to the bulk PMN-PT micro-actuators while placed in an oven that was then heated up to $200\ \deg C$ in 60 minutes, kept there for 30 minutes and then allowed to cool down to room temperature for $90 - 120$ more minutes before reducing the voltage to zero. Although there is a visible gain in displacement two other

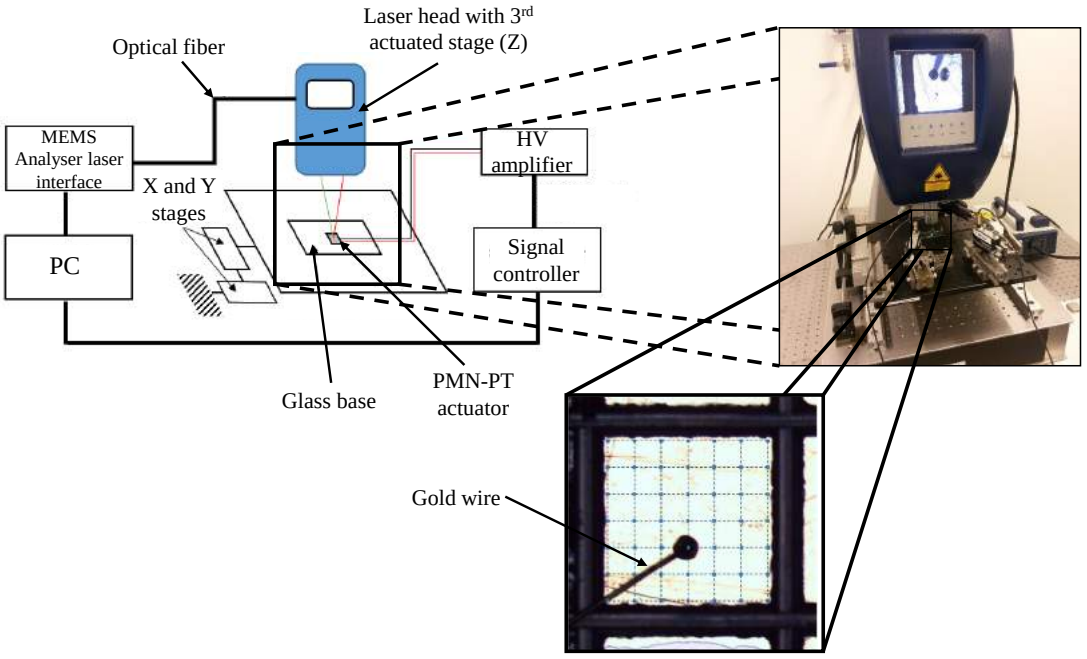

Figure 4.28: Experimental PMN-PT micro-actuator surface analysis setup using a Polytec MSA-500 Micro Systems Analyser ©.

features stand out: the loss in linearity of the voltage to displacement curve i.e. saturation is reached at lower voltages and there is an increase in nonlinearities like the hysteresis value reaching 11% from a low of under 6%. Even with this close to twofold increase in hysteresis, PMN-PT is still situated at close to half of PZT (with values between 18% and 22%). The measurements of repoled actuators are then compared with the simulated results in terms of curvature through the displacement along the diagonal of the PMN-PT patch actuator as can be observed in Annex D.1. Bringing together the displacement

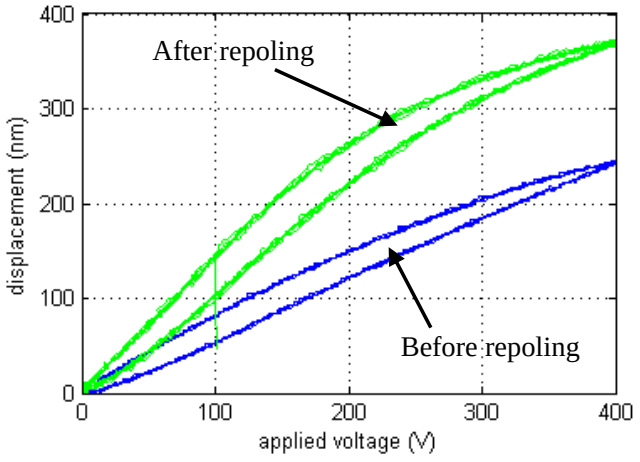

Figure 4.29: Displacement gain following a high temperature repoling procedure.

values for actuators with widths between $400\ \mu m$ and $800\ \mu m$ in the areas of interest i.e.

centre region and corners for both measurements and the FEM predictions, although the trend is similar, it is clear that the actuator size will have an impact on the voltage value at which the minimum required displacement ($\lambda/2$) is reached. These values are pre-

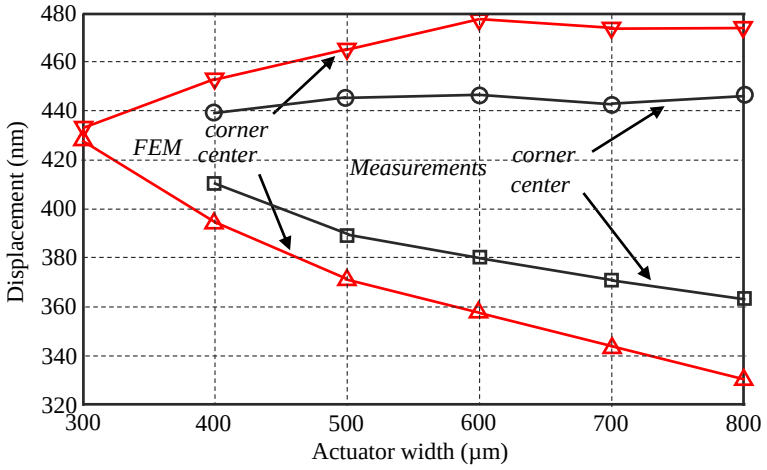

Figure 4.30: Comparison between displacement values in the interest region (centre) and outer corners.

sented in Annex E.1, alongside the schematic of how the maximum laser beam diameter is considered.

By shaping PMN-PT[001] in the presented manner and using an elastic solder to take advantage of its high piezoelectric coefficients, the usable micro-actuator surface is maximized for laser beams reaching diameters close to the actuator free face width. For a fully flat moving surface a similar elastic solder can be used to attach a Si micro-mirror.

Dynamic behaviour

In terms of dynamics, PMN-PT[001] presents very high resonance modes. The experimental values were found also with the aid of the MEMS Analyser. For a rectangular shaped patch actuator measuring $600\ x\ 600\ x\ 200\ \mu m^3$ the first mode was found at $2.7\ MHz$, in the same Fixed-Free scenario while having the same soldering solution.

For an integrated actuation solution, different size actuators were sandwiched between Si plates as to simulate working conditions for PMN-PT when a micro-mirror is added. As the available surface, in the case of the proposed RFS-MOB, is $800\ x\ 675\ \mu m^2$ only three sizes were considered: $400\ x\ 400\ \mu m^2$, $500\ x\ 500\ \mu m^2$ and $600\ x\ 600\ \mu m^2$. Figure 4.31 presents the proposed experimental sample and the manufactured one. The

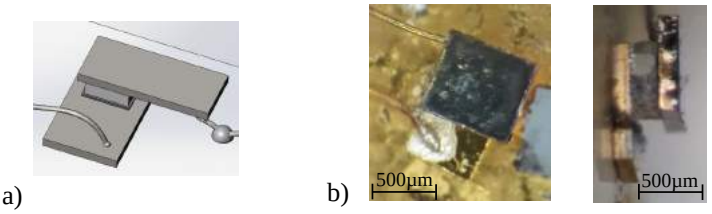

Figure 4.31: PMN-PT experimental sample for an integrated micro-mirror actuation: CAD design and fabricated samples.

experimental measures results do show a reduction of the resonance frequency of close to 0.5 MHz, but even by varying the width of the actuator, the first mode is stable at $2.19\ MHz$, as seen in Figure 4.32.

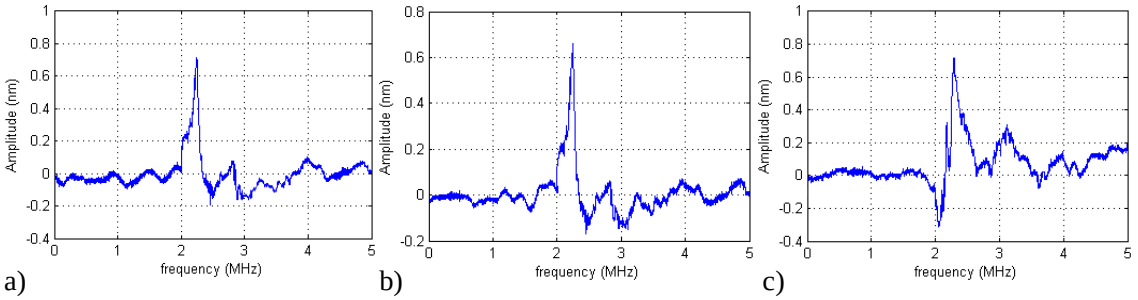

Figure 4.32: Experimental dynamic response for PMN-PT patch actuators dimensioned at a) $400\ x\ 400\ \mu m^2$, b) $500\ x\ 500\ \mu m^2$ and c) $600\ x\ 600\ \mu m^2$.

4.3.2/ CONCLUSION

PMN-PT [[001] shows high potential for micro-mirror actuation as an integrated solution while is fulfils displacement needs as well as being easily prefabricated and integrated in the proposed RFS-MOB design. The simple fabrication has the added benefit of not requiring clean-room techniques. The displacement values of over $400\ nm$ for the designed actuator further demonstrates the level at which the very high piezoelectric coefficients (d_{33} for the longitudinal effect) can be exploited in less than ideal, in-plane freedom ensuring soldering conditions. The very high dynamic response of PMN-PT [001] makes it a likely candidate for multiple high-frequency applications, restrictions being imposed only by the integrating structure.

4.4/ FABRICATION OF A RFS-MOB COMPATIBLE ELEMENT ENCOMPASSING PMN-PT [001]

In order to prove the large displacement and very high frequency capabilities of PMN-PT as an integrated actuator, as well as its low hysteretic behaviour, an element compatible with the MIOP project proposed RFS-MOB was fabricated.

4.4.1/ TECHNIQUES USED FOR FABRICATING THE FINAL STRUCTURE

Several techniques were used in the process of integrating the PMN-PT patch microactuator to a Si holder of the RFS-MOB and will be detailed here:

Electrode deposition

In order to ensure a uniform field distribution through the PMN-PT actuator, the quality of the electrodes is of high importance. By using a Plassys MP500 Metal Sputtering System©), a previously cleaned PMN-PT plate was covered with a Cr-Au electrode

with thickness of $30\ nm$ and $140\ nm$ respectively. the thickness of the gold layer was chosen as to be sufficient for the wire bonding procedure.

Saw dicing

For the RFS-MOB compatible Si element, several techniques were employed, the order of which is laid out in Annex F.1. Like with PMN-PT[011], used for the micro-gripper presented in Chapter 3, PMN-PT[001] can also be prepared using a saw dicing machine. Different width blades were used to observe the impact over the fabrication procedure while maintaining the same $30000\ rpm$ and advancement speed of $0.3\ mm/s$. The chamfered profile presented in a previous section was obtained by using a $200\ mum$ wide trapezoid tipped blade.

Soldering

There were two types of soldering involved in the fabrication of the demonstrator: **silver based soldering**, for the fixture of both the PMN-PT actuator to the Si holder and for the Si micro-mirror placed atop the micro-actuator and a **wire-bonding technique** used for the electrical connections needed between the top electrode of the actuator and the supporting structure. Both of these soldering techniques are exemplified in Figure 4.33. While the silver solder can be applied at room temperature and fast-cured in

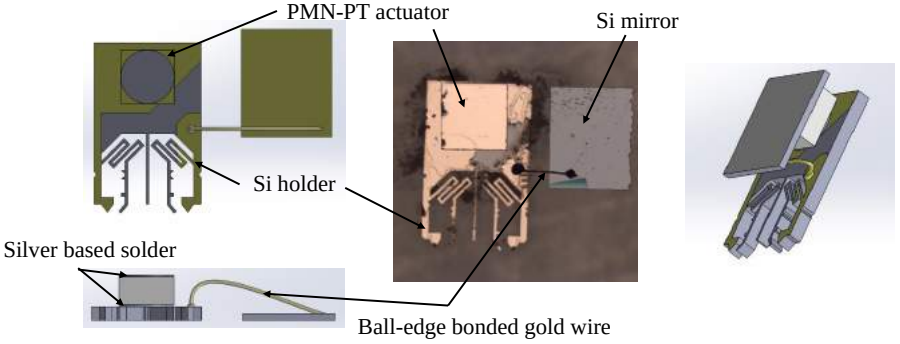

Figure 4.33: Where the two soldering techniques are used in the fabrication of an intermediate experimental prototype for the RFS-MOB compatible Si element.

an oven at temperatures low as $80\deg C$, for the wire bonding technique a Wire bonder TPT16© machine was used. The $35\mu m$ in diameter gold wire was bonded at the chosen temperature of $70\deg C$ for a ball-wedge (exemplified in Figure 4.34) tip measuring 200μ m for its exterior diameter.

4.4.2/ THE ACTUATOR AND THE FINAL STRUCTURE

The final prototype needs to be compatible with the existing RFS-MOB design and thus, in order to integrate the PMN-PT actuator some preparations had to be made. All these steps are enumerated schematically in Annex G.

First, Si micro-mirrors were fabricated by recycling $50\ \mu m$ thick RFS-MOB elements. Micro-mirrors measuring $800\ x\ 675\ \mu m^2$ resulted. Along with $100\ \mu m$ thick Si holders they were thermally coated with a $1\ \mu m$ thick oxide by being placed in an oven at $1200\ \deg C$. This was done in order to ensure the safety from short circuits later on in

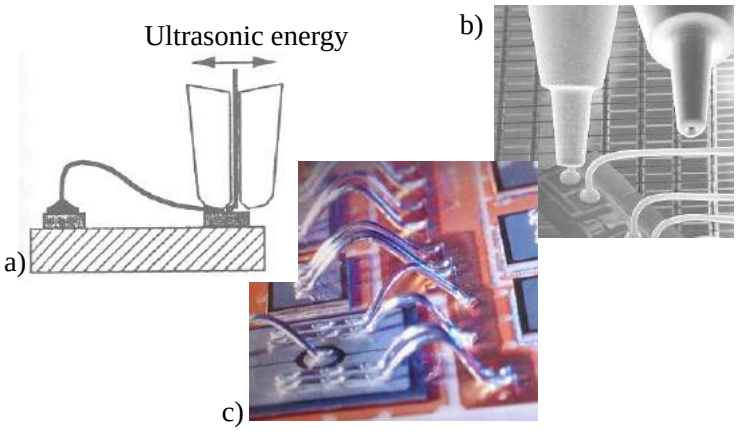

Figure 4.34: The ball edge procedure for wire bonding (a) with an Electron Microscope image of teh cone shaped tip (b) and an exemplifing picture of complete wire-bonded circuit (c).

the fabrication procedure. Then the acetone and ethanol cleaned micro-mirrors were coated with a Cr-Al layer for a mirror finish. The Si holders were then glued to a glass plate and a mechanical mask placed on top in order to generate two electrodes on its surface. The now Cr-Al coated micro-mirrors were flipped and placed by the holder so that a GR-Au electrode could be made. Using the EpoTek® H22 silver based solder the PMN-PT actuator was placed in contact with the larger electrode, making sure it does not connect with the smaller available electrode. Figure 4.35 presents the three different size cut micro-actuators soldered to the Si holder. After the curing procedure a gold wire is bonded using the ball-edge technique, connecting the small electrode and the micro-mirror. This is needed so that when flipped on top of the structure, the micro-mirror can be soldered to the PMN-PT patch actuator. Finally, the whole structure

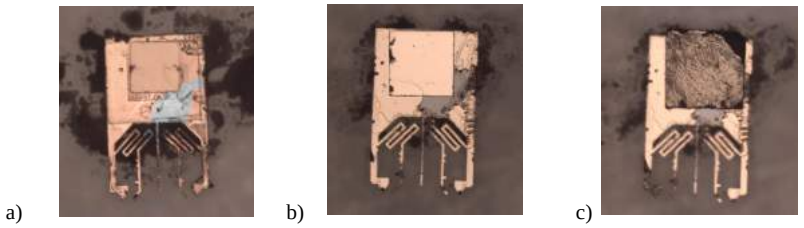

Figure 4.35: Si holders with the three sizes of PMN-PT[001] cut micro-actuators $400\ x\ 400\ \mu m^2$ (a), $500\ x\ 500\ \mu m^2$ (b) and $600\ x\ 600\ \mu m^2$ (c).

(smart RFS-MOB element) can now be placed inside a RFS-MOB configuration in a vertical position, having an integrated PMN-PT[001] micro-actuator capable of out of plane displacement.

4.4.3/ PROTOTYPE DESCRIPTION AND PERFORMANCES

The completed structure was set on a test rail for both static and dynamic measurements. The command signal is delivered to the actuator through the two support legs by soldering

wires at their base. The measurements were done with a SIOS® SP-120 interferometer connected to a dSpace®, used also for data acquisition, as seen in Figure 4.36. Scanning Electron Microscope (SEM) acquired images of the structured used in the experiment are presented in 4.37, highlighting in the dimensions and making the profile of the actuator visible in the close-up.

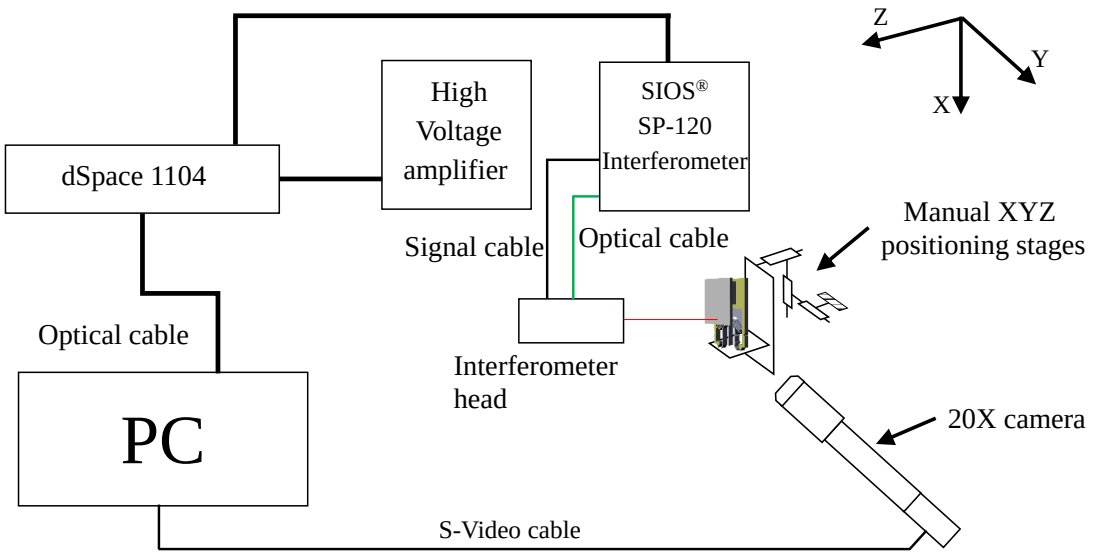

Figure 4.36: Experimental setup for static and dynamic measurements of an RFS-MOB compatible silicon holder with integrated PMN-PT actuated micro-mirror.

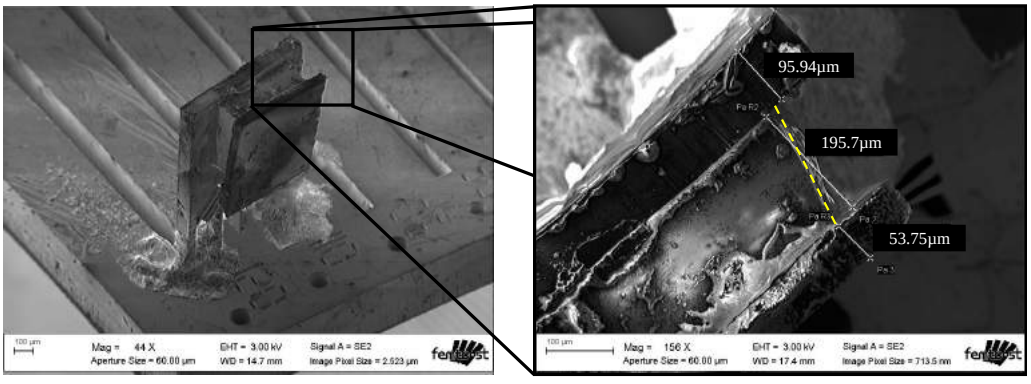

Figure 4.37: SEM images of the prototype active element with a close up of the elements and their thickness. The dashed line highlights the PMN-PT actuator profile.

Static behaviour

The measuring setup presented was used as the structure is now in a vertical configuration and the displacement is out of plane. The measurements were obtained by ap-

plying a sine actuation signal with a frequency $f = 3\ Hz$ for $3s$ and having a peak-to-peak amplitude $A = 400\ V$ and a $200\ V$ shift, in the positive front, to keep the unipolar actuation solution. The results shown in Figure 4.38 are a comparison of the static measurements between the sandwiched PMN-PT actuator (intermediate stage where a PMN-PT actuator was soldered between two silicon plates - Figure 4.31) and the PMN-PT actuator integrated in the final prototype.

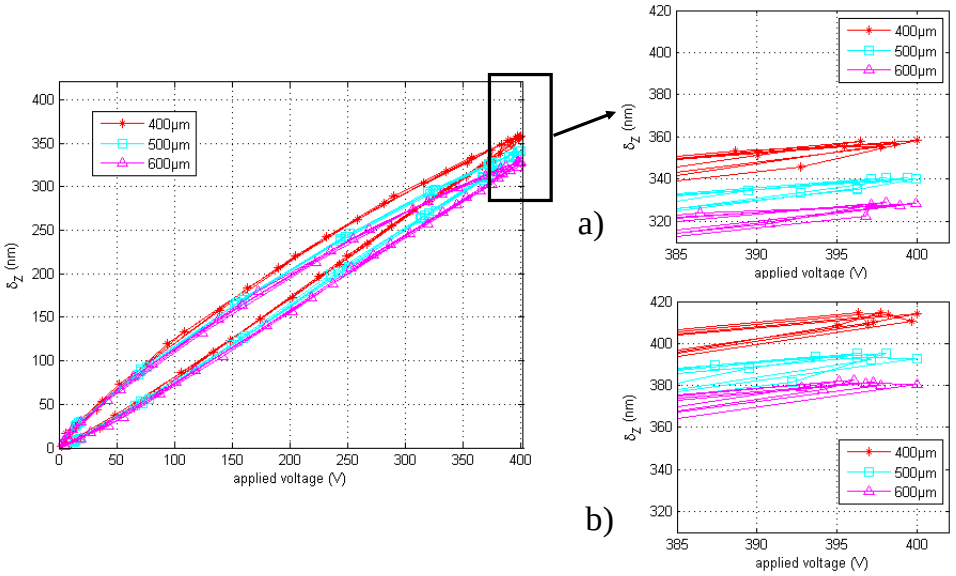

Figure 4.38: Displacement curve, measured at the centre, for a $400x400\ \mu m^2$, a $500x500\ \mu m^2$ and a $600x600\ \mu m^2$ integrated PMN-PT actuator. a) presents the displacements measured on the prototypes, while b) presents the measurements done on the *Fixed-Free* PMN-PT actuator.

Although there is a decrease of maximum 14% between the *Fixed-Free* PMN-PT actuator and the integrated one, the required minimum limit is surpassed (especially for the smaller dimension actuators), making this a viable solution for micro-mirror actuation where the reflective surface needs to remain planar or when a specific coating needs to be applied.

Dynamic behaviour

As the integrating structure has a much lower resonance frequency then just the PMN-PT actuator, at around $12\ KHz$ (value found using FEM simulations) it is expected that the final silicon holder will have it's first mode close to this frequency. By applying an electrical Dirac signal $(10\ V)$ to the PMN-PT actuator the first 5 modes were found (Figure 4.39). This confirms that the smart RFS-MOB element can be used as part of either an interferometer or a vibrometer as the dynamic work modes of these devices are in the $5 - 6\ KHz$ bandwidth.

The experimental setup involves soldering the prototyped RFS-MOB compatible element to the guiding rail. Signal carrying wires are soldered in the same points. This makes the structure gain stiffness in comparison to the spring-only fixed silicon holder. In a real-case scenario, the fixing solder can be added after the positioning and alignment of the actuated mirror incorporating holder. The first mode is situated at $\backsim\ 10.5\ KHz$. Although this is $20\ \%$ lower than FEM predictions, it is still double the minimum frequency

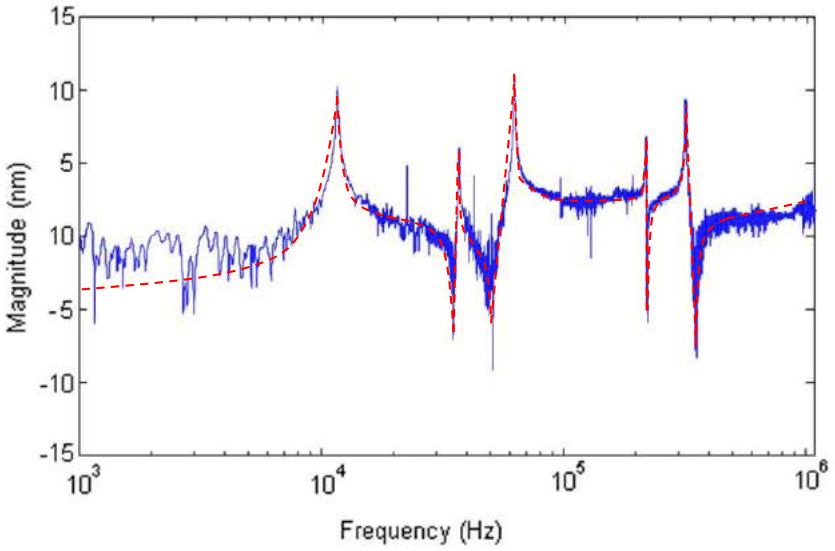

Figure 4.39: Frequency response for a silicon smart RFS-MOB element integrating a $400x400\ \mu m^2$ PMN-PT actuator.

required in interferometry or vibrometry. Figure 4.40 compares the experimental values with those resulted from two FEM software SolidWorks® Simulations© and Comsol®.

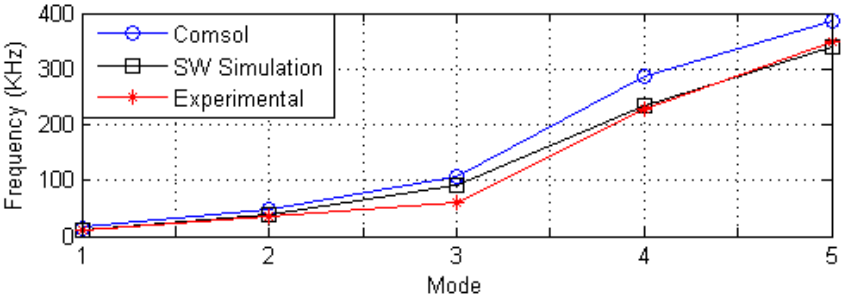

Figure 4.40: Comparison of the first 5 modes of an RFS-MOB with an integrated $400x400\ \mu m^2$ PMN-PT actuator between FEM simulations and experimental results.

The results enforce the hypothesis that the dynamics of the final product are directly influenced by the integrating structure, as PMN-PT is able to work at frequencies in the MHz region ($> 2.2\ MHz$).

4.5/ CONCLUSION

In this chapter PMN-PT has been investigated as a potential material to be used for an integrated actuator for displacing a micro-mirror on a holder compatible with the RFS-MOB designed by [Bargiel et al., 2010] at Femto-ST. As it uses the longitudinal effect, the forward model provides a good prediction of the displacements PMN-PT [001] is able to generate, in close to ideal conditions.

Considering the size restrictions of $800x675\ \mu m^2$ maximum surface and the displace-

ment requirements of more than $325\ nm$ ($\lambda/2$ of visible red light) with a maximum surface aberration limit of $32.5\ nm$ ($\lambda/20$), PMN-PT [001] proves to be a well suited candidate as it is able to generate the required displacement while used in bulk, for a $200\ \mu m$ thick layer. Another application imposed requirement is the balance between the very high dynamics of PMN-PT [001] (above $2.2\ MHz$) with the displacement limiting fixture. The proposed solution involves both using a silver based solder, for surpassing the $325\ nm$ limit, and altering the profile of the actuator, for reducing the surface aberrations.

The low non-linearities behaviour of PMN-PT [001] (hysteresis of under 6%) demonstrate the benefits this smart material brings to MOEMS (micro-mirror actuation) as it is easy to integrate in existent optical structures, such as the proposed RFS-MOB compatible silicon micro-mirror holder. A prototype has been fabricated and tested with successful results.

5

CONCLUSION AND FUTURE WORKS

This PhD thesis has addressed high performance smart materials that are not only suitable for micro-robotics but also MOEMS integration. The PhD work is encompassed by two projects, the Romanian funded ADMAN and the French funded MIOP, each tacking with one aspect of the micro-world: micro-manipulation using novel actuation principles and actuator integration in MOEMS devices, respectively. At the micro-scale, the functional requirements keep ever increasing. Many involve high dynamics, precision and high integration.

This PhD work has proposed to investigate PMN-PT as the piezoelectric material presenting specificities that make it a suitable candidate for both types of applications: as an integrated microgripper actuator (ADMAN) and as a MOEMS, RFS-MOB compatible, integrated micro-mirror actuator (MIOP). The specific cuts were chosen, the anisotropic [011] cut for beam flexural actuation and the regular uniaxial [001] cut for maximum longitudinal actuation. The contributions of the work will be detailed by chapters, after which some perspectives will b presented. The current stage in micro-robotics and complex micro-systems, both MEMS and MOEMS, coupled with the ever increasing variety of materials available point toward better accuracy and performances. Although there are limitations caused by the size reduction, in terms of the fabrication of systems that incorporate multiple functions, the development and understanding of smart materials in general and of piezoelectric ones in particular, direct to micro-robotic systems.

5.1/ CONTRIBUTIONS OF THE WORK

These systems can be fabricated easier and can themselves be more precise and fast in the assembly of multi-dimensional (3D) micro-structures. The limitations imposed by the two encompassing projects, large displacement and multiple DoFs for an actuator usable in micro-robotics (3 DoF per microgripper arm), or displacement at frequencies over $15\ KHz$ of more than $325\ nm$ (red light $\lambda/2$) for MOEMS compatible actuators, are tackled through the material choice. For the properties it presents, PMN-PT is chosen.

PMN-PT offers a wide diversity, through crystalline orientation, of piezoelectric capabilities and electro-mechanical properties. Not only can it be manufactured with techniques very specific to its end use, but it can also be grown in large crystals with good control over the bicomposite ratio. This is highly important as depending on that ratio and the orientation of the cut in relation to the crystalline growth, PMN-PT can exhibit very different behaviours and is capable of generating different types of displacement

like flexure, longitudinal or shearing, each beneficial for very specific applications. This benefit is only augmented by the fact that PMN-PT exhibits very high piezoelectric and mechanical coefficients, thus reducing the complexity of some systems or simplifying the manufacturing procedures of different integrated actuators and their encompassing systems. A dedicated experimental setup has been developed to measure these piezoelectric coefficients on manufacturer precut PMN-PT plates. Values of $2520\ pm/V$ (for d_{33}), which concur with literature, have been measured on PMN-PT[001] plates and a positive $476\ pm/V$ (for d_{31}) value measured on PMN-PT[011]. Previoulsy found coercive field values have also been confirmed and a control approach has been implemented, to thus protect against depoling. It thus presents itself as a candidate with high potential regarding the integrability and displacement requirements set by the two encompassing projects: PMN-PT[011] for a cantilevered actuator suitable for the ADMAN project and PMN-PT[001] for an integrated, patch micro-mirror actuator suitable for the MIOP project.

In the third chapter, the model used for predicting the PMN-PT based cantilever behaviour is first presented and then verified through experimental measurements. Given the much more linear behaviour of PMN-PT, in comparison to other, more traditional piezoelectric materials, such as the popular PZT piezo-ceramic, complex trajectories can be generated, without the need of closed loop controllers.

PMN-PT[001] proves to be a well suited candidate for a large-stroke, integrated actuation solutions. It has a high enough d_{31} piezoelectric coefficient to add a 3rd degree of freedom to a generic duo-bimorph cantilever actuator. As noted from the flexural beam actuator integration, it offers large displacements along all axes: over $650\ \mu m$ along the Z-axis, over $460\ \mu m$ along the Y-axis and over $40\ \mu m$ along the X-axis, for a 25 x 0.6 x $0.41\ mm$ beam, more than double what a similarly dimensioned PZT beam generates along the Z and Y axes and adds usability alon the X-axis. This is achieved while having a very low hysteresis ($\approx 6\%$), more than three times lower than PZT ($\approx 18-20\%$)as it is demonstrated by the describing of complex trajectories with the tip of the PMN-PT duo-bimorph. The proposed experimental trajectories vary with under 4% error from the intended, theoretical ones. The forces generated are comparable to hard PZT cantilever actuators of similar dimensions: over $22\ mN$ along the Z-axis, over $16\ mN$ along the Y-axis and over $48\ mN$ along the X-axis. The presented PMN-PT specific Voltage and Force to displacement model is in very good agreement with the experimental results.

As it can be integrated using simple, current, non-cleanroom, micro-fabrication techniques, PMN-PT [001] was successfully integrated in a microgripper, the capabilities of which have been demonstrated through a pick-and-place manipulation task.

In the fourth chapter, PMN-PT has been investigated as a potential material to be used for an integrated actuator for displacing a micro-mirror on a holder compatible with the RFS-MOB designed by [Bargiel et al., 2010] at Femto-ST. As it uses the longitudinal effect, the forward model provides a good prediction of the displacements PMN-PT [001] is able to generate, in close to ideal conditions.

Considering the size restrictions of 800 x $675\ \mu m^2$ maximum surface and the displacement requirements of more than $325\ nm$ ($\lambda/2$ of visible red light) with a maximum surface aberration limit of $32.5\ nm$ ($\lambda/20$), PMN-PT [001] proves to be a well suited candidate as it is able to generate the required displacement while used in bulk, for a $200\ \mu m$ thick layer. Another application imposed requirement is the balance between the very high dynamics of PMN-PT [001] (above $2.2\ MHz$) with the displacement limiting fixture. The proposed solution involves both using a silver based solder, for surpassing the $325\ nm$

limit, and altering the profile of the actuator, for reducing the surface aberrations.

The low non-linearities behaviour of PMN-PT [001] (hysteresis of under 6%) demonstrate the benefits this smart material brings to MOEMS (micro-mirror actuation) as it is easy to integrate in existent optical structures, such as the proposed RFS-MOB compatible silicon micro-mirror holder. A prototype has been fabricated and tested with successful results.

One of the main contributions of the PhD is the gain in dexterity while reducing the complexity of a microgripper by using PMN-PT. Another main contribution is the addition of a smart, RFS-MOB compatible silicon holder by integrating a PMN-PT actuator, thus increasing the functionality of the optical bench (interferometry, spectrometry etc.) The presented perspectives are some examples of works which would improve several research topics in the coming years.

5.2/ FUTURE WORKS

This work has proposed solutions for integrated actuation by using a novel piezoelectric material called PMN-PT due to its high performances and easy machining. The preliminary results enable several perspectives in both micro-gripping usage and MOEMS integration.

During this PhD, PMN-PT has been investigated in order to quantify its usability as an integrated actuator. Some of the goals involve the usage of PMN-PT[011] as microgripper actuator that enables for more types of motion to be generated with the presented duo-bimorph configuration, such as rotation along the actuator length. Another goal is the development of a multi-DoF control that's able to take advantage of PMN-PT in its partial bipolar actuation without risking repoling. For the integration of the [001] cut, a more streamline procedure for integration needs to be developed, as well as improving the model to better fit the experimental results.

Considering the optical properties the PMN-PT crystal has and which has been investigated by [Tong et al., 2009] and [Wei et al., 2012], actuators can be developed that use these properties for displacement sensing. A schematic is presented in the Figure 5.1 to how this might be approached.

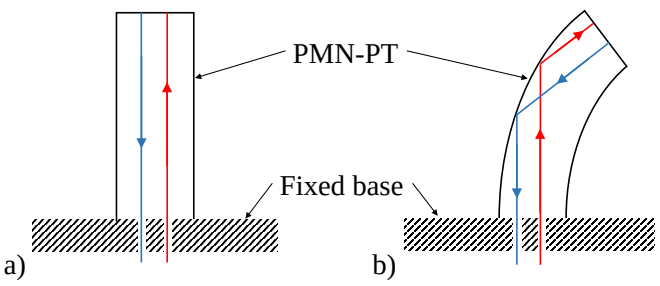

Figure 5.1: Laser based deflection sensing through a PMN-PT beam actuator where a) is the equilibrium position and b) is the deflected one.

Despite the very high performances of this monocrystal piezoelectric material, there is no definitive work on a model that describes how it behaves according to the PMN to PT ratio, the crystalline orientation or the mechanical behaviour. Although this PhD has tackled with some of the aforementioned issues by investigating the differences in actuation between the [011] and the [001] cuts, such as the different values at which each one start to be repoled and how that affects displacement and the control used, future works will focus on extending the knowledge base even more, especially in the mechanical behaviour of the monocrystal.

In terms of MOEMS, apart for streamlining a fabrication procedure in which the PMN-PT is used as the integrated actuator, new works regarding thin film actuators can be envisioned. Such works would involve an analysis on the minimum thickness at which PMN-PT can be used without piezoelectric properties losses, how to obtain such films, and how to stack them to create surface controlled micro-mirrors, in order to generate specific shapes. Figure 5.2 attempts such an approach that would have applicability in image correction and laser beam data losses.

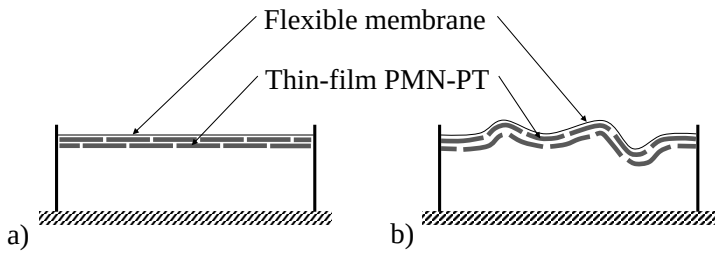

Figure 5.2: Mirror using PMN-PT thin-film actuator where a) is the equilibrium position and b) is the reshaped one.

I

ANNEXES

A

THE CZOCHRALSKI METHOD

1) Czochralski Method large crystal fabrication unit

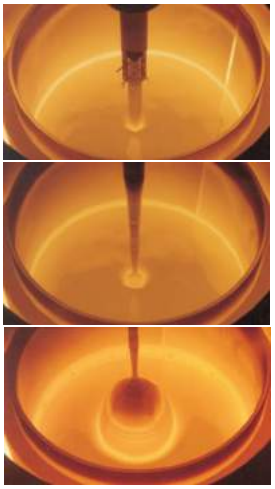

2) Crystal seed introduction and growth (as seen inside the crucible)

3) Mn doped PMN-PT single crystal

4) Other single crystals grown using the same method (all over 20mm in diameter)

Figure A.1: Czochralski Method specific details.

B

COEFFICIENTS TABLES

Properties	$\mathbf{s_{11}^E}$	$\mathbf{s_{12}^E}$	$\mathbf{s_{13}^E}$	$\mathbf{s_{33}^E}$	$\mathbf{s_{44}^E}$	$\mathbf{s_{66}^E}$
PMN-PT	52.1	−24.6	−26.4	59.9	16.0	28.3
PIN-PMN-PT	49.0	−20.0	−26.5	57.3	15.2	39.4
Mn:PIN-PMN-PT	45.4	−15.9	−28.1	62.4	15.4	27.8
Properties	$\mathbf{s_{11}^D}$	$\mathbf{s_{12}^D}$	$\mathbf{s_{13}^D}$	$\mathbf{s_{33}^D}$	$\mathbf{s_{44}^D}$	$\mathbf{s_{66}^D}$
PMN-PT	41.8	−34.8	−3.9	10.3	14.0	28.3
PIN-PMN-PT	38.2	−30.8	−4.0	10.3	14.3	39.4
Mn:PIN-PMN-PT	34.4	−26.9	−3.9	9.2	13.9	27.8
Properties	$\mathbf{c_{11}^E}$	$\mathbf{c_{12}^E}$	$\mathbf{c_{13}^E}$	$\mathbf{c_{33}^E}$	$\mathbf{c_{44}^E}$	$\mathbf{c_{66}^E}$
PMN-PT	12.4	11.1	10.4	10.8	6.3	3.5
PIN-PMN-PT	11.9	10.5	10.4	11.4	6.6	2.5
Mn:PIN-PMN-PT	12.8	11.1	10.8	11.3	6.5	3.6
Properties	$\mathbf{c_{11}^D}$	$\mathbf{c_{12}^D}$	$\mathbf{c_{13}^D}$	$\mathbf{c_{33}^D}$	$\mathbf{c_{44}^D}$	$\mathbf{c_{66}^D}$
PMN-PT	12.6	11.3	9.3	16.8	7.1	3.5
PIN-PMN-PT	12.3	10.9	9.0	16.7	7.0	2.5
Mn:PIN-PMN-PT	13.3	11.7	9.0	17.0	7.2	3.6

Figure B.1: Elastic compliance (s_{ij} measured in $10^12\ m^2/N$) and stiffness (c_{ij} measured in $10^{10}\ N/m^2$) constants respectively.

Properties	d_{33}	d_{31}	d_{15}	e_{33}	e_{31}	e_{15}
PMN-PT	1540	−699	164	22.3	−3.9	10.3
PIN-PMN-PT	1320	−634	105	18.6	−4.8	6.9
Mn:PIN-PMN-PT	1341	−609	133	16.8	−5.2	8.6
Properties	g_{33}	g_{31}	g_{15}	h_{33}	h_{31}	h_{15}
PMN-PT	31.8	−15.4	9.9	26.2	−8.4	7.0
PIN-PMN-PT	35.6	−17.0	8.8	28.9	−7.4	6.5
Mn:PIN-PMN-PT	39.7	−18.1	11.3	34.2	−10.7	8.3

Figure B.2: Piezoelectric coefficients, d_{ij} (pC/N), e_{ij} (C/m^2), g_{ij} $(10^3\ Vm/N)$ and h_{ij} $(10^8\ V/m)$.

Properties	k_{33}	k_{31}	k_{15}	k_t	k_{31} **(45 °C)**
PMN-PT	1540	−699	164	22.3	−3.9
PIN-PMN-PT	1320	−634	105	18.6	−4.8
Mn:PIN-PMN-PT	1341	−609	133	16.8	−5.2
Properties	ε_{33}^T	ε_{11}^T	ε_{33}^S	ε_{11}^S	
PMN-PT	31.8	−15.4	9.9	26.2	
PIN-PMN-PT	35.6	−17.0	8.8	28.9	
Mn:PIN-PMN-PT	39.7	−18.1	11.3	34.2	

Figure B.3: Electromechanical coupling factors, k_{ij}, and dielectric constants, ε_{ij} (ε_0).

C

BEAM FABRICATION PROCEDURE

1. Cleaning the PMN-PT plates with Acetone and Ethanol

2. Preparing of the EPO-TEK® H22 (4.5% epoxy)

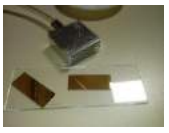

3. Cleaning the special shaped vacuum grip

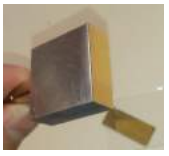

4. Aligning one layer with the special vacuum pump grip

5. Covering of the layer with a thin layer of EPO-TEK® H22

6. Cleaning the excess adhesive after pressing together (small circular motions) with the second PMN-PT layer

7. Repositioning (shifting) the layers to gain access to the common electrode and cleaning the visible EPO-TEK® H22

8. Placing the sandwiched PMN-PT layers on absorbent paper, atop an Al flat plate

9. Placing absorbent paper on top of the PMN-PT

10. Placing weights on the PMN-PT for an evenly thick EPO-TEK® H22 adhesive layer

11. Placing the PMN-PT inside an electric oven for EPO-TEK® H22 adhesive curing

Figure C.1: Fabrication procedure for the double PMN-PT ”sandwich”.

D

MICRO-ACTUATOR SURFACE CURVATURE

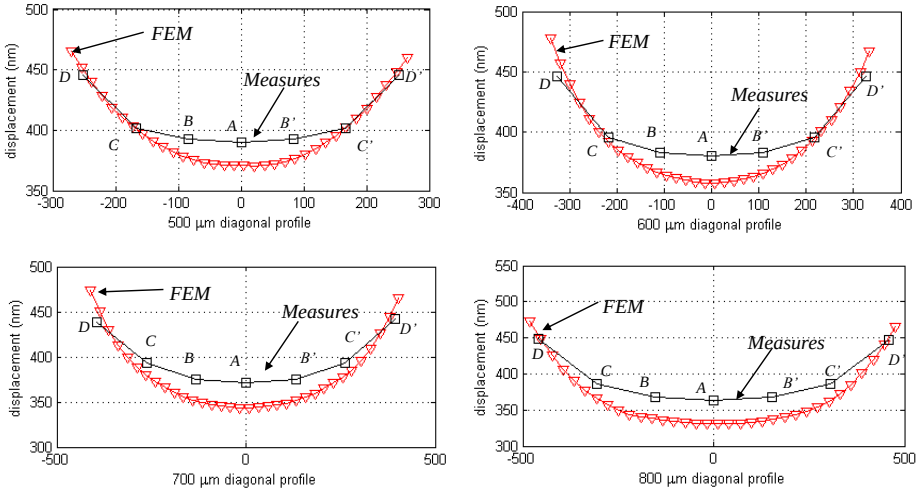

Figure D.1: Comparison between the measurements made in points along the diagonal of 4 sizes PMN-PT [001] patch micro-actuators and the FEM predictions for the respective sizes.

E

DISPLACEMENT AND LASER BEAM DIAMETER

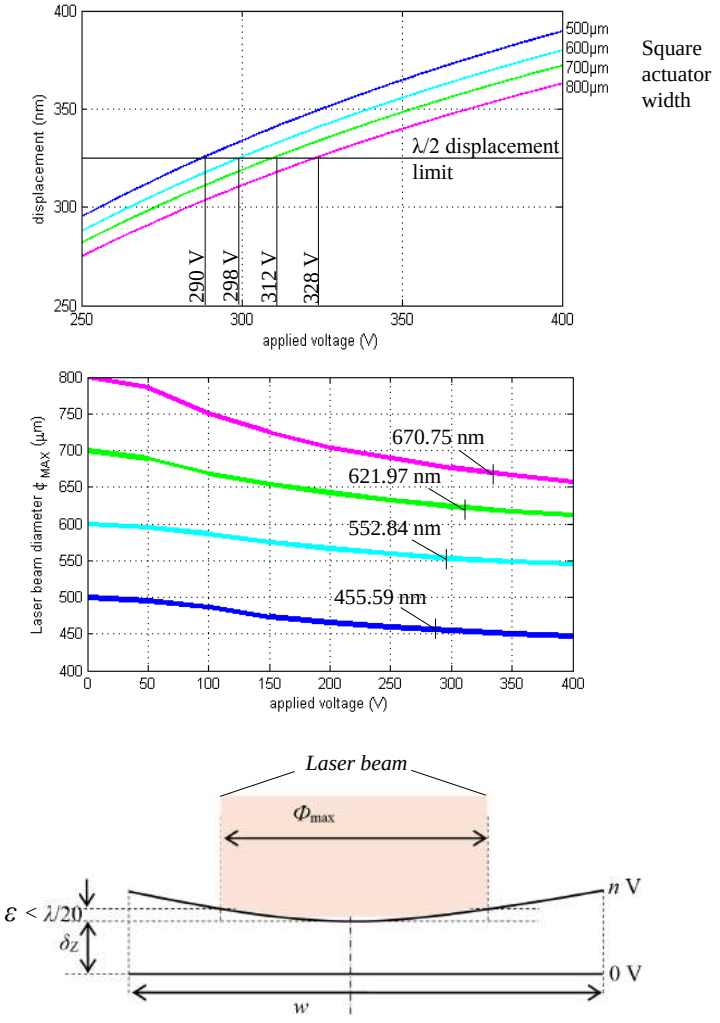

Figure E.1: Application imposed displacement limit (surpassed at under $300\ V$). Schematic for the maximum allowed planar deviation $\lambda/20$ for δ_Z displacement maximum diameter of the usable surface Φ_{max} for an actuator of w free face width.

F

PMN-PT MICRO-ACTUATOR FABRICATION

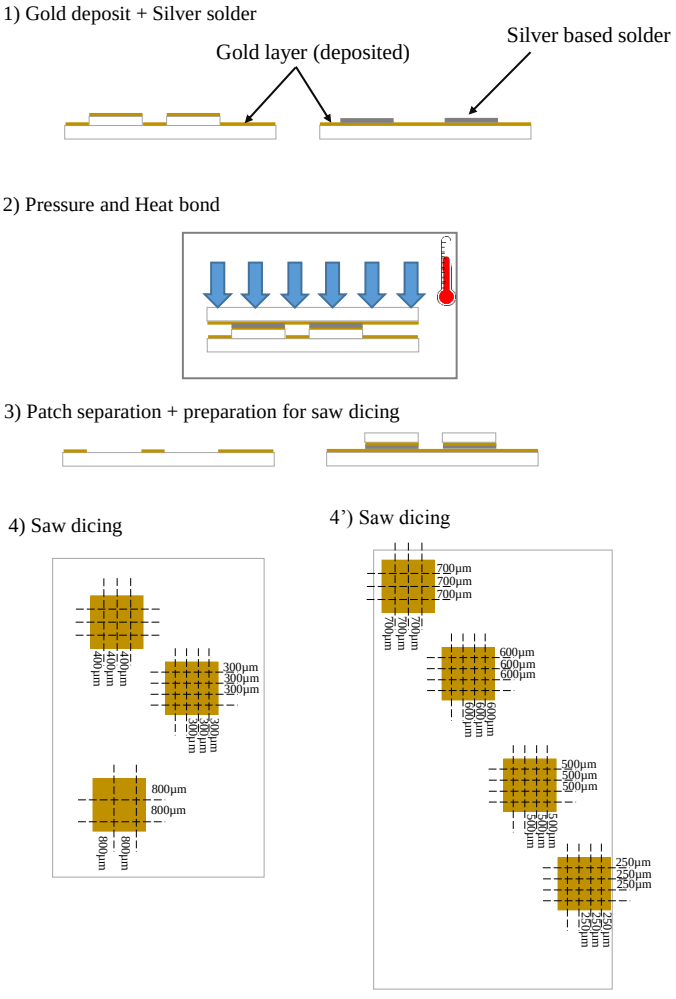

Figure F.1: The PMN-PT patch micro-actuator fabrication procedure.

G

Si holder plus PMN-PT actuator and mirror assembly

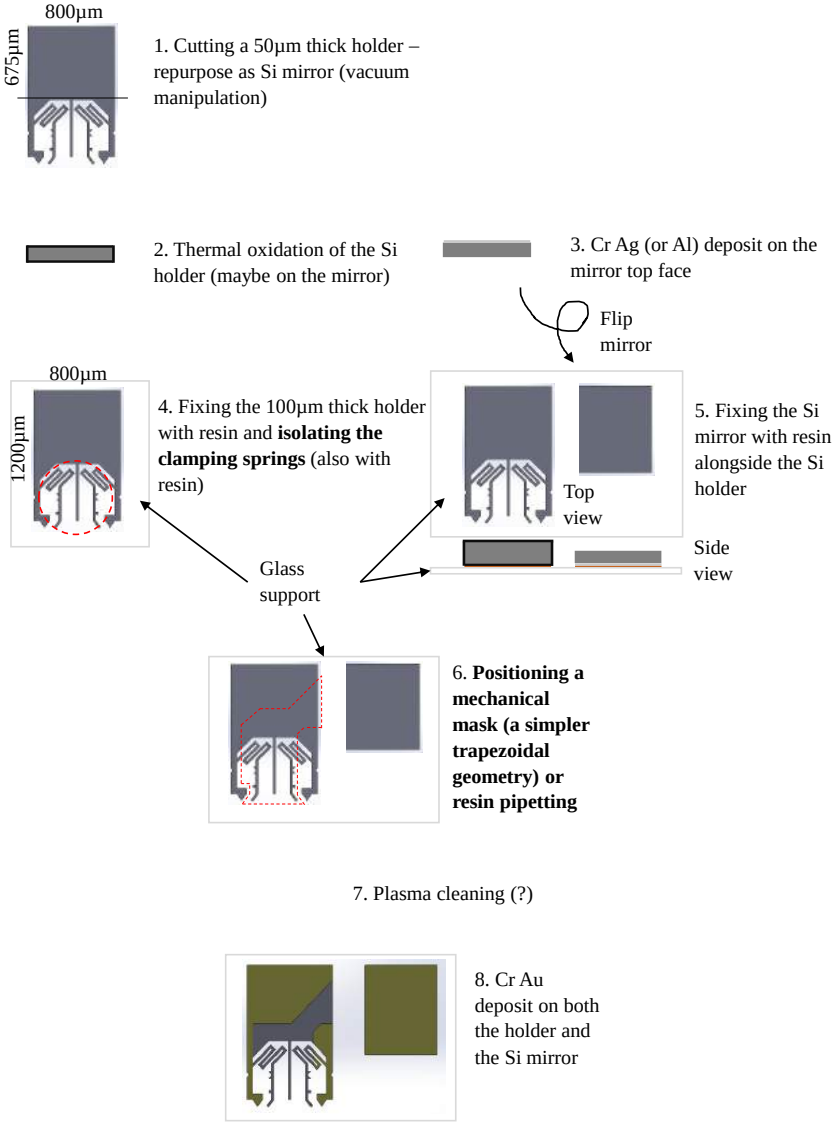

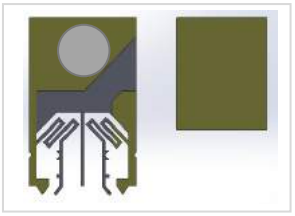

9. Conductive solder pipetting on the Si holder

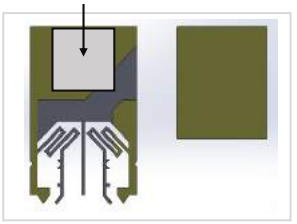

10. PMN-PT actuator positioning

11. Adhesive Curing

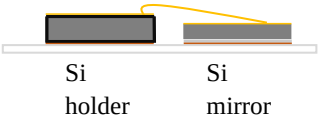

12. Ball-edge Au wire bonding (Φ=35µm)

13. Washing of the partial assembly with acetone/water/alcohol

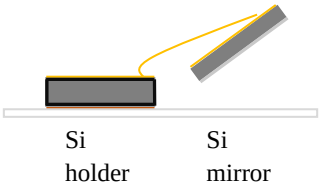

14. Fixing only the Si holder with resin on a glass plate

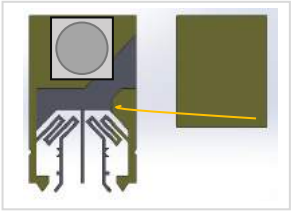

15. Conductive solder pipetting on the PMN-PT actuator

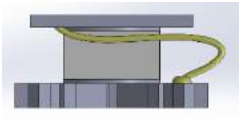

16. **Si mirror flip, precise orientation and holding**

17. Localized curing (heated substrate)

17. Washing of the assembly with acetone/water/alcohol

LIST OF PERSONAL PUBLICATIONS

[Ciubotariu et al., 2014a] Ciubotariu, D. A., Cleévy, C., Lutz, P., et Iva, I. A. (2014a). **Actuated moems micro-mirror based on pmn pt piezoelectric material**. In *Optomechatronic Technologies (ISOT), 2014 International Symposium on*, pages 182–186. IEEE.

[Ciubotariu et al., 2015a] Ciubotariu, D. A., Clévy, C., Ivan, I. A., et Lutz, P. (2015a). **Shape behavior analysis of a pmn-pt [001] actuated moems micro-mirror**. In *Advanced Intelligent Mechatronics (AIM), 2015 IEEE International Conference on*, pages 453–458. IEEE.

[Ciubotariu et al., 2014b] Ciubotariu, D. A., Ivan, I. A., Clevy, C., et Lutz, P. (2014b). **Size-dependent analysis and experiments of bulk pmn-pt [001] piezoelectric actuator for moems micro-mirrors**. In *Advanced Intelligent Mechatronics (AIM), 2014 IEEE/ASME International Conference on*, pages 1267–1272. IEEE.

[Ciubotariu et al., 2015b] Ciubotariu, D. A., Ivan, I. A., Clévy, C., et Lutz, P. (2015b). **Piezoelectric 3d actuator for micro-manipulation based on [011]-poled pmn-pt single crystal**. *Sensors and Actuators A: Physical*, pages 1–18.

[Ivan et al., 2013] Ivan, I. A., Ciubotariu, D. A., Clévy, C., Lutz, P., et Chaillet, N. (2013). **Duo-bimorph actuator made of pmn-pt [011]: 3d modeling, development and characterization**. In *Advanced Intelligent Mechatronics (AIM), 2013 IEEE/ASME International Conference on*, pages 140–145. IEEE.

BIBLIOGRAPHY

[Agnus et al., 2013] Agnus, J., Chaillet, N., Clévy, C., Dembélé, S., Gauthier, M., Haddab, Y., Laurent, G., Lutz, P., Piat, N., Rabenorosoa, K., et others (2013). **Robotic microassembly and micromanipulation at femto-st**. *Journal of Micro-Bio Robotics*, 8(2):91–106.

[Agnus et al., 2009] Agnus, J., Hériban, D., Gauthier, M., et Pétrini, V. (2009). **Silicon end-effectors for microgripping tasks**. *Precision engineering*, 33(4):542–548.

[Ahmed et al., 2013] Ahmed, M., Bishay, S. T., et Salem-Gaballah, S. (2013). **Structural characterization and magnetic properties of smart cucd ferrite/lasrco manganite nanocomposites**. *Journal of Magnetism and Magnetic Materials*, 334:96–101.

[Akbari et al., 2012] Akbari, S., et Shea, H. R. (2012). **An array of 100μm$\times$ 100μm dielectric elastomer actuators with 80% strain for tissue engineering applications**. *Sensors and Actuators A: Physical*, 186:236–241.

[Alberta et al., 2001] Alberta, E. F., et Bhalla, A. S. (2001). **Piezoelectric and dielectric properties of transparent pb (ni 1/3 nb 2/3) 1- x- y zr x ti y o 3 ceramics prepared by hot isostatic pressing**. *International Journal of Inorganic Materials*, 3(7):987–995.

[Aljasem et al., 2011] Aljasem, K., Froehly, L., Seifert, A., et Zappe, H. (2011). **Scanning and tunable micro-optics for endoscopic optical coherence tomography**. *Microelectromechanical Systems, Journal of*, 20(6):1462–1472.

[Aljasem et al., 2008] Aljasem, K., Werber, A., Seifert, A., et Zappe, H. (2008). **Fiber optic tunable probe for endoscopic optical coherence tomography**. *Journal of Optics A: Pure and Applied Optics*, 10(4):044012.

[Alogla et al., 2012] Alogla, A., Scanlan, P., Shu, W., et Reuben, R. (2012). **A scalable syringe-actuated microgripper for biological manipulation**. *Procedia Engineering*, 47:882–885.

[Andersen et al., 2008] Andersen, K. N., Carlson, K., Petersen, D. H., Mølhave, K., Eichhorn, V., Fatikow, S., et Bøggild, P. (2008). **Electrothermal microgrippers for pick-and-place operations**. *Microelectronic Engineering*, 85(5):1128–1130.

[Aoki et al., 1999] Aoki, Y., Kato, T., Jun Mizuno, R., et Iga, K. (1999). **Micro-optical bench for alignment-free optical coupling**. *Applied optics*, 38(6):963–965.

[Asaka et al., 2014] Asaka, K., et Okuzaki, H. (2014). **Soft Actuators: Materials, Modeling, Applications, and Future Perspectives**. Springer.

[Bahadur et al., 2005] Bahadur, I. B., Mills, J., et Sun, Y. (2005). **Design of a mems-based resonant force sensor for compliant, passive microgripping**. In *Mechatronics and Automation, 2005 IEEE International Conference*, volume 1, pages 77–82. IEEE.

[Bargiel et al., 2010] Bargiel, S., Rabenorosoa, K., Clevy, C., Gorecki, C., et Lutz, P. (2010). **Towards micro-assembly of hybrid moems components on a reconfigurable silicon free-space micro-optical bench**. *Journal of Micromechanics and Microengineering*, 20(4):045012.

[Battaglia et al., 2004] Battaglia, R., Palomba, E., Palumbo, P., Colangeli, L., et Della Corte, V. (2004). **Development of a micro-balance system for dust and water vapour detection in the mars atmosphere**. *Advances in Space Research*, 33(12):2258–2262.

[Beyeler et al., 2007] Beyeler, F., Neild, A., Oberti, S., Bell, D. J., Sun, Y., Dual, J., et Nelson, B. J. (2007). **Monolithically fabricated microgripper with integrated force sensor for manipulating microobjects and biological cells aligned in an ultrasonic field**. *Microelectromechanical Systems, Journal of*, 16(1):7–15.

[Beyeler et al., 2014] Beyeler, F., Simon, M., et Bradley, N. (2014). **Ft-s microforce sensing probe**.

[Bishop et al., 2002] Bishop, D. J., Giles, C. R., et Austin, G. P. (2002). **The lucent lambdarouter: Mems technology of the future here today**. *Communications Magazine, IEEE*, 40(3):75–79.

[Blomberg et al., 2009] Blomberg, M., Kattelus, H., et Miranto, A. (2009). **Electrically tunable surface micromachined fabry-perot interferometer for visible light**. *Procedia Chemistry*, 1(1):552–555.

[Böhringer et al., 1998] Böhringer, K.-F., Goldberg, K., Cohn, M., Howe, R., et Pisano, A. (1998). **Parallel microassembly with electrostatic force fields**. In *Robotics and Automation, 1998. Proceedings. 1998 IEEE International Conference on*, volume 2, pages 1204–1211. IEEE.

[Boppart, 2012] Boppart, S. A. (2012). **Handheld 3d medical scanner**. *http://www.kurzweilai.net/handheld-3d-medical-scanner-to-provide-high-resolution-3d-imaging-in-doctors-offices*.

[Boppart, 2013] Boppart, S. A. (2013). **"live" network optical switch**. *http://sharecomputernetwork.blogspot.fr/*.

[Boudaoud et al., 2010] Boudaoud, M., Haddab, Y., et Le Gorrec, Y. (2010). **Modelling of a mems-based microgripper: application to dexterous micromanipulation**. In *Intelligent Robots and Systems (IROS), 2010 IEEE/RSJ International Conference on*, pages 5634–5639. IEEE.

[Boukai et al., 2008] Boukai, A. I., Bunimovich, Y., Tahir-Kheli, J., Yu, J.-K., Goddard Iii, W. A., et Heath, J. R. (2008). **Silicon nanowires as efficient thermoelectric materials**. *Nature*, 451(7175):168–171.

[Bourjault et al., 2002] Bourjault, A., Chaillet, N., et Foulard, C. (2002). **La microrobotique**. Hermès science publications.

[Brochu et al., 2010] Brochu, P., et Pei, Q. (2010). **Advances in dielectric elastomers for actuators and artificial muscles**. *Macromolecular rapid communications*, 31(1):10–36.

[Cao et al., 2004] Cao, H., Schmidt, V. H., Zhang, R., Cao, W., et Luo, H. (2004). **Elastic, piezoelectric, and dielectric properties of 0.58 pb (mg1/3nb2/3) o3-0.42 pbtio3 single crystal**. *Journal of applied physics*, 96(1):549–554.

[Carpi et al., 2006] Carpi, F., et De Rossi, D. (2006). **Contractile dielectric elastomer actuator with folded shape**. In *Smart Structures and Materials*, pages 61680D–61680D. International Society for Optics and Photonics.

[Carrozza et al., 2000] Carrozza, M. C., Eisinberg, A., Menciassi, A., Campolo, D., Micera, S., et Dario, P. (2000). **Towards a force-controlled microgripper for assembling biomedical microdevices**. *Journal of Micromechanics and Microengineering*, 10(2):271.

[Chaipanich et al., 2012] Chaipanich, A., Potong, R., Rianyoi, R., Jareansuk, L., Jaitanong, N., et Yimnirun, R. (2012). **Dielectric and ferroelectric hysteresis properties of 1–3 lead magnesium niobate–lead titanate ceramic/portland cement composites**. *Ceramics International*, 38:S255–S258.

[Chang et al., 2010] Chang, B., Jääskeläinen, M., et Zhou, Q. (2010). **Hybrid micro assembly of microchips on segmented patterns**. In *Automation Science and Engineering (CASE), 2010 IEEE Conference on*, pages 15–20. IEEE.

[Chau et al., 2008] Chau, F. S., Du, Y., et Zhou, G. (2008). **A micromachined stationary lamellar grating interferometer for fourier transform spectroscopy**. *Journal of Micromechanics and Microengineering*, 18(2):025023.

[Chen, 2008] Chen, C. J. (2008). **Introduction to scanning tunneling microscopy**. Oxford University Press.

[Chen et al., 2015] Chen, Y., Qiu, W., Lam, K., Liu, B., Jiang, X., Zheng, H., Luo, H., Chan, H., et Dai, J. (2015). **Focused intravascular ultrasonic probe using dimpled transducer elements**. *Ultrasonics*, 56:227–231.

[Cheng et al., 2000] Cheng, K., Chan, H. L., Choy, C., Yin, Q., Lu, H., et Yin, Z. (2000). **Piezoelectric coefficients of pmn-0.33 pt single crystals**. In *Applications of Ferroelectrics, 2000. ISAF 2000. Proceedings of the 2000 12th IEEE International Symposium on*, volume 2, pages 533–536. IEEE.

[Chronis et al., 2005] Chronis, N., et Lee, L. P. (2005). **Electrothermally activated su-8 microgripper for single cell manipulation in solution**. *Microelectromechanical Systems, Journal of*, 14(4):857–863.

[Coppola et al., 2014] Coppola, G., Zhang, D., et Liu, K. (2014). **A 6-dof reconfigurable hybrid parallel manipulator**. *Robotics and Computer-Integrated Manufacturing*, 30(2):99–106.

[Coutte et al., 2002] Coutte, J., Dubus, B., Debus, J.-C., Granger, C., et Jones, D. (2002). **Design, production and testing of pmn–pt electrostrictive transducers**. *Ultrasonics*, 40(1):883–888.

[Das et al., 2012] Das, A. N., Murthy, R., Popa, D. O., et Stephanou, H. E. (2012). **A multiscale assembly and packaging system for manufacturing of complex micro-nano devices**. *Automation Science and Engineering, IEEE Transactions on*, 9(1):160–170.

[Das et al., 2008] Das, A. N., Sin, J., Popa, D. O., et Stephanou, H. E. (2008). **On the precision alignment and hybrid assembly aspects in manufacturing of a microspectrometer**. In *Automation Science and Engineering, 2008. CASE 2008. IEEE International Conference on*, pages 959–966. IEEE.

[Das et al., 2007] Das, A. N., Zhang, P., Lee, W. H., Popa, D., et Stephanou, H. (2007). **μ 3: multiscale, deterministic micro-nano assembly system for construction of on-wafer microrobots**. In *Robotics and Automation, 2007 IEEE International Conference on*, pages 461–466. IEEE.

[Davis et al., 2006] Davis, M., Damjanovic, D., et Setter, N. (2006). **Electric-field-, temperature-, and stress-induced phase transitions in relaxor ferroelectric single crystals**. *Physical Review B*, 73(1):014115.

[De Lit et al., 2003] De Lit, P., Agnus, J., et Chaillet, N. (2003). **The constitutive equations of a piezoelectric duo-bimorph**. In *Assembly and Task Planning, 2003. Proceedings of the IEEE International Symposium on*, pages 1–6. IEEE.

[De Mattei et al., 1981] De Mattei, R. C., Elwell, D., et Feigelson, R. S. (1981). **Electrodeposition of silicon at temperatures above its melting point**. *Journal of the Electrochemical Society*, 128(8):1712–1714.

[Dechev et al., 2004] Dechev, N., Cleghorn, W. L., et Mills, J. K. (2004). **Microassembly of 3-d microstructures using a compliant, passive microgripper**. *Microelectromechanical Systems, Journal of*, 13(2):176–189.

[Deeds et al., 2005] Deeds, M., Sandborn, P., et others (2005). **Moems chip-level optical fiber interconnect**. *Advanced Packaging, IEEE Transactions on*, 28(4):612–618.

[Derjaguin et al., 1975] Derjaguin, B. V., Muller, V. M., et Toporov, Y. P. (1975). **Effect of contact deformations on the adhesion of particles**. *Journal of Colloid and interface science*, 53(2):314–326.

[Descour et al., 2002] Descour, M. R., Kärkkäinen, A. H., Rogers, J. D., Liang, C., Weinstein, R. S., Rantala, J. T., Kilic, B., Madenci, E., Richards-Kortum, R. R., Anslyn, E. V., et others (2002). **Toward the development of miniaturized imaging systems for detection of pre-cancer**. *Quantum Electronics, IEEE Journal of*, 38(2):122–130.

[Despa et al., 2013] Despa, V., Ardeleanu, M., et Ivan, I. A. (2013). **Mechatronic device for bio-medical samples micromanipulation.** *Scientific Bulletin of'Valahia'University. Materials & Mechanics*, 11(8).

[Despa et al., 2014] Despa, V., Catangiu, A., Ivan, I. A., Gurgu, V., et Ardeleanu, M. (2014). **Modeling and control of a microgripper based on electromagnetic actuation.** *Scientific Bulletin of'Valahia'University. Materials & Mechanics*, 12(9).

[Detalle et al., 2007] Detalle, M., Wang, G., Rémiens, D., Ruterana, P., Roussel, P., et Dkhil, B. (2007). **Comparison of structural and electrical properties of pmn-pt films deposited on si with different bottom electrodes**. *Journal of crystal growth*, 305(1):137–143.

[Dosch et al., 1992] Dosch, J. J., Inman, D. J., et Garcia, E. (1992). **A self-sensing piezoelectric actuator for collocated control**. *Journal of Intelligent Material Systems and Structures*, 3(1):166–185.

[Dudley et al., 2003] Dudley, D., Duncan, W. M., et Slaughter, J. (2003). **Emerging digital micromirror device (dmd) applications**. In *Micromachining and Microfabrication*, pages 14–25. International Society for Optics and Photonics.

[Ebefors et al., 1999] Ebefors, T., Ulfstedt-Mattsson, J., Kälvesten, E., et Stemme, G. (1999). **3d micromachined devices based on polyimide joint technology**. In *Asia Pacific Symposium on Microelectronics and MEMS*, pages 118–132. International Society for Optics and Photonics.

[Edwards et al., 2006] Edwards, G., Chan, H., Batten, A., Lam, K., Luo, H., et Scott, D. (2006). **Pmn–pt single-crystal transducer for non-destructive evaluation**. *Sensors and Actuators A: Physical*, 132(2):434–440.

[Epzcaw, 2012] Epzcaw (2012). **Michelson interferometer**.

[Fang et al., 2006] Fang, H.-B., Liu, J.-Q., Xu, Z.-Y., Dong, L., Wang, L., Chen, D., Cai, B.-C., et Liu, Y. (2006). **Fabrication and performance of mems-based piezoelectric power generator for vibration energy harvesting**. *Microelectronics Journal*, 37(11):1280–1284.

[Fiala et al., 2013] Fiala, J., Bingger, P., Ruh, D., Foerster, K., Heilmann, C., Beyersdorf, F., Zappe, H., et Seifert, A. (2013). **An implantable optical blood pressure sensor based on pulse transit time**. *Biomedical microdevices*, 15(1):73–81.

[Finkel et al., 2010] Finkel, P., Robinson, H., Stace, J., et Amin, A. (2010). **Study of phase transitions in ternary lead indium niobate-lead magnesium niobate-lead titanate relaxor ferroelectric morphotropic single crystals**. *Applied Physics Letters*, 97(12):122903.

[Flanders et al., 2003] Flanders, D. C., et Whitney, P. S. (2003). **Optical system active alignment process including alignment structure attach, position search, and deformation**. US Patent 6,559,464.

[Fujimoto, 2003] Fujimoto, J. G. (2003). **Optical coherence tomography for ultrahigh resolution in vivo imaging**. *Nature biotechnology*, 21(11):1361–1367.

[Gauthier et al., 2011] Gauthier, M., et Régnier, S. (2011). **Robotic micro-assembly**. John Wiley & Sons.

[Gautschi, 2002] Gautschi, D.-I. E. G. (2002). **Piezoelectric sensors**. Springer.

[Gebhardt et al., 2007] Gebhardt, S., Seffner, L., Schlenkrich, F., et Schönecker, A. (2007). **Pzt thick films for sensor and actuator applications**. *Journal of the European Ceramic Society*, 27(13):4177–4180.

[Gilchrist et al., 2009] Gilchrist, K. H., McNabb, R. P., Izatt, J. A., et Grego, S. (2009). **Piezoelectric scanning mirrors for endoscopic optical coherence tomography**. *Journal of Micromechanics and Microengineering*, 19(9):095012.

[Glenn et al., 1997] Glenn, T. S., et Hagood, N. W. (1997). **Development of a two-sided piezoelectric rotary ultrasonic motor for high torque**. In *Smart Structures and Materials' 97*, pages 326–338. International Society for Optics and Photonics.

[Gorecki et al., 2011] Gorecki, C., Bargiel, S., Albero, J., Passilly, N., Rousselot, C., Zeitner, U., et Gastinger, K. (2011). **Micromachined array-type mirau interferometer for mems metrology**. In *Solid-State Sensors, Actuators and Microsystems Conference (TRANSDUCERS), 2011 16th International*, pages 546–549. IEEE.

[Goulbourne et al., 2005] Goulbourne, N., Mockensturm, E., et Frecker, M. (2005). **A nonlinear model for dielectric elastomer membranes**. *Journal of Applied Mechanics*, 72(6):899–906.

[Gullapalli et al., 2010] Gullapalli, H., Vemuru, V. S., Kumar, A., Botello-Mendez, A., Vajtai, R., Terrones, M., Nagarajaiah, S., et Ajayan, P. M. (2010). **Flexible piezoelectric zno–paper nanocomposite strain sensor**. *Small*, 6(15):1641–1646.

[Guo et al., 2002] Guo, Y., Luo, H., Chen, K., Xu, H., Zhang, X., et Yin, Z. (2002). **Effect of composition and poling field on the properties and ferroelectric phase-stability of pb (mg1/3nb2/3) o3-pbtio3 crystals**. *Journal of applied physics*, 92:6134–6138.

[Guo et al., 2003] Guo, Y., Luo, H., He, T., Pan, X., et Yin, Z. (2003). **Electric-field-induced strain and piezoelectric properties of a high curie temperature pb (in 1/2 nb 1/2) o 3–pbtio 3 single crystal**. *Materials research bulletin*, 38(5):857–864.

[Hackenberger et al., 2008] Hackenberger, W., Luo, J., Jiang, X., Snook, K., Rehrig, P., et Ye, Z. (2008). **Handbook of advanced dielectric, piezoelectric and ferroelectric materials**.

[Hall et al., 2005] Hall, A., Allahverdi, M., Akdogan, E., et Safari, A. (2005). **Piezoelectric/electrostrictive multimaterial pmn-pt monomorph actuators**. *Journal of the European Ceramic Society*, 25(12):2991–2997.

[Hao et al., 2009] Hao, H., Zhang, S., Liu, H., et Shrout, T. R. (2009). **Dielectric, piezoelectric, and electromechanical properties of morphotropic phase boundary compositions in the pb „mg ta 2/3... o 3–pbzro 3–pbtio 3 ternary system**. *Journal of Applied Physics*, 105:024104.

[Hao et al., 2008] Hao, H., Zhang, S., et Shrout, T. R. (2008). **Dielectric and piezoelectric properties of the morphotropic phase boundary composition in the (0.8- x) pb (mg1/3ta2/3) o3- 0.2 pbzro3- xpbtio3 ternary system**. *Journal of the American Ceramic Society*, 91(7):2232–2235.

[Hawwa et al., 2001] Hawwa, M. A., et Bozorgi, J. (2001). **Piezoelectric vibration damping for disk drives**. US Patent 6,310,746.

[Herdier et al., 2008] Herdier, R., Detalle, M., Jenkins, D., Soyer, C., et Remiens, D. (2008). **Piezoelectric thin films for mems applications—a comparative study of pzt, 0.7 pmn–0.3 pt and 0.9 pmn–0.1 pt thin films grown on si by rf magnetron sputtering**. *Sensors and Actuators A: Physical*, 148(1):122–128.

[Hériban et al., 2008] Hériban, D., et Gauthier, M. (2008). **Robotic micro-assembly of microparts using a piezogripper**. In *Intelligent Robots and Systems, 2008. IROS 2008. IEEE/RSJ International Conference on*, pages 4042–4047. IEEE.

[Hornbeck, 2012] Hornbeck, L. (2012). **Optical bare code scanner**. *http://www.sharp-world.com/products/data$_{p}$roject/xgph70x/index.html*.

[Hosono et al., 2006] Hosono, Y., et Yamashita, Y. (2006). **Piezoelectric ceramics and single crystals for ultrasonic medical transducers**. *Journal of electroceramics*, 17(2-4):577–583.

[Hsieh et al., 2007] Hsieh, J., Hsiao, S.-Y., Lai, C.-F., et Fang, W. (2007). **Integration of a uv curable polymer lens and mumps structures on a soi optical bench**. *Journal of Micromechanics and Microengineering*, 17(8):1703.

[Huang et al., 1991] Huang, D., Swanson, E. A., Lin, C. P., Schuman, J. S., Stinson, W. G., Chang, W., Hee, M. R., Flotte, T., Gregory, K., Puliafito, C. A., et others (1991). **Optical coherence tomography**. *Science*, 254(5035):1178–1181.

[Huang et al., 2012] Huang, S., Leary, M., Ataalla, T., Probst, K., et Subic, A. (2012). **Optimisation of ni–ti shape memory alloy response time by transient heat transfer analysis**. *Materials & Design*, 35:655–663.

[Huo et al., 2012] Huo, X., Zhang, S., Liu, G., Zhang, R., Luo, J., Sahul, R., Cao, W., et Shrout, T. R. (2012). **Elastic, dielectric and piezoelectric characterization of single domain pin-pmn-pt: Mn crystals**. *Journal of applied physics*, 112(12):124113.

[Huo et al., 2013] Huo, X., Zhang, S., Liu, G., Zhang, R., Luo, J., Sahul, R., Cao, W., et Shrout, T. R. (2013). **Complete set of elastic, dielectric, and piezoelectric constants of [011] c poled rhombohedral pb (in0. 5nb0. 5) o3-pb (mg1/3nb2/3) o3-pbtio3: Mn single crystals**. *Journal of Applied Physics*, 113(7):074106.

[Ivan et al., 2011] Ivan, I. A., Agnus, J., Rakotondrabe, M., Lutz, P., et Chaillet, N. (2011). **Microfabricated pmn-pt on silicon cantilevers with improved static and dynamic piezoelectric actuation: development, characterization and control**. In *Advanced Intelligent Mechatronics (AIM), 2011 IEEE/ASME International Conference on*, pages 403–408. IEEE.

[Ivan et al., 2012] Ivan, I. A., Ardeleanu, M., et Despa, V. (2012). **Dispozitiv de actionare magneto-pezoelectric pentru micromanipulare**. patent nr. A2012/00471.

[Ivan et al., 2013] Ivan, I. A., Ciubotariu, D. A., Clévy, C., Lutz, P., et Chaillet, N. (2013). **Duo-bimorph actuator made of pmn-pt [011]: 3d modeling, development and characterization**. In *Advanced Intelligent Mechatronics (AIM), 2013 IEEE/ASME International Conference on*, pages 140–145. IEEE.

[Ivan et al., 2010] Ivan, I. A., Rakotondrabe, M., Agnus, J., Bourquin, R., Chaillet, N., Lutz, P., Poncot, J.-C., Duffait, R., et Bauer, O. (2010). **Comparative material study between pzt ceramic and newer crystalline pmn-pt and pzn-pt mateirals for composite bimorph actuators.** *Review on Advanced Materials Science (RAMS)*, 24(15-16):1–9.

[Jackle et al., 2000] Jackle, S., Gladkova, N., Feldchtein, F., Terentieva, A., Brand, B., Gelikonov, G., Gelikonov, V., Sergeev, A., Fritscher-Ravens, A., Freund, J., et others (2000). **In vivo endoscopic optical coherence tomography of esophagitis, barrett's esophagus, and adenocarcinoma of the esophagus**. *Endoscopy*, 32(10):750–755.

[Janolin et al., 2007] Janolin, P.-E., Davis, M., Dkhil, B., Damjanovic, D., et Setter, N. (2007). **Uniaxial-stress induced phase transitions in [001] c-poled 0.955 pb (zn1/3nb2/3) o3-0.045 pbtio3**. *arXiv preprint cond-mat/0703615*.

[Jiang et al., 2011] Jiang, J., Hwang, H.-H., Lee, W.-J., et Yoon, S.-G. (2011). **Microstructural and electrical properties of 0.65 pb (mg 1/3 nb 2/3) o 3–0.35 pbtio 3 (pmn–pt) epitaxial films grown on si substrates**. *Sensors and Actuators B: Chemical*, 155(2):854–858.

[Johnson et al., 1987] Johnson, K. L., et Johnson, K. L. (1987). **Contact mechanics**. Cambridge university press.

[Jung et al., 2006] Jung, W., McCormick, D. T., Zhang, J., Wang, L., Tien, N. C., et Chen, Z. (2006). **Three-dimensional endoscopic optical coherence tomography by use of a two-axis microelectromechanical scanning mirror**. *Applied physics letters*, 88(16):163901.

[Kania et al., 2006] Kania, A., Słodczyk, A., et Ujma, Z. (2006). **Flux growth and characterization of (1- x) pbmg 1/3 nb 2/3 o 3–xpbtio 3 single crystals**. *Journal of crystal growth*, 289(1):134–139.

[Kenjiro, 2012] Kenjiro, I. (2012). **The czochralski process**.

[Keplinger et al., 2013] Keplinger, C., Sun, J.-Y., Foo, C. C., Rothemund, P., Whitesides, G. M., et Suo, Z. (2013). **Stretchable, transparent, ionic conductors**. *Science*, 341(6149):984–987.

[Kharboutly, 2011] Kharboutly, M. (2011). **Modelling, realization and control a dielectrophoresis-based micromanipulation system**. *PhD thesis*.

[Kim et al., 2012a] Kim, B.-S., Park, J.-S., Kang, B. H., et Moon, C. (2012a). **Fabrication and property analysis of a mems microgripper for robotic micro-manipulation**. *Robotics and Computer-Integrated Manufacturing*, 28(1):50–56.

[Kim et al., 2004] Kim, D.-H., Kim, B., et Kang, H. (2004). **Development of a piezoelectric polymer-based sensorized microgripper for microassembly and micromanipulation**. *Microsystem technologies*, 10(4):275–280.

[Kim et al., 2014] Kim, J., et Roh, Y. (2014). **Homogenization of pmn-pt/epoxy 1–3 piezocomposites by resonator measurements and finite element analysis**. *Sensors and Actuators A: Physical*, 206:97–106.

[Kim et al., 2006] Kim, J., Yun, S., et Ounaies, Z. (2006). **Discovery of cellulose as a smart material**. *Macromolecules*, 39(12):4202–4206.

[Kim et al., 2012b] Kim, K., Ahn, D., et Gweon, D. (2012b). **Optimal design of a 1-rotational dof flexure joint for a 3-dof h-type stage**. *Mechatronics*, 22(1):24–32.

[Kim et al., 2008] Kim, K., Liu, X., Zhang, Y., et Sun, Y. (2008). **Nanonewton force-controlled manipulation of biological cells using a monolithic mems microgripper with two-axis force feedback**. *Journal of Micromechanics and Microengineering*, 18(5):055013.

[Kim et al., 2010] Kim, K.-B., Hsu, D. K., Ahn, B., Kim, Y.-G., et Barnard, D. J. (2010). **Fabrication and comparison of pmn-pt single crystal, pzt and pzt-based 1-3 composite ultrasonic transducers for nde applications**. *Ultrasonics*, 50(8):790–797.

[Kim et al., 2007] Kim, K. H., Park, B. H., Maguluri, G. N., Lee, T. W., Rogomentich, F. J., Bancu, M. G., Bouma, B. E., de Boer, J. F., et Bernstein, J. J. (2007). **Two-axis magnetically-driven mems scanning catheter for endoscopic high-speed optical coherence tomography**. *Optics express*, 15(26):18130–18140.

[Kim et al., 2003] Kim, Y., Lee, S., Lee, H., et Roh, Y. (2003). **Measurement of all the material properties of pmn-pt single crystals grown by the solid-state-crystal-growth (sscg) method**. In *Ultrasonics, 2003 IEEE Symposium on*, volume 2, pages 1987–1990. IEEE.

[Ko et al., 2006] Ko, B., Jung, J.-S., et Lee, S.-Y. (2006). **Design of a slim-type optical pick-up actuator using pmn-pt bimorphs**. *Smart materials and structures*, 15(6):1912.

[Kohl et al., 2002] Kohl, M., Krevet, B., et Just, E. (2002). **Sma microgripper system**. *Sensors and Actuators A: Physical*, 97:646–652.

[Komati, 2014] Komati, B. (2014). **Automated Microassembly Using an Active Microgripper with Sensorized End-Effectors and Hybrid Force/Position Control**. PhD thesis, Université de Franche-Comté.

[Kuang et al., 2015] Kuang, Y., Sadiq, M., Cochran, S., et Huang, Z. (2015). **Design and characterization of an ultrasonic surgical tool using d 31 pmn-pt plate**. *Physics Procedia*, 63:182–188.

[Kuhnen et al., 2001] Kuhnen, K., et Janocha, H. (2001). **Inverse feedforward controller for complex hysteretic nonlinearities in smart-material systems**. *Control and Intelligent systems*, 29(3):74–83.

[Kuwata et al., 1982] Kuwata, J., Uchino, K., et Nomura, S. (1982). **Dielectric and piezoelectric properties of 0.91 pb (zn1/3nb2/3) o3-0.09 pbtio3 single crystals**. *Japanese Journal of Applied Physics*, 21(9R):1298.

[Lam et al., 2005] Lam, K., Chan, H., Luo, H., Yin, Q., et Yin, Z. (2005). **Piezoelectrically actuated ejector using pmn–pt single crystal**. *Sensors and Actuators A: Physical*, 121(1):197–202.

[Lang, 2008] Lang, D. (2008). **A study on micro-gripping technologies**. TU Delft, Delft University of Technology.

[Lara-Quintanilla et al., 2013] Lara-Quintanilla, A., Hulskamp, A. W., et Bersee, H. E. (2013). **A high-rate shape memory alloy actuator for aerodynamic load control on wind turbines**. *Journal of Intelligent Material Systems and Structures*, page 1045389X13478271.

[Lau et al., 2010] Lau, S., Zhao, L., Chan, H., et Luo, H. (2010). **60-mhz pmn-pt single crystal transducers for microfluidic analysis systems**. *Sensors and Actuators A: Physical*, 161(1):78–82.

[Lee et al., 2009] Lee, B., Lin, S., Wu, W., Wang, X., Chang, P., et Lee, C. (2009). **Piezoelectric mems generators fabricated with an aerosol deposition pzt thin film**. *Journal of Micromechanics and Microengineering*, 19(6):065014.

[Lee et al., 2010] Lee, C.-C., Cao, G., et Shen, I. (2010). **Effects of residual stresses on lead–zirconate–titanate (pzt) thin-film membrane microactuators**. *Sensors and Actuators A: Physical*, 159(1):88–95.

[Lei et al., 2011] Lei, A., Xu, R., Thyssen, A., Stoot, A. C., Christiansen, T. L., Hansen, K., Lou-Moller, R., Thomsen, E. V., et Birkelund, K. (2011). **Mems-based thick film pzt vibrational energy harvester**. In *Micro Electro Mechanical Systems (MEMS), 2011 IEEE 24th International Conference on*, pages 125–128. IEEE.

[Li et al., 2011] Li, X., Wu, W., Chung, Y., Shih, W. Y., Shih, W.-H., Zhou, Q., et Shung, K. K. (2011). **80-mhz intravascular ultrasound transducer using pmn-pt free-standing film**. *Ultrasonics, Ferroelectrics, and Frequency Control, IEEE Transactions on*, 58(11):2281–2288.

[Li et al., 2014] Li, Y., Ma, Y., Liu, S., Luo, Z., Mei, J., Huang, T., et Chetwynd, D. (2014). **Integrated design of a 4-dof high-speed pick-and-place parallel robot**. *CIRP Annals-Manufacturing Technology*, 63(1):185–188.

[Lim et al., 2007] Lim, L. C., Rajan, K. K., et Jin, J. (2007). **Characterization of flux-grown pzn-pt single crystals for high-performance piezo devices**. *Ultrasonics, Ferroelectrics, and Frequency Control, IEEE Transactions on*, 54(12):2474–2478.

[Lin et al., 2012] Lin, C.-Y., et Chiou, J.-C. (2012). **Design and fabrication of mems-based thermally-actuated image stabilizer for cell phone camera**. *Solid-State Electronics*, 77:64–71.

[Lin et al., 1996] Lin, L., Shen, J., Lee, S., et Wu, M. (1996). **Realization of novel monolithic free-space optical disk pickup heads by surface micromachining**. *Optics letters*, 21(2):155–157.

[Lin et al., 1997] Lin, L. Y., Shen, J., Lee, S., et Wu, M. (1997). **Surface-micromachined micro-xyz stages for free-space microoptical bench**. *IEEE Photonics Technology Letters*, 9(3):345–347.

[Lines et al., 1977] Lines, M. E., et Glass, A. M. (1977). **Principles and applications of ferroelectrics and related materials**. Oxford University Press.

[Liu et al., 2010] Liu, F., et Zhong, X.-C. (2010). **Transient response of two collinear dielectric cracks in a piezoelectric solid under inplane impacts**. *Applied Mathematics and Computation*, 217(8):3779–3791.

[Luo et al., 1999] Luo, H., Xu, G., Wang, P., et Yin, Z. (1999). **Growth and characterization of relaxor ferroelectric pmnt single crystals**. *Ferroelectrics*, 231(1):97–102.

[Luo et al., 2010] Luo, J., Hackenberger, W., Zhang, S., et Shrout, T. R. (2010). **A high q m relaxor ferroelectric single crystal: Growth and characterization**. In *Ultrasonics Symposium (IUS), 2010 IEEE*, pages 68–71. IEEE.

[Luo et al., 2014] Luo, J., et Zhang, S. (2014). **Advances in the growth and characterization of relaxor-pt-based ferroelectric single crystals**. *Crystals*, 4(3):306–330.

[Luo et al., 2009] Luo, L., Li, W., Zhu, Y., et Wang, J. (2009). **Growth and characteristics of mn-doped pmn–pt single crystals**. *Solid State Communications*, 149(25):978–981.

[Ma et al., 2011] Ma, J., Liu, Y., Chen, C., Li, B., et Chu, J. (2011). **Deformable mirrors based on piezoelectric unimorph microactuator array for adaptive optics correction**. *Optics Communications*, 284(21):5062–5066.

[Malek et al., 2004] Malek, C. K., et Saile, V. (2004). **Applications of liga technology to precision manufacturing of high-aspect-ratio micro-components and-systems: a review**. *Microelectronics journal*, 35(2):131–143.

[Manzardo, 2002] Manzardo, O. (2002). **Micro-sized Fourier Spectrometers, Neuchatel, University**. PhD thesis, Thesis (doctoral).

[Marin-Franch et al., 2004] Marin-Franch, P., Cochran, S., et Kirk, K. (2004). **Progress towards ultrasound applications of new single crystal materials**. *Journal of Materials Science: Materials in Electronics*, 15(11):715–720.

[Mason, 1948] Mason, W. (1948). **Piezoelectric or electrostrictive effect in barium titanate ceramics**. *Physical Review*, 73(11):1398.

[McCluskey et al., 2012] McCluskey, M. D., et Haller, E. E. (2012). **Dopants and defects in semiconductors**. CRC Press.

[Meisner et al., 2014] Meisner, G. P., et Yang, J. (2014). **Thermoelectric generators incorporating phase-change materials for waste heat recovery from engine exhaust**. US Patent 8,646,261.

[Millet et al., 2004] Millet, O., Bernardoni, P., Régnier, S., Bidaud, P., Tsitsiris, E., Collard, D., et Buchaillot, L. (2004). **Electrostatic actuated micro gripper using an amplification mechanism**. *Sensors and Actuators A: Physical*, 114(2):371–378.

[Miyagawa et al., 2013] Miyagawa, C., Kobayashi, T., Taishi, T., et Hoshikawa, K. (2013). **Demonstration of crack-free c-axis sapphire crystal growth using the vertical bridgman method**. *Journal of Crystal Growth*, 372:95–99.

[Niclass et al., 2012] Niclass, C., Ito, K., Soga, M., Matsubara, H., Aoyagi, I., Kato, S., et Kagami, M. (2012). **Design and characterization of a 256x64-pixel single-photon imager in cmos for a mems-based laser scanning time-of-flight sensor**. *Optics express*, 20(11):11863–11881.

[Noell et al., 2002] Noell, W., Clerc, P.-A., Dellmann, L., Guldimann, B., Herzig, H.-P., Manzardo, O., Marxer, C. R., Weible, K. J., Dändliker, R., et De Rooij, N. (2002). **Applications of soi-based optical mems**. *Selected Topics in Quantum Electronics, IEEE Journal of*, 8(1):148–154.

[Nye, 1985] Nye, J. F. (1985). **Physical properties of crystals: their representation by tensors and matrices**. Oxford university press.

[Otsuka et al., 1999] Otsuka, K., et Wayman, C. M. (1999). **Shape memory materials**. Cambridge university press.

[Pan et al., 2001] Pan, Y., Xie, H., et Fedder, G. K. (2001). **Endoscopic optical coherence tomography based on a microelectromechanical mirror**. *Optics letters*, 26(24):1966–1968.

[Park et al., 2008] Park, H., et others (2008). **Mems deformable mirrors for adaptive optics using single crystal pmn-pt**. In *2008 IEEE/LEOS International Conference on Optical MEMs and Nanophotonics*, pages 90–91.

[Park et al., 2011] Park, H., Horsley, D., et others (2011). **Single-crystal pmn-pt mems deformable mirrors**. *Microelectromechanical Systems, Journal of*, 20(6):1473–1482.

[Pelrine et al., 2000] Pelrine, R., Kornbluh, R., et Kofod, G. (2000). **High-strain actuator materials based on dielectric elastomers**. *Advanced Materials*, 12(16):1223–1225.

[Pelrine et al., 2001] Pelrine, R., Kornbluh, R. D., Eckerle, J., Jeuck, P., Oh, S., Pei, Q., et Stanford, S. (2001). **Dielectric elastomers: Generator mode fundamentals and applications**. In *SPIE's 8th Annual International Symposium on Smart Structures and Materials*, pages 148–156. International Society for Optics and Photonics.

[Pelrine et al., 2002] Pelrine, R., Kornbluh, R. D., Pei, Q., Stanford, S., Oh, S., Eckerle, J., Full, R. J., Rosenthal, M. A., et Meijer, K. (2002). **Dielectric elastomer artificial muscle actuators: toward biomimetic motion**. In *SPIE's 9th Annual International Symposium on Smart Structures and Materials*, pages 126–137. International Society for Optics and Photonics.

[Pérez et al., 2005] Pérez, R., Agnus, J., Clévy, C., Hubert, A., et Chaillet, N. (2005). **Modeling, fabrication, and validation of a high-performance 2-dof piezoactuator for micromanipulation**. *Mechatronics, IEEE/ASME Transactions on*, 10(2):161–171.

[Piriyanont et al., 2013] Piriyanont, B., et Moheimani, S. R. (2013). **Design, modeling, and characterization of a mems microgripper with an integrated electrothermal force sensor**. In *Advanced Intelligent Mechatronics (AIM), 2013 IEEE/ASME International Conference on*, pages 348–353. IEEE.

[Puliafito et al., 1995] Puliafito, C. A., Hee, M. R., Lin, C. P., Reichel, E., Schuman, J. S., Duker, J. S., Izatt, J. A., Swanson, E. A., et Fujimoto, J. G. (1995). **Imaging of macular diseases with optical coherence tomography**. *Ophthalmology*, 102(2):217–229.

[Qi et al., 2012] Qi, Z., Liang, P. C., Ting, M. Y., Rang, K. F., et Hua, F. Z. (2012). **Piezoelectric rotary motor based on active bulk torsional element with grooved helical electrodes**. *Mechatronics, IEEE/ASME Transactions on*, 17(2):260–268.

[Rakbamrung et al., 2010] Rakbamrung, P., Lallart, M., Guyomar, D., Muensit, N., Thanachayanont, C., Lucat, C., Guiffard, B., Petit, L., et Sukwisut, P. (2010). **Performance comparison of pzt and pmn–pt piezoceramics for vibration energy harvesting using standard or nonlinear approach**. *Sensors and Actuators A: Physical*, 163(2):493–500.

[Rastani et al., 1991] Rastani, K., Marrakchi, A., Habiby, S. F., Hubbard, W. M., Gilchrist, H., et Nahory, R. E. (1991). **Binary phase fresnel lenses for generation of two-dimensional beam arrays**. *Applied optics*, 30(11):1347–1354.

[Régnier et al., 2010] Régnier, S., et Chaillet, N. (2010). **Microrobotics for micromanipulation**. .

[Ren et al., 2010] Ren, B., Or, S. W., Zhang, Y., Zhang, Q., Li, X., Jiao, J., Wang, W., Liu, D., Zhao, X., et Luo, H. (2010). **Piezoelectric energy harvesting using shear mode 0.71 pb (mg1/3nb2/3) o3–0.29 pbtio3 single crystal cantilever**. *Applied Physics Letters*, 96(8):083502.

[Ren et al., 2006] Ren, K., Liu, Y., Geng, X., Hofmann, H. F., et Zhang, Q. M. (2006). **Single crystal pmn-pt/epoxy 1-3 composite for energy-harvesting application**. *Ultrasonics, Ferroelectrics, and Frequency Control, IEEE Transactions on*, 53(3):631–638.

[Ritter et al., 2002] Ritter, T., Shrout, T. R., Tutwiler, R., Shung, K. K., et others (2002). **A 30-mhz piezo-composite ultrasound array for medical imaging applications**. *Ultrasonics, Ferroelectrics, and Frequency Control, IEEE Transactions on*, 49(2):217–230.

[Sadoc et al., 2010] Sadoc, A., Mercey, B., Simon, C., Grebille, D., Prellier, W., et Lepetit, M.-B. (2010). **Large increase of the curie temperature by orbital ordering control**. *Physical review letters*, 104(4):046804.

[Sameoto et al., 2007] Sameoto, D., Tsang, S.-H., et Parameswaran, M. (2007). **Polymer mems processing for multi-user applications**. *Sensors and Actuators A: Physical*, 134(2):457–464.

[Sariola et al., 2010] Sariola, V., Jaaskelainen, M., et Zhou, Q. (2010). **Hybrid microassembly combining robotics and water droplet self-alignment**. *Robotics, IEEE Transactions on*, 26(6):965–977.

[Serruys et al., 1994] Serruys, P. W., de Jaegere, P., Kiemeneij, F., Macaya, C., Rutsch, W., Heyndrickx, G., Emanuelsson, H., Marco, J., Legrand, V., Materne, P., et others (1994). **A comparison of balloon-expandable-stent implantation with balloon angioplasty in patients with coronary artery disease**. *New England Journal of Medicine*, 331(8):489–495.

[Shanthi et al., 2009] Shanthi, M., et Lim, L. (2009). **Combined electric field and stress-induced ro phase transformation in [011]-poled pb (mg1/3nb2/3) o3-(28-32)% pbtio3 single crystals of [011]-length cut**. *Applied Physics Letters*, 95(10):2901.

[Shen et al., 2008] Shen, D., Park, J.-H., Ajitsaria, J., Choe, S.-Y., Wikle III, H. C., et Kim, D.-J. (2008). **The design, fabrication and evaluation of a mems pzt cantilever with an integrated si proof mass for vibration energy harvesting**. *Journal of Micromechanics and Microengineering*, 18(5):055017.

[Shen et al., 2014] Shen, Z.-Y., Tang, Y., Zhang, S., Luo, J., Li, Y., et Shrout, T. R. (2014). **Enhanced piezoelectric activity and temperature stability of [111]-oriented orthorhombic 0.68 pb (mg 1/3 nb 2/3) o 3–0.32 pbtio 3 single crystals by domain size engineering**. *Scripta Materialia*, 72:17–20.

[Sherlock et al., 2012] Sherlock, N. P., et Meyer Jr, R. J. (2012). **Modified single crystals for high-power underwater projectors**. *Ultrasonics, Ferroelectrics, and Frequency Control, IEEE Transactions on*, 59(6):1285–1291.

[Sherlock et al., 2010] Sherlock, N. P., Zhang, S., Luo, J., Lee, H.-Y., Shrout, T. R., et Meyer Jr, R. J. (2010). **Large signal electromechanical properties of low loss (1- x) pb (mg1/3nb2/3) o3- xpbtio3 single crystals**. *Journal of Applied Physics*, 107(7):074108.

[Shin et al., 2008] Shin, S. W., Qureshi, A. R., Lee, J.-Y., et Yun, C. B. (2008). **Piezoelectric sensor based nondestructive active monitoring of strength gain in concrete**. *Smart Materials and Structures*, 17(5):055002.

[Shung et al., 2007] Shung, K. K., Cannata, J., et Zhou, Q. (2007). **Piezoelectric materials for high frequency medical imaging applications: A review**. *Journal of Electroceramics*, 19(1):141–147.

[Siewert et al., 2002] Siewert, T., Liu, S., Smith, D., et Madeni, J. (2002). **Properties of lead-free solders, release 4.0**. *National Institute of Standards and Technology & Colorado School of Mines*.

[Silberberg et al., 1987] Silberberg, Y., Perlmutter, P., et Baran, J. (1987). **Digital optical switch**. *Applied Physics Letters*, 51(16):1230–1232.

[Sivak et al., 2000] Sivak, M. V., Kobayashi, K., Izatt, J. A., Rollins, A. M., Ung-Runyawee, R., Chak, A., Wong, R. C., Isenberg, G. A., et Willis, J. (2000). **High-resolution endoscopic imaging of the gi tract using optical coherence tomography**. *Gastrointestinal endoscopy*, 51(4):474–479.

[Smith et al., 1971] Smith, R., et Welsh, F. (1971). **Temperature dependence of the elastic, piezoelectric, and dielectric constants of lithium tantalate and lithium niobate**. *Journal of applied physics*, 42(6):2219–2230.

[Smith, 2005] Smith, R. C. (2005). **Smart material systems: model development**, volume 32. Siam.

[Smits et al., 1991] Smits, J. G., et Choi, W.-s. (1991). **The constituent equations of piezoelectric heterogeneous bimorphs**. *Ultrasonics, Ferroelectrics, and Frequency Control, IEEE Transactions on*, 38(3):256–270.

[Smolenskiy, 1972] Smolenskiy, G. A. (1972). **Ferroelectrics and antiferroelectrics**. Technical Report, DTIC Document.

[Spießberger et al., 2011] Spießberger, S., Schiemangk, M., Sahm, A., Wicht, A., Wenzel, H., Peters, A., Erbert, G., et Tränkle, G. (2011). **Micro-integrated 1 watt semiconductor laser system with a linewidth of 3.6 khz**. *Optics express*, 19(8):7077–7083.

[Srinivasan et al., 2001] Srinivasan, U., Liepmann, D., et Howe, R. T. (2001). **Microstructure to substrate self-assembly using capillary forces**. *Microelectromechanical Systems, Journal of*, 10(1):17–24.

[Sun et al., 2010] Sun, P., Wang, G., Wu, D., Zhu, B., Hu, C., Liu, C., Djuth, F. T., Zhou, Q., et Shung, K. K. (2010). **High frequency pmn-pt 1-3 composite transducer for ultrasonic imaging application**. *Ferroelectrics*, 408(1):120–128.

[Sun et al., 2002a] Sun, W., Noell, W., de Rooij, N., Herzig, H., Manzardo, O., et Dändliker, R. (2002a). **Optical mems based on silicon-on-insulator (soi) for monlithic optical microoptics**. In *LEOS Annual Meeting 2002*.

[Sun et al., 2005] Sun, Y., Fry, S. N., Potasek, D., Bell, D. J., et Nelson, B. J. (2005). **Characterizing fruit fly flight behavior using a microforce sensor with a new comb-drive configuration**. *Microelectromechanical Systems, Journal of*, 14(1):4–11.

[Sun et al., 2014] Sun, Y., et Kim, K. (2014). **Mems-based micro and nano grippers with two axis force sensors**. US Patent 8,623,222.

[Sun et al., 2002b] Sun, Y., Nelson, B. J., Potasek, D. P., et Enikov, E. (2002b). **A bulk microfabricated multi-axis capacitive cellular force sensor using transverse comb drives**. *Journal of Micromechanics and Microengineering*, 12(6):832.

[Sun et al., 2012] Sun, Y., Sheng, P., Di, C., Jiao, F., Xu, W., Qiu, D., et Zhu, D. (2012). **Organic thermoelectric materials and devices based on p-and n-type poly (metal 1, 1, 2, 2-ethenetetrathiolate) s**. *Advanced Materials*, 24(7):932–937.

[Syms et al., 2006] Syms, R., Zou, H., et Stagg, J. (2006). **Micro-opto-electromechanical systems alignment stages with vernier latch mechanisms**. *Journal of Optics A: Pure and Applied Optics*, 8(7):S305.

[Syms, 2005] Syms, R. R. (2005). **Optical mems in bonded silicon on insulator**. *Design Automation and Test in Eupre*, page 007.

[Syms et al., 2002] Syms, R. R., et Moore, D. F. (2002). **Optical mems for telecoms**. *Materials today*, 5(7):26–35.

[Tan et al., 2001] Tan, K., Lee, T. H., et Zhou, H. X. (2001). **Micro-positioning of linear-piezoelectric motors based on a learning nonlinear pid controller**. *Mechatronics, IEEE/ASME Transactions on*, 6(4):428–436.

[Tan, 2013] Tan, N. (2013). **Calibration of micro and nanorobotic systems: Contribution of influential parameters to the geometric accuracy.** PhD thesis, Université de Franche-Comté.

[Tang et al., 2014] Tang, G., Yang, B., Liu, J.-q., Xu, B., Zhu, H.-y., et Yang, C.-s. (2014). **Development of high performance piezoelectric d 33 mode mems vibration energy harvester based on pmn-pt single crystal thick film**. *Sensors and Actuators A: Physical*, 205:150–155.

[Tang et al., 2013] Tang, H., Zhang, M., Zhang, S., Feng, Y., Li, F., et Shrout, T. (2013). **Investigation of dielectric and piezoelectric properties in pb (ni 1/3 nb 2/3) o 3–pbhfo 3–pbtio 3 ternary system**. *Journal of the European Ceramic Society*, 33(13):2491–2497.

[Thomas et al., 2004] Thomas, D., et Duguid, G. (2004). **Optical coherence tomography—a review of the principles and contemporary uses in retinal investigation**. *Eye*, 18(6):561–570.

[Thompson et al., 2001] Thompson, J., et Fearing, R. S. (2001). **Automating microassembly with ortho-tweezers and force sensing**. In *Intelligent Robots and Systems, 2001. Proceedings. 2001 IEEE/RSJ International Conference on*, volume 3, pages 1327–1334. IEEE.

[Tiwari et al., 2013] Tiwari, P., Gupta, N., et Gupta, K. (2013). **Advanced thermoelectric materials in electrical and electronic applications**. In *Advanced Materials Research*, volume 685, pages 161–165. Trans Tech Publ.

[Tolfree et al., 2007] Tolfree, D., et Jackson, M. J. (2007). **Commercializing micro-nanotechnology products**. CRC Press.

[Tong et al., 2009] Tong, X., Lin, K., Lv, D., Yang, M., Liu, Z., et Zhang, D. (2009). **Optical properties of pmn–pt thin films prepared using pulsed laser deposition**. *Applied Surface Science*, 255(18):7995–7998.

[Tortschanoff et al., 2010] Tortschanoff, A., Lenzhofer, M., Frank, A., Wildenhain, M., Sandner, T., Schenk, H., Scherf, W., et Kenda, A. (2010). **Position encoding and phase control of resonant moems mirrors**. *Sensors and Actuators A: Physical*, 162(2):235–240.

[Toz et al., 2013] Toz, M., et Kucuk, S. (2013). **Dexterous workspace optimization of an asymmetric six-degree of freedom stewart–gough platform type manipulator**. *Robotics and Autonomous Systems*, 61(12):1516–1528.

[Tsai et al., 2005] Tsai, Y.-C., Lei, S. H., et Sudin, H. (2005). **Design and analysis of planar compliant microgripper based on kinematic approach**. *Journal of Micromechanics and Microengineering*, 15(1):143.

[Tuzcu et al., 2013] Tuzcu, I., et Gonzalez-Rocha, J. (2013). **Modeling and control of a thermoelastic beam**. In *ASME 2013 Dynamic Systems and Control Conference*, pages V001T06A004–V001T06A004. American Society of Mechanical Engineers.

[Uršič et al., 2008] Uršič, H., Hrovat, M., Holc, J., Santo Zarnik, M., Drnovšek, S., Maček, S., et Kosec, M. (2008). **A large-displacement 65pb (mg 1/3 nb 2/3) o 3–35pbtio 3/pt bimorph actuator prepared by screen printing**. *Sensors and Actuators B: Chemical*, 133(2):699–704.

[Van der Meer et al., 2012] Van der Meer, W. J., Andriessen, F. S., Wismeijer, D., Ren, Y., et Glogauer, M. (2012). **Application of intra-oral dental scanners in the digital workflow of implantology**. *PLoS One*, 7(8):e43312.

[Vasiliev et al., 1996] Vasiliev, Y. V., Akhmetshin, R., Borovliev, Y. A., Grigoriev, D., Gusev, V., Shlegel, V., et Smakhtin, V. (1996). **Bgo crystals grown by a low thermal gradient czochralski technique**. *Nuclear Instruments and Methods in Physics Research Section A: Accelerators, Spectrometers, Detectors and Associated Equipment*, 379(3):533–535.

[Wang et al., 2012] Wang, D., Cao, M., et Zhang, S. (2012). **Investigation of ternary system pbhfo3–pbtio3–pb (mg1/3nb2/3) o3 with morphotropic phase boundary compositions**. *Journal of the American Ceramic Society*, 95(10):3220–3228.

[Wang et al., 2013] Wang, D., Yang, Q., et Dong, H. (2013). **A monolithic compliant piezoelectric-driven microgripper: Design, modeling, and testing**. *Mechatronics, IEEE/ASME Transactions on*, 18(1):138–147.

[Wang et al., 2007] Wang, F., Luo, L., Zhou, D., Zhao, X., et Luo, H. (2007). **Complete set of elastic, dielectric, and piezoelectric constants of orthorhombic 0.71 pb (mg1/3nb2/3) o3-0.29 pbtio3 single crystal**. *Applied physics letters*, 90(21):2903.

[Wang et al., 2008a] Wang, L., Mills, J. K., et Cleghorn, W. L. (2008a). **Automatic microassembly using visual servo control**. *Electronics Packaging Manufacturing, IEEE Transactions on*, 31(4):316–325.

[Wang et al., 2008b] Wang, Q.-M., Sun, C., et Qin, L. (2008b). **Piezoelectric energy harvesting using single crystal pb (mg1/3nb2/3) o3-xpbtio3 (pmn-pt) device**. *Journal of Intelligent Material Systems and Structures*.

[Wang et al., 2010] Wang, Z., Yao, K., Deng, B., et Ding, K. (2010). **Quantitative study of metal magnetic memory signal versus local stress concentration**. *Ndt & E International*, 43(6):513–518.

[Wang et al., 2006] Wang, Z., Zhu, W., Miao, J., Zhu, H., Chao, C., et Tan, O. K. (2006). **Micromachined thick film piezoelectric ultrasonic transducer array**. *Sensors and Actuators A: Physical*, 130:485–490.

[Weber et al., 2012] Weber, N., Zappe, H., et Seifert, A. (2012). **A tunable optofluidic silicon optical bench**. *Microelectromechanical Systems, Journal of*, 21(6):1357–1364.

[Wei et al., 2012] Wei, Z., Huang, Y., Tsuboi, T., Nakai, Y., Zeng, J., et Li, G. (2012). **Optical characteristics of er 3+-doped pmn–pt transparent ceramics**. *Ceramics International*, 38(4):3397–3402.

[Weinberg, 1999] Weinberg, M. S. (1999). **Working equations for piezoelectric actuators and sensors**. *Microelectromechanical Systems, Journal of*, 8(4):529–533.

[Weis et al., 1985] Weis, R., et Gaylord, T. (1985). **Lithium niobate: summary of physical properties and crystal structure**. *Applied Physics A*, 37(4):191–203.

[Welzel, 2001] Welzel, J. (2001). **Optical coherence tomography in dermatology: a review**. *Skin Research and Technology*, 7(1):1–9.

[Wester et al., 2011] Wester, B. A., Rajaraman, S., Ross, J. D., LaPlaca, M. C., et Allen, M. G. (2011). **Development and characterization of a packaged mechanically actuated microtweezer system**. *Sensors and Actuators A: Physical*, 167(2):502–511.

[Wilkie et al., 2006] Wilkie, W. K., Inman, D. J., Lloyd, J. M., et High, J. W. (2006). **Anisotropic laminar piezocomposite actuator incorporating machined pmn–pt single-crystal fibers**. *Journal of Intelligent material systems and structures*, 17(1):15–28.

[Wolffenbuttel, 2005] Wolffenbuttel, R. (2005). **Mems-based optical mini-and microspectrometers for the visible and infrared spectral range**. *Journal of Micromechanics and Microengineering*, 15(7):S145.

[Woody et al., 2005] Woody, S. C., Smith, S. T., Jiang, X., et Rehrig, P. W. (2005). **Performance of single-crystal pb (mg1/ 3nb2/ 3)-32% pbtio3 stacked actuators with application to adaptive structures**. *Review of scientific instruments*, 76(7):075112.

[Wu et al., 1999] Wu, M. C., Solgaard, O., et Ford, J. E. (1999). **Optical mems for lightwave communication**. *Lightwave Technology, Journal of*, 24(12):4433–4454.

[Xiang-Xia et al., 2011] Xiang-Xia, M., Zhi-Yu, W., Zhi-Hai, Z., et Yuanjun, G. (2011). **Analysis and experiment of encoding errors for moems micro mirror spectrometer**. *Physics Procedia*, 19:285–290.

[Xie et al., 2003] Xie, H., Pan, Y., et Fedder, G. K. (2003). **Endoscopic optical coherence tomographic imaging with a cmos-mems micromirror**. *Sensors and Actuators A: Physical*, 103(1):237–241.

[Xu et al., 2001] Xu, G., Luo, H., Guo, Y., Gao, Y., Xu, H., Qi, Z., Zhong, W., et Yin, Z. (2001). **Growth and piezoelectric properties of pb (mg 1/3 nb 2/3) o 3–pbtio 3 crystals by the modified bridgman technique**. *Solid state communications*, 120(7):321–324.

[Yamamoto et al., 2013] Yamamoto, N., Yamashita, Y., Hosono, Y., et Itsumi, K. (2013). **Electrical and physical properties of repoled pmn–pt single-crystal sliver transducer**. *Sensors and Actuators A: Physical*, 200:16–20.

[Yamashita et al., 1997] Yamashita, Y., et Harada, K. (1997). **Crystal growth and electrical properties of lead scandium niobate-lead titanate binary single crystals**. *Japanese journal of applied physics*, 36(9S):6039.

[Yan et al., 2011] Yan, T., Zhang, J., Feng, G., et Chen, J. (2011). **Early inspection of wet steam generator tubes based on metal magnetic memory method**. *Procedia Engineering*, 15:1140–1144.

[Yang et al., 2010] Yang, C., Shi, K., Edwards, P., et Liu, Z. (2010). **Demonstration of a pdms based hybrid grating and fresnel lens (g-fresnel) device**. *Optics express*, 18(23):23529–23534.

[Yasuda et al., 2002] Yasuda, N., Ohwa, H., Hasegawa, D., Hosono, H., Yamashita, Y., Iwata, M., et Ishibashi, Y. (2002). **Dielectric and piezoelectric properties of lead indium niobate-lead titanate single crystal with high curie temperature near morphotropic phase boundary**. *Ferroelectrics*, 270(1):247–252.

[Yasuda et al., 2001] Yasuda, N., Ohwa, H., Kume, M., Hayashi, K., Hosono, Y., et Yamashita, Y. (2001). **Crystal growth and electrical properties of lead indium niobate–lead titanate binary single crystal**. *Journal of crystal growth*, 229(1):299–304.

[Yeow et al., 2001] Yeow, T.-W., Law, K. E., et Goldenberg, A. (2001). **Mems optical switches**. *Communications Magazine, IEEE*, 39(11):158–163.

[Yi et al., 2009] Yi, J., Chang, S., et Shen, Y. (2009). **Disturbance-observer-based hysteresis compensation for piezoelectric actuators**. *Mechatronics, IEEE/ASME Transactions on*, 14(4):456–464.

[Yokoyama et al., 1992] Yokoyama, Y., Miura, T., Tsai, A.-P., Inoue, A., et Masumoto, T. (1992). **Preparation of a large al 70 pd 20 mn 10 single-quasicrystal by the czochralski method and its electrical resistivity**. *Materials Transactions, JIM*, 33(2):97–101.

[Yoon et al., 2015] Yoon, S., Williams, J., Kang, B. J., Yoon, C., Cabrera-Munoz, N., Jeong, J. S., Lee, S. G., Shung, K. K., et Kim, H. H. (2015). **Angled-focused 45mhz pmn-pt single element transducer for intravascular ultrasound imaging**. *Sensors and Actuators A: Physical*, 228:16–22.

[Yoshida, 2010] Yoshida, R. (2010). **Self-oscillating gels driven by the belousov–zhabotinsky reaction as novel smart materials**. *Advanced Materials*, 22(31):3463–3483.

[Yu et al., 2006] Yu, K., Lee, D., Krishnamoorthy, U., Park, N., et Solgaard, O. (2006). **Micromachined fourier transform spectrometer on silicon optical bench platform**. *Sensors and Actuators A: Physical*, 130:523–530.

[Yu et al., 2005] Yu, Y., et Ikeda, T. (2005). **Photodeformable polymers: A new kind of promising smart material for micro-and nano-applications**. *Macromolecular Chemistry and Physics*, 206(17):1705–1708.

[Zawilski et al., 2005] Zawilski, K. T., DeMattei, R. C., et Feigelson, R. S. (2005). **Zone leveling of lead magnesium niobate–lead titanate crystals using rf heating**. *Journal of crystal growth*, 277(1):393–400.

[Zhang et al., 2015a] Zhang, J., Ren, W., Jing, X., Shi, P., et Wu, X. (2015a). **Deep reactive ion etching of pzt ceramics and pmn-pt single crystals for high frequency ultrasound transducers**. *Ceramics International*.

[Zhang et al., 2011a] Zhang, K., Choy, S.-H., Zhao, L., Luo, H., Chan, H. L.-W., et Wang, Y. (2011a). **Shear-mode pmn-pt piezoelectric single crystal resonator for microfluidic applications**. *Microelectronic Engineering*, 88(6):1028–1032.

[Zhang et al., 2002a] Zhang, Q., Li, H., Poh, M., Xia, F., Cheng, Z.-Y., Xu, H., et Huang, C. (2002a). **An all-organic composite actuator material with a high dielectric constant**. *Nature*, 419(6904):284–287.

[Zhang et al., 2014] Zhang, Q., Sun, Y., Xu, W., et Zhu, D. (2014). **Organic thermoelectric materials: emerging green energy materials converting heat to electricity directly and efficiently**. *Advanced Materials*, 26(40):6829–6851.

[Zhang et al., 2006] Zhang, R., Jiang, B., Jiang, W., et Cao, W. (2006). **Complete set of elastic, dielectric, and piezoelectric coefficents of 0.93 pb „zn nb 2/3... o 3–0.07 pbtio 3 single crystal poled along† 011**. *Applied physics letters*, 89:242908.

[Zhang et al., 2015b] Zhang, S., Li, F., Jiang, X., Kim, J., Luo, J., et Geng, X. (2015b). **Advantages and challenges of relaxor-pbtio 3 ferroelectric crystals for electroacoustic transducers–a review**. *Progress in materials science*, 68:1–66.

[Zhang et al., 2008] Zhang, S., Luo, J., Hackenberger, W., et Shrout, T. R. (2008). **Characterization of pb (in1/2nb1/2) o3–pb (mg1/3nb2/3) o3–pbtio3 ferroelectric crystal with enhanced phase transition temperatures**. *Journal of applied physics*, 104(6):064106.

[Zhang et al., 2003] Zhang, S., Randall, C. A., et Shrout, T. R. (2003). **High curie temperature piezocrystals in the bisco3-pbtio3 perovskite system**. *Applied physics letters*, 83(15):3150–3152.

[Zhang et al., 2004a] Zhang, S., Randall, C. A., et Shrout, T. R. (2004a). **Characterization of perovskite piezoelectric single crystals of 0.43 bisco3-0.57 pbtio3 with high curie temperature**. *Journal of applied physics*, 95(8):4291–4295.

[Zhang et al., 2004b] Zhang, S., Randall, C. A., et Shrout, T. R. (2004b). **Dielectric, piezoelectric and elastic properties of tetragonal bisco 3-pbtio 3 single crystal with single domain**. *Solid state communications*, 131(1):41–45.

[Zhang et al., 2002b] Zhang, S., Rhee, S., Randall, C. A., et Shrout, T. R. (2002b). **Dielectric and piezoelectric properties of high curie temperature single crystals in the pb (yb1/2nb1/2) o3–xpbtio3 solid solution series**. *Japanese journal of applied physics*, 41(2R):722.

[Zhang et al., 2011b] Zhang, Y., Wang, S., Liu, D., Zhang, Q., Wang, W., Ren, B., Zhao, X., et Luo, H. (2011b). **Fabrication of angle beam two-element ultrasonic transducers with pmn–pt single crystal and pmn–pt/epoxy 1–3 composite for nde applications**. *Sensors and Actuators A: Physical*, 168(1):223–228.

[Zhao et al., 2009] Zhao, S., Li, Q., Feng, Y., et Nan, C. (2009). **Microstructure and dielectric properties of pmn–pt ceramics prepared by the molten salts method**. *Journal of Physics and Chemistry of Solids*, 70(3):639–644.

[Zhao et al., 2003] Zhao, X., Wang, J., Chan, H., Choy, C., et Luo, H. (2003). **Effect of a bias field on the dielectric properties of 0.69 pb (mg1/3nb2/3) o3–0.31 pbtio3 single crystals with different orientations**. *Journal of Physics: Condensed Matter*, 15(40):6899.

[Zhihai et al., 2011] Zhihai, Z., Xiangxia, M., Yuanjun, G., et Wei, W. (2011). **A novel moems nir spectrometer**. *Physics Procedia*, 19:110–114.

[Zhong et al., 2006] Zhong, Z., et Yeong, C. (2006). **Development of a gripper using sma wire**. *Sensors and Actuators A: Physical*, 126(2):375–381.

[Zhou et al., 2012] Zhou, L., Sun, J., Zheng, X., Deng, S., Zhao, J., Peng, S., Zhang, Y., Wang, X., et Cheng, H. (2012). **A model for the energy harvesting performance of shear mode piezoelectric cantilever**. *Sensors and Actuators A: Physical*, 179:185–192.

[Zou et al., 2001] Zou, J., Chen, J., Liu, C., et Schutt-Ainé, J. E. (2001). **Plastic deformation magnetic assembly (pdma) of out-of-plane microstructures: technology and application**. *Microelectromechanical Systems, Journal of*, 10(2):302–309.

[Zuwei et al., 2012] Zuwei, Z., Zhiyu, W., Zhengguo, S., Dongling, L., et Jing, H. (2012). **Design and process test of a novel moems accelerometer based on raman—nath diffraction**. *Journal of Semiconductors*, 33(9):094009.

List of Figures

LIST OF TABLES

Document generated with LaTeX and:
the LaTeX style for PhD Thesis created by S. Galland — http://www.multiagent.fr/ThesisStyle
the tex-upmethodology package suite — http://www.arakhne.org/tex-upmethodology/

Abstract:

This work proposes the use of a novel material, called PMN-PT, that futher aids the miniaturization of complex systems used in different technologies. The work is presented within the collaborative framework of two projects, MIOP and ADMAN. The end-needs account for actuators capable of delivering high displacement, while maintaining system simplicity and reliability. The focus is on the versatility of the PMN-PT piezoelectric material, due to its electro-mechanical properties. The work includes an overview on what influences the electro-mechanical properties focusing on two different, though very potent cuts: anisotropic [011] and longitudinal [001]. They were chosen for generating large displacement and high dynamics with small volume. For PMN-PT[001] a cantilever structure was studied, for which the model was improved taking into account the material specificities. Displacements and forces were found to be superior to a similarly dimensioned PZT actuator, whilst having reduced non-linearities. This is exemplified with a 6 DoF capable microgripper. The PMN-PT[001] longitudinal cut based actuator study follows. This is done by using PMN-PT as a simple, easy to integrate, bulk actuator. The findings demonstrate the improvements PMN-PT can bring to micro-spectrometry and image correction with micro-mirror displacement. A bulk PMN-PT micro actuator was integrated into a MOEMS compatible structure and presented.

Keywords: PMN-PT, piezoelectric actuator, microgripper, dexterous, optics, MOEMS, Reconfigurable Free Space Micro Optical Bench

Résumé :

Ce travail propose l'utilisation d'un nouveau matériau, appelé PMN-PT, qui continue aider la miniaturisation des systèmes complexes, utilisés dans des différentes technologies. Le travail est présenté dans le cadre de collaboration entre deux projets, MIOP et ADMAN. Les besoins tien compte que les actionneurs soient capables de délivrer de haute déplacement tout en conservant la simplicité et la fiabilité du système. L'accent est mis sur la polyvalence de ce matériau piézo-électrique, PMN-PT, en raison de ses propriétés électro-mécanique. Le travail comprend un aperçu sur quoi influence les propriétés électro-mécaniques du PMN-PT. L'accent est mis sur deux différentes, mais très puissants coupes: anisotrope [011] et longitudinale [001], choisi pour grand déplacement et haute dynamique avec un volume petit. Pour le PMN-PT[001], une structure de type poutre a été étudié, avec un modèle amélioré pour prendre en compte les spécificités de matériel. Les déplacements et forces ont été trouvés d'être supérieur à un actionneur en PZT, similairement dimensionnée, tandis que avoir des non-linéarités réduites. Ceci est illustré avec une micropince avec 6DDL. L'étude de PMN-PT [001] coupé longitudinal suit. Cette étude a été fait en utilisant PMN-PT comme un actionneur avec une structure simple, facile à intégrer. Les résultats démontrent les améliorations PMN-PT peut apporter à micro-spectrométrie et la correction d'image avec des micro-miroir mobiles. Un micro actionneur PMN-PT a été intégré dans une structure compatible avec des MOEMS et présenté.

Mots-clés : PMN-PT, Actuateur piezoelectrique, micropince, dexterité, optique, MOEMS, Micro Banc Optique Reconfigurable

SPIM

■ École doctorale SPIM 16 route de Gray F - 25030 Besançon cedex
■ tél. +33 (0)3 81 66 66 02 ■ ed-spim@univ-fcomte.fr ■ www.ed-spim.univ-fcomte.fr

UFC
UNIVERSITÉ DE FRANCHE-COMTÉ